UNIVERSITAT DE BARCELONA

New therapeutic approaches to modulate metabolic alterations in the cardiovascular system. In vivo studies

Aleyda Benítez Amaro

UNIVERSITAT DE BARCELONA

DOCTORAL THESIS

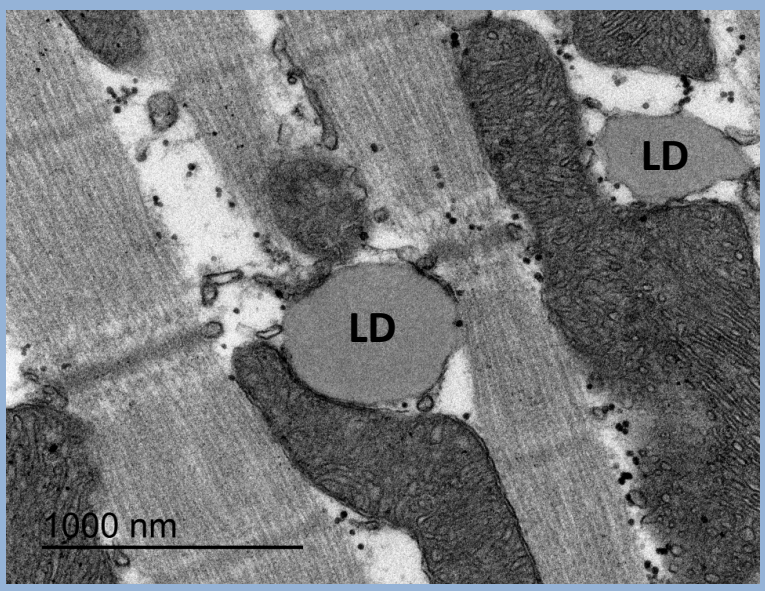

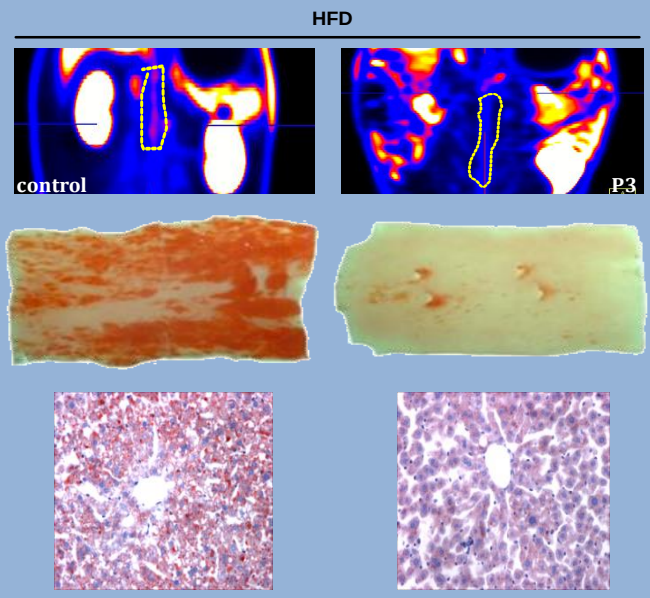

New therapeutic approaches to modulate metabolic alterations in the cardiovascular system. In vivo studies

Aleyda Benítez Amaro

2022

Doctoral Thesis

New therapeutic approaches to modulate metabolic alterations in the cardiovascular system. *In vivo* studies

Aleyda Benítez Amaro

Doctoral Program in Biomedicine

Faculty of Biology

University of Barcelona

Institute of Biomedical Research of Barcelona

Barcelona, December 2022

University of Barcelona
Faculty of Biology
Doctoral Program in Biomedicine
Institute of Biomedical Research of Barcelona (IIBB-CSIC)

New therapeutic approaches to modulate metabolic alterations in the cardiovascular system. *In vivo* studies

Manuscript presented by Aleyda Benítez Amaro in order to obtain the degree of Doctor of Philosophy by the University of Barcelona.

This thesis has been completed in the Lipids and Cardiovascular Pathology group directed by Dra. Concepción Vicenta Llorente Cortés

Director
Dra. Concepción Vicenta Llorente Cortés
Institute of Biomedical Research of Barcelona (IIBB-CSIC)

Tutor
Dr. Antonio Zorzano Olarte
Department of Biochemistry and Molecular Biomedicine, University of Barcelona.

Doctoral candidate
Aleyda Benítez Amaro
Institute of Biomedical Research of Barcelona (IIBB-CSIC)

INDEX

INDEX

FIGURE INDEX

FIGURE INDEX

TABLE INDEX

TABLE INDEX

ABSTRACT

ABSTRACT

Background: Low-density lipoprotein receptor-related protein 1 (LRP1) plays a key role in fatty acid metabolism and glucose homeostasis. In the context of dyslipidemia, LRP1 is positively regulated in the heart. The LRP1 domain (CR9) and, in particular, the sequence Gly^{1127}-Cys^{1140} (P3 peptide) is essential in the binding and internalization of aggregated LDL (agLDL). AgLDL internalization leads to intracellular cholesterol ester (CE) loading and foam cell formation in different cell types. The link between intracellular CE accumulation and insulin response is largely unknown. The first study aimed to evaluate the impact of cardiomyocyte *Lrp1* deficiency on high-fat diet (HFD)-induced cardiac and metabolic alterations in a murine model and to explore the possible mechanisms involved. In the second and third studies, we aimed to evaluate whether immunization of rabbits with the P3 peptide reduces HFD-induced atherosclerosis and HFD-induced alterations in cardiac insulin response, respectively.

Methods Study I: We used TnT-iCre transgenic mice to generate an experimental mouse model with conditional *Lrp1* deficiency in cardiomyocytes (TNT-$iCre^{+}$-$LRP1^{flox/flox}$). cm-$Lrp1^{-/-}$ (deficient) and cm-$Lrp1^{+/+}$ (control) mice were fed with HFD and treated daily with Doxycycline Cyclate in drinking water for six weeks to inhibit *Lrp1*. After two weeks, mice were randomly assigned to untreated (PBS) or treated with natriuretic peptide receptor type A (NPRA) inhibitor until the end of the experiment. The indirect calorimetry study was performed at week 5 and glucose tolerance test at week 6. At the end of the experiment, target tissues were collected for molecular, lipidic, proteomic and immunohistochemical studies.

Methods Study II and III: Rabbits immunized with irrelevant peptides (IrP) or P3 were randomized into HFD- or Chow-fed groups. Anti-P3 antibody (Abs) levels were determined by ELISA. Lipoprotein profile, circulating and tissue lipids, and vascular proinflammatory mediators were determined by standardized methods. Atherosclerosis was determined by confocal microscopy and noninvasive imaging studies. LRP1, Insulin receptor (InsR) and glucose transporter type 4 (GLUT4) levels were determined in rabbit heart membranes and total lysates. The interaction between InsR and LRP1 was analyzed by immunoprecipitation and confocal microscopy. *Ex-vivo* studies of cultured human macrophages (hMΦ), HL-1 cardiomyocytes, and vascular smooth muscle cells (VSMC) exposed to rabbit serum were conducted to explore the cell-specific effects of anti-P3 Abs.

Findings of the studies: cm-$Lrp1^{-/-}$ mice have normal cardiac function combined with a favorable metabolic phenotype against HFD-induced glucose intolerance and obesity. Protection against glucose intolerance was associated with higher hepatic fatty acid oxidation (FAO), lower hepatic steatosis, and higher whole-body energy expenditure. Proteomic studies of the heart revealed reduced levels of cardiac pro-atrial natriuretic peptide (pro-ANP), which paralleled higher circulating levels and signaling of ANP.

In the rabbit model, anti-P3 Abs reduced HFD-induced vascular CE accumulation and intracellular CE loading of hMΦ and VSMC as well as HFD-induced pro-inflammatory effects in these cells. Microscopy studies revealed that anti-P3 abs reduced the percentage of lipids, macrophages, and SMCs in the arterial intima, as well as the atherosclerotic extent and injured area in the aorta of hypercholesterolemic rabbits. Noninvasive imaging studies showed that aortic standardized mean uptake value (SUVmean) and carotid arterial resistance index (ARI) were upregulated by HFD to a much higher extent in control groups than in the P3-immunized group. In addition, anti-P3 abs not only decreases the amount of HFD-induced generation of lipid droplets (LDs) and glycogen drops into cardiomyocytes but also modify LD size, content and electrodensity. In addition, anti-P3 Abs restored the downregulatory effect of HFD on membrane InsR and GLUT4 levels as well as on LRP1/InsR interactions in rabbit hearts, and normalized the insulin signaling cascade and glucose uptake in HL-1 cells exposed to rabbit HFD serums.

ABBREVIATIONS

ABBREVIATIONS

5HT2C: 5-hydroxytryptamine2c receptor

AAV: Adeno-associated viral

ACAP1: ANK repeat and PH domain-containing protein 1

ACC: Acetyl-CoA carboxylase

AGE: Advanced glycation end-product

Akt: Protein kinase B

AMPK: Adenosine monophosphate-activated protein kinase

ANGPTL2: Angiopoietin-like protein 2

ANP: Atrial natriuretic peptide

ApoB48: Apolipoprotein B48

ApoC-II: Apolipoprotein C-II

ApoE: Apolipoprotein E

AS160: Akt Substrate 160 kDa

BACE1: β-site APP cleaving enzyme 1

BAT: Brown adipose tissue

BMI: Body mass index

BMPER: Bone morphogenetic protein-binding endothelial regulator

BNP: Brain natriuretic peptide

CatS: Cathepsin S

CE: Cholesterol ester

CETP: Cholesteryl ester transfer protein

cGKs: cGMP-dependent protein kinases

cGMP: Cyclic guanosine monophosphate

CLAMS: Comprehensive lab animal monitoring system

CNP: C-type natriuretic peptide

CPT1: Carnitine palmitoyl transferase I

CR: Cysteine-rich complement-type repeat

CTGF: Connective tissue growth factor

DGAT: Acyl-CoA:diacylglycerol acyltransferase

ERK1/2: Extracellular signal-regulated kinase ½

eWAT: Epididymal white adipose tissue

FA: fatty acids

FAO: Fatty acid oxidation

FAS: Fatty acid synthase

FAST: Fibro Scan-AST

FC: Free cholesterol

FFA: Free fatty acids

GGA: ADP-ribosylation factor (ARF)-binding proteins

GLP-1: Glucagon-like peptide-1

GLUT3: Glucose transporters type 3

GLUT4: Glucose transporters type 4

GSK3: Glycogen synthase kinase 3

GTP: Guanosine-5'-triphosphate

GTT: Glucose tolerance test

HbA1c: Glycated hemoglobin

HCC: Hepatocellular carcinoma

HDL: High-density lipoprotein

HFD: High fat diet

HL: Hepatic Lipase

HMG-CoA: 3-hydroxy-3-methylglutaryl-coenzyme A reductase

IDL: Intermediate-density lipoprotein

IKK-β: Inhibitor kB kinase β

IL-18: Interleukin 18

IL-1β: Interleukin 1β

IL-6: Interleukin 6

InsR: Insulin receptor

iPSCs: Induced pluripotent stem cells

IRAK-1: Interleukin-1 receptor associated kinase-1

IRS-1: Insulin receptor substrate-1

JNK: c-Jun N-terminal kinase

LDL: Low-density lipoprotein

LDLR: Low density lipoprotein receptor

LpL: Lipoprotein lipase

LRP1: Low-density lipoprotein receptor-related protein-1

MGAT: Acyl-CoA:monoacylglycerol acyltransferase

mGPD: Mitochondrial glycerophosphate dehydrogenase

MMPs: Matrix metalloproteinases

NAFL: Nonalcoholic fatty liver

NAFLD: Nonalcoholic fatty liver disease

NASH: Nonalcoholic steatohepatitis

NFATc1: Nuclear factor of activated T cells 1

NF-κB: Nuclear factor kappa B

NP: Natriuretic peptides

NPRA: Natriuretic peptide receptor A

NPRB: Natriuretic peptide receptor B

NPRC: Natriuretic peptide receptor C

OFG: Oral fat gavage

PAI-1: Plasminogen activator inhibitor-1

PCSK9: Proprotein convertase subtilisin/kexin type 9

PI3K: Phosphatidylinositol 3-kinase

PN1: Protease nexin 1

pVASP: Phosphorylated VASP

Rab-GDP: Rab-bound guanosine diphosphate

Rab-GTP: Rab-bound guanosine triphosphate

RAGE: AGE receptor

RAP: Receptor associated protein

RBP-4: Retinol-binding protein 4

RCT: Reverse cholesterol transport

ROS: Reactive oxygen species

RyR: Ryanodine receptors

SERCA2: Sarco (endo) reticulum plasma calcium ATPase-2 protein

SGLT2: Sodium glucose cotransporter-2

sLRP1: Soluble LRP1

SMC: Smooth muscle cell

T1DM: Diabetes mellitus type 1

T2DM: Diabetes mellitus type 2

TF: Tissue factor

TG: Triglycerides

TGF-β: Transforming growth factor-β

TNF-R1: Tumor necrosis factor receptor-1

TNF-α: Tumor necrosis factor-alpha

VASP: Vasodilator stimulated phosphoprotein

VLDL: Very-low-density lipoprotein

VSMC: Vascular smooth muscle cells

WHO: World Health Organization

Wnt5a: Wnt family member 5A

GENERAL INTRODUCTION

GENERAL INTRODUCTION

1 Causes of metabolic disorders in the cardiovascular system and potential treatments

Metabolism involves a complex chain of interconnected chemical reactions that occur inside the cells to produce energy [1]. Metabolic dysfunction is involved in the pathophysiology of several diseases, including cardiovascular disease. In this chapter, the principal causes of metabolic disorders and the current treatment will be discussed.

1.1 Obesity

The World Health Organization (WHO) has defined overweight and obesity as an abnormal or excessive storage of fat that constitutes a health problem. According to WHO statistics, more than 4 million people die each year as a result of this disease. The WHO uses the body mass index (BMI) to classify body fat at the population level (Table 1). In adults, "overweight" is defined as a BMI equal or greater than 25 kg/m^2, and "obesity", a BMI equal or greater than 30 kg/m^2 [2]. However, due to the great variability in the clinical manifestations of obesity, it cannot be classified by BMI alone. For instance, the BMI index is not a completely effective diagnostic tool in adults over 65 years of age due to their sarcopenic obesity. Sarcopenic obesity, which is characteristic of aging, is defined as the loss of muscle mass, strength, and/or physical function. This leads to patients with comparable body weight or BMI scores exhibiting different health risk levels [3,4].

General information	BMI (kg/m^2)	Weight Range	Health risk
Underweight	< 18.5	124 lbs or less	Minimal
Healthy weight	18.5 to <25	125 lbs to 168 lbs	Minimal
Overweight	25 to <30	169 lbs to 202 lbs	Increased
Obesity class I	30 to < 35	203 lbs or more	High
Obesity class II	35 to < 40	203 lbs or more	Very high
Obesity class III	≥ 40	271 lbs or more	Extremely high

Table 1. Body mass index-based WHO classification of obesity (adapted from [2]). lbs: pounds

Obesity contributes to an increased cardiovascular risk through direct and indirect mechanisms. Direct mechanisms include the structural and functional adjustments of the cardiovascular system to become adapted to the body weight excess and excessive adipokine production. Indirect mechanisms include insulin resistance, type 2 diabetes mellitus (T2DM), visceral adiposity, hypertension, and dyslipidemia [5].

The main cardiac adjustments that occur in obese patients include elevation in circulating blood volume due to higher sodium retention, resulting in intravascular volume expansion.

To satisfy the metabolic requirements of an oversized adipose tissue, the sympathetic nervous system increases stroke volume and heart rate, leading to increased cardiac output and finally elevated systemic vascular resistance caused by reduced-grade inflammation, hyperinsulinemia, excessive sympathetic activity and respiratory sleep disturbances. All these alterations lead to dilatation and hypertrophy of the left ventricle and enlargement of the left atrium [5].

In obesity, adipose tissue undergoes uncontrolled growth and hypertrophy that, combined with decreased tissue vascularization, results in hypoxia and adipocyte apoptosis. Apoptotic cells trigger macrophage infiltration and the onset of an inflammatory response. This adipose tissue dysfunction promotes the release of proinflammatory adipokines, including leptin, tumor necrosis factor α (TNF-α), interleukin 6 (IL-6), interleukin 18 (IL-18), resistin, retinol-binding protein 4 (RBP-4), lipocalin 2 and angiopoietin-like protein 2 (ANGPTL2) which are highly atherogenic [5]. IL-6, interleukin 1β (IL-1β), TNF-α, and free fatty acids (FFA) are involved in activating c-Jun N-terminal kinase (JNK) and inhibitor kB kinase β (IKK-β) in the adipose tissue. JNK activation triggers insulin receptor substrate-1 (IRS-1) phosphorylation, insulin signaling alterations, systemic insulin resistance, metabolic syndrome, and T2DM [6].

Current treatments for obesity combine lifestyle, pharmacological, and surgical procedures [4]. The less expensive and less dangerous option to achieve weight control in patients with obesity is lifestyle modification. Behavioral counseling and high intensity therapies focused on diet improvements and physical activity cause a moderate weight loss. However, weight regain is very common, and patients have to be usually encouraged to continue receiving long-term behavioral counseling after intensive therapy completion [7].

Orlistat is one of the drugs prescribed for the treatment of obesity. This drug causes a decrease in the absorption of fats from the diet by inhibiting pancreatic and gastric lipase. Other drugs, such as lorcaserin, increase the feeling of satiety, thereby promoting a decrease in food intake by acting as an agonist of the serotonin receptor 5-hydroxytryptamine 2c (5HT2c). Liraglutide uses the mechanism of a glucagon-like peptide-1 (GLP-1) agonist to slow down gastric depletion and reduce food consumption. There are also combinations of drugs, such as phentermine/topiramate and naltrexone/bupropion, which reduce food intake by different mechanisms. Phentermine/topiramate induces the release of norepinephrine (phentermine) along with the modulation of gamma-aminobutyric acid (GABA) receptor (topiramate). Naltrexone/bupropion is a potent opioid blocker (naltrexone) and promotes suppression of dopamine and norepinephrine reuptake (bupropion). Of note, none of these drugs are suitable for use during pregnancy or by patients with thyroid problems [7].

There are three main types of bariatric surgery: adjustable gastric banding, gastric bypass, and sleeve gastrectomy. Laparoscopic adjustable gastric banding is a minimally invasive and reversible procedure that involves inserting an adjustable silicone band into the gastric fundus to create a small bag. Another procedure is the Roux-en-Y gastric bypass, in which surgeons place a band in the upper gastric fundus that attaches to a Roux-en-Y branch of the jejunum. Both surgeries are aimed at reducing food intake. Vertical sleeve gastrectomy consists of removing 70% of the stomach, reducing the ability to process food and leading to reaching satiety more quickly. The limitation of these surgeries are a high cost, a considerable risk of complications, and the possibility of regaining weight within a few years after the operation [7]. All of these therapies aim to reduce the escalating epidemic of obesity and associated cardiovascular diseases around the world by creating healthier lifestyles.

1.2 Diabetes mellitus

Diabetes mellitus is a chronic disease with a high prevalence on a worldwide basis. According to the International Diabetes Federation, 1 in 10 people across the world will develop Diabetes mellitus by 2035 [8]. The disease has two main types: diabetes mellitus type 1 (T1DM) and T2DM (Table 2). T2DM is the most prevalent in many countries [9–11].

Classification	Characteristics	Causes	Treatment	Epidemiology	Associated disease	Ref
Gestational	Occurs during pregnancy. Insulin deficiency and hyperglycemia.	Placental secretion of diabetogenic hormones	Insulin and oral equivalent drugs	Global prevalence of 13.2%.	Fetal macrosomia, Obesity and T2DM	[12–14]
T1DM	Autoimmune Reaction (participation of innate and adaptive immunity)	Insulin deficiency due to pancreatic β-cells damage	Insulin	Prevalence of 9.5% worldwide	Obesity, Metabolic syndrome	[15,16]
T2DM	Polygenic and affected by environment	Insufficient insulin secretion and response in peripheral tissues	Metformin and others drugs, in certain circumstances insulin	6.28% of the world population	Obesity, Aging	[15,17]
T3DM (Alzheimer's)	Deficiencies in Brain glucose leading to neurodegeneration. Tau gene expression and	Neuronal cytoskeleton breakdown and deposition of hyperphosphorylated and	Aducanumab	50–70% of cases	T2DM, Obesity	[18–20]

	phosphorylation is controlled by the insulin/IGF pathway.	polyubiquitinated microtubule-associated proteins				
Secondary	Medication related effect, pancreatic malfunction or rare autoimmune disorders	Different causes (antagonization of insulin by different hormones, drug or chemical abuse, infections)	There are different treatments adapted to the pathogenesis of the disease.	1%-2% of all diabetes cases	T2DM, Obesity and Metabolic syndrome	[21,22]
Genetic (MODY)	Development of Hyperglycemia at a young age	Genetic defects in insulin secretion with minimal or no defects in insulin action	Glucose-lowering medications	1-5% of all diabetes cases	Monogenic Diabetes	[21,23]

Table 2. Characteristics of the different types of diabetes mellitus. IGF: Insulin-like growth factor, MODY: Maturity onset diabetes of the young

Diabetes mellitus causes significant structural and functional changes in the heart muscle that lead to cardiovascular alterations and subsequently to death. These changes in the myocardium are known as diabetic cardiomyopathy. Among the molecular mechanisms that have been described to explain this process is the so-called advanced glycation end products (AGEs) [24]. AGEs are molecules that have undergone irreversible alterations due to reactions involving sugars and the amino groups on proteins and nucleic acids. The formation of AGEs increases with hyperglycemia, and their uncontrolled accumulation causes myocardial stiffness because they provoke structural modifications in collagen, making their elimination more difficult. When AGEs are recognized by their receptor (RAGE), they activate signaling cascades that result in vascular fibrosis, calcification, inflammation, prothrombotic effects, and vascular damage [25].

The large amount of collagen deposits in the heart of diabetics has been related to an increase in the activity of transforming growth factor-β (TGF-β) and connective tissue growth factor (CTGF), both of which induce collagen formation. In addition, uncontrolled degradation of the extracellular matrix has been observed as a consequence of alterations in the expression of matrix metalloproteinases (MMPs) leading to higher connective tissue production [26].

Another molecular mechanism leading to the development of diabetic cardiomyopathy is enhanced inflammation. Increased glucotoxicity and lipotoxicity in diabetes have been linked to enhanced macrophage and leukocyte infiltration as well as to elevated levels of inflammatory cytokines. Other factor that augments inflammation is oxidative stress, which leads to an increased generation of reactive oxygen species (ROS). ROS can interact with

DNA and activate redox-sensitive signaling pathways. In addition, activation of redox-sensitive protein kinase C leads to mitochondrial dysfunction, oxidative stress, and endoplasmic reticulum damage [25].

Several treatments for diabetes based on gene therapy are currently under development. Different insulin-related genes have been delivered to various tissues using lentivirus, adenovirus, adeno-associated virus (AAV), and particles such as liposomes and naked DNA [27].

Both T1DM and T2DM are characterized by a total or partial loss of β-cells; therefore, some current treatments aim to replenish these lost cells. An example of such treatments is the induction of transdifferentiation of ductal cells into β-cells, which has been shown to be effective in improving insulin production in pancreas. Further attempts were made to transdifferentiate pancreatic progenitor cells or α-cells into β-cells. Currently, induced pluripotent stem cells (iPSCs) have become an alternative for the treatment of diabetes. One main advantage of iPSCs is that they come from the patients themselves and are therefore not recognized by the immune system [27].

One of the most widely used drugs for the treatment of diabetes is metformin. This drug is implicated in the upregulation of AMP-activated protein kinase (AMPK) as well as inactivation of mitochondrial respiratory chain complex 1 and the mitochondrial glycerophosphate dehydrogenase (mGPD), which leads to a block of glucagon effects and impaired gluconeogenesis in the liver [27]. A recent study in patients with T2DM has shown that slow-release metformin has a greater effect on reducing glycated hemoglobin (HbA1c) than fast-release metformin. In diabetic patients for whom metformin has failed to lower HbA1c levels, the use of sodium glucose cotransporter-2 (SGLT2) inhibitors (canagliflozin, dapagliflozin, and empagliflozin) has been recommended as an add-on therapy. The mechanism of action of these inhibitors is to decrease glucose reabsorption in the renal tubules, and therefore, in the bloodstream, by blocking SGLT2 receptors [28].

1.3 Nonalcoholic fatty liver disease

Nonalcoholic fatty liver disease (NAFLD) describes the whole group of fatty liver diseases, starting with nonalcoholic fatty liver (NAFL), nonalcoholic steatohepatitis (NASH), and NASH cirrhosis, and including the development of hepatocellular carcinoma (HCC) (Figure 1). A recently published study revealed an increase in the number and percentage of liver transplants carried out for NASH in Europe in 2016 as compared to 2002 [29].

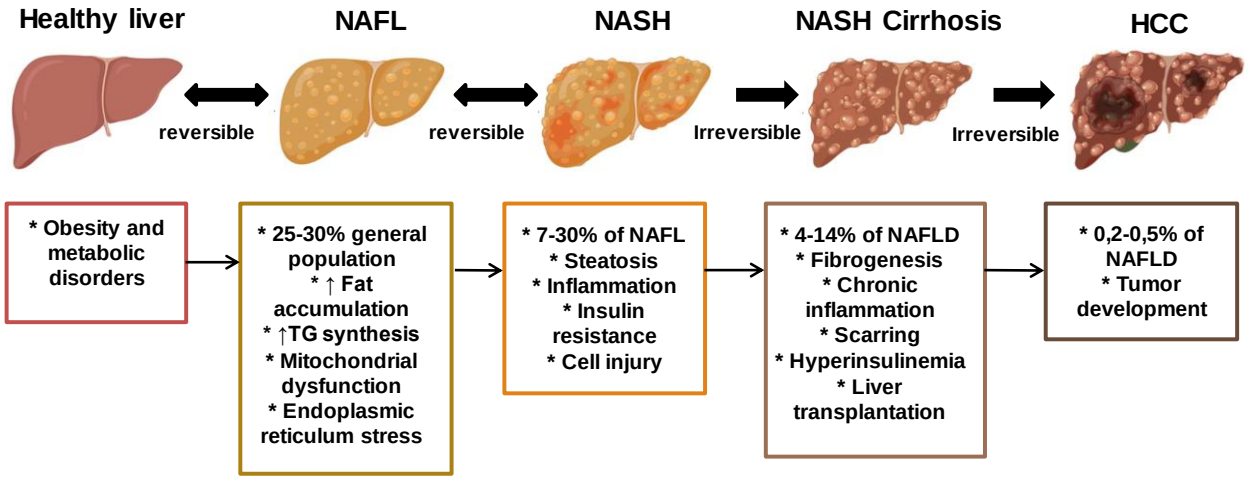

Figure 1. Schematic representation of NAFLD disease progression over time along with the main characteristics of the disease stages (adapted from [30])

NAFLD begins when hepatocytes are no longer able to completely metabolize the ingested nutrients (fatty acids and carbohydrates), causing the accumulation of toxic lipids in the intercellular space of the liver. The association of toxic lipids with inflammatory processes triggers the evolution of the disease to more advanced stages [30]. The excessive hepatic accumulation of lipids is caused by pathological lipolysis of adipose tissue, alterations in *de novo* lipogenesis, and poor nutrition (for instance, diets rich in fats and sugars) [6].

In particular, NASH illness is characterized by decreased levels of acetyl-coenzyme-A carboxylase 1 (ACC1) responsible for *de novo* lipogenesis, inhibition of carnitine palmitoyltransferase 1 (CPT1) leading to decreased mitochondrial fatty acid, and overexpression of fatty acid synthase (FAS) responsible for the conversion of malonyl-CoA to palmitic acid. An alteration in the functionality of these enzymes leads to the accumulation of toxic lipids, which is the hallmark of NAFLD [6]. Other pathological processes associated with NAFLD are endoplasmic reticulum stress, increased presence of unfolded proteins, induction of apoptotic pathways, stimulation of stellate cells leading to fibrosis, and recruitment of pro-inflammatory cells (such as monocytes) [30].

The diagnosis of NAFLD is currently based on imaging and histological techniques that allow the determination of hepatic steatosis degree. Currently, spatially resolved three-dimensional models of human liver tissue are being developed to determine quantitative multiparametric cellular and tissue signatures that will provide a better understanding of the pathophysiology of the disease and help us to prevent its progression. These customized 3D dynamic computer simulations reveal the bile fluid anticipated an elevated pericentral biliary pressure and micro cholestasis, in agreement with high cholesterol levels in the serum of NAFLD patients. The non-invasive fibro scan-AST (FAST) score allows the identification of patients who have an increased NAFLD activity score (equal 4

or higher) and advanced fibrosis (stage 2 or higher), and it is likely to replace liver biopsies in clinical practice. Despite these diagnostic advances, there are still no pharmaceutical effective therapies approved by the U.S. Food and Drug Administration [31].

1.4 Hyperlipidemia or dyslipidemia

Hyperlipidemia is described as increased levels of lipids or lipoproteins in the blood stream that can be the result of a heterogeneous group of disorders. People with hyperlipidemia are at high risk of having cardiovascular disease [32].

Lipoproteins, the molecular complexes that transport lipids in the blood, are formed by a hydrophobic central core made up of cholesterol ester (CE) and triglycerides (TG) surrounded by a hydrophilic membrane containing glycerophospholipids, free cholesterol (FC) and apolipoproteins (Figure 2) [33].

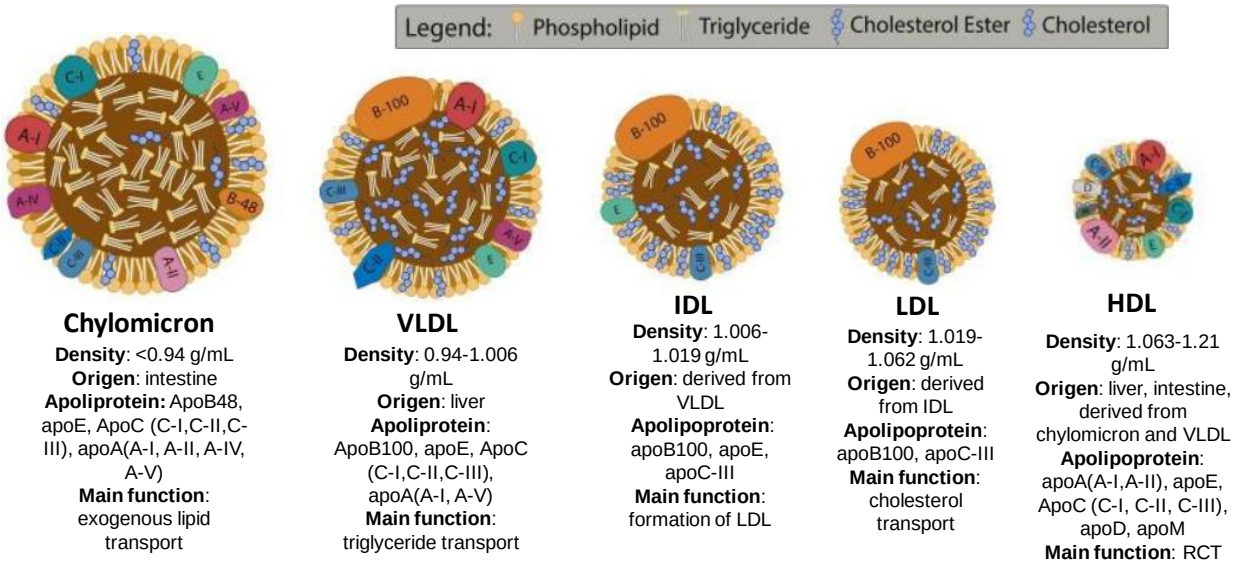

Figure 2. Classification and properties of major plasma lipoproteins (adapted from [33]). RCT: Reverse cholesterol transport

Hyperlipidemic states are caused by alterations in lipid and lipoprotein metabolism. Lipid metabolism includes two pathways: the exogenous pathway responsible for dietary lipid metabolism, and the endogenous pathway responsible for endogenously-synthesized lipid metabolism.

In the exogenous pathway, dietary fats are degraded by liver bile acids and are absorbed by the small intestines (Figure 3). In the intestinal mucosal cell, FFAs are bound to monoglycerides generating TGs. Over the last two decades, genes encoding many of the enzymes involved in the synthesis of triglycerides have been identified, including acyl-CoA:monoacylglycerol acyltransferase (MGAT) and acyl-CoA:diacylglycerol acyltransferase (DGAT) [34]. Cholesterol is converted into CE by the enzyme cholesterol acyltransferase. TGs and CEs then merge with

apolipoprotein B48 (ApoB48) to form chylomicrons, the main lipoproteins that transport dietary lipids. Chylomicrons enter the systemic bloodstream through the lymphatic system; once in the blood circulation, they acquired apolipoprotein C-II (ApoC-II) and apolipoprotein E (ApoE) through interactions with other lipoproteins, such as high-density lipoprotein (HDL) and remnant very-low-density lipoprotein (VLDL). In circulation, chylomicrons also interact with lipoprotein lipase (LpL) that degrades chylomicron TG to FFAs and glycerol, generating the remnant chylomicrons. FFAs can then enter into the peripheral tissues, where they are used for energy production and/or into fat tissue, where they are stored as TG. Remnant chylomicrons are detected by specific hepatic receptors that eliminate them from the circulation. In the liver, cholesterol from remnant chylomicrons is either used to generate lipoproteins and bile acids or is stored as CE [35,36].

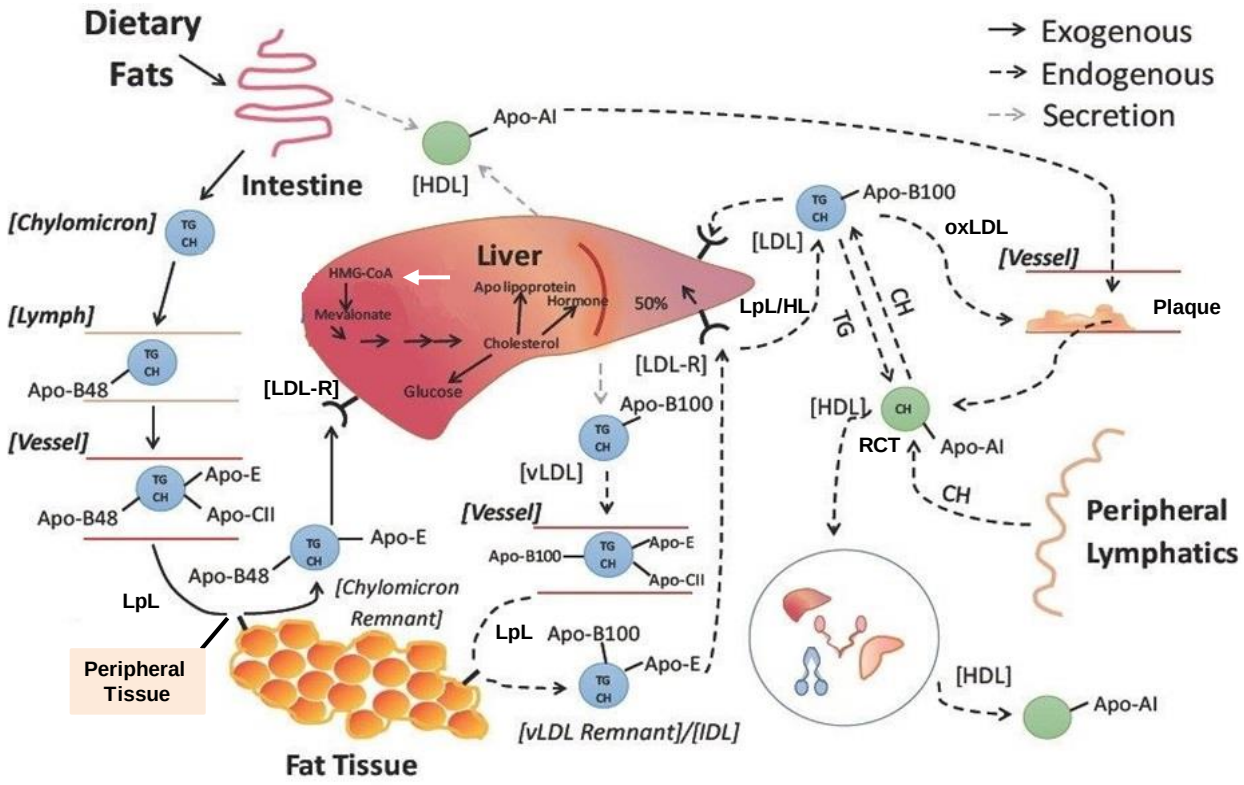

Figure 3. Lipid metabolism (adapted from [37])

The endogenous pathway mainly involves VLDL, LDL, and HDL (Figure 3). VLDLs generated and secreted by the liver enter into the circulation, where they are recognized by LpL, enzyme that degrades the TGs of VLDL to FFA and glycerol. The remnant VLDL/ intermediate-density lipoprotein (IDL) can either be eliminated from the circulation by the liver or suffer major transformations by LpL and/or hepatic lipase (HL) to become LDL. The resulting LDL, which is responsible for transporting cholesterol to the peripheral

tissues, undergo modifications such as oxidation (oxLDL) and is then taken up by scavenger receptors of intimal local macrophages, contributing to the formation of atherosclerotic plaques in the vessels. On the other hand, HDL plays a crucial role in the reverse cholesterol transport (RCT) [35,36]. In RCT, HDL collects all excessive cholesterol present in peripheral cells and transports it to the liver, where it is excreted in the bile or converted into bile acids prior to excretion [38].

Among the alterations that occur in lipid metabolism leading to dyslipidemia are enhanced TG production, impaired TG-rich lipoprotein (LDL, IDL and VLDL) metabolism, and loss of HDL function [39].

Current treatments for hyperlipidemia focus on reducing the risk of having ischemic heart disease, cardiovascular disease, or cerebrovascular disease. Statins are some of the most widely used drugs to counteract the adverse effects of hyperlipidemia. Statins suppress the activity of 3-hydroxy-3-methylglutaryl-coenzyme A reductase (HMG-CoA) in the liver, leading to decreased cholesterol synthesis and increased LDLR-mediated uptake of CE-enriched lipoproteins (Figure 3, white arrow). Another treatment consists of inhibitors against the proprotein convertase subtilisin/kexin type 9 (PCSK9), which also upregulates LDLR expression at the cell membrane. PCSK9 is a protease produced by hepatocytes that binds to the receptor and promotes its degradation causing a decrease in the uptake of CE-enriched lipoproteins. Additionally, bile acid sequestering agents can be administered to patients with hyperlipidemia to block the entry of bile acids into the bloodstream, keeping them from reaching the liver and indirectly enhancing the uptake of lipoproteins from the circulation. Another hypolipemiant treatment is the use of cholesteryl ester transfer protein (CETP) inhibitors, which increase HDL levels and decrease cholesterol concentrations in ApoB-containing lipoproteins. Other types of inhibitors used in clinical practice are those that decrease the amount of cholesterol reaching the liver by blocking the absorption of cholesterol at the intestine level [39].

1.5 Metabolic syndrome

The metabolic syndrome encompasses a broad group of metabolic diseases, including obesity, hypertension, diabetes mellitus, and dyslipidemia, that have heterogeneous causes and symptoms. Metabolic syndrome is more prevalent in men than in women, and its risk factors can be hereditary as well as environmental. In Spain, between 22% to 32% of the general population has from metabolic syndrome [40].

Insulin resistance is a crucial variable in the diagnosis of metabolic syndrome. A determining cause for the evolution of insulin resistance is an elevated number of fatty acids in the bloodstream. Metabolic syndrome begins with the release of large amounts of FFA from visceral adipose tissue lipolysis into the liver that is stored as triglycerides, thereby stimulating hepatic glucose generation and VLDL release leading to

hypertriglyceridemia. The VLDL released into the circulation exchanges TGs for the CE in HDL-C, leading to the rapid clearance of HDL and a deterioration of the condition. Increased TGs are also taken up by LDL, making them more prone to hepatic lipase-induced degradation resulting in smaller and denser LDL. Small-dense LDL accumulates in the arterial wall, where it undergoes modifications leading to the development of atherosclerosis (Figure 4) [41,42].

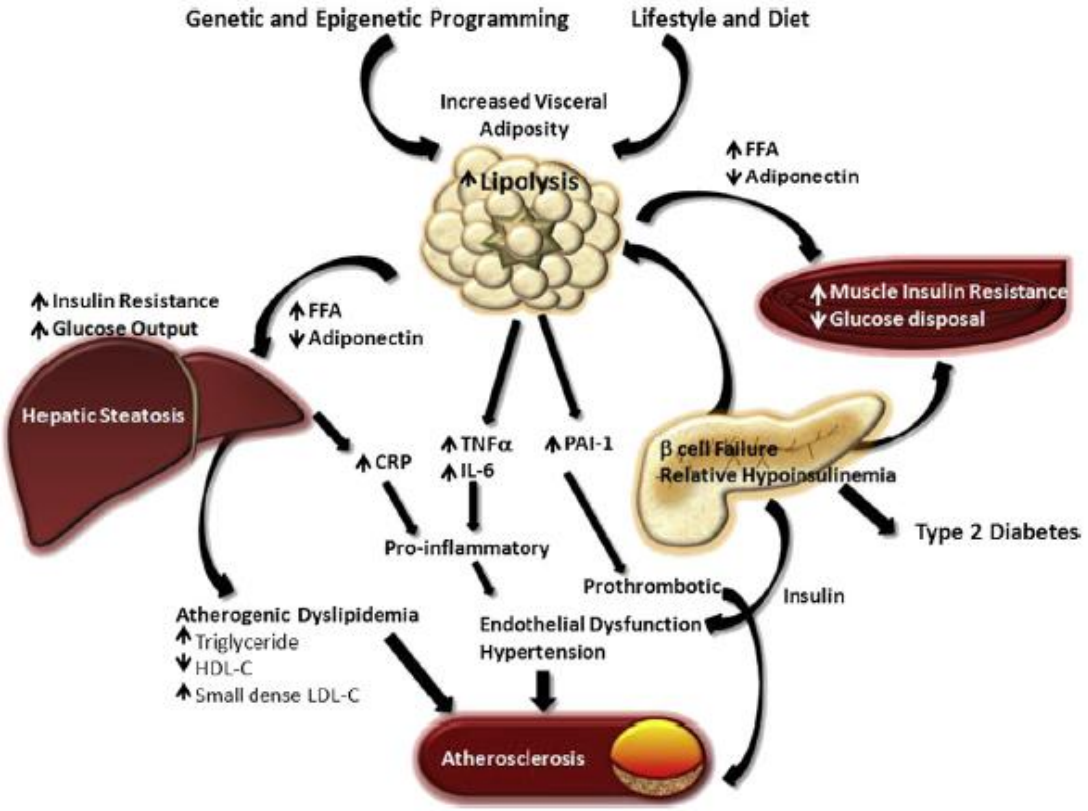

Figure 4. Pathophysiology of metabolic syndrome (Image from [41]).

Excess FFA also affects skeletal muscle by suppressing insulin-induced glucose uptake and enhancing blood glucose levels, leading to insulin resistance. Glucose overload in circulation stimulates insulin release by pancreatic β cells, triggering hyperinsulinemia. A key pathological consequence of hyperinsulinemia is hypertension, which is caused by activation of the sympathetic nervous system and suppression of nitric oxide synthase along with endothelial tissue dysfunction. In addition, the increased secretion of adipokines, such as IL-6 and TNF-α, by adipose tissue leads to increased production of fibrinogen and plasminogen activator inhibitor-1 (PAI-1), resulting in a pro-thrombotic condition, decreased anti-inflammatory cytokine, and reduced insulin sensitivity [41,42].

Currently, the main treatments for metabolic syndrome are based on healthy dietary and lifestyle habits. Among the therapeutic strategies that have proven to be effective are

improving the quality of food and modifying the distribution of macronutrients (e.g., balancing the amount of proteins, fats, and carbohydrates in the diet)[43].

2 Animal models of metabolic disorders

Animal models have played an essential role in our comprehension about and progress in developing treatments for metabolic diseases. For instance, animal experimentation has led to the discovery of vaccines, antibiotics, and a better understanding of human diseases. Approximately 20 million animal models are currently being used in biomedical studies, the majority of which are mice and rats. Table 3 summarizes some animal models used for research in metabolic diseases and their main features [44].

Disease	Animal model	Characteristics	Ref
Obesity	ob/ob mice	Mutation on leptin gen, reduced blood pressure, increased body weight, impaired glucose tolerance	[45]
	DIO animals	Diet-induced models of obesity (DIO) generates obesity, hyperinsulinemia, hyperglycemia and hypertension	[46]
	NONcNZO10/LtJ mice	Combination of New Zealand Obese (NZO/HlLt) and Nonobese Nondiabetic (NON/LtJ) mice. Visceral obesity, moderate liver steatosis.	[47]
	TALLYHO/JngJ mice	Obesity, hyperinsulinemia, hyperglycemia (males), and hyperlipidemia	[48]
	B6(cg)-Tubtub/J mice	High blood lipid levels. No atherosclerotic lesions	[49]
T2DM	db/db mice	Mutation on leptin receptor gene. Reproductive impairment and chronic insulin resistance	[45]
	BKS db mice	Spontaneous mutation producing hyperinsulinemia that progressively worsens to insulinopenia	[49]
	Obese domestic cats	Polygenic disease. Prediabetes (insulin resistance) as well as neuropathy and retinopathy. Also characterized by pancreatic amyloidosis, hypertension and dyslipidemia.	[46]
	$BTBR^{ob/ob}$ mice	Increase in body fat. Motor and sensory nerve conduction velocities deficits	[50, 51]
	$eNOS^{-/-}$ mice	Nitric Oxide Synthase 3 (NOS) endothelial cell knockout allele. Glucose intolerance, endothelial dysfunction and dyslipidemia	[52]
	Goto-Kakizaki (GK) rat	Leptin resistance. Hyperlipidemia. Unchanged blood pressure. Reduced neuronal glucose utilization. Oxidative stress	[45, 53]

T1DM	Akita mice	Mutation in insulin gene. Pancreatic β-cell dysfunction and hyperglycemia. Osteopenia and impaired fracture healing	[54]
	LEW.1AR1/-IDDM Rat	Spontaneous mutation in the intra- Major histocompatibility complex (MHC). Diabetes occurs between 60 and 90 days of age.	[55, 56]
	STZ-treated animals	Administration of streptozotocin (STZ) induces β-cells destruction. Severe hyperglycemia, synaptic degeneration	[53]
NAFLD	Zebrafish (slc16a6$^{-/-}$)	Fasting-induced fatty liver disease that is reversed by feeding	[57]
	Zebrafish (ahcy$^{-/-}$)	Hepatic steatosis and liver degeneration	[57]
	foz/foz mice	Mutation in *Alms1* gene. Morbid obesity and hyperphagia. Insulin resistance. Decreased levels of adiponectin. Hypercholesterolemia and steatosis.	[58]
	Ossabaw miniature swine	Dyslipidemia, obesity, hypertension, and insulin resistance	[59]
Dyslipidemia	LDLR$^{-/-}$ mouse	Mutations in *ldlr* gene. Acute hyperlipidemia and severe atherosclerosis	[53, 60]
	apoE$^{-/-}$ mouse	Increases in VLDL and decreases in HDL. Presence of fibrous plaque in the aortic root	[61]
	Zebrafish (ApoC-II mutant)	Hypertriglyceridemia, chylomicronemia	[57]
Metabolic Syndrome	Zucker fatty (ZF) rat	Missense mutation on leptin receptor gene. Obesity, hyperinsulinemia, hypertension	[45]
	Zucker Diabetic Fatty (ZDF) rat	Non-functional leptin receptor. Insulin resistance, hyperglycemia, mild hypertension	[45]
	Koletsky rat	Increased abdominal fat, normal fasting blood glucose, severe hypertension	[45]
	POUND mouse	Mutation in leptin receptor. Hypercholesterolemia. Obese, hyperinsulinemia	[45]

Table 3. Animal models mainly used in the investigation of metabolic disorders.

In the near future, animal models will still be necessary to progress in biomedical research. However, due to concerns about their clinical applicability and ethics, alternatives such as computational simulations are emerging as new approaches (in a sometimes complementary manner) to progressing in biomedicine research [44].

2.1 LRP1 animal models

Previous studies have shown that low-density lipoprotein receptor-related protein-1 (LRP1) is involved in early embryo development. LRP1 expressed on the surface of trophoblast cells recognizes uPA-PAI-1 complexes, promoting their degradation and allowing blastocyst implantation in the uterus [62]. On the basis of these results, an animal model with a complete deletion of LRP1 is not feasible.

The recombinant Cre protein (38 KDa) is essential in the integration and cleavage of bacteriophage P1 at a specific site in the host genome. LoxP (locus of x-over, P1) sites are composed of a 34-bp palindromic sequence with an 8-bp core sequence that establishes the orientation of the site. The Cre protein can recognize two single-directional loxP sites situated on the same linear DNA molecule, resulting in the cleavage and circularization of the targeted DNA sequence. This discovery allowed transgenic animals to be created in which any region of the genome can be eliminated in a precise and controlled manner. To generate animals with a conditional mutation using the Cre-loxP system, animals homozygous for loxP have to be crossed with animals expressing Cre recombinase coupled to a specific promoter of the cell or tissue of interest (Figure 5) [63,64].

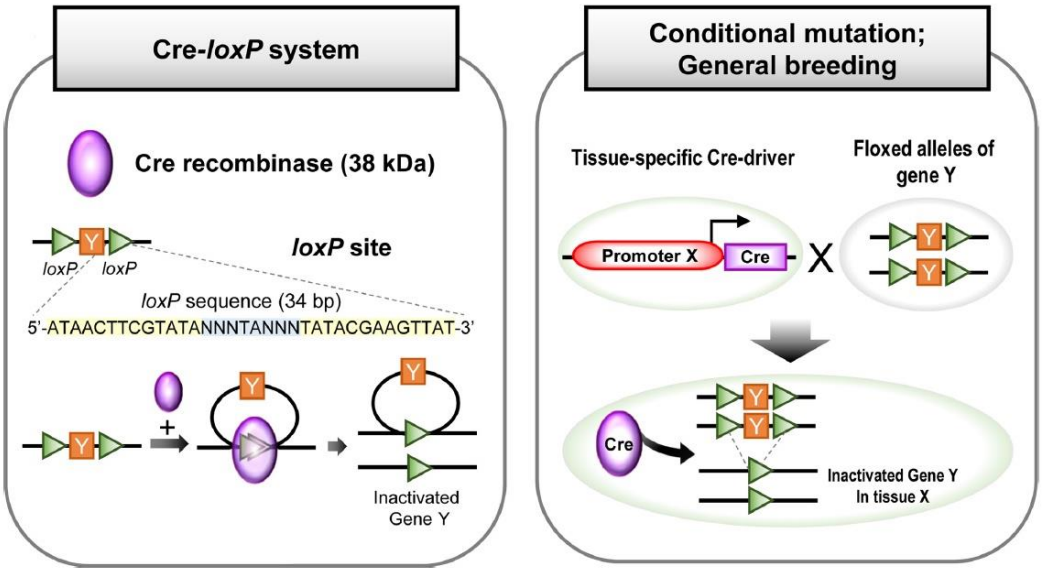

Figure 5. Representative diagram showing how the Cre-loxP system works and the general breeding approach for conditional mutation involving the loxP and Cre knockout mice strain (Image from [64]).

To improve the functioning of the Cre/loxP system, exogenous inducers are used to control the activation of Cre at the specific moment (Table 4) [64].

Exogenous inducer	Animal model	Administration route	Promoter	Ref

Tamoxifen	LRP1$^{fl/fl}$Cx3cr1^{creER} mice	Intraperitoneal injection	Cx3cr1 promoter	[65]
	Club Lrp1$^{-/-}$	Intraperitoneal injection	Scgb1a1 (secretoglobin)	[66]
	NG2-CreERT2$^{ct2/wt}$xR26eGFP$^{flox/flox}$ xLRP1$^{flox/flox}$	Intraperitoneal injection	nerve/glia antigen-2 (NG2)	[67]
	smaLRP1$^{-/-}$ mice (lrp1$^{flox/flox}$, SMA-Cre-ER^{T2})	Intraperitoneal injection	smooth muscle actin (SMA)	[68]
Doxycycline	LRP-1-βKO mice (MIP-rtTA; TRE-Cre; Lrp1$^{fl/fl}$)	Doxycycline diet	mouse insulin promoter	[69]

Table 4. Mouse models of conditional LRP1 deficiency using Cre-loxP system.

Rohlmann *et al.* were the first group to create a mouse model containing loxP sites inserted into the gene coding for LRP1 (LRP$^{flox/flox}$). LRP$^{flox/flox}$ mice are viable and have a normal phenotype. These investigators were able to remove LRP1 from the liver of loxP homozygous mice by injecting a recombinant adenovirus containing the recombinant Cre gene coupled to the cytomegalovirus promoter [63]. This approach has been used to generate different models of conditional LRP1 deficiency, including transgenic mice with LRP1 deficiency in oligodendrocyte precursor cells [67]. Club Lrp1$^{-/-}$ (Scgbla1-Cre/ER^{TM}LRP1$^{flox/flox}$) mice are tamoxifen-inducible, airway-specific LRP1 knockout mice. These mice were developed to study the role of LRP1 in chronic obstructive pulmonary disease [66]. Another deficient mouse model induced with tamoxifem is LRP1$^{fl/fl}$Cx3cr1^{creER}, which was created to study the role of LRP1 in multiple sclerosis. Researchers found that LRP1 is upregulated in multiple sclerosis lesions as compared to healthy tissue (pathological function). At the same time, they found that LRP1 is required to maintain microglia in an anti-inflammatory and neuroprotective state during inflammatory aggression (protective function) [65]. Other studies have used a mouse model with a specific LRP1 deficiency in vascular smooth muscle cells (VSMCs) (smaLRP1$^{-/-}$). This model has tamoxifen-inducible Cre coupled with a modified estrogen receptor ligand-binding domain (ERT2) that is under the control of a specific smooth muscle actin promoter. Overall, these studies demonstrate the essential function of LRP1 in the control of VSMC contraction by mediating calcium signaling that protected against the formation of aneurysms [68].

2.2 Animal models for antibody-based therapies

In recent years, antibody-based therapies have rapidly gained importance and have emerged as the best-selling drugs in the pharmaceutical market in 2018. Moreover, approximately 570 therapeutic monoclonal antibodies have reached the clinical trial in

recent years, of which 79 have been approved by the US Food and Drug Administration (US FDA). These biologic drugs are useful for treating cancer, autoimmune, metabolic and infectious illnesses [70].

According to the method of production, antibodies are classified as polyclonal or monoclonal. Monoclonal antibodies are generated from a single cell such as specific immortalized B cells and are therefore a constant source of antibodies. Polyclonal antibodies are produced from numerous cells, so immunized animals need booster doses each time before collecting specific antibodies [71]. Generally, in the production of polyclonal antibodies, adjuvants that enhance the immunogenicity of the antigens are usually used. The main adjuvants used for immunization are Freund's complete and incomplete adjuvants, although others based on water-soluble bacterial cell wall components can also be used [72].

For more than 100 years, animals have been used to produce useful antibodies for research, diagnosis, and treatment of diseases. Among the benefits of this process are high affinity and stability *in vivo*, gaining valuable knowledge of antibody lineage, and paratope (antibody region that binds to the antigen) patterns using high-throughput sequencing [73].

Polyclonal antibodies are generally produced in mammals, although other species can be used. The animals most commonly used for large-scale antibody production are large or dairy animals such as horses, buffaloes, cows, sheep, and goats. For smaller productions such as those used in research, small animals such as rabbits, rats, or mice are usually used. Avian models are also used to generate antibodies, of which the chicken is the most widely used [71].

Balb-c mice are a widely used strain for the generation of monoclonal antibodies. Females are mainly used due to their ease of housing. New Zealand rabbits are used to produce antibodies due to their easy handling, their great capacity to adapt to housing conditions, and their drooping ears that make it easier to see the marginal veins for blood collection [72,74].

In the field of atherosclerosis treatment, oxidized LDL has been reported to be targeted by adaptive immune responses, generating oxidized LDL antibodies [75,76]. In this context, vaccines generated on the basis of native and modified ApoB100 peptides reduce atherosclerosis in hypercholesterolemic animals through different mechanisms [77,78]. These previous studies support the use of immunization as a potential treatment for atherosclerosis. Different anti-atherosclerosis immunotherapeutic approaches have been evaluated in preclinical and clinical studies with the purpose of specifically modulating immune responses to LDL [79–81].

Table 5 summarizes some of the antibody-based immunotherapy that has reached clinical trials for the treatment of cardiovascular risk factors.

Therapeutic/ study name	Agent	Method of action	Company	Conclusions	Preclinical Development	Stage/ref
CANTOS (NCT01327846)	Canakinumab	IL-1β antibody	Novartis	Reduction in recurrent CV events and HF mortality	Transgenic mouse strain	Completed [82–84]
LDL immunization V6 (NCT03042741)	V6 (antigens from adipose tissue)	Vaccination	Immunitor LLC	Ongoing	Pig	Phase 3 [85,86]
ATTACH	Infliximab (chimeric human-murine monoclonal Antibody)	Anti-TNF-α antibody	Centocor	Increased risk of death or hospitalization for CHF on high dose	1006-T transgenic mice	[87,88]
FOURIER (NCT01764633)	Evolocumab (monoclonal antibody)	PCSK9 Inhibition	Amgen	Reduced LDL-C levels and the risk of CV events	Transgenic mice, non-human primates	Completed [89,90]
ODYSSEY OUTCOMES (NCT01663402)	Alirocumab (monoclonal antibody)	PCSK9 Inhibition	Sanofi	Reduced risk of recurrent ischemic CV events	Transgenic mice, non-human primates	Completed [90,91]

Table 5. Clinical trials involving antibody-based therapies for the treatment of cardiovascular risk factors (adapted from [92]) CV: cardiovascular, HF: heart failure, CHF: congestive HF, LDL-C, low-density lipoprotein cholesterol

Most of these vaccines are directed to treat cardiovascular risk factors such as dyslipidemia, obesity and diabetes by modulating inflammatory processes or lipid metabolism.

3 LRP1 as a key endocytic receptor in metabolic disorders

LRP1 is a cell surface glycoprotein belonging to the LDL receptor super family. The receptor is synthesized as a pro-receptor with a molecular weight of 600 kDa. The active form of the receptor is a heterodimer consisting of two subunits, the extracellular α-subunit of 515 kDa and the transmembrane and intracellular β-subunit of about 85 kDa. The α-subunit consists of four clusters, each cluster containing numerous ligand-binding domains called modular arrays of acidic cysteine-rich complement-type repeats (CRs). The

CRs consist of 40 amino acid residues with three conserved disulfide linkages. The main function of the β-chain (formed by two NPxY motifs, one YxxL motif, and two di-leucine motifs) is the activation of intracellular signaling and endocytosis (Figure 6) [93,94].

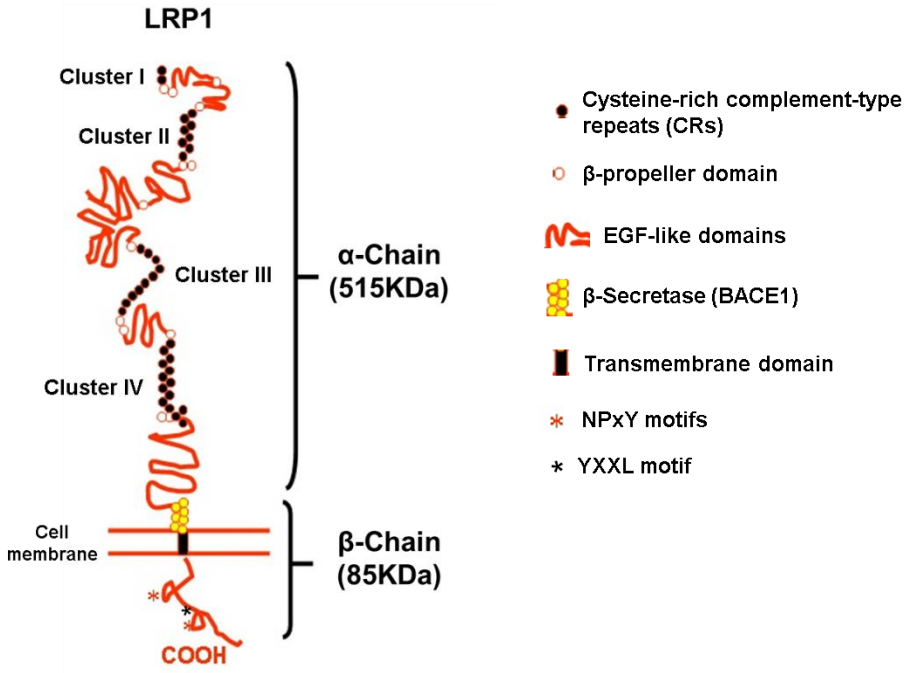

Figure 6. Schematic representation of mature LRP1 (Adapted from [93])

LRP1 can be cleaved from the plasma membrane by the action of proteases, such as hepatic metalloproteinases, tPA, and neuronal β-secretase protease (β-site APP cleaving enzyme 1, BACE1). Soluble LRP1 (sLRP1) is composed of the α-chain (that binds to extracellular ligands) and a fragment of the β-chain. sLRP1 can be measured in blood and is therefore being used as a biomarker for atherosclerosis and cardiometabolic diseases [95]. Moreover, an association between sLRP1 and the incidence of coronary events has been demonstrated [96]. Finally, this receptor may serve as a biomarker of epicardial adipose tissue volume present in T1DM patients [97].

There are more than 100 ligands recognized by LRP1, most of them bind to cluster II and IV and do not compete with each other for binding to the receptor with the exception of receptor associated protein (RAP), which blocks the binding of all other ligands [94,98,99]. Table 6 summarizes the main ligands of extracellular LRP1α-subunit.

Ligand	Function	Caracteristic	Ref
α-2 macroglobulin (α-2-M)	Inhibits a diverse range of proteinases. Enhanced GLUT4 translocation	Protease inhibitor belonging to the α-2 globulin family.	[100]

Amyloid β peptide (Aβ)	Elevated production and deposition of Aβ in Alzheimer's disease leading to the formation of extracellular plaques.	Peptide resulting from the processing of β-amyloid precursor protein. Aβ is cleared by BBB-associated pericytes though LRP1/apoE-specific mechanism.	[101,102]
Apolipoprotein E and apo E-enriched lipoproteins	Mediates lipoproteins interaction, catabolism and transport. LRP1 is the main apoE receptor in the brain, becoming a major cholesterol transporter.	Lipoprotein compound that is produced mainly in the liver	[103,104]
Calreticulin	Critical for heart's development. Promote the preservation of cellular proteostasis. Contribute to the initiation of the immune response against cancer.	Calcium-binding chaperone protein	[105–107]
Heat shock protein 90, 96, 70	Main proteins responsible for the folding of other proteins. Key player in cell proliferation, differentiation and carcinogenesis.	Intracellular chaperon proteins whose expression is influenced by stressors.	[108,109]
Heparan sulfate proteoglycans (HSPGs)	Endocytic and adhesion receptors. Control cell migration.	Glycoproteins expressed on the cell surface and in the extracellular matrix.	[110,111]
Hepatic Lipase	Degradation of phospholipids and triglycerides from plasma lipoproteins	enzyme synthesized by hepatocytes	[112,113]
Leptin	Plays an essential role in energy homeostasis	Hormone secreted by adipocytes	[114]
Matrix metalloproteinase 2 (MMP-2), 9 (MMP-9) and 13 (MMP-13)	Group of proteinases whose main function is the degradation of the extracellular matrix. Essential for tumor progression and metastasis	zinc-dependent endopeptidase family	[115–118]
Plasminogen activator inhibitor-1 (PAI-1)	Serpin responsible for the suppression of uPA and tPA activity. Involved in tissue remodeling, angiogenesis and tumor progression.	Member of the serine protease inhibitor, encoded by the gene SERPINE1	[119,120]
Platelet-derived	Enhanced activity has been	PDGF-BB is a dimeric	

growth factor (PDGF)-BB PDGF receptor (PDGFR) β	associated with several diseases and pathological states.	glycoprotein composed of two B subunits	[121,122]
TGF-β 1 and TGF-β 2	Participate in the associations with extracellular proteins, cell proliferation, differentiation and vascular remodeling.	Multifunctional growth factor	[123,124]
Apo B100 and apo B100-enriched lipoproteins	Lipid metabolism	Alternative ApoB100 epitope (different from that involved in the binding to LDLR)	[125]

Table 6. List of the best-known ligands of the extracellular LRP1α-subunit (adapted from [94]) BBB: Blood-brain barrier, uPA: Urokinase-type plasminogen activator, tPA: Tissue-type plasminogen activator

The cytoplasmic domain of LRP1 can also bind to several adaptor proteins involved in signal transduction (Table 7).

Molecule	Function	Characteristic	Ref
Disabled protein 1 (Dab1)	Control of neurogenesis and neuronal motility	Contain a Phosphotyrosine-binding (PTB) domain. Undergoes tyrosine phosphorylated during embryogenesis	[126]
Protein kinase α (PKCα)	Involved in the regulation of apoptosis, inflammation, proliferation, differentiation and motility.	The activation requires the generation of secondary messengers and is enhanced in insulin-resistant conditions.	[127]
Shc	Activation of downstream tyrosine kinases	Contain PTB domain, a central region that contains several tyrosine phosphorylation sites, and a carboxyl-terminal SH2 domain.	[128]
JNK interacting protein 1 (JIP-1) and 2 (JIP-2)	Activation of downstream mitogen-activated protein kinase (MAPK) kinases	Scaffold proteins, highly expressed in Brain and Pancreatic β-cells	[129]
Engulfment adapter protein (GULP)	Implicated in stabilin-1-mediated phagocytosis.	It is able to bind the NPXY motif	[130,131]
Postsynaptic density	Master regulator of neuronal plasticity and	Most abundant protein in the excitatory postsynaptic density capable to coupling	[132]

protein 95 (PSD95)	memory	to N-methyl-D-aspartate (NMDA) receptors	
FE65	Regulation of actin dynamics, APP processing, neuronal growth and migration	Contains two PTB domains and one WW binding domain. Highly expressed in Central Nervous System	[133]

Table 7. List of the best-known ligands of intracellular LRP1 β-subunit (adapted from [95,134].

3.1 Relationship between LRP1 and atherosclerosis

The process of atherosclerosis takes place mainly in the intima of medium and large caliber arteries. The first stage of this disease is intimal thickening and is mostly associated with the retention of LDL by the proteoglycans of the arterial intima. LDL retained in the intima undergoes modifications such as LDL aggregation (agLDL), oxidation (oxLDL), and fusion, which is a key event in the progression of atherosclerosis [135–137]. The progression of atherosclerotic lesions is a discrete process that develops over decades without clinical symptoms. Atherosclerosis can begin at a very early age, with cases being reported of 10-year-old children with fatty streaks in aortas and coronary arteries [36]. The incidence of atherosclerosis has increased considerably due to risk factors such as hypercholesterolemia (LDL-cholesterol), obesity, diabetes mellitus, and hypertension [138].

New research has indicated that LRP1 has dual and opposite roles in the development and regulation of atherosclerosis [95]. A large body of research supports its protective role. For instance, the correct functioning of macrophages and VSMCs depends on proper signaling of the β-chain of LRP1 [139–141]. VSMC proliferation is regulated by PDGF-BB–induced LRP1 (β-chain) phosphorylation at the distal NPxY motif [142,143]. Monocyte recruitment, susceptibility to macrophage apoptosis, and efferocytosis are restricted through LRP1 signaling [144,145]. The lack of LRP1 tyrosine phosphorylation causes macrophage intracellular lipid deposition and abnormal elimination of apoptotic cells, resulting in accelerated atherosclerosis in mice [146]. Together, these results indicate that LRP1 β-chain–mediated signaling is essential for vascular normal function. LRP1 signaling is promoted by certain extracellular LRP1 ligands. Extracellular TGF-β binding to the α-chain of LRP1 mediates the atheroprotective induction of Wnt family member 5A (Wnt5a) in macrophages [147]. Binding of ApoE to LRP1 α-chain mediates interleukin-1 receptor associated kinase-1 (IRAK-1) signaling that downregulates nuclear factor kappa B (NF-κB)-induced inflammation [148]. Binding of protease-inhibitor complexes to LRP1 α-chain inhibit the NF-kB inflammatory response and induce a cytoprotective effect through phosphorylation of protein kinase B (Akt) and extracellular signal-regulated kinase 1/2 (ERK1/2) protein kinases [134,149,150].

Research supporting the pathological role of LRP1 identified aggregated LDL (agLDL) as an extracellular ligand of LRP1; of note, this receptor has a high capacity to take up this modified LDL and cause intracellular CE accumulation and foam cell formation in human coronary VSMC [151–153] and human macrophages [154,155]. In murine macrophages, LRP1 promotes the translocation of 12/15-lipoxygenase, leading to the generation of oxidized LDL [156]. LRP1 induces bone morphogenetic protein-binding endothelial regulator (BMPER) signaling that generates an acute inflammatory response through LPS-induced nuclear factor of activated T cells 1 (NFATc1) activation in endothelial cells [95]. LRP1 is overexpressed in atherosclerotic lesions due to positive upregulation of LRP1 by hypercholesterolemia [151,157,158], hypertension [159], and hypoxia [160,161]. LRP1-mediated internalization of agLDL causes tissue factor (TF) activation and TF microparticle liberation, which contributes to the progression of the atherosclerotic lesion to more advanced stages (thrombus)[162].

Consequently, on the basis of controlling LDL retention and aggregation in the vascular wall, several anti-atherosclerotic strategies have emerged. These strategies include the use of antibodies against proteoglycans [163], and of ApoA-I and ApoJ peptidomimetics [164,165]. These anti-atherosclerotic options, with a focus on preventing LDL aggregation, have gained additional relevance due to the findings that the intrinsic properties of circulating LDL in patients with coronary artery disease can promote aggregation of LDL and are predictive of future cardiovascular deaths [166].

3.2 Relationship between LRP1 and cardiac function

Patients with diabetes mellitus have elevated lipid accumulation in the heart, leading to diastolic dysfunction [167]. High levels of VLDL induce lipid accumulation in the heart [168] and act as antagonists of LRP1 signaling [143]. Therefore, there is controversial evidence on the protective or pathological role of LRP1 overexpression in the heart. Abnormal LRP1 signaling may depend not only on LRP1 but also on LRP1 ligand levels. In a situation of high circulating VLDL, decreased LRP1 levels could be beneficial to cardiomyocytes.

A recent study revealed that activation of LRP1 signaling during experimental acute myocardial infarction induces a cardioprotective signal, which decreases infarct size and maintains cardiac systolic function in young adult mice without comorbidities [134,150]. Several studies performed by our group in different *in vivo* models of myocardial infarction [169] and in explanted hearts of patients with ischemic cardiomyopathy [170] have demonstrated that LRP1 levels are markedly increased in ischemic compared to non-ischemic areas of the heart. Furthermore, in our studies, myocardial overexpression of LRP1 was associated with myocardial cholesterol accumulation [169].

High cholesterol diets can affect the expression of proteins essential for proper heart function, such as sarco (endo) reticulum plasma calcium ATPase-2 protein (SERCA), ryanodine receptors (RyR), and Na^+/Ca_2^+ exchangers. Rabbits fed with cholesterol-enriched diet had reduced SERCA2 mRNA levels after four days [32]. Our group has shown that LRP1 promotes intracellular accumulation of cholesterol into cardiomyocytes, leading to reduced levels of the SERCA2, key in calcium metabolism [171]. SERCA2 levels are inversely related to diastolic dysfunction [172]. Additionally, intracellular cholesterol accumulation leads to alterations in the structure and physical conformation of tropoelastin secreted by vascular cells [173] and cardiomyocytes [174] due to increased levels of cathepsin S (CatS). These results suggest that LRP1 and intracellular CE accumulation have a potential role in cardiac remodeling.

3.3 Relationship between LRP1 and insulin resistance

Insulin is a pancreatic hormone that promotes glucose uptake by tissues such as skeletal muscle, liver, and adipose tissue. Insulin resistance is associated to a decrease in the response of peripheral tissues to insulin stimuli. Many studies support a strong association between insulin resistance and the development of atherosclerotic cardiovascular disease [175–181].

Binding of insulin to the insulin receptor (InsR) results in the activation of insulin signaling. InsR belongs to the tyrosine kinase receptor family and is composed of α and β chains. The α-chain is extracellular and contains the insulin binding domain, while the β-chain is divided into 3 domains (extracellular, transmembrane, and cytoplasmic). The cytoplasmic domain of the β-chain is formed by clusters of tyrosine residues and tyrosine protein kinase activity (Figure 7) [182]. Different studies have shown that LRP1 interacts with the InsR to regulate InsR-associated intracellular signaling in neurons, hepatocytes and cardiomyocytes [183–185]. Depending on insulin signaling, LRP1 is able to translocate to the intracellular storage sites of InsR, while LRP1 can act as a scaffolding protein to allow proper phosphorylation of InsR by insulin action. However, the molecular mechanisms by which LRP1 binds to InsR are not yet known [183].

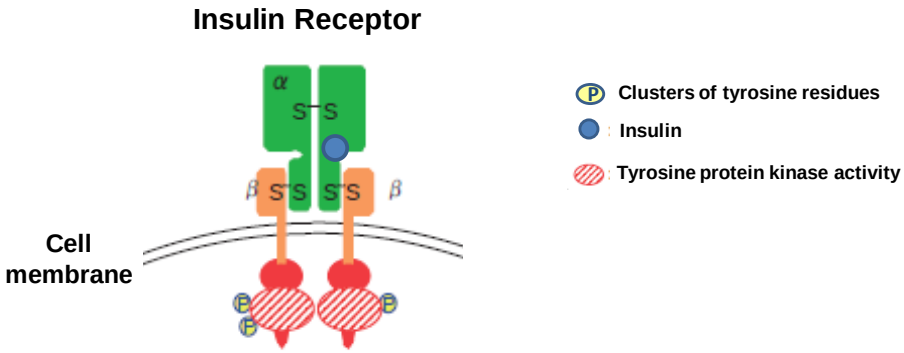

Figure 7. Insulin receptor structure (image from [186]).

Insulin signaling regulates the translocation of glucose transporters (GLUT) to the cell surface contributing to the elimination of circulating glucose. The best studied members of the GLUT family are GLUT1, GLUT2, GLUT3, and GLUT4. Table 8 summarizes the main characteristics and functions of these glucose transporters.

Criteria	GLUT1	GLUT2	GLUT3	GLUT4
Main location	Pancreas, CNS and red blood cells	Liver, intestine, pancreas and kidney	Pancreas, brain, testis, spermatozoa, and lymphocytes	Adipose tissue, heart and skeletal muscle
Primary function	Basal glucose uptake	Glucose-stimulated insulin secretion	High-affinity for glucose, neuronal transport	whole-body glucose homeostasis
Characteristics	Insulin-signaling independent	Insulin-signaling independent	Insulin-signaling independent	Insulin-signaling dependent
Subtrates	Glucose, galactose, mannose and glucosamine	Glucose and glucosamine	Glucose, xylose and mannose	Glucose, dehydroascor bica cid and glucosamine

Table 8. Characteristics of the main glucose transporters (Table adapted from [187,188]). CNS: central nervous system

The insulin signaling pathway in which LRP1 participates in different peripheral tissues is the phosphoinositide 3-kinase (PI3K) pathway (Figure 8). Activation of the pathway begins with phosphorylation of insulin receptor substrates 1 (IRS-1) by insulin, leading to PI3K stimulation. PI3K promotes the phosphorylation of protein kinase B (Akt), a kinase critical for this signaling process [189,190]. Activation of Akt by insulin causes phosphorylation of Akt Substrate 160 kDa (AS160) at multiple sites and phosphorylation of glycogen synthase kinase 3 (GSK3), leading to AS160 and GSK3 inactivation. AS160 protein participates in the

hydrolysis of Rab-bound guanosine triphosphate (Rab-GTP) producing Rab-bound guanosine diphosphate (Rab-GDP), a compound capable of preventing the exocytosis of insulin responsive vesicles (IRVs) containing the GLUT (indicated by dashed arrows in Figure 8). Inhibition of AS160 by Akt leads to the formation of more Rab-GTPase, which promotes the expression of cell surface glucose transporters (indicated by red arrows in Figure 8) [191]. While AS160 is known to bind to the NPxY motif of the LRP1 β-chain, how this process works is still unknown [189].

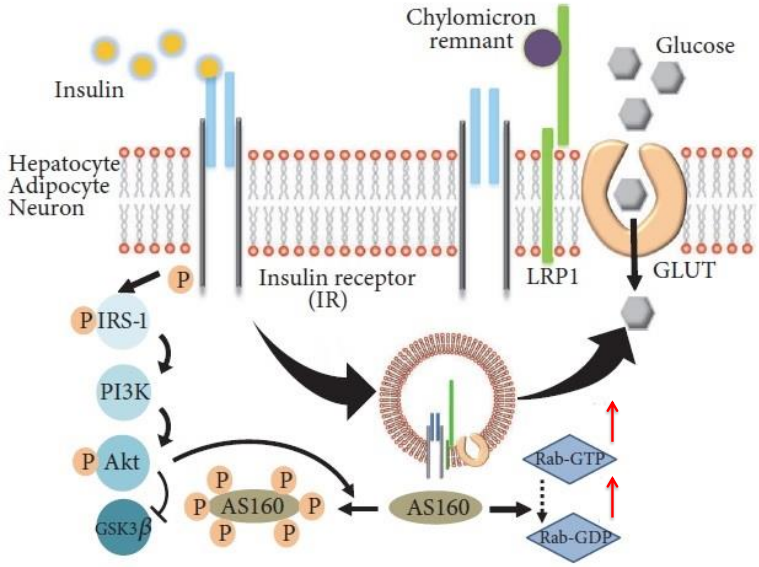

Figure 8. Insulin signaling pathway, in which LRP1 participates in different tissues (image from [189]).

LRP1 helps to conform the IRVs containing GLUT4 in adipocytes and muscle cells [192]. IRV formation is initiated by the recruitment of protein coats at specific sites on the donor plasma membrane through the action of adapter proteins such as Golgi-localized-γ-ear-containing-Arf-binding-protein (GGA), ANK repeat and PH domain-containing protein 1 (ACAP1), clathrin, and phosphatidylinositol 4-phosphate (PI4P). ACAP1 is responsible for the recruitment of clathrin for the formation of the vesicular coat, while GGA interacts with sortilin. GGA-dependent sortilin is responsible for assembling the main IRV component proteins such as GLUT4, Insulin-regulated aminopeptidase (IRAP) and LRP1 into a large oligomeric complex. [193].

In the brain, LRP1 can interact with the InsR and thereby help to determine the levels of glucose transporters such as GLUT3 and GLUT4 [184], modulating insulin resistance and glucose uptake, respectively. In addition, in retinal Müller glial cells, blocking LRP1 exocytosis towards the plasma membrane disturbs intracellular signaling induced by insulin [194]. Our group has recently shown that binding between agLDL and LRP1 inhibits

insulin-induced intracellular signaling and translocation of GLUT4 to the plasma membrane in HL-1 cells [183].

4 Role of cardiac natriuretic peptides on metabolic disorders

The heart can influence the metabolism of peripheral organs (by the secretion of certain proteins called cardiokines), leading to more efficient coordination of the entire body [195,196]. Some of the best-studied cardiokines include the natriuretic peptides (NPs). Circulating NP levels traditionally have significant implications for the diagnosis, prognosis, and treatment of patients with suspected or established heart failure [197,198]. Studies have shown that obese and type 2 diabetic patients have lower level of NPs in the plasma, suggesting a protective role of NP against metabolic syndrome [199]. A pivotal mechanism contributing to the metabolic protection conferred by NPs is its capacity to promote lipolysis and thermogenesis in human adipose tissues [200–202].

The natriuretic peptide family consists of three members: the atrial natriuretic peptide (ANP), the brain natriuretic peptide (BNP), and the C-type natriuretic peptide (CNP) [203]. ANP is mainly expressed in the atria, although it has also been detected in the ventricles. ANP is translated from its gene in the form of the prepropeptide preproANP (151 amino acids), which is split by a signal peptidase to obtain the (still inactive) proANP (126 amino acids). ProANP is stored and transported in secretory granules to the plasma membrane of cardiomyocytes. The enzyme corin is responsible for cleaving proANP, producing two N-terminal (NT)-proANP peptides and the active form ANP [204](Figure 9).

Corin is a transmembrane serine protease that consists of a transmembrane domain, an N-terminal cytoplasmic tail, and several extracellular domains. The extracellular region comprises 19 N-glycosylation sites and is essential for the conversion of proANP to ANP. ANP is cleaved by corin on the cell surface of cardiomyocytes during the secretion process. The membrane-bound corin in cardiomyocytes is released into the blood circulation by self-cleavage or metalloproteinase-mediated hydrolysis [205]. Cell-based assays showed that soluble corin retains the same ability to convert proANP to ANP as membrane-bound corin [206]. On the other hand, circulating soluble corin levels do not correlate with tissue corin levels [205].

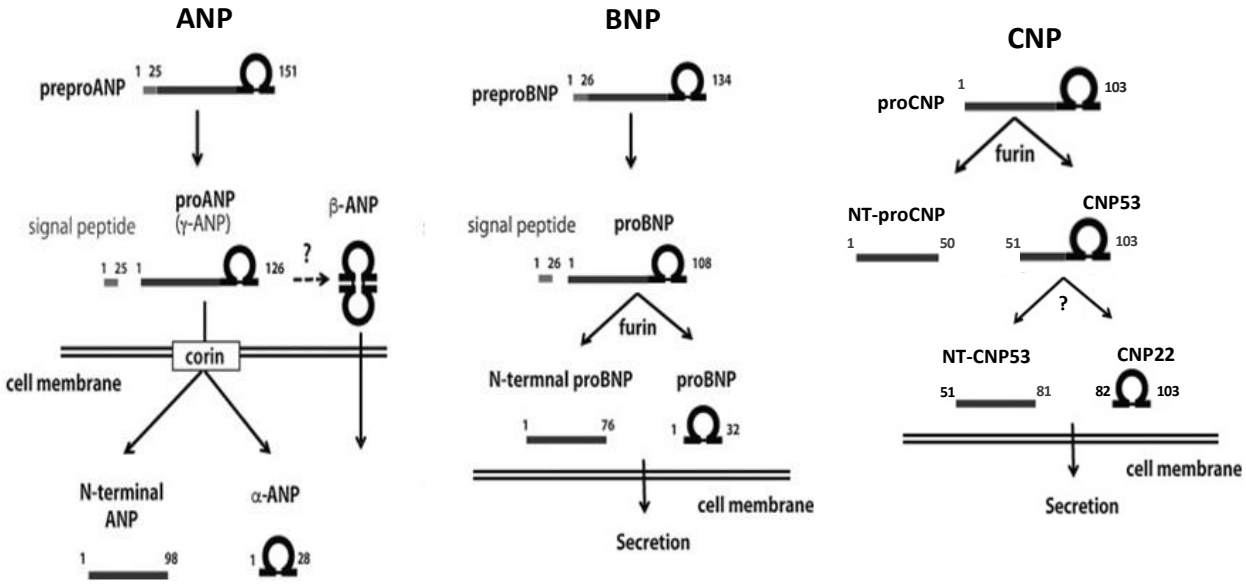

Figure 9. Cellular production and release of natriuretic peptides (adapted from [207,208]).

Systemic effects of ANP include the maintenance of the water–salt balance and the regulation of blood pressure through diuretic, natriuretic and vasodilator effects. In addition, ANP exhibits important pleiotropic effects on the heart, acting as a main regulator of cardiovascular homeostasis in an autocrine and paracrine manner [209].

BNP is a cardiac hormone mainly synthesized by the ventricles that, in contrast to ANP, is not stored in granules but rather is produced on request, depending on the blood inflow stimulus to the ventricles [207,210]. Like ANP, BNP is synthesized as a pro-peptide that is converted into an active hormone through the action of the enzyme furin. Furin is an intracellular serine endopeptidase that cuts proBNP into two BNP molecules (the active form, of 32 amino acids) and NT-proBNP (the inactive form, of 76 amino acids) [211] (Figure 9). Corin can also cleave proBNP but with lower efficacy and specificity than proANP [205]. BNP is involved in the browning of white adipose tissue and increased energy expenditure, effects that improve insulin resistance [212].

CNP is synthesized in the vascular endothelium, central nervous system, and kidney. ProCNP is cleaved by furin, giving rise to a smaller, active peptide of 53 amino acids, which in turn is cleaved by an unknown enzyme to produce an active peptide of 22 amino acids (Figure 9). The levels in cardiac tissue of these mature peptides are much higher in patients with chronic heart failure than in healthy individuals; however, there are no differences in circulating blood CNP levels between healthy individuals and patients with cardiovascular conditions [210,213]. Mature CNP is essential for the regulation of muscle tone, blood pressure, inflammation, and angiogenesis. By binding to its receptors, natriuretic peptide receptor B (NPRB) and natriuretic peptide receptor C (NPRC), CNP activates different

signaling pathways involved in atherosclerosis, hypertrophy, fibrosis and cardiac electrophysiology [213,214].

Natriuretic peptides released into the bloodstream are recognized by three receptors found in peripheral tissues, natriuretic peptides receptor A (NPRA), NPRB, and NPRC [212]. Binding of natriuretic peptides to NPRA and NPRB receptors triggers the conversion of guanosine-5'-triphosphate (GTP) to cyclic guanosine-3',5'-monophosphate (cGMP). cGMP has numerous downstream effectors inside the cell, including cGMP-dependent protein kinases (cGKs). cGKs 1 are involved in the phosphorylation of vasodilator-stimulated phosphoprotein (VASP), a protein involved in focal adhesion sites and adherents junctions [215]. The NPRC receptor has among its functions the internalization of natriuretic peptides into the cell for their lysosomal degradation. In addition, the receptor intracellular C-terminal tail contains Gi-binding domains that are critical for the detection of pertussis toxin, which targets adenylyl cyclase inhibition and phospholipase C- activation [213].

Circulating levels of ANP and BNP are increased in patients with cardiovascular disease and decreased in patients with obesity, metabolic syndrome, or T2DM [210,216]. Therefore, several of these peptides are currently under study for the treatment of diseases. For instance, carperitide, a recombinant human ANP, is widely used in Japan to treat pulmonary congestion in patients with decompensated heart failure [217]. Nesiritide, a recombinant B-type natriuretic peptide, has been reported to improve cardiac function in patients with acute myocardial infarction and heart failure in a recent meta-analysis [218]. Vosoritide, a CNP-derived peptide, has also recently been approved by the European Union for the treatment of achondroplasia (genetic bone disorder causing disproportionate short stature in infants) in children ≥ 2 years [219,220].

HYPOTHESES AND OBJECTIVES

HYPOTHESIS AND OBJECTIVES

Insulin resistance is associated with pathological remodeling of the heart, characterized by concentric left ventricular hypertrophy, interstitial fibrosis, and extracellular matrix (ECM) remodeling leading to diastolic dysfunction [221–223]. Recently, left ventricular myocardial remodeling was linked to high levels of CE-enriched lipoproteins, such as LDL, using paired cardiovascular magnetic resonance imaging and lipid data in a Mendelian randomization study of a sample including 17 311 individuals [15]. However, the molecular mechanisms underlying the link between lipoprotein-derived cardiac lipid accumulation, insulin action, and cardiac dysfunction are largely unknown.

Our group has previously identified a peptide sequence (P3: H-GDNDSEDNSDEENC-NH_2) (Gly^{1127}-Cys^{1140}) in the CR9 domain of LRP1 that is crucial for its interaction with aggregated LDL [93]. We showed that polyclonal antibodies generated against the P3 sequence (anti-P3 antibodies) efficiently blocked VSMC foam cell formation. Importantly, the CR8/CR9 tandem is the only pair of consecutive CR modules in cluster II of LRP1 that shows negligible affinity for serpins, such as PAI-1 and protease nexin 1 (PN1) [25]. This makes CR9 an ideal target to counteract LRP1-agLDL interactions without disrupting the binding of other essential ligands, such as protease inhibitor complexes, which are key inhibitors of proinflammatory signaling.

On the other hand, the heart can also exert control over peripheral organ metabolism through the secretion of certain molecules, called cardiokines. These cardiokines can affect the metabolic function of various cell types that influence whole-body homeostasis [195,196,224]. However, it is unknown at this time whether lrp1 in cardiomyocytes modulates the production and release of cardiokines potentially involved in whole-body metabolism.

Based on these previous results, the aim of the present work was to study the consequences of Lrp1 modulation through different approaches on vascular and cardiac metabolism. For this purpose, we developed two different *in vivo* models: mice with Lrp1-deficient cardiomyocytes (herein, cm-*Lrp1*$^{-/-}$) and P3-immunized hypercholesterolemic rabbit.

5 Specific Objectives of Study I

1) Generate a murine experimental model of conditional and specific Lrp1 deficiency in cardiomyocytes (cm-*Lrp1*$^{-/-}$).
2) Analyze differential proteins in the heart of cm-*Lrp1*$^{-/-}$ mice and controls.
3) Explore the impact of differential proteins, in particular cardiokines, on target tissue fatty acid metabolism and uptake.

4) Study the impact of cardiomyocyte *Lrp1* deficiency on whole-body metabolism.

6 Specific Objectives of Study II

1) Study the capacity of P3 immunization to generate specific anti-P3 antibodies in a rabbit model of hypercholesterolemia.
2) Study the effect of anti-P3 antibodies to inhibit foam cell formation from smooth muscle cell and macrophages, and the associated proinflammatory signaling.
3) Determine the efficacy of anti-P3 antibodies to block atherosclerosis through inhibition of foam cell formation and associated proinflammation.

7 Specific Objectives of Study III

1) Evaluate the impact of CE-enriched lipoproteins on cardiac lipid accumulation.
2) Study the effect of anti-P3 antibodies on cardiac lipid accumulation.
3) Analyze the impact of cardiomyocte intracellular CE accumulation on cardiac insulin response.

MATERIALS AND METHODS

MATERIALS AND METHODS

8 Study I

8.1 Mice model generation

We generated an experimental mouse model with conditional and cardiomyocyte-specific Lrp1 deficiency (TNT-iCre^{+}-LRP1$^{flox/flox}$ or cm-Lrp1$^{-/-}$) by treatment with Doxycycline [225]. Specific controls for these deficient mice are TNT-iCre^{-}-Lrp1$^{flox/flox}$ (cm-Lrp1$^{+/+}$). The experimental procedure for the generation of cardiomyocyte-specific Lrp1 deficient mice (cm-Lrp1$^{-/-}$) transgenic mice is illustrated in Figure 10. To accomplish cardiomyocyte-specific inactivation of LRP1, we used a cardiomyocyte-specific Cre suppressor and a floxed Lrp1 allele. We bred commercial LRP1$^{flox/flox}$ mice (B6;129S7-Lrp1tm2Her/J; stock: #012604, Jackson Laboratories) carrying loxP sites within the LRP1 gene to TNT-iCre transgenic mice (kindly provided by Prof. Bin Zhou, Albert Einstein College of Medicine, USA) [225], for eight generations (Figure 10A).

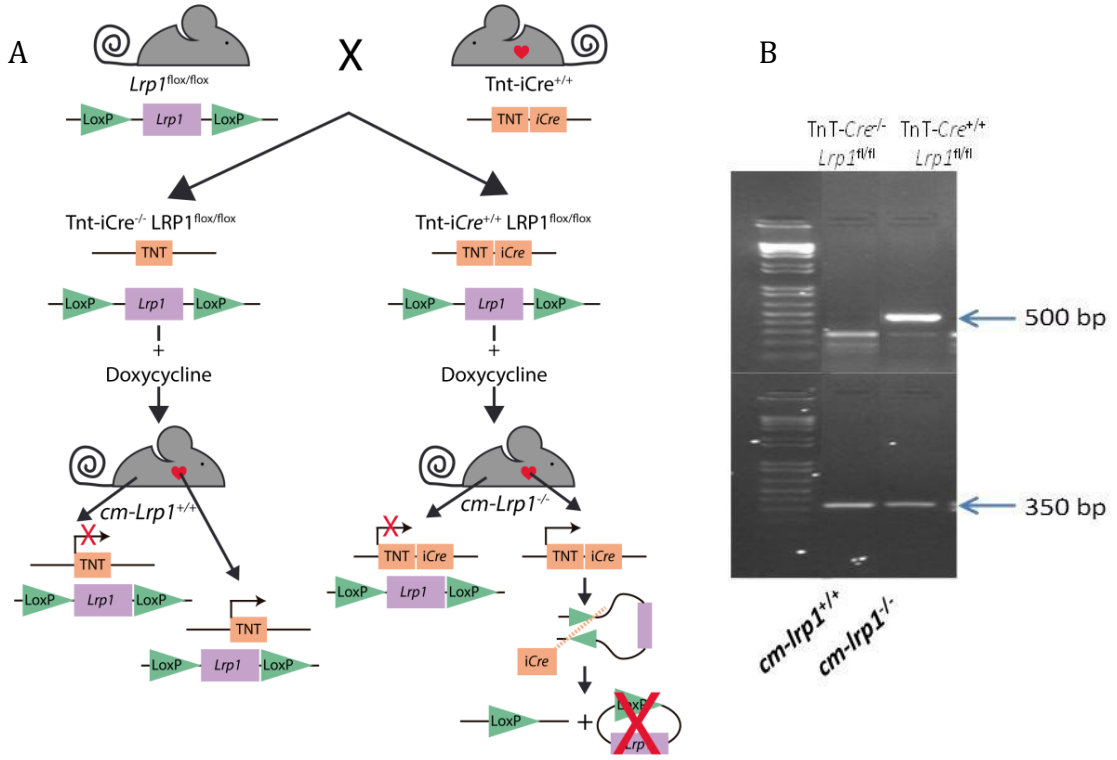

Figure 10. Generation of the cm-*Lrp1*$^{-/-}$ transgenic mice. (A) Generation schedule of an in vivo model with a doxycycline-inducible attenuation of Lrp1 expression selectively in cardiomyocytes. In cm-*Lrp1*$^{-/-}$ mice with the genotype TnTCre$^{+/+}$Lrp1$^{flox/flox}$, the activation of Cre recombinase by doxycycline converts the Lrp1 floxed alleles to KO (–) alleles. (B) Cre and Flox transgenes were detected by PCR. A fragment of 500 bp was amplified from mouse tail genomic DNA when the Cre transgene driven by the TnT promoter was present. A fragment of 350 bp was amplified when flox sequences flank lrp1 gen.

Transgenic founder mice were genotyped by PCR analysis of tail tip genomic DNA using primers for floxed LRP1, Cre and Nrt (endogenous positive control gene) (Figure 10B). Genomic DNA was extracted with a Wizard® SV Genomic DNA Purification System (Promega, Madison, WI, USA) and PCR analysis was performed with IDT-synthesized oligonucleotides (Integrated DNA Technologies, Inc.; Coralville, IA, USA. High-fidelity PCR system (Roche Molecular Systems). The oligonucleotides used are specified in Table 9.

Oligonucleotides	Sequence	Ref.
Flox forward	5'-CAT ACC CTC TTC AAA CCC CTT CCT G-3'	64542236
Flox reverse	5'-GCA AGC TCT CCT GCT CAG ACC TGG A-3'	64542237
Cre forward	5'-GGC GCG GCA ACA CCA TTT TT-3'	63600505
Cre reverse	5'-TCC GGG CTG CCA CGA CCA A-3'	63600506
Nrt forward	5'-TCG ACG CCT TAG CCA TTG AGA T-3'	63600507
Nrt reverse	5'-GGC TGT ACG CGG ACC CAC TTT C-3'	63600508

Table 9. Oligonucleotides used for mice genotyping

8.2 Experimental design and sample collection

Mice were housed in specific pathogen-free facilities with a 12-hour light/12-hour dark cycle. Age-matched littermates were used for all experiments. In the first experimental setting (Figure 11, green arrow), ten-week-old male cm-*Lrp1*$^{-/-}$ (deficient) and cm-*Lrp1*$^{+/+}$ (control) mice were fed a high-fat, high-cholesterol diet (TD.88137) or a chow diet and treated with doxycycline cyclate administered in their drinking water (1,5 mg/ml/kg) for six weeks to assess attenuation of Lrp1 levels in cardiomyocytes. In the second experimental setting (Figure 11, blue arrow), after two weeks of HFD diet and doxycycline cyclate administered in their drinking water, both groups of mice were randomly assigned to untreated (PBS) or treated with the NPRA inhibitor A71915 (200 µg/kg in PBS in a final volume of 100 µl) for the last four weeks. The Comprehensive Laboratory Animal Monitoring System (CLAMS) study was performed at week 5. Mice from both experimental setting were harvest at week six and samples from liver, skeletal muscle, heart, epididymal white adipose tissue (eWAT), and brown adipose tissue (BAT), were kept frozen at -80°C. One aliquot of tissue was resuspended in Tripure™ Isolation Reagent (Roche Molecular Systems) for total protein and mRNA isolation according to the manufacturer's instructions, another aliquot for lipid extraction was resuspended in 0.1 M NaOH and a portion of these tissues was also embedded in Tissue-Tek optimum cutting temperature (O.C.T.) compound (Sakura Finetek™, ref. 4583) for immunohistochemistry. Blood plasma samples were collected for ELISA and biochemical analysis. Glucose tolerance test (GTT) was performed at week six of the dietary intervention. All experimental protocols were approved by the Institutional Animal Care and Use Committees at the Research Institute IR

SANTPAU, and complied with all guidelines concerning the use of animals in research and teaching as defined by the Guide for the Care and Use of Laboratory Animals (NIH Publication N°.80-23, revised 1996).

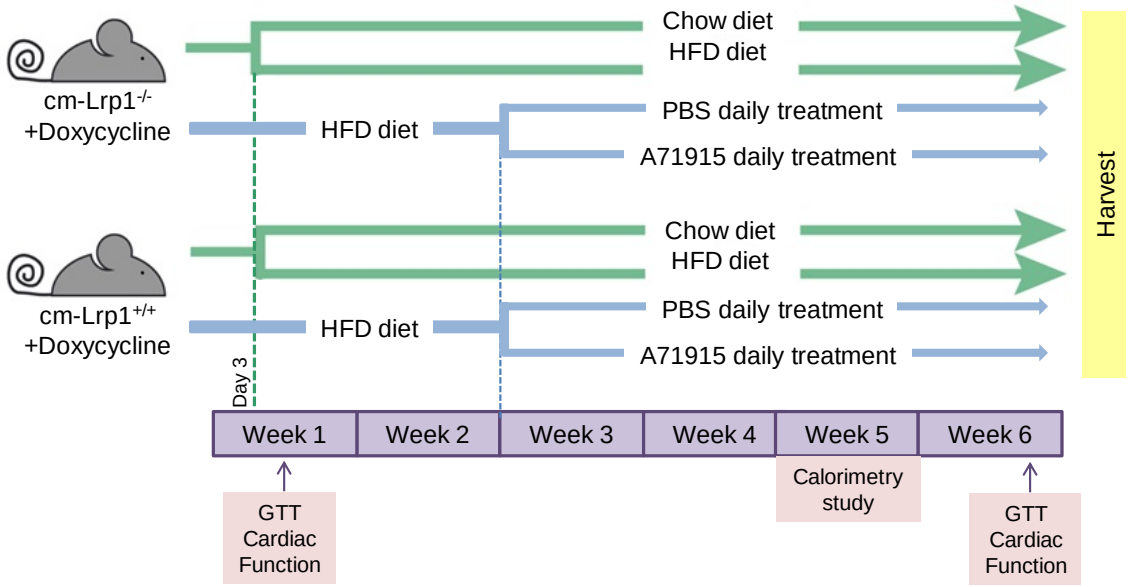

Figure 11. Diagram of the experimental design of the study I.

8.3 Tissue homogenization

Frozen tissues (25 mg) (heart, liver, skeletal muscle, eWAT and BAT) were pulverized in liquid nitrogen using a mortar and a pestle. Samples were then homogenized in TriPure™ isolation reagent (Roche Molecular Systems) for total RNA and protein extraction according to the manufacturer's instructions. Total RNA from skeletal muscle was extracted using the RNeasy mini kit (Qiagen) according to the manufacturer's instructions after the previous addition of Proteinase K. For RNA extraction from eWAT, the tissue was processed with the kit RNeasy Mini Kit (Qiagen). DNA was digested with DNase I (Invitrogen). Extracted RNA was eluted in 25 µL of nuclease-free water. The yield and quality of RNA was tested by agarose electrophoresis and spectrophotometry. Isolated RNA was stored at −80 °C until use. All the techniques used in study I are explained in article 1 and shown in Figure 12.

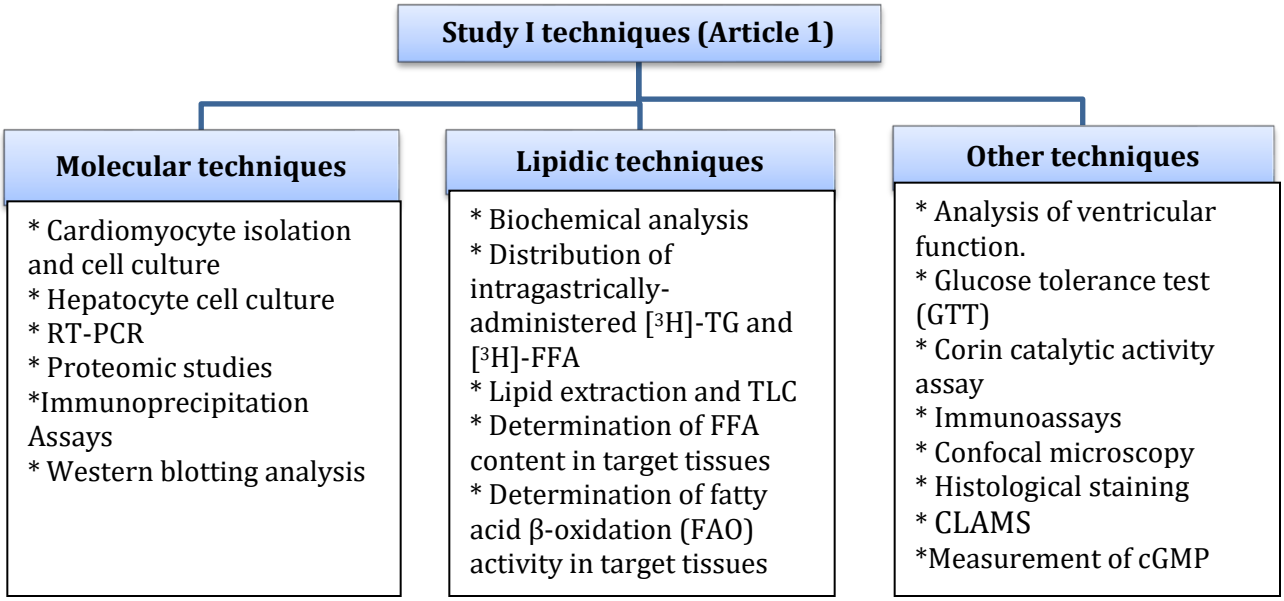

Figure 12. Schematic representation of all the techniques used in the study I (Article 1).

8.4 Molecular techniques

8.4.1 Cardiomyocytes isolation

Cardiomyocytes were obtained from the heart of cm-*Lrp1*$^{-/-}$ and cm-*Lrp1*$^{+/+}$ mice by the Langendorff method. First, the heart was surgically removed and washed with a Ca^{2+} free Tyrode solution at 4 °C and oxygenated. The aorta was suspended in the Langendorff apparatus, and the heart was perfused via the aorta with Ca^{2+} free Tyrode solution at 37°C to clean blood remnants. The Ca^{2+} free Tyrode solution was then carefully removed, and the enzyme solution composed of Ca^{2+} free Tyrode solution with bovine serum albumin (BSA), collagenases and proteinases was added. Two reperfusion cycles (3 mL/ minute during 6 minutes) were performed to add the stop solution (Ca^{2+} free Tyrode solution without collagenases and proteinases). Once the perfusion was finished, the heart was removed from the Langendorff system and treated with an enzymatic solution for 5 minutes at 37 °C under shaking. The pieces of tissue were extracted with tweezers and, with shaking, submerged into stop solution to continue disaggregation. Tissue pieces were then removed and the solution containing the cardiomyocytes was centrifuged for 5 minutes at 450 rpm. The cell pellet was resuspended in stop solution or Tripure™ Isolation Reagent®, depending on the further methodology used.

8.4.2 Cardiomyocyte HL-1 cells

The HL-1 mouse atrial myocyte cell line was generated by Dr. W. C. Claycomb (Louisiana State University Medical Center, New Orleans, LA, USA) and kindly provided by Dr. U. Rauch (Charité-Universitat medizin Berlin). These cells showed cardiac characteristics similar to those of adult cardiomyocytes, such as the presence of highly ordered myofibrils

and specific cardiac junctions in the form of intercalated disks, as well as the presence of cardio specific voltage-dependent currents such as rapid delayed rectifier (IKr) channels and an ultrastructure similar to primary cultures of adult atrial cardiac myocytes [226].

HL-1 cardiomyocytes were grown on gelatinized plates with 12.5µg/mL of 0.1% Fibronectin bovine plasma (Sigma-Aldrich, ref. F1141) and 0.02% Difco™ Gelatin (BD Bioscience, ref. 214340) and maintained in Claycomb medium (Sigma-Aldrich, ref. 51800C) with supplements at 37°C in a 5% CO_2 atmosphere (Table 10).

HL-1 Claycomb medium		
Medium	**Composition**	**Concentration**
Proliferation state	Fetal Bovine Serum	10%
	Penicillin G	100 Units/mL
	Streptomycin	100µg/mL
	L-Glutamine	2 mmol/L
	Norepinephrine	100 µM
Quiescence state	Fetal Bovine Serum	0.2%/day
	Penicillin G	100 Units/mL
	Streptomycin	100µg/mL
	L-Glutamine	2 mmol/L
	Norepinephrine	100 µM
Treatment	Fetal Bovine Serum	0%
	Penicillin G	100 Units/mL
	Streptomycin	100µg/mL
	L-Glutamine	2 mmol/L
	Norepinephrine	100 µM

Table 10. Preparation of cell culture medium for HL-1 cells.

Our group has developed a stable LRP1-deficient HL-1 line by transfection of the HL-1 cardiomyocyte cell line with lentivirus. Addition of Blasticidina S HCl (10 ug/mL, Thermo Fisher, ref. A11139-03) to the culture medium allowed selective growth of LRP1-deficient HL-1. LRP1-deficient HL-1 ($LRP1^-$) and control HL-1 ($LRP1^+$) cells were cultured in Claycomb medium for 48 h and then the supernatants were collected. After determination of their ANP content by ELISA, the supernatants were added directly to the cultured hepatocytes (Hepa 1-6). HL-1 cells were also collected in lysis buffer (Tris-HCl 1M, KCl 1M,

cOmplete™, Mini, EDTA-free Protease Inhibitor Cocktail (Roche Diagnostics ref. 11 936 170 001)) to determine LRP1 levels by Western blot.

8.4.3 Hepatocyte cell culture

8.4.3.1 Hepatocyte isolation

Hepatocytes were isolated from the livers of fed anesthetized control mice by a modification of the collagenase method [227]. Livers were perfused with Hank's balanced salt solution (HBSS, pH 7.4, 37ºC, gassed with 95% O_2 and 5% CO_2: 5.4 mM KCl, 0.44 mM KH_2PO_4, 138 mM NaCl, 4.17 mM $NaHCO_3$, 0.338 mM Na_2HPO_4, 5.56 mM glucose, 50 mM HEPES, and 0.5 mM EGTA) through the inferior vena cava for 5 minutes at a rate of 5 ml/ minute. Livers were then perfused with HBSS (without EGTA) containing 5 mM $CaCl_2$ and 0.25% (w/v) collagenase IV (Sigma) for 12 minutes approximately. The liver was then removed and gently disintegrated in HBSS, and the cell suspension was washed three times in HBSS. Cell viability as assessed by the Trypan Blue exclusion test was always higher than 80%. Hepatocytes were seeded at a density of $3.5x10^6$ cells in 0.1% (w/v) gelatin-treated 25 cm^2 flasks in DMEM medium (Gibco #11966), supplemented with 10% Fetal Bovine Serum (FBS), 10 mM Glucose, 10 µg/ml Streptomycin, 100 units/ml Penicillin, 100 nM Dexamethasone (Sigma), and 100 nM Insulin (Sigma). After cell attachment (5 h), the medium was replaced for 16 h by fresh DMEM medium containing either 0.1% BSA, 1 mM Carnitine, 20 mM Glucose, 10 nM Insulin, 10 µg/ml Streptomycin and 100 units/ml Penicillin.

8.4.3.2 Hepatocyte treatment

Hepa 1–6 cells were cultured in DMEM with supplement (Table 11). Quiescent cells were used for two different experimental approaches. First, quiescent Hepa 1–6 were exposed to supernatants from $LRP1^-$ and $LRP1^+$ HL-1 cells. Second, quiescent Hepa 1–6 were exposed to increasing dose of ANP (0 to 10 nM) for 18 hours.

Hepatocyte DMEM medium		
Medium	**Composition**	**Concentration**
Proliferation state	Fetal Bovine Serum	10%
	Penicillin G	100Units/mL
	Streptomycin	100µg/mL
	L-Glutamine	2 mmol/L
Quiescence state	Fetal Bovine Serum	0.2%/day
	Penicillin G	100 Units/mL

	Streptomycin	100µg/mL
	L-Glutamine	2 mmol/L
Treatment	Fetal Bovine Serum	0%
	Penicillin G	100 Units/mL
	Streptomycin	100µg/mL
	L-Glutamine	2 mmol/L

Table 11. Preparation of cell culture media for hepatocytes.

8.4.4 Measurement of gene expression

8.4.4.1 RNA Isolation, integrity and quantification

Total RNA was isolated with Tripure™ Isolation Reagent following the manufacturer's instructions. The integrity was verified by electrophoresis in a horizontal agarose gel TBE (Tris/Borate/EDTA buffer) 1% stained with Ethidium Bromide (EtBr) 0.4 µg / mL. The mix of RNA and Bromophenol Blue dye were heated at 65 ° C for 10 minutes before loading samples on the gel. RNA integrity was observed by transillumination with ultraviolet light at 260 nm. The quantification of the total RNA was done using a NanoDrop ND-100 spectrophotometer (NanoDrop Technologies) at a wavelength of 260 nm. The optimum purity of the RNA was indicated by the values close to 2 of the ratios of absorbances at 260/280.

8.4.4.2 cDNA synthesis

Total RNA was used for cDNA synthesis according to the protocol provided with the High Capacity cDNA Reverse Transcription kit (Applied Biosystems, ref. 4368813). Total RNA (1 µg) was mixed with 2 µL of RT buffer, 0.8 µL dNTP Mix, 2 µL random primers and 1 µL of enzyme Multiscribe™, and made up to 20 µL with nuclease free water. The PCR reaction consisted of a 10 minutes cycle at 25°C, another 2 hours at 37°C and 5 minutes at 85°C, using Gene Amp PCR System 9700 equipment (Applied Biosystems). cDNA was stored at −20C until its use.

8.4.4.3 RT-PCR

Target gene expression analyses were performed by Quantitative Real-Time Reverse Transcriptase-Polymerase Chain Reaction (q-RT-PCR) in the PCR-7600 equipment (Applied Biosystems; Foster City, CA, USA) (Table 12).

Receptors Assays		Lipid metabolism Assays		Other Assays	
Lrp1	Mm00464608_m1	**Cpt1**	Mm00550438	**Cav1**	Mm00483057_m1
Vldlr	Rn01498166_m1	**Fasn**	Mm00662319_m1		
Ldlr	Mm01151339_m1	**Acaca**	Mm01304257_m1		
Cd36	Mm01135198-m1	**Acsl3**	Mm01255804_m1		
Nppa	Mm01255747_g1	**Slc27a2**	Mm00449517_m1		
Nppb	Mm01255770_g1	**Slc27a4**	Mm01327405_m1		

Table 12. List of assays on demand for the genes analyzed by RT-PCR.

The SensiFAST™ Probe Hi-ROX Kit (Meridian BIOSCIENCE, ref. CSA-01113) was used for this technique with the thermal cycling conditions detailed in the Table 13 below.

Cycles	Temperature	Time	Observation
1	95 °C	5 minutes	Polymerase activation
40	95 °C	10 seconds	Denaturation
	60 °C	30 seconds	Annealing/extension

Table 13. Thermal cycling conditions of RT-PCR.

18srRNA (4319413E) was used as a housekeeping gene. The mRNA expression levels were measured in triplicate. The threshold cycle (Ct) values were normalized to the housekeeping gene.

8.4.5 Proteomic studies

The mass spectrometry proteomics data have been deposited to the ProteomeXchange Consortium via the PRIDE partner repository with the dataset identifier PXD011564.

8.4.5.1 Protein extraction and digestion

Samples were suspended in lysis buffer (4% (w/v) SDS, 100 mM Tris/HCl, pH 7.6, 0.1 M DTT) and incubated at 95ºC for 5 minutes. To complete cell disruption, the cell extract was sonicated 5 times for 5 seconds (Sonic Vibracell TM). The cell debris was removed by centrifugation at 16000g for 20 minutes at 13ºC. Protein concentration measurement was performed with the Bradford Protein Assay (Bio-Rad). Three biological replicates from each condition were processed. Each replicate was a pool of tissue obtained from three different animals. A total of 36 animals were processed.

8.4.5.2 Peptide labeling by Isobaric Tandem Mass Tag

Each tryptic peptide mixture obtained from 80 µg of protein extract was labeled with Tandem Mass Tags (TMT) (Thermo Scientific) based on the standard procedure. The tryptic peptide mixtures were evaporated to final volumes of about 60 µl. For each experiment, the six labeled peptide mixtures were combined in a low-bind 1.5 mL Eppendorf tube, evaporated, and desalted using a C18 SPE cartridge (3 mL, 15 mg, Agilent Technologies, USA) before separation by Strong Cation Exchange (SCX) chromatography.

8.4.5.3 Separation of peptides by Strong Cation Exchange Chromatography

Peptide separation by SCX chromatography was performed on an Agilent 1100 HPLC system (Agilent Technologies) using a Polysulfoethyl A TM, 50×2.1 mm, 5 µm, 200 Å columns. Peptides were suspended in 200 µl of SCX buffer A (30% ACN, 0.1% formic acid) and separated at 200 µl/ minute using a linear gradient of SCX buffer B (30% ACN, 0.1% formic acid, 500 mM NH_4Cl) from 0 to 25% in 38 minutes and then to 100% in 20 minutes. Five fractions were collected from minute 10 to 52.

8.4.5.4 Liquid Chromatography/Multiple-Stage Mass Spectrometry (LC/MSn) Analysis

Between 5-10% of each collected fraction were separately analyzed by LC/MSn using an LTQ-Orbitrap XL instrument equipped with a nanoESI ion source (Proxeon). Samples were evaporated to dryness and redissolved in 5 µl of 1% formic acid and 5% MeOH. The HPLC system was composed of an Agilent 1200 capillary nano pump, a binary pump, a thermostated microinjector and a micro switch valve. Separation was carried out using a C18 pre-concentration cartridge (Agilent Technologies) connected to a 15 cm-long 100 µm i.d. C18 columns (Nikkyo Technos Co, Japan). Separation was performed at 0.4 µl/ minute using a linear ACN gradient from 0 to 40% in 120 minutes (solvent A: 0.1% formic acid, solvent B: acetonitrile 0.1% formic acid). The LTQ-Orbitrap instrument was set up in the positive ion mode with a spray voltage of 1.8 kV. The scan range of each full MS was m/z 400-2000. Spectrometric analysis was performed in an automatic data dependent mode. A full scan followed by 1 HCD and 1 CID MS/MS for the 8 most abundant signals were acquired. Dynamic exclusion was set to 1 with a time window of 30 seconds to minimize the redundant selection of precursor ions.

8.4.5.5 Database search and quantitative analysis

Thermo RAW files were processed using the EasierMgf software [228], which combines the low mass range data from each HCD MS/MS spectrum with the corresponding CID data obtained for the same precursor in the scan cycle. A database search was done using Proteome Discoverer v1.4 (Thermo-Instruments) with a 1% FDR and the Uniprot 2015-10 database restricted to *Mus musculus* and the following parameters: parent tolerance, 20 ppm; fragment tolerance, 0.8 Da; enzyme, trypsin; missed cleavages, 1; fixed modifications, TMTsixplex (N-terminal, K), carbamidomethyl (C); variable modifications, oxidation (M).

DanteR was used for relative quantification and statistical analysis of TMT-labeled peptides. DanteR ANOVA was performed at protein level and only unique peptides were used. P-values were adjusted by using the Benjamini & Hochberg False Discovery Rate (FDR) correction. Regulated peptides were determined using an adjusted p-value cutoff of 0.05 and a fold change lower than 0.66 (down) or higher than 1.5 (up).

8.4.6 Immunoprecipitation Assays

Protein G Dynabeads (Invitrogen™, ref. 10003D) were bound to the polyclonal anti-corin antibody (abcam ab125254) for 1 h at room temperature. The protein extract was incubated with the Dynabeads Protein G-anti-corin complex overnight at 4 °C. After incubation, the protein immune-complex beads were washed 3 times with the wash buffer and eluted with 50 mM Glycine. Samples were separated by SDS-PAGE and transferred blots were incubated with antibody against Serpin 1 (Biorbyt, orb319062).

8.4.7 Western Blotting analysis

Protein expression was measured by Western Blotting. Protein was isolated using the Tripure™ Isolation Reagent (Roche, Ref. 11667165001) procedure, resuspended in 1% SDS and quantified by the Pierce™ BCA Protein Assay Kit (Thermo Scientific, ref. 23225).

8.4.7.1 Acrylamide gel electrophoresis

Protein extracts (10-50µg) were added to Laemmli Buffer and heated to 100°C for 5 minutes before loading onto 10-15% SDS-PAGE which allows separation of proteins according to their molecular weight. The electrophoresis system used was the Mini Protean-II system (Bio-rad) following the instructions of the company.

8.4.7.2 Nitrocellulose membrane transfer

The proteins separated on the SDS-PAGE gels were transferred to a 0.45 µm nitrocellulose membrane (Bio-Rad) using the Trans-Blot Apparatus Transfer System (Bio-Rad) following the instructions of the company. The quality of the transfer was shown by reverse staining with 0.2% Ponceau (Sigma-Aldrich, Ref. P3504) in 0.1% acetic acid.

The membranes were blocked for 1h using TBS-Tween 20 (0.1M NaCl, 10mM Tris Base, pH7.4, 0.05% Tween20) with 5% BSA or skimmed milk powder depending on the protein, before incubation with the primary antibodies against target proteins. The primary antibodies and conditions used are described in the Table 14.

Primary Antibody	Company	MW (KDa)	Dilution	Host	Reference
LRP1 (β-chain)	Fitzgerald	85	1/50	Mouse	10R-L107b
total AMPK	Cell Signaling Technology	62	1/1000	Rabbit	2532S
phospho AMPK	Cell Signaling Technology	62	1/1000	Rabbit	2535S
phospho VASP	Santa Cruz Biotechnology	50	1/1000	Mouse	sc-101439

total VASP	Santa Cruz Biotechnology	50	1/1000	Mouse	sc-46668
BNP	Santa Cruz Biotechnology	17	1/1000	Goat	sc-67455
ANP	Everest Biotech	16	1/1000	Goat	EB11166
Serpin A1	Biorbyt	47	1/1000	Rabbit	orb319062
phospho ACC	Cell Signaling Technology	280	1/1000	Rabbit	3661S
total ACC	Cell Signaling Technology	280	1/1000	Rabbit	3662S
phospho Akt	Cell Signaling Technology	60	1/2000	Rabbit	4060S
total Akt	Cell Signaling Technology	60	1/1000	Rabbit	4685S
UCP3	Abcam	34	1/1000	Rabbit	ab10985
OXPHOS mitochondrial complexes	Abcam	20-50	1/1000	Mouse	ab110413
CPT1	antibodyregistry.org RRID:AB_2636894	88	1/6000	Rabbit	[227,229]

Table 14. List of primary antibodies used for western blot analysis in the study I.

Prior to incubation with the secondary antibody, three washes with TBS-Tween 20 for 5 minutes were performed to remove antibody excess not adhered to the membrane. The secondary antibodies used were anti-Rabbit (Dako, P0448), anti-mouse (Dako, P0161) and anti-Goat (Dako, P0160) at a dilution of 1/10 000 for 1h at room temperature. Subsequently, 3 washes with TBS-Tween 20 plus one additional wash with TBS alone were performed for 5 minutes before protein detection. Equal protein loading in each lane was verified by incubating blots with monoclonal antibodies against Troponin T (TnT) (Thermo Scientific #MS-295-P) or β-tubulin (Cell Signaling Technology, Inc., #2146).

8.4.7.3 Protein detection

Signal detection was performed with Amersham™ ECL™ Prime Western Transfer Detection Reagent (GE Healthcare, Ref. RPN2232) and we used the Chemidoc XRS kit (Bio-Rad) to capture the luminescence emitted by the secondary antibody. The results were analyzed quantitatively with Quantity One software (Bio-Rad). The membranes were treated with Restore Western Blot Stripping Buffer (Thermo Scientific, ref. 21059) to be reused and incubated with the antibodies of the different proteins of interest and endogens.

8.4.8 Biochemical and lipidic analysis

Insulin serum levels were measured using a Mouse Insulin ELISA (Mercodia, Uppsala, Sweden) following the manufacturer's instructions. The HOMA index (Homeostatic Model Assessment for Insulin Resistance), an estimation of insulin resistance, was calculated as: [fasting serum insulin (ng/mL) × fasting serum glucose (mM)]/22.5. Serum lipids and

lipoproteins, including Cholesterol, Phospholipids, Triglyceride (TG), FFAs, HDL-cholesterol and HDL-phospholipids, were enzymatically determined using commercial kits adapted to a COBAS 6000/c501 autoanalyzer (Roche Diagnostics, Basel, Switzerland)[230]. TG measurements were adjusted for free glycerol contained (Sigma-Aldrich St Louis, MO).

8.4.9 Distribution of intragastrically-administered [^{3}H]-TG and [^{3}H]-FFA

Mice were given an oral fat gavage (OFG) consisting of 20 μCi [^{3}H]-labeled triolein (glycerol tri[9, 10(n)-^{3}H]oleate, 21.0 Ci/mmol; Amersham Biosciences, Buckinghamshire, UK) in 150 μL of olive oil. Mice were bled by cardiac puncture at 1.5 h after the OFG. Serum and target tissues (liver, eWAT and Skeletal Muscle) were collected after perfusion with NaCl solution 0.9%. Radiolabeled serum and tissue TG were separated from the FA using methanol:chloroform:heptane 1.4:1.25:1 (v:v:v) and 0.1 mol/L H_3BO_3-KCO_3 at pH 10.5. The radioactivity in the TG and FA fraction, in total serum and target tissues was determined by scintillation counting [231].

8.4.10 Intracellular lipid content determination in target cells and tissues

8.4.10.1 Cell and tissue lipid extraction

Frozen cell and pulverized tissues (10mg) were homogenized in NaOH 0.1M and the protein content was quantified using Pierce™ BCA Protein Assay Kit to normalize for protein content. The lipid extraction protocol is a modification of the method described by Bligh [232]. Cell extract (600-800 μL) or homogenized tissue (100-600 μg) was mixed with distilled water (until 1mL) and 3mL of the dichloromethane:methanol mixture (1:2) was added to round bottom glass tubes previously washed with dichloromethane. After vigorous vortexing, 1mL of dichloromethane was added and shaken for about 10 seconds. Centrifugation was performed at 3500 rpm for 15 minutes at room temperature and an aqueous upper phase separated from the organic lower phase (containing the intracellular lipids) by a protein intermediate phase was obtained. The organic phase was collected with the aid of a glass Hamilton syringe and transferred to a new conical bottom glass tube. The process was repeated with the aqueous phase by adding 1 mL of dichloromethane, shaking and centrifuging again at the same conditions. The organic phases were pooled and concentrated by evaporating the organic solvent under a stream of N_2 to avoid oxidation of the lipids.

8.4.10.2 Thin-Layer Chromatography

The lipid extract was redissolved in 80 μL dichloromethane, vortexed and loaded onto a chromatography silica plate (DC-Fertigplatten SIL G-25UV, Macherey-Nagel, ref. 809023). Different known concentrations of standard (a mixture of cholesterol, triglycerides, and cholesterol palmitate) were applied to each plate in order to quantify the samples.

Two different mobile phases were run. The first phase composed of a mixture of heptane: diethylether:acetic acid (72:21:4) separated the different lipids. The second phase

(washing) (composed only with heptane) carries away all unwanted lipids 4 cm above the previous phase. Once the plate was dried, it was stained with a solution of 5% phosphomolybdic acid and 5% sulfuric acid in ethanol for 1 minute. The plates were again dried and heated at 100°C for 7 minutes. The lipid components were observed as blue bands. The plates were captured by densitometry using the Chemidoc XRC (Bio-Rad). Spots corresponding to Cholesterol Esters, Triglycerides and Free Cholesterol were quantified by densitometry against the standard curve of cholesterol palmitate, triglyceride, and cholesterol, respectively, using a Chemidoc XRC (Bio-Rad) and quantified with the Quantity One program (Bio-Rad).

8.4.11 Determination of fatty acid β-oxidation (FAO) activity in the liver

An aliquot of liver was homogenized in a buffer composed of 150 mM NaCl, 1 mM dithiothreitol, 30 mM EDTA and 50 mM KH_2PO_4. Tissue fatty acid oxidation (FAO) was determined with 30 µg of post nuclear supernatant by determining the conversion of palmitoyl CoA-1-[^{14}C] into acetyl-CoA [233].

8.5 Other techniques

8.5.1 Analysis of ventricular function

Transthoracic Echocardiography was assessed using an 18 to 38 MHz linear array transducer with a digital ultrasound system (Vevo 2100 Imaging System, Visual Sonics, Toronto, Ontario, Canada, http://www.visualsonics.com). The technique was conducted with the mice under light sedation (1% Isoflurane in oxygen) three days after starting doxycycline treatment (baseline). A second echocardiography was conducted six weeks later at the end of the experimental procedure. Images were obtained in B-mode and M-mode in the parasternal short-axis views. Standard Functional parameters were measured, including left ventricle (LV) internal diameter diastole (LVIDd) and LV internal diameter systole (LVIDs), LV end diastolic volume (LVEDV), LV end systolic volume (LVESV), LV ejection fraction (LVEF), LV fractional shortening (LVFS), LV anterior wall at end cardiac diastole (LVAWd), LV posterior wall at end cardiac diastole (LVPWd), and heart rate [234].

8.5.2 Glucose Tolerance Test

The glucose tolerance test (GTT) was performed three days after starting doxycycline treatment (baseline) and at week six of the dietetic intervention in fasting conditions. Basal blood glucose levels were measured from a tail nick through ACCU-CHEK® Aviva glucometer (Roche Molecular Systems). The mice were then intraperitoneally injected with glucose (1.3 mg/g of body mass). Blood glucose was measured at 15, 30, 60, 120 and 180 minutes after glucose injection. The area under the curve (AUC) of the response curve was then calculated using the software Prism 4.0 [235].

8.5.3 Corin catalytic activity assay

Membrane fractions from heart tissues were prepared by homogenizing 25 µg tissues in 400 µl buffer A (25mM Tris-HCl pH 7.4, 5mM EDTA pH 8). The homogenate was centrifuged at 200 000 g for 1h at 4ºC. The pellet was resuspended in NP-40 buffer (150mM NaCl, 50mM Tris-HCl pH 7.4, 1% P-40). Protein concentration was measured by Pierce™ BCA Protein Assay Kit following the manufacturer instructions. Corin catalytic activity assay was performed in 96-well plates with 20µM/L (p-tosyl-Gly-Pro-Arg)$_2$-rhodamine 110 (Molecular Probes) with 5 µg of heart membrane proteins. To determine the specificity of corin activity, a specific thrombin inhibitor (hirudin, Sigma-Aldrich) was mixed with samples at 37ºC during 5 minutes before addition of substrate. The fluorescence was monitored at wavelengths of 485nm and 538 nm, excitation, and emission respectively, at room temperature at 2 minutes interval during 1 hour in a plate reader. Corin activity was presented as V_{max} for the maximal rate of reaction [236].

8.5.4 Immunoassays

ANP (ab108797, Abcam), GDF-15 (MGD150, R&D Systems) and adrenalin/epinephrine (abx257158, Abbexa) plasma levels were measured by commercially available-enzyme-linked immunosorbent assays (ELISA), according to the manufacturer's recommendations.

8.5.5 Measurement of cyclic GMP levels in target tissues

The cyclic guanosine monophosphate (cGMP) levels in heart, liver and skeletal muscle were measured using an ELISA kit according to the manufacturer's instructions for non-acetylated methodology (ADI-900-014, Enzo Life Sciences). An aliquot of tissue (20 mg) was homogenized in 200 µl of 0.1 M HCl to inhibit endogenous phosphodiesterase activity and stabilize the freed cyclic GMP. They were then centrifuged at 600 g at 4 °C for 10 minutes and the resulting supernatant was stored at -80 °C prior to assay. The unacetylated samples (100µl) and standards were added to the wells containing a GxR IgG antibody. Then, the blue solution of cGMP conjugated with alkaline phosphatase was added, followed by the yellow solution of rabbit polyclonal antibody against cGMP. The plate was incubated at room temperature for 2 hours with shaking at 500 rpm allowing the antibody to bind to the cGMP. After incubation, 3 washes were performed with 400µL of wash solution provided with the kit to remove unbound cGMP excess. The blue Conjugate (5 µL) plus p-nitrophenyl phosphate (pNpp) substrate solution (200 µL) was added and incubated for 1h without shaking. The substrate generated a yellow color when catalyzed by alkaline phosphatase that is conjugated to cGMP. The reaction was stopped by trisodium phosphate solution, and the optical density was immediately read at 405 nm. The amount of signal is indirectly proportional to the amount of cGMP in the sample (Figure 13).

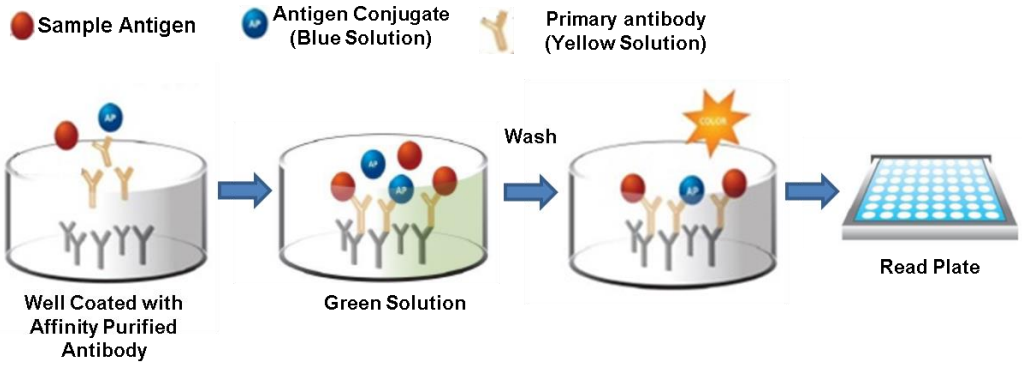

Figure 13. Diagram of the technique used for the detection of cGMP in tissues (image obtained from Enzo Life Sciences)

The cGMP concentrations (pmol/mL) in the tissues were normalized to the total protein concentration (mg/mL). The final concentration was expressed as pmol/mg protein.

8.5.6 Confocal microscopy

Mouse heart cryosections were subjected to target retrieval (10 mM Tris-HCl, pH = 6) and permeabilized with Triton X-100 (0.5%). Isolated cardiomyocytes were fixed with paraformaldehyde and preserved in PBS with sodium acid 0.2%. Cells were permeabilized with glycine (0.1 M) and Triton X-100 (0.2%), blocked with PBS, Tween-20 (0.2%) and BSA (1%) and incubated with primary anti-LRP1 Abs (2 µg/mL, Abcam). Secondary Abs conjugated with Alexa488 and Cy3 (1 µg/mL) (Jackson Immuno Research) were used for detection. Cell and heart cryosections nuclei were counterstained with 4′,6-diamidino-2-phenylindole (DAPI) (Sigma-Aldrich, ref 32670). Results were analyzed with an Axio-Observer Z1 (Zeiss) laser confocal microscope.

8.5.7 Histological staining

Tissue samples were frozen and sectioned (5 µm). Sections were stained with Hematoxilin/Eosin, Herxheimer, Oil red O and Sirius red stains. Herxheimer and Oil red O stainings were used for the detection of lipids. A polarized light microscope was used to measure collagen types I and III on randomly selected Sirius red-stained sections.

8.5.8 Indirect calorymetry system

Measurements of oxygen consumption (VO_2) and CO_2 production (VCO_2) were performed using a comprehensive lab animal monitoring system (Oxymax-CLAMS, Columbus Instruments). Mice were acclimated in metabolic chambers for 1 day before the start of the recordings. Animals were continuously recorded for 2 days with measurements of their locomotor activity (in the x, y and z axes) and gas exchange (O_2 and CO_2) taken every 20 minutes for three consecutive days. Energy expenditure (EE) was calculated using VO_2 and VCO_2 values from indirect calorimetry using the Weir equation [237]: EE (in kJ/h) =

(15.818 × VO_2) + (5.176 × VCO_2). The respiratory quotient was estimated by calculating the ratio of CO_2 production to O_2 consumption.

9 Studies II and III

9.1 Rabbit model

This experimental procedure included 30 New Zealand White (NZW) female rabbits from the Granja San Bernardo animal center (Navarra, Spain) weighing 1.8-2 kg (6-7 months of age). In this study we used female rabbits based on several previous studies suggesting that there are sex hormone interactions involved in the process of atherogenesis [238,239]. The rabbits were housed in a Tecniplast R-Suite cage with a surface area of 4,264 cm^2. Housing temperature was maintained at 21°C, relative humidity ranged from 40-60%, and the light period was 12 hours per day. All animals had food and water *ad libitum*. The experimental procedures were approved by the Animal Experimentation Ethics Committee of the Vall d'Hebron Research Institute with registration number 46/17 and performed in accordance with Spanish legislation and also with the European Union Directives (2010/63/EU).

9.2 Experimental design and sample collection

NZW rabbit were fed the chow R-01 diet from Granja San Bernardo or HFD TD.140140 (1% cholesterol) from Harlan Laboratories (Teklad Diets) (Table 15). Animals were acclimated for one week before the first immunization and immunized with a primary injection and four reminder doses (R1-R4) of IrP (irrelevant peptide) (IrP group; N=12) or P3 (P3 group; N=15) conjugated to the carrier every 21 days. An additional group of rabbits was injected with carrier alone (control group; N=3). This immunization pattern in which reminder doses are administered every 21 days allows an isotype change from a primary response (IgM type) to a secondary response (IgG type), that promotes higher cellular production of antibodies that recognize the target antigen. In addition, this immunization pattern contributes to somatic hypermutation (programmed process that occurs in the variable regions of immunoglobulin genes to produce higher affinity B-cell receptors), which improves the affinity of antibody-antigen reactions.

Rabbit diets	
Chow R-01 diet	**HFD TD.140140**
Protein (by weight): 16.1%	Protein (by weight): 16.7%
Fiber: 16.7%	Fiber: 13.7%
Cholesterol: None	Cholesterol: 1%
Oil and fat: 3.5%	Peanut oil: 5%
Calcium: 0,76 %	Fat (by weight): 7.6%
Phosphorus: 0,57 %	Carbohydrate (by weight): 29.4%
Sodium: 0,26 %	Calcium: 1%

Table 15. Composition of the diet used in the studies II and III.

The four doses of IrP or P3 antigen conjugated with KLH (or carrier) were administered subcutaneously (138 µg/kg, maximum volume 150 µL) every 21 days. For the first immunization, IrP or P3-KLH peptides were emulsified in Freund's Adjuvant Complete, and the rest of the immunizations were done using IrP or P3-KLH conjugated in Freund's Incomplete Adjuvant (both from Sigma Aldrich). The ratio between peptide and adjuvant (Freund's Adjuvant Complete and Freund's Incomplete Adjuvant) was 1:1, the volume of antigen administered was mixed with an equivalent volume of adjuvant, emulsified, and administered to the rabbits. During the immunization period, the animals were fed a chow diet. Starting at the R4 time point, IrP and P3-immunized rabbits were randomly divided into normal diet group and high-fat diet (HFD)-fed group. Twelve rabbits (N=6 IrP-injected and N=6 P3-injected) continued fed on the chow diet, whereas fifteen rabbits (N=6 IrP-injected and N=9 P3-injected) and one rabbit control group (N=3 injected with carrier alone) received HFD for 30 days. In pre-diet (Chk1) and post-diet (Chk2) time points, animals were weighed, serum levels of specific anti-P3 Abs were determined by home-made ELISA, and animals were submitted to PET-CT and carotid Doppler ultrasonography (CDU) imaging studies. After imaging studies, animals were euthanized and aortas, carotids, heart, and liver were dissected and processed for molecular, lipid, confocal and immunohistochemical studies (Figure 14).

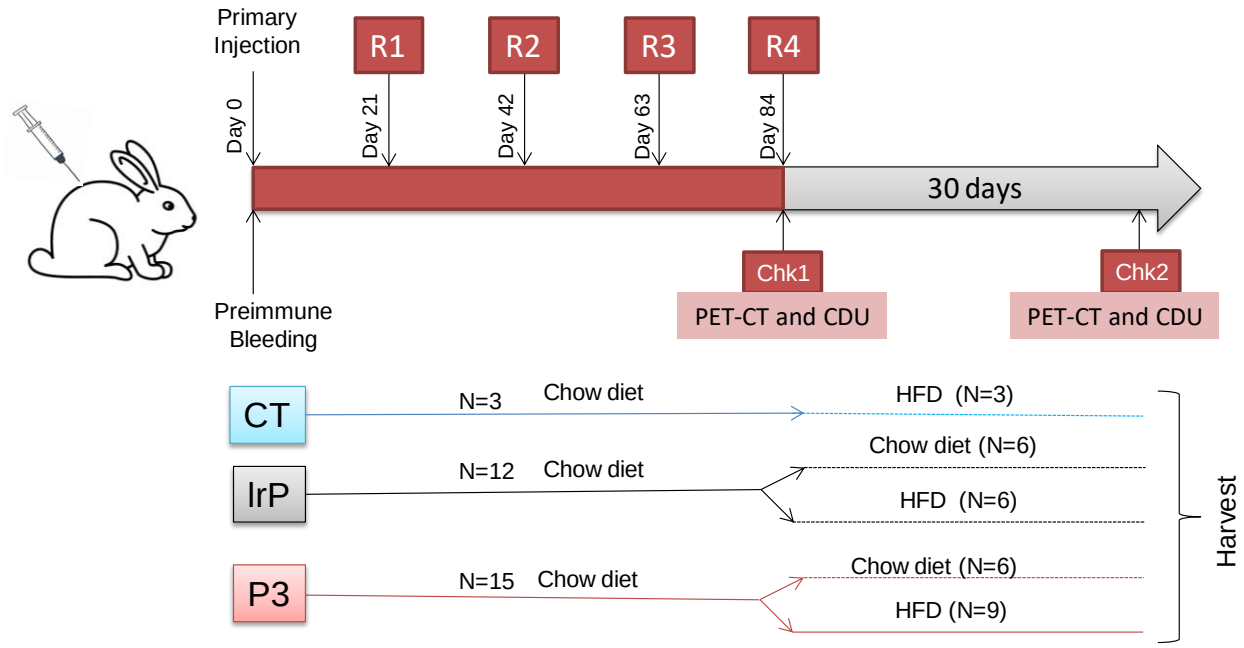

Figure 14. Diagram of the experimental design of the studies II and III.

9.3 Peptide Synthesis and conjugation

The P3 peptide used to immunize rabbits contained the following sequence H-GDNDSEDNSDEENC-NH_2 corresponding to amino acids 1127 to 1140 located in the cluster II of LRP1 (CR9 domain) [93]. The P3 sequence corresponds to an area of high homology

between human and rabbit LRP1, with the difference that the asparagine (N) in humans was replaced by a serine (S) in the rabbit protein. In addition, amino acid C1148 in the rabbit sequence (GDNDCEDNSDEENC) was replaced by S for higher immunogenic efficacy of the peptide. The irrelevant peptide (IrP) has the same sequence as P3 but with amino acids in enantiomer configuration D. Both peptides were synthesized as C-terminal amides on a Rink amide MBHA resin (Iris Biotech GmbH, Marktredwitz, Germany) by the Proteomics and Protein Chemistry Laboratory, Department of Experimental and Health Sciences, Pompeu Fabra University, following the Fmoc solid-phase method using a Prelude peptide synthesizer (Protein Technologies, Inc.). After deprotection and cleavage with trifluoroacetic acid/water/ethanedithiol/triisopropylsilane (94:2.5:2.5:2.5:1, v/v/v/v/v) for 90 minutes, the peptides were isolated by precipitation with ice cold diethyl ether, dissolved in 10 % acetic acid and lyophilized. Peptides were purified by high-performance liquid chromatography to 95 % homogeneity (HPLC, Waters 600) using UV detection at 254 nanometers (Waters 2487) and characterized by electrospray mass spectrometry (Applied Biosystems 4700 Proteomics Analyzer). Peptides were conjugated to the Californian limpet hemocyanin (KLH) carrier molecule or to BSA via their N- or C-terminal cysteine residues. Peptide conjugation with KLH and BSA (Sigma, St. Louis, MO) was performed as previously described [240]. Peptide-KLH conjugates were used for rabbit immunization and peptide-BSA conjugates were used as substrate in the immunoassay ELISA to detect specific anti-P3 antibodies in rabbit serum.

9.4 Determination of circulating lipids and the lipid content in lipoproteins

Serum total cholesterol, choline-containing phospholipids, triglycerides and non-esterified fatty acids (NEFA) levels were determined enzymatically using commercial kits adapted to a COBAS 501 autoanalyzer (Roche Diagnostics, Rotkreuz, Switzerland). VLDL, LDL and HDL lipoproteins were isolated by sequential ultracentrifugation at 100 000 g for 24 h at a density of 1.006, 1.019-1.063 and 1.063-1.21 g/ml, respectively, using a fixed-angle analytical rotor (50.3, Beckman Coulter) [231]. The composition of each lipoprotein, including total and free cholesterol, triglycerides, and phospholipids, was determined by commercial methods adapted to the COBAS 501 autoanalyzer. Lipoprotein protein concentrations were determined by the bicinchoninic acid method (Termo Scientific, Rockford, IL). Lipoprotein composition was used to calculate the total mass of each lipoprotein.

9.5 Detection of specific antibodies

We standardized immunoELISA to detect specific antibodies against P3 peptides. All serum were tested using 96-well polystyrene plates (Ref. 442404 Maxisorp, NUNC, Labclinics, Spain) coated with peptide-BSA and BSA as a control for the detection of nonspecific antibodies. ELISA plates were incubated with various serum dilutions for 90 minutes and, after washes, peroxidase-conjugated anti-rabbit IgG (Ref 170-6515, BioRad, Spain) were

added to detect antigen-antibody complexes. The ELISA was developed using OPD substrate (Ref P9187, Sigma Aldrich, Spain), and the absorbance was read on a Multilabel Victor3 reader (Perkin Elmer, Turku, Finland) at 450 nm. The absorbances obtained were fitted to a 4PL curve to calculate the IC50. The parameter 1/IC50 was taken as the antibody titer.

9.6 Glucose tolerance test

The GTT was performed at week four of the dietetic intervention under fasting conditions. Basal blood glucose levels were measured from an ear nick through ACCU-CHEK® Aviva glucometer (Roche Molecular Systems). Rabbits were then intraperitoneally injected with glucose (1.3 mg/g of body mass). Blood glucose was measured at 15, 30, 60, 120 and 180 minutes after glucose injection. The AUC of the response curve was then calculated using the software Prism 4.0.

Table 16 summarized the specific techniques used in each paper of the study II and III and the detailed described is afterward.

Study techniques	
Article 2/ Study II	**Article 3/ Study III**
Isolation of Rabbit Aortic Smooth Muscle Cells	Glucose tolerance test
Isolation of hMΦ primary cultures	Culture of murine HL-1 cardiomyocyte-derived cell line
Culture of VSMC	Determination of neutral lipid content in heart and liver
Treatment of hMΦ and VSMC with rabbit serums	Electron microscopy of the heart
^{18}F-FDG PET/CT and image analysis	Confocal microscopy studies of the heart and HL-1
Ultrasonography	FTIR, freeze-dried state of the heart and lipoproteins
Preparation of histological sections and immunohistochemistry	Heart subfractionation
Confocal microscopy studies of the Arteries	Biotin-labeling of HL-1 cell surface proteins
Image analysis	Western blot analysis of the heart
Western blotting analysis of the Arteries	Immunoprecipitation assay of the heart and HL-1
	2-NBDG uptake assay

Table 16. Summary list of techniques used in the studies II and III

9.7 *In vitro* studies

9.7.1 Culture of Rabbit Aortic Smooth Muscle Cells

Rabbit Aortic Smooth Muscle Cells (rSMCs) were obtained by gentle scraping of the medial layer of NZW rabbit aortas after endothelial layer removal. Cells were incubated at 37°C in a humidified atmosphere of 5% CO_2 in Ham's F12-DMEM (8:2) supplemented with 20% Fetal Bovine Serum, 100 U/mL Penicillin and 0.1 mg/mL Streptomycin. To maintain exponential growth, cells were subcultured by trypsinization and seeded at a density of 10 000 cells/cm^2. A solution of BSA at 1% in PBS was used as a blocking agent. Monoclonal antibodies against LRP1 (Fitzgerald, 10R-L107c) and polyclonal antibodies obtained from P3-immunized rabbits were diluted in PBS/1% BSA/0.01% Triton X-100. Finally, FITC-conjugated goat anti-mouse IgG and FITC-conjugated goat anti-rabbit IgG were used as secondary antibodies. Images were captured and analysed on a Leica inverted fluorescence confocal microscope (Leica TCS SP2-AOBS)

9.7.2 Human Macrophages (hMΦ)

9.7.2.1 hMΦ Isolation

hMΦ were obtained from buffy coats of healthy blood donors. Cells were applied on 15 ml of Ficoll-Hypaque (GE Healthcare, ref. 17-1440-03) and centrifuged at 300 g for 1 hour at 22°C, with no brake. Mononuclear cells were obtained from the central white band of the gradient, exhaustively washed in Dulbecco's phosphate buffer saline, and suspended in RPMI 1640 Glutamax medium (Gibco, ref. 61870-010) supplemented with Human Serum AB (Lonza, ref. 14-490E), Penicillin/Streptomycin and HEPES 1M (Gibco, ref. 15630-056). Cells were left 7 days in culture and allowed to differentiate into macrophages by changing the cell culture media every 3 days (Table 17).

Human Macrophages RPMI medium		
Medium	**Composition**	**Concentration**
Proliferation state	Human serum AB	10%
	HEPES	1%
	Penicillin G	100Units/mL
	Streptomycin	100µg/mL
Quiescence state	Human serum AB	0.2%/day
	HEPES	1%
	Penicillin G	100 Units/mL
	Streptomycin	100µg/mL
Treatment	Human serum AB	0%

	HEPES	1%
	Penicillin G	100 Units/mL
	Streptomycin	100µg/mL

Table 17. Preparation of cell culture media for Human Macrophages.

9.7.2.2 hMΦ Treatment

Quiescent hMΦ were exposed to increasing concentrations of serum (0.25%, 0.5% and 1%) from the different rabbit groups for 2 hours. In some experiments, quiescent hMΦ were exposed to aggregated LDL (100 µg/mL, 2 hours), in the presence of increasing concentrations (1%, 5% and 10%) of chow serum from the different group of rabbits. Following the serum incubation period, cells were exhaustively washed and harvested in NaOH 0.1 M or lysis buffer for lipidic and Western blot analysis.

9.7.3 Human Coronary Vascular Smooth Muscle Cells

9.7.3.1 VSMC Isolation

VSMC were obtained from the medium layer isolated from macroscopically healthy coronary artery segments collected from patients undergoing cardiac transplantation at Hospital de la Santa Creu i Sant Pau (Barcelona, Spain). VSMCs were isolated by a modification of the explant technique. The coronary arteries were cleaned, opened longitudinally and gently scraped to remove the endothelial cell layer. The medial layer was separated from the adventitia and cut into 1mm x 1mm fragments. The explants of the middle tunic were incubated at 37 °C in a humidified atmosphere of 5% CO_2. After 1 week, the cells start to migrate from the explants and proliferate, covering the floor of the culture well. The medium was exchanged every 3 days after the onset of cell outgrowth; a significant outgrowth was reached after 10 days. Tissue fragments were collected with forceps and placed in a new dish with fresh medium. The cells that remained in the dish were cultured until confluence. For characterization, we performed a western blot analysis for specific differentiation markers revealed high levels of-actin (45 kDa) and calponin (33 kDa). Cell monolayers were grown in medium 199 (Gibco, ref. 22340-087) supplemented with FBS (Invitrogen, ref. 04-001-1A), human serum obtained from healthy donor of Sant Pau hospital, L-glutamine (Sigma-Aldrich, ref. 25030-024) and penicillin/ streptomycin (Sigma-Aldrich, ref. 15140-122) (Table 18). The study was approved by the Institutional Ethics Committee at Hospital de la Santa Creu i Sant Pau and conducted in accordance with the Declaration of Helsinki.

VSMC M199 medium		
Medium	**Composition**	**Concentration**
Proliferation state	Fetal Bovine Serum	20%
	Human serum	2%
	Penicillin G	100Units/mL
	Streptomycin	100µg/mL
	L-Glutamine	2 mmol/L
Quiescence state	Fetal Bovine Serum	0.2%/day
	Human serum	0%
	Penicillin G	100Units/mL
	Streptomycin	100µg/mL
	L-Glutamine	2 mmol/L
Treatment	Fetal Bovine Serum	0%
	Human serum	0%
	Penicillin G	100Units/mL
	Streptomycin	100µg/mL
	L-Glutamine	2 mmol/L

Table 18. Preparation of cell culure media for VSMC cells.

9.7.3.2 VSMC treatment

VSMCs were seeded on plates and cultured until 80% confluence was reached. Cell quiescence was induced by maintaining the cell culture for 24 h in medium containing 0.2 % FBS or for 48 h in medium containing 0.4 % serum. Resting VSMCs were treated with increasing concentrations of serum (0.25 %, 0.5 % and 1 %) from the different groups of rabbits for 2 h or with agLDL (100 µg/mL, 2 h) in the presence of increasing concentrations (1 %, 5 % and 10 %) of chow serum from the different groups of rabbits. All experiments used cells between passages 4 and 6; VSMCs at these passages appeared as a relatively homogeneous population, showing a pattern of hills and valleys at confluence. After treatment, cells were washed extensively and collected in 0.1 M NaOH or lysis buffer for lipid transfer and Western analysis.

9.7.4 Culture of HL-1 cardiomyocyte and treatment

HL-1 cells were maintained in Claycomb medium in plastic dishes as described above (8.4.2). the cells were fasted with 0.2 % FBS for 24 h and then were incubated with serum (0.25 %, 1.5 h) from the different rabbit groups i) chow IrP-immunized, ii) chow P3-

immunized, iii) HFD IrP-immunized, and iv) HFD P3-immunized-rabbits. HL-1 cells exposed to increased serum concentrations (0.25, 0.5 and 1%) from the different rabbit groups. to determine the intracellular content of neutral lipids, HL-1 cells were exposed to increased serum concentrations (0.25, 0.5 and 1%) of the different groups of rabbits and collected in 0.1M NaOH for thin layer chromatography.

9.7.4.1 Biotin-labeling of HL-1 cell surface proteins

HL-1 cells were exposed to rabbit's serum (0.25 %) for 1.5 h and then treated with insulin (100 nM) for 30 minutes. Biotin-labeling protein assay (EZ-Link Sulfo-NHS-SS-Biotin, ref. 21 331, Thermo Scientific) was used to determine the protein levels of GLUT4 at the cell surface. Cells were incubated first with a biotin solution 0.12 mg/ml for 2 h at 4ºC and, then with 0.1 mM Glycine solution for 30 minutes at 4 ºC and then washed three times with PBS 1X. Biotinylated proteins were pulled down by streptavidin-conjugated agarose beads (Pierce Streptavidin Agarose, ref. 20 353, Thermo Scientific) for 2 h at room temperature. Biotinylated and total proteins (10 % of proteins incubated with agarose beads) were analyzed by Western blot after incubated with rabbit anti-GLUT4 (sc-7938; Santa Cruz Biotechnology), mouse monoclonal anti-ATP1A1 (MA3–928, Invitrogen), or mouse monoclonal anti-β-actin (A2228; Sigma-Aldrich) antibodies overnight at 4 ºC, following by incubation with secondary antibodies (goat anti-mouse and goat anti-rabbit; Dako) diluted 1/10 000 for 1 h at room temperature. Signals were detected with the ECL immunoblotting detection system (GE Healthcare) and results were quantitatively analyzed using Chemidoc (BioRad). Biotinylated-ATP1A1 and β-actin were used as loading control of plasma membrane protein and total protein extracts, respectively.

9.7.4.2 HL-1 NBDG uptake assay

HL-1 cells were exposed to rabbit's serum (0.25 %) for 1.5 h and then treated with insulin (100 nM) in the presence of 2-deoxy-2-[(7-nitro-2,1,3-benzoxadiazol-4-yl) amino]-D-glucose (2-NBDG solution; Sigma-Aldrich) (80 µM) for 30 minutes. Cells were then washed with 1X PBS, fixed with 4 % paraformaldehyde, blocked with 2 % BSA, and incubated with Hoechst 33 258 colorant (1/2000) for 1 h. Fluorescence was detected with a Leica DMI8 biological microscope (Leica, Germany). Total fluorescence in the whole cell area was quantified by Image J software.

9.8 Imaging techniques

9.8.1 ^{18}F-FDG PET/CT

An injection of ^{18}F-FDG (0.5 mCi/kg) was administered through a catheter in the marginal vein of the ear of each animal. The image study was performed on a Siemens Biograph mCT S64 hybrid PET/CT instrument. Specialized technicians carried out an angiographic PET/CT study at 120 and 180 minutes, which allowed the anatomical and metabolic

localization of the studied structures. The CT and PET studies were recorded for 5-6 seconds and 15 minutes, respectively.

9.8.1.1 Acquisition parameters

Thoracic-abdominal imaging studies of the heart, great vessels, and abdominal aorta in only one bed position (15 minutes) were performed at the maximum resolution of the PET/CT equipment (1.5 mm in the PET and 0.5 mm in the CT). CT characteristics (attenuation correction) AngioCT characteristics: An angiographic study was performed before PET acquisition. VISIPAQUETM (iodixanol) contrast was used and injected at 0.7ml/second.

9.8.1.2 Image analyses

The co-registration of both studies (PET and CT) was automatically carried out by the Software of the Siemens Biograph mCT S64 hybrid PET/CT equipment. PET/CT data were displayed in axial planes on a Syngovia (Siemens) workstation. Mean standard uptake values (SUVs) were recorded on contiguous axial slices of the aorta superior, central, and inferior (one ROI in each area). The corresponding SUV units were calculated in each animal. These units allow the comparison and standardization of the emission values of each structure studied, including decay correction between dual time-point images. PET/CT outcome variables were the maximum and averaged SUVs.

9.8.2 Ultrasonography

Ultrasonography was performed with a Mindray M7 device (Shenzen Mindray Bio-medical Electronics, Shenzen, PRC) and a 7.5 MHz central frequency lineal probe. All animals were anaesthetized with propofol and maintained with Isoflurane (2-3% in oxygen) to respect their welfare and to avoid tachycardia or stress-induced pulse frequency. Ultrasonographic exams were performed for carotid arteries. The morphology of carotid arteries was measured using B mode images, followed by colour and pulsed wave Doppler analysis to check the blood flow. The specific location at the internal and external carotid division was selected following previously published reference [241], assuming that this location is a target for lipid deposits. The parameters included were systolic and diastolic velocities, as well as arterial resistance index (ARI). ARI=(Systolic velocity-Diastolic velocity)/Systolic velocity). In all the ultrasonographic parameters, three different measurements were performed in each image, and the mean value was used for parameter calculation. The software used for measurements was that included in the ultrasound device, and mathematical calculations were obtained.

9.8.3 Electron microscopy

Cells growing in 60 mm plates were washed in PBS 1X and then fixed with 2.5 % glutaraldehyde in 0.1 M phosphate buffer at room temperature for 1 h. Next, cells were gently scraped and then pelleted in 1.5 ml tubes. Cardiac tissue was cut into small pieces,

extensively washed in PBS 1X, and fixed with 2.5 % glutaraldehyde, 2 % Paraformaldehyde in 0.1 M phosphate buffer overnight. Samples were dehydrated, embedded in Spurr and sectioned using Leica ultramicrotome (Leica Microsystems). Ultrathin sections (50–70 nm) were stained with 2 % uranyl acetate for 10 minutes, a lead-staining solution for 5 minutes and then analyzed with a transmission electron microscope, JEOL JEM-1010 fitted with a Gatan Orius SC1000 (model 832) digital camera at the Unit of Electron Microscopy, Scientific and Technological Centers of the University of Barcelona, School of Medicine and Health Sciences (Barcelona, Spain).

9.8.4 Confocal microscopy studies

Serial sections of arteries (5 μm) were immunostained with Phalloidin-488 to identify smooth muscle cells and RAM11for detection of macrophages, as well as other antibodies for the detection of anti-inflammatory proteins such as NF-kB p65 and TNF-R1 (Table 19). Alexa Fluor 633 IgG (1/100) was used as secondary antibody. Images were recorded on a Leica inverted fluorescence confocal microscope (Leica TCS SP2-AOBS, Germany). Arteries were imaged with the HCX PL APO 20x/0.75 IMM Corr CS_2 objective. Fluorescent images were acquired in a 1024 x 1024-pixel scan format and processed with standard Leica TCS-AOBS software

Heart sections from each study group were washed with PBS 1X, permeabilized for 5 minutes with PBS 1X with 1 % Tween and blocked with PBS 1X with 1 % BSA. Antibodies were used for 1 h and secondary antibody conjugated with alexa fluor (1/100) and Hoechst 33 258 (1/1000) for 1 h. Some sections were incubated only with 100 μl of BODIPY (1 mg/ml in DMSO) for 30 minutes for detection of lipid droplets. The slides were then mounted with ProLong™ Gold Antifade Mountant (P10144, Thermoscientific). Images were obtained with an Olympus FluoView FV1200 confocal microscope (Olympus), processed with FV10-ASW Viewer 3.1 (Olympus) and quantified with ImageJ software.

Primary Antibody	Company	Reference
Phalloidin-488	Invitrogen™	A12379
RAM11	Dako	M063301-8
NF-kB	Cell Signalling	4764S
TNF-R1	MyBiosource	MBS840939
anti-LRP1	Abcam	ab92544
anti-InsR	Abcam	ab69508
anti-GLUT4	LS-Bio	LS-C123618
BODIPY 493/503	Molecular probes	D3922

Table 19. List of primary antibodies used for confocal microscopy analysis in the studies II and III.

HL-1 cardiomyocytes were washed with PBS 1X, fixed with 4 % Paraformaldehyde, permeabilized for 30 minutes with 0.5 % (v/v) saponin, and blocked with 2 % BSA. The primary antibodies were used for 1 h. After incubation, washes were performed with PBS 1X, and secondary antibodies conjugated with Alexa Fluor (1/800) and Hoechst 33 258 (1 /2000) were added to the nuclei and incubated for 1 h. The cells were then washed with PBS 1X and finally mounted with Mowiol 4-88 (Calbiochem (Merck, Darmstadt). Images were obtained with an Olympus FluoView FV1200 confocal microscope (Olympus), processed with FV10-ASW Viewer 3.1 (Olympus) and quantified with ImageJ software. Quantification of the colocalization level was analyzed using the JACoP add-on of ImageJ software [183]. Controls without primary antibody did not show fluorescent labeling in any tissue or cell sample analyzed.

9.9 Other techniques

9.9.1 Tissue subfractionation

Tissue was washed with PBS 1X and homogenized using a POLYTRON ® Immersion Dispersers PT 2500 as previously described [161,174]. To obtain membrane protein fraction, the homogenized tissue was filtered using QIAshredder spin columns (79 656, QIAGEN), incubated with lysis buffer A (NaCl 150 mM, HEPES 50 mM, digitonin 25 µg/ml, 1 M hexylene glycol, protease inhibitor cocktail 1 % v-v) using an end-over-end rotator. After centrifugation, the supernatant containing mainly cytosolic proteins was removed and the the pellet was incubated with lysis buffer B (NaCl 150 mM, HEPES 50 mM, igepal 1 % v-v, 1 M hexylene glycol, protease inhibitor cocktail 1 % v-v). After centrifugation, the supernatant containing mainly plasma membrane proteins was collected. Proteins were analyzed by Western blot with antibodies against rabbit LRP1 (ab92544 Abcam) or InsR (LS-C63091, LSBio) or GLUT4 (LS-C123618, LSBio). Total cardiac lysates were obtained using RIPA buffer (50 mM Tris-HCl pH 8.0, 150 mM NaCl, 1 % Triton X-100, 0.5 % sodium deoxycholate, 0.1 % SDS, 1 mM PMSF, 10 mM sodium ortho-vanadate, and protease inhibitor cocktails (Sigma-Aldrich, St. Louis, MO, USA), and proteins were analyzed by Western blot. Anti-ATP1A1 (MA3–928, Invitrogen) and anti-GAPDH (sc-81 545, Santa Cruz Biotechnology) were used as total and plasma membrane loading controls, respectively.

9.9.2 Western blotting analysis

Protein extracts were obtained using RIPA buffer. Cell protein extracts (10-40 µg) were diluted in 5X sample buffer with dithiothreitol (DTT) and heated for 5 minutes at 95 ◦C. Electrophoresis was performed on 10 -12% SDS-polyacrylamide gels and the proteins were transferred to a nitrocellulose membrane (GE Healthcare Life Science, Amsterdam, The Netherlands) as described above (8.4.7). Table 20 shows the primary and secondary antibodies used.

Primary Antibody	Company	MW (KDa)	Dilution	Host	Reference
LRP1 β-chain	Fitzgerald	85	1/50	Mouse	10R-L107b
SREBP-2	Santa Cruz Biotechnology	68/125	1/1000	Mouse	sc-13552
phospho-NF-kB p65	Cell Signaling technology	65	1/1000	Rabbit	3039S
NF-kB p65	Cell Signalling Technology	65	1/1000	Rabbit	4764S
TNF-R1	My- Biosource	50	1/2000	Rabbit	MBS840939
Akt	Cell Signaling Technology	60	1/1000	Rabbit	9272S
Phosphor-Akt	Merck	60	1/1000	Rabbit	07–789
AS160	Abcam	147	1/1000	Rabbit	ab24469
Phosphor-AS160	Abcam	147	1/1000	Sheep	ab65753
Secondary Antibody		**Company**			**Reference**
Anti-Mouse		Dako			P0161
Anti-Rabbit		Dako			P0448
Anti-Sheep		Dako			P0163

Table 20. List of primary antibodies used for western blot analysis in the studies II and III.

Equal protein loading in each lane was verified by incubating transfers with monoclonal antibodies against β-actin (Cell Signaling Technology, Inc, #3700S). Signals were detected with the ECL immunoblot detection system (GE Healthcare) and the results were quantitatively analyzed with Chemidoc (BioRad).

9.9.3 Immunohistochemistry studies

The aorta was cleaned of external fat and divided into two sections: thoracic aorta, from the aortic arch to the hepatic aorta, and abdominal aorta, from the hepatic aorta to the bifurcation of the iliac aortas (Figure 15). As shown in Figure 15, the first 2cm section of the thoracic aorta was opened by a longitudinal incision. The remainder of the aorta was divided into 1cm pieces. Alternatively, each piece was frozen and sectioned for histological and molecular studies. The carotids were frozen and kept at -80 ºC for subsequent analysis of lipid composition.

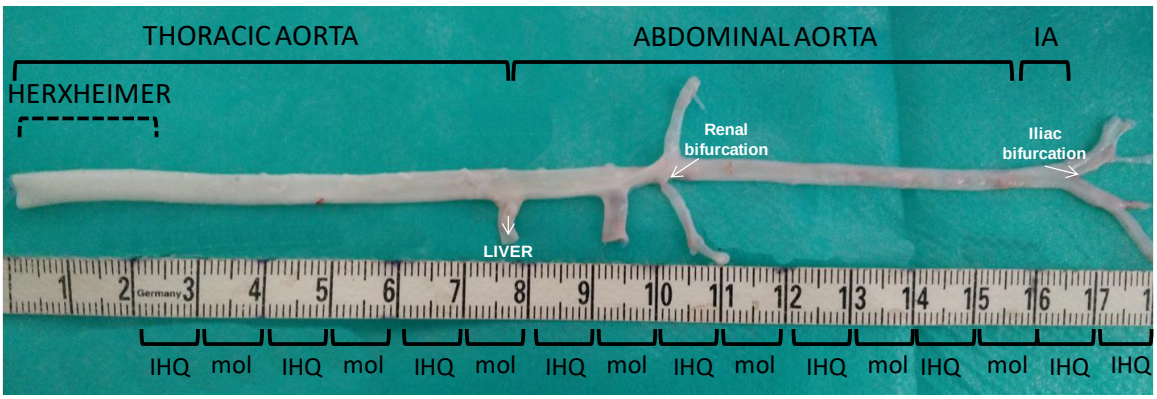

Figure 15. Representative image of isolated aorta indicating the consecutive sections (1 cm) used for immunohistochemistry (IHQ) and molecular studies (mol). IA: Iliac bifurcation.

Longitudinally opened aortic sections were fixed in a 4% Paraformaldehyde-PBS solution for the detection and quantification of fatty streaks by the Herxheimer staining method. Samples for immunohistochemistry were cross-sectioned with a cryostat into serial 5-µm sections and mounted on gelatinized slides. Cross-sections were also stained with the Herxheimer staining method to detect lipids. Images were captured with an Olympus Vanox AHBT3 microscope and digitized with a Sony 3CCD camera.

9.9.4 Lipid analyses and determination of aortic, carotid, and hepatic neutral lipid content

Aorta (10 mg), liver (2.5 mg) and the whole extracted carotid were homogenized in NaOH 0.1 M. Lipids were extracted and quantified as describe above (8.4.10.2). Cholesteryl esters (CE) triglycerides (TG) and free cholesterol (FC) were analysed by thin-layer chromatography (TLC).

9.9.5 Immunoprecipitation assay

Cardiac tissue from the rabbit groups and HL-1 cells exposed to rabbit's serum from each of the four groups were subjected to immunoprecipitation (IP) assays as previously described [183]. Protein extracts were incubated with rabbit anti-LRP1 monoclonal antibody (ab92544, Abcam) or rabbit non-immune IgG as control (2 µg/200 µg of total proteins) for 2 h at 4 ºC. Samples were then incubated with protein A–conjugated agarose beads following the manufacturer's procedure (sc-2001; Santa Cruz Biotechnology) overnight at 4 ºC. Immunoprecipitated proteins were characterized by Western blot using anti-InsR (ab69508; Abcam) and anti-LRP1 (ab92544; Abcam) monoclonal antibodies, and secondary antibodies (goat anti-mouse or goat anti-rabbit; Dako). Signals were detected using ECL immunoblotting detection system (GE Healthcare) and the results were quantitatively analyzed using Chemidoc (BioRad).

9.9.6 FTIR, freeze-dried state

Fourier transform infrared spectroscopy/attenuated total reflectance (FTIR/ATR) spectra of the freeze-dried lipoproteins and tissues were acquired using a Nicolet 5700 FTIR instrument (Thermo Fisher Scientific, Waltham, MA) equipped with an ATR device with a KBr beam splitter and a MCT/B detector as previously described [174,242]. The ATR accessory used was a Smart Orbit with a type IIA diamond crystal (refractive index 2.4). Freeze-dried samples (1 mg) were directly deposited on the entire active surface of the crystal and gently pressed with a Teflon tip to assure good contact. For each sample, 80 interferograms were recorded in the 4000–450/cm-1 region, co-added and Fourier transformed to generate an average spectrum of the segmented heart part with a nominal resolution of 1 cm-1 using Omnic 8.0 (Thermo Fisher Scientific, Waltham, MA). A single-beam background spectrum was collected from the clean diamond crystal before each experiment, and this background was subtracted from the spectra. Spectra were then subjected to ATR and baseline corrections and normalized using the maximum of the Amide II peak. Second derivatives were used to enhance the chemical information present in overlapping infrared absorption bands of spectra.

REPORT OF THE IMPACT FACTOR OF THE PUBLISHED ARTICLES AND THE PARTICIPATION OF THE DOCTORAL CANDIDATE

10 Article 1

Title: Low-density lipoprotein receptor-related protein 1 deficiency in cardiomyocytes reduces susceptibility to insulin resistance and obesity.

Journal: *Metabolism Clinical and Experimental,* 2020 May; 106:154191. doi: 10.1016/j.metabol.2020.154191. Epub 2020 Feb 26. PMID: 32112822

Journal impact factor: 8.694

Authors: Aleyda Benitez-Amaro[a,b,1], Elena Revuelta-López[c,d,1], Olga Bornachea[a,b], Lídia Cedó[e,f], Àngela Vea[a], Laura Herrero[g,h], Nuria Roglans[i], Carolina Soler-Botija[c,d], David de Gonzalo-Calvo[a,b,d], Laura Nasarre[a], Sandra Camino-López[a], Eduardo García[a,b], Eugenia Mato[j], Francisco Blanco-Vaca[e,f,k], Antoni Bayes-Genis[c,d,l], David Sebastian[f,m,n], Joan Carles Laguna[i], Dolors Serra[g,h], Antonio Zorzano[f,m,n], Joan Carles Escola-Gil[e,f,*], Vicenta Llorente-Cortes[a,b,d,*]

a Institute of Biochemical Research of Barcelona (IIBB)-Spanish National Research Council (CSIC), Barcelona, Spain
b Lipids and Cardiovascular Pathology Group, Biomedical Research Institute Sant Pau (IIB Sant Pau), Barcelona, Spain
c Heart Failure and Cardiac Regeneration (ICREC) Research Program, Health Sciences Research Institute Germans Trias i Pujol (IGTP), Badalona, Barcelona, Spain
d Centro de Investigación Biomédica en Red Enfermedades Cardiovasculares (CIBERCV), Instituto de Salud Carlos III, Madrid, Spain
e Metabolic Basis of Cardiovascular Risk, Biomedical Research Institute Sant Pau (IIB Sant Pau), Barcelona, Spain
f Centro de Investigación Biomédica en Red de Diabetes y Enfermedades Metabólicas Asociadas (CIBERDEM), Instituto de Salud Carlos III, Madrid, Spain
g Department of Biochemistry and Physiology, School of Pharmacy, Institut de Biomedicina de la Universitat de Barcelona (IBUB), Universitat de Barcelona, Spain
h Centro de Investigación Biomédica en Red Fisiopatología de la Obesidad y Nutrición (CIBEROBN), Instituto de Salud Carlos III, Madrid, Spain
i Department of Pharmacology, Toxicology and Therapeutic Chemistry, School of Pharmacy and Food Sciences, Institut de Biomedicina de la Universitat de Barcelona (IBUB),
Universitat de Barcelona, Spain
j CIBER Bioingeniería, Biomateriales y Nanomedicina, CIBER-BBN, Instituto de Salud Carlos III, Madrid, Spain
k Departament de Bioquímica, Biología Molecular i Biomedicina, Universitat Autònoma de Barcelona, Barcelona, Spain
l Cardiology Service and Heart Failure Unit, Hospital Universitari Germans Trias i Pujol, Badalona, Spain, Department of Medicine, Autonomous University of Barcelona, Barcelona, Spain
m Institute for Research in Biomedicine (IRB Barcelona), The Barcelona Institute of Science and Technology, Barcelona, Spain
n Departament de Bioquímica i Biomedicina Molecular, Facultat de Biologia, Universitat de Barcelona, Barcelona, Spain

Abstract

Background: Low-density lipoprotein receptor-related protein 1 (LRP1) plays a key role in fatty acid metabolism and glucose homeostasis. In the context of dyslipemia, LRP1 is upregulated in the heart. Our aimwas to evaluate the impact of cardiomyocyte LRP1

deficiency on high fat diet (HFD)-induced cardiac and metabolic alterations, and to explore the potential mechanisms involved.

Methods: We used TnT-iCre transgenic mice with thoroughly tested suitability to delete genes exclusively in cardiomyocytes to generate an experimental mouse model with conditional Lrp1 deficiency in cardiomyocytes (TNT-iCre^{+}-LRP1$^{flox/flox}$).

Findings: Mice with Lrp1-deficient cardiomyocytes (cm-*Lrp1*$^{-/-}$) have a normal cardiac function combined with a favorable metabolic phenotype against HFD-induced glucose intolerance and obesity. Glucose intolerance protection was linked to higher hepatic fatty acid oxidation (FAO), lower liver steatosis and increased whole-body energy expenditure. Proteomic studies of the heart revealed decreased levels of cardiac pro-atrial natriuretic peptide (pro-ANP), which was parallel to higher ANP circulating levels in cm-Lrp1$^{-/-}$ mice and higher hepatic signaling.

Participation of the doctoral candidate: The director of the thesis CERTFIES that Aleyda Benítez Amaro participated in the article "Low-density lipoprotein receptor-related protein 1 deficiency in cardiomyocytes reduces susceptibility to insulin resistance and obesity" as following: Aleyda Benítez Amaro participated in the generation and characterization of cm-*lrp1*$^{-/-}$ mice, in the ecography studies to analyze ventricular function, in lipidic and molecular studies in target tissues, in biochemical serum analysis and biodistribution experiments. She was also involved in cell culture experiments, and the associated lipidic, molecular and confocal microscopy studies. She also participated in the Method section configuration and redaction, in the analysis and interpretation of results, and in the general correction of the article.

Firmado por
LLORENTE CORTES
CONCEPCION VICENTA
- DNI ***4113** el
día 07/11/2022 con
un certificado
emitido por AC
Director Signature

11 Article 2

Title: Immunization with the Gly[1127]-Cys[1140] amino acid sequence of the LRP1 receptor reduces atherosclerosis in rabbits. Molecular, immunohistochemical and nuclear imaging studies

Journal: *Theranostics,* 2020 Feb 10;10(7):3263-3280. doi: 10.7150/thno.37305. eCollection 2020. PMID: 32194867

Journal impact factor: 11.556

Authors: Olga Bornachea[1,2], **Aleyda Benitez-Amaro**[1,2], Angela Vea[1], Laura Nasarre[1], David de Gonzalo-Calvo[1,2,3], Juan Carlos Escola-Gil[4], Lidia Cedo[4], Antoni Iborra[5], Laura Martínez-Martínez[6], Candido Juarez[6], Juan Antonio Camara[7], Carina Espinet[8], Maria Borrell-Pages[3,9], Lina Badimon[3,9,10], Joan Castell[8], Vicenta Llorente-Cortés[1,2,3*]

1. Institute of Biomedical Research of Barcelona (IIBB). Spanish National Research 1. Council (CSIC), Barcelona, Spain.
2. Lipids and Cardiovascular Pathology. Biomedical Research Institute Sant Pau (IIB Sant Pau), Hospital de la Santa Creu i Sant Pau. Barcelona. Spain.
3. CIBER enfermedades cardiovasculares (CIBERcv).
4. Metabolic Basis of Cardiovascular Risk, Biomedical Research Institute Sant Pau (IIB Sant Pau), Hospital de la Santa Creu i Sant Pau. CIBER de Diabetes y enfermedades
Metabólicas Asociadas (CIBERDEM), Barcelona. Spain.
5. SCAC, Universitat Autònoma de Barcelona (UAB), Bellaterra, Spain
6. Department of Immunology, Institut de Recerca and Hospital Santa Creu i Sant Pau, Barcelona, Spain.
7. Preclinical Imaging Platform. Vall dHebron Institute of Research. Barcelona, Spain.
8. Department of Nuclear Medicine, Institut de Diagnòstic per la Imatge (IDI), Hospital General Universitari Vall d'Hebrón, Universitat Autònoma de Barcelona,
Barcelona, Spain.
9. Cardiovascular Program ICCC, Institut de Recerca Hospital de la Santa Creu i Sant Pau, Barcelona, Spain
10. Cardiovascular Research Chair, UAB, Barcelona, Spain

Abstract:

Background: The LRP1 (CR9) domain and, in particular, the sequence Gly1127-Cys1140 (P3) plays a critical role in the binding and internalization of aggregated LDL (agLDL). We aimed to evaluate whether immunization with P3 reduces high-fat diet (HFD)-induced atherosclerosis.

Methods: Female New Zealand White (NZW) rabbits were immunized with a primary injection and four reminder doses (R1-R4) of IrP (irrelevant peptide) or P3 conjugated to the carrier. IrP and P3-immunized rabbits were randomly divided into a normal diet group and a HFD-fed group. Anti-P3 antibody levels were determined by ELISA. Lipoprotein profile, circulating and tissue lipids, and vascular pro-inflammatory mediators were determined using standardized methods while atherosclerosis was determined by confocal microscopy studies and non-invasive imaging (PET/CT and Doppler ultrasonography).

Studies treating human macrophages (hMΦ) and vascular smooth muscle cells (VSMC) with rabbit serums were performed to ascertain the potential impact of anti-P3 Abs on the functionality of these crucial cells.

Results: P3 immunization specifically induced the production of anti-P3 antibodies (Abs) and did not alter the lipoprotein profile. HFD strongly induced cholesteryl ester (CE) accumulation in the aorta of both the control and IrP groups, and their serum dose-dependently raised the intracellular CE content of hMΦ and VSMC, promoting TNF-R1 and phospho-NF-kB (p65) overexpression. These HFD pro-inflammatory effects were dramatically decreased in the aorta of P3-immunized rabbits and in hMΦ and VSMC exposed to the P3 rabbit serums. Microscopy studies revealed that P3 immunization reduced the percentage of lipids, macrophages, and SMCs in the arterial intima, as well as the atherosclerotic extent and lesion area in the aorta. PET/CT and Doppler ultrasonography studies showed that the average standardized uptake value (SUVmean) of the aorta and the arterial resistance index (ARI) of the carotids were more upregulated by HFD in the control and IrP groups than in the P3 group.

Conclusions: P3 immunization counteracts HFD-induced fatty streak formation in rabbits. The specific blockade of the LRP1 (CR9) domain with Anti-P3 Abs dramatically reduces HFD-induced intracellular CE loading and harmful coupling to pro-inflammatory signaling in the vasculature.

Participation of the doctoral candidate: The director of the thesis CERTFIES that Aleyda Benítez Amaro participated in the article "Immunization with the Gly^{1127}-Cys^{1140} amino acid sequence of the LRP1 receptor reduces atherosclerosis in rabbits. Molecular, immunohistochemical and nuclear imaging studies" as following: Aleyda Benítez Amaro participated in the validation of P3-immunized rabbit as an hypercholesterolemic model protected against atherosclerosis. She was mainly involved in blood and tissue collection, aorta dissection and lipidic, molecular, and immunohistochemical and confocal studies in the model. She participated in cell culture experiments, collection of cell and supernatants, and molecular and lipidic studies in cells. She was mainly involved in the drafting of the methodology section. She also performed statistical analysis of the results and participated in their interpretation.

Firmado por LLORENTE CORTES CONCEPCION VICENTA - DNI ***4113** el día 07/11/2022 con un certificado emitido por AC Sector Público

Director Signature

12 Article 3

Title: Targeting cholesteryl ester accumulation in the heart improves cardiac insulin response

Journal: *Biomedicine and Pharmacotherapy,* 2022 Aug;152:113270. doi: 10.1016/j.biopha.2022.113270. Epub 2022 Jun 13. PMID: 35709652

Journal impact factor: 6.529

Authors: Virginia Actis Dato[a,b,1], Aleyda Benitez-Amaro[c,d,1], Eduardo Garcia[c,d,1], Lene Claudi[c,d], Maria Teresa LaChica Lho¨est[c,d], Antoni Iborra[e], Joan Carles Escola-Gil[f], Jose Maria Guerra[g,h], Valerie Samouillan[i], Carlos Enrich[j,k], Gustavo Chiabrando [a,b,*,2], Vicenta Llorente-Cortés[c,d,h,**,3]

a Departamento de Bioquímica Clínica, Facultad de Ciencias Químicas, Universidad Nacional de C´ordoba, Argentina
b Consejo Nacional de Investigaciones Científicas y T´ecnicas (CONICET), Centro de Investigaciones en Bioquímica Clínica e Inmunología (CIBICI), C´ordoba, Argentina
c Institute of Biomedical Research of Barcelona (IIBB)-Spanish National Research Council (CSIC), Barcelona, Spain
d Biomedical Research Institute Sant Pau (IIB Sant Pau), Barcelona, Spain
e SCAC, Universitat Aut`onoma de Barcelona (UAB), Bellaterra, Spain
f Metabolic Basis of Cardiovascular Risk, Biomedical Research Institute Sant Pau (IIB Sant Pau), Hospital de la Santa Creu i Sant Pau. CIBER de Diabetes y enfermedades
Metab´olicas Asociadas (CIBERDEM), Barcelona. Spain
g Department of Cardiology, Hospital de la Santa Creu i Sant Pau, Biomedical Research Institute Sant Pau (IIB Sant Pau), Universitat Autonoma de Barcelona, Barcelona,
Spain
h CIBERCV, Institute of Health Carlos III, 28029 Madrid, Spain
i CIRIMAT, Universit´e de Toulouse, Universit´e Paul Sabatier, Equipe PHYPOL, 31062 Toulouse, France
j Unitat de Biologia Cel·lular, Departament de Biomedicina, Facultat de Medicina i Ci`encies de la Salut, Universitat de Barcelona, Barcelona, Spain
k Centre de Recerca Biom`edica CELLEX, Institut d' Investigacions Biom`ediques August Pi i Sunyer (IDIBAPS), Barcelona, Spain

Abstract:

Background: Antibodies against the P3 sequence (Gly^{1127}-Cys^{1140}) of LRP1 (anti-P3 Abs) specifically block cholesteryl ester (CE) accumulation in vascular cells. LRP1 is a key regulator of insulin receptor (InsR) trafficking in different cell types. The link between CE accumulation and the insulin response are largely unknown. Here, the effects of P3 peptide immunization on the alterations induced by a high-fat diet (HFD) in cardiac lipid accumulation and insulin response were evaluated.

Methods: Irrelevant (IrP)- or P3 peptide-immunized rabbits were randomized into groups fed either HFD or normal chow feeding. Cardiac lipid content was characterized by thin-layer chromatography, confocal microscopy, and electron microscopy. LRP1, InsR and

glucose transporter type 4 (GLUT4) levels were determined in membranes and total lysates from rabbit heart. The interaction between InsR and LRP1 was analyzed by immunoprecipitation and confocal microscopy. Insulin signaling activity and glucose uptake were evaluated in HL-1 cells exposed to rabbit serum from the different groups.

Findings: HFD reduces cardiac InsR and GLUT4 membrane levels and the interactions between LRP1/InsR. Targeting the P3 sequence on LRP1 through anti-P3 Abs specifically reduces CE accumulation in the heart independently of changes in the circulating lipid profile. This restores InsR and GLUT4 levels in cardiac membranes as well as the LRP1/InsR interactions of HFD-fed rabbits. In addition, anti-P3 Abs restores the insulin signaling cascade and glucose uptake in HL-1 cells exposed to hypercholesterolemic rabbit serum.

Participation of the doctoral candidate: The director of the thesis CERTFIES that Aleyda Benítez Amaro participated in the article "Targeting cholesteryl ester accumulation in the heart improves cardiac insulin response" as following: Aleyda Benítez Amaro participated in the preparation of samples for transmission electron microscopy (TEM) imaging, in the capture and selection of TEM images, in the molecular and lipidic studies in cardiac samples. She was also mainly involved in the immunoprecipitation and confocal microscopy studies required to study the potential interactions between different receptors and transporters. She was also in charge to prepare cardiac samples for biophysical studies, and in cell culture experiments. She configured the methodological section and participated in the analysis and interpretation of results.

Firmado por LLORENTE
CORTES CONCEPCION
VICENTA - DNI ***4113**
el día 07/11/2022 con
un certificado emitido
por AC Sector Público

Director Signature

RESULTS

13 RESULTS: Article 1

Metabolism Clinical and Experimental 106 (2020) 154191

Contents lists available at ScienceDirect

Metabolism Clinical and Experimental

journal homepage: www.metabolismjournal.com

Basic Science

Low-density lipoprotein receptor-related protein 1 deficiency in cardiomyocytes reduces susceptibility to insulin resistance and obesity

Aleyda Benitez-Amaro [a,b,1], Elena Revuelta-López [c,d,1], Olga Bornachea [a,b], Lídia Cedó [e,f], Àngela Vea [a], Laura Herrero [g,h], Nuria Roglans [i], Carolina Soler-Botija [c,d], David de Gonzalo-Calvo [a,b,d], Laura Nasarre [a], Sandra Camino-López [a], Eduardo García [a,b], Eugenia Mato [j], Francisco Blanco-Vaca [e,f,k], Antoni Bayes-Genis [c,d,l], David Sebastian [f,m,n], Joan Carles Laguna [i], Dolors Serra [g,h], Antonio Zorzano [f,m,n], Joan Carles Escola-Gil [e,f,*], Vicenta Llorente-Cortes [a,b,d,*]

[a] Institute of Biochemical Research of Barcelona (IIBB)-Spanish National Research Council (CSIC), Barcelona, Spain
[b] Lipids and Cardiovascular Pathology Group, Biomedical Research Institute Sant Pau (IIB Sant Pau), Barcelona, Spain
[c] Heart Failure and Cardiac Regeneration (ICREC) Research Program, Health Sciences Research Institute Germans Trias i Pujol (IGTP), Badalona, Barcelona, Spain
[d] Centro de Investigación Biomédica en Red Enfermedades Cardiovasculares (CIBERCV), Instituto de Salud Carlos III, Madrid, Spain
[e] Metabolic Basis of Cardiovascular Risk, Biomedical Research Institute Sant Pau (IIB Sant Pau), Barcelona, Spain
[f] Centro de Investigación Biomédica en Red de Diabetes y Enfermedades Metabólicas Asociadas (CIBERDEM), Instituto de Salud Carlos III, Madrid, Spain
[g] Department of Biochemistry and Physiology, School of Pharmacy, Institut de Biomedicina de la Universitat de Barcelona (IBUB), Universitat de Barcelona, Spain
[h] Centro de Investigación Biomédica en Red Fisiopatología de la Obesidad y Nutrición (CIBEROBN), Instituto de Salud Carlos III, Madrid, Spain
[i] Department of Pharmacology, Toxicology and Therapeutic Chemistry, School of Pharmacy and Food Sciences, Institut de Biomedicina de la Universitat de Barcelona (IBUB), Universitat de Barcelona, Spain
[j] CIBER Bioingeniería, Biomateriales y Nanomedicina, CIBER-BBN, Instituto de Salud Carlos III, Madrid, Spain
[k] Departament de Bioquímica, Biología Molecular i Biomedicina, Universitat Autònoma de Barcelona, Barcelona, Spain
[l] Cardiology Service and Heart Failure Unit, Hospital Universitari Germans Trias i Pujol, Badalona, Spain, Department of Medicine, Autonomous University of Barcelona, Barcelona, Spain
[m] Institute for Research in Biomedicine (IRB Barcelona), The Barcelona Institute of Science and Technology, Barcelona, Spain
[n] Departament de Bioquímica i Biomedicina Molecular, Facultat de Biología, Universitat de Barcelona, Barcelona, Spain

ARTICLE INFO

Article history:
Received 22 August 2019
Accepted 24 February 2020

Keywords:
Cardiomyocyte
Lrp1
ANP
Heart
Liver
AMPK
Fatty acid oxidation

ABSTRACT

Background: Low-density lipoprotein receptor-related protein 1 (LRP1) plays a key role in fatty acid metabolism and glucose homeostasis. In the context of dyslipemia, LRP1 is upregulated in the heart. Our aim was to evaluate the impact of cardiomyocyte LRP1 deficiency on high fat diet (HFD)-induced cardiac and metabolic alterations, and to explore the potential mechanisms involved.

Methods: We used *TnT-iCre* transgenic mice with thoroughly tested suitability to delete genes exclusively in cardiomyocytes to generate an experimental mouse model with conditional *Lrp1* deficiency in cardiomyocytes (*TNT-iCre*$^{+}$-LRP1$^{flox/flox}$).

Findings: Mice with *Lrp1*-deficient cardiomyocytes (*cm-Lrp1*$^{-/-}$) have a normal cardiac function combined with a favorable metabolic phenotype against HFD-induced glucose intolerance and obesity. Glucose intolerance protection was linked to higher hepatic fatty acid oxidation (FAO), lower liver steatosis and increased whole-body energy expenditure. Proteomic studies of the heart revealed decreased levels of cardiac pro-atrial natriuretic peptide (pro-ANP), which was parallel to higher ANP circulating levels. *cm-Lrp1*$^{-/-}$ mice showed ANP signaling

Abbreviations: ACC, Acetyl-CoA carboxylase; Akt, Protein Kinase B; AMPK, AMP-activated protein kinase; ANP, Atrial natriuretic peptide; AUC, Area under the curve; BAT, Brown adipose tissue; BSA, bovine serum albumin; BNP, Brain natriuretic peptide; CE, Cholesteryl esters; cGMP, Cyclic guanosine monophosphate; CLAMS, Comprehensive lab animal monitoring system; CPT1, Carnitine palmitoyltransferase I; DAPI, 4′,6-diamidino-2-phenylindole; eWAT, epididymal white adipose tissue; FA, Fatty acid; FAO, Fatty acid oxidation; FASP, Filter Aided Sample Preparation; FC, Free cholesterol; FFA, Free fatty acid; GDF15, Growth and differentiation factor 15; GLUT, Glucose transporter; GTT, Glucose tolerance test; HDL, High density lipoprotein; HF, Heart failure; HFD, High fat diet; IR, Insulin resistance; LDLR, Low density lipoprotein receptor; LIPG, Endothelial lipase; LpL, Lipoprotein lipase; LRP1, Low-density lipoprotein receptor-related protein 1; LV, left ventricle; LVAWd, LV anterior wall at end cardiac diastole; LVEDV, LV end-diastolic volume; LVEF, LV ejection fraction; LVESV, LV end-systolic volume; LVFS, LV fractional shortening; LVIDd, LV internal diameter diastole; LVIDs, LV internal diameter systole; LVPWd, LV posterior wall at end cardiac diastole; NP, Natriuretic peptide; NPR-A, Natriuretic peptide receptor A; NPR-C, Natriuretic peptide receptor C; OFG, Oral fat gavage; OXPHOS, Mitochondrial Oxidative Phosphorylation System; pAMPK, Phosphorylated AMP-activated protein kinase; pNpp, p-nitrophenyl phosphate; Pro-ANP, Pro-atrial natriuretic peptide; Pro-BNP, Pro-brain natriuretic peptide; pVASP, Phosphorylated VASP; q-RT-PCR, Quantitative real-time reverse transcriptase-polymerase chain reaction; RER, Respiratory exchange ratio; SCX, Strong Cation Exchange; TG, Triglyceride; TLC, Thin layer chromatography; TMT, Tandem mass tags; TnT, Troponin T; UCP3, Mitochondrial uncoupling protein 3; VASP, Vasodilator-stimulated phosphoprotein; VCO_2, CO_2 production; VO_2, Oxygen consumption; VLDLR, Very low-density lipoprotein receptor; ZDF, Zucker Diabetic Fatty.

* Corresponding authors at: Biomedical Research Institute IIB Sant Pau, IIBB-CSIC, Hospital de la Santa Creu i Sant Pau, Sant Antoni Mª Claret, 167, 08025, Barcelona, Spain.
E-mail addresses: JEscola@santpau.cat (J.C. Escola-Gil), vicenta.llorente@iibb.csic.es, cllorente@santpau.cat (V. Llorente-Cortes).
[1] These authors contributed equally to this work.

https://doi.org/10.1016/j.metabol.2020.154191

activation that was linked to increased fatty acid (FA) uptake and increased AMPK/ ACC phosphorylation in the liver. Natriuretic peptide receptor A (NPR-A) antagonist completely abolished ANP signaling and metabolic protection in *cm-Lrp1*$^{-/-}$ mice.

Conclusions: These results indicate that an ANP-dependent axis controlled by cardiac LRP1 levels modulates AMPK activity in the liver, energy homeostasis and whole-body metabolism.

1. Introduction

The metabolic syndrome preceding type 2 diabetes is mainly caused by an inefficient coordination of energy utilization by key organs [1]. It is known that alterations in fatty acid (FA) metabolism play a crucial role in inter-organ dyscoordination and insulin resistance (IR) [2]. Further, in metabolic diseases, the heart shows an exacerbated uptake of free FAs (FFAs) [3] and lipoproteins [4] underlying neutral lipid accumulation in cardiomyocytes.

The low-density lipoprotein receptor-related protein 1 (LRP1) is a key receptor that modulates energy utilization by different tissues. LRP1 is both a carrier and a signaling receptor that regulates processes related with lipid metabolism and glucose homeostasis [5,6]. In the hallmark of lipid metabolism, LRP1 is involved in the uptake of unmodified and modified lipoproteins in different tissues causing alterations in the lipid content, generally associated with dyslipemic conditions. LRP1 is involved in the lipid transport from lipoproteins to hepatocytes [5], coronary vascular smooth muscle cells [7,8], cardiomyocytes [9,10] and adipocytes [11]. Specifically, adipocyte LRP1 modulates not only lipid transport but also glucose homeostasis through the control of insulin sensitivity and energy expenditure [11]. In the context of glucose homeostasis, LRP1 has a regulatory action on the insulin receptor and GLUT4 activation in different tissues and organs including the brain [12,13]. Interestingly, insulin favors LRP1 translocation to the cell membrane in the liver, increasing thus postprandial lipoprotein uptake [14]. Recently, it has been shown that hepatic LRP1 protects against IR and hepatic steatosis [13,15].

The liver plays a central role in the regulation of metabolism, receiving signals from multiple organs such as the pancreatic islets, the central nervous system, adipose tissue and kidneys [16]. It has also been suggested that the heart may also exert control over the metabolism of peripheral organs through the secretion of certain molecules called cardiokines. These cardiokines can affect the metabolic function of various cell types influencing whole-body homeostasis [17–19]. However, it is unknown at this moment whether *lrp1* in cardiomyocytes modulates the production and release of cardiokines potentially involved in whole-body metabolism. The objectives of this study have been to 1) generate a murine experimental model of conditional *Lrp1* deficiency in cardiomyocytes by using the *TnT-iCre* transgenic mice with thoroughly tested suitability to delete genes exclusively in cardiomyocytes [20]; 2) study the impact of cardiomyocyte *Lrp1* deficiency in whole-body metabolism; 3) analyze the differential proteins in the heart of *cm-Lrp1*$^{-/-}$ mice and controls and 4) examine the impact of differential proteins, in particular of cardiokines, on target-tissue fatty acid uptake and metabolism.

2. Material and methods

2.1. *cm-Lrp1*$^{-/-}$ transgenic mice generation and characterization

We generated an experimental mouse model with conditional and cardiomyocyte-specific *Lrp1* deficiency (TNT-iCre^{+}-LRP1$^{flox/flox}$ or *cm-Lrp1*$^{-/-}$) by treatment with doxycycline [20]. The specific controls for this animal controls are TNT-iCre^{-}-Lrp1$^{flox/flox}$ or *cm-Lrp1*$^{+/+}$. The generation of *cm-Lrp1*$^{-/-}$ transgenic mice is described in online Fig. S1. To achieve cardiomyocyte-specific LRP1 inactivation, we use a cardiomyocyte-specific Cre deletor and a floxed allele of *Lrp1*. We crossed commercial LRP1$^{flox/flox}$ mice (B6;129S7-Lrp1^{tm2Her}/J; stock: #012604, Jackson Laboratories) carrying loxP sites within the LRP1 gene with TNT-iCre transgenic mice (kindly provided by Prof. Bin Zhou, Albert Einstein College of Medicine, USA) [20], for eight generations (Fig. 1A).

Transgenic founder mice were genotyped by PCR analysis on tail tip genomic DNA using primers for LRP1, *Cre* and *Nrt* (Fig. 1B). Genomic DNA was extracted with a Wizard® SV Genomic DNA Purification System (Promega, Madison, WI, USA) and PCR analysis was performed with oligonucleotides synthesized by IDT (Integrated DNA Technologies, Inc.; Coralville, IA, USA), using an Expand High Fidelity PCR System (Roche Molecular Systems). The oligonucleotides used are specified in Table S1.

Mice were housed in specific pathogen-free facilities with a 12-hour light/12-hour dark cycle. Both groups, ten-week-old males *cm-Lrp1*$^{+/+}$ and *cm-Lrp1*$^{-/-}$, were treated daily with doxycycline cyclate (Sigma-Aldrich) (Dox) through their drinking water (1.5 mg/mL/kg) *ad libitum* to assess the conditional *Lrp1* inhibition in cardiomyocytes. The control group (*cm-Lrp1*$^{+/+}$) was also treated with Dox to avoid interference with the treatment. Robertson et al., showed that Dox has a long half-life [21].

In the first experimental setting (*online* Fig. S1A), after checking cardiac function, *cm-Lrp1*$^{+/+}$ and *cm-Lrp1*$^{-/-}$ ten-week-old mice were fed high-fat cholesterol-containing diet (HFD TD.88137; Harlan Teklad) for six weeks. In the second experimental setting, *cm-Lrp1*$^{+/+}$ and *cm-Lrp1*$^{-/-}$ ten-week-old mice were randomized to placebo (PBS) or to NPRA antagonist (A71915, 200 μg/Kg in PBS, volume 100 uL) treatment during the 6 weeks on HFD (*online* Fig. S1B). Age-matched littermates were used for all experiments and at least 6 mice per group were analyzed considering $\alpha = 0.05$, power = 80%, and an effect size of 2 mM glucose and 0.1 μg/L insulin.

Blood samples were taken in fasting conditions in the fourth week (150 μL) and after sacrificing (400 μL). The serum was frozen at −20 °C and used to measure glucose, insulin and lipid levels. The mice were euthanized at week six and samples from liver, skeletal muscle, heart, epididymal white adipose tissue (eWAT), and brown adipose tissue (BAT), were kept frozen at −80 °C for lipid and molecular analysis. A piece of these tissues was also embedded in OCT for immunohistochemistry. All experimental protocols were approved by the Institutional Animal Care and Use Committees at the Research Institute (IR)-Sant Pau, and complied with all guidelines concerning the use of animals in research and teaching as defined by the Guide for the Care and Use of Laboratory Animals (NIH Publication N°.80-23, revised 1996).

2.2. Biochemical analysis

Insulin serum levels were measured using a Mouse Insulin ELISA (Mercodia) following the manufacturer's instructions. The HOMA index, an estimation of insulin resistance, was calculated as: [fasting serum insulin (ng/mL) × fasting serum glucose (mM)]/22.5. Serum lipids and lipoproteins, including cholesterol, triglyceride (TG) (corrected from free glycerol), phospholipids, FFAs, high density lipoprotein (HDL) cholesterol and phospholipids, were enzymatically determined using commercial kits adapted to a COBAS 6000 autoanalyzer (Roche Diagnostics) [22].

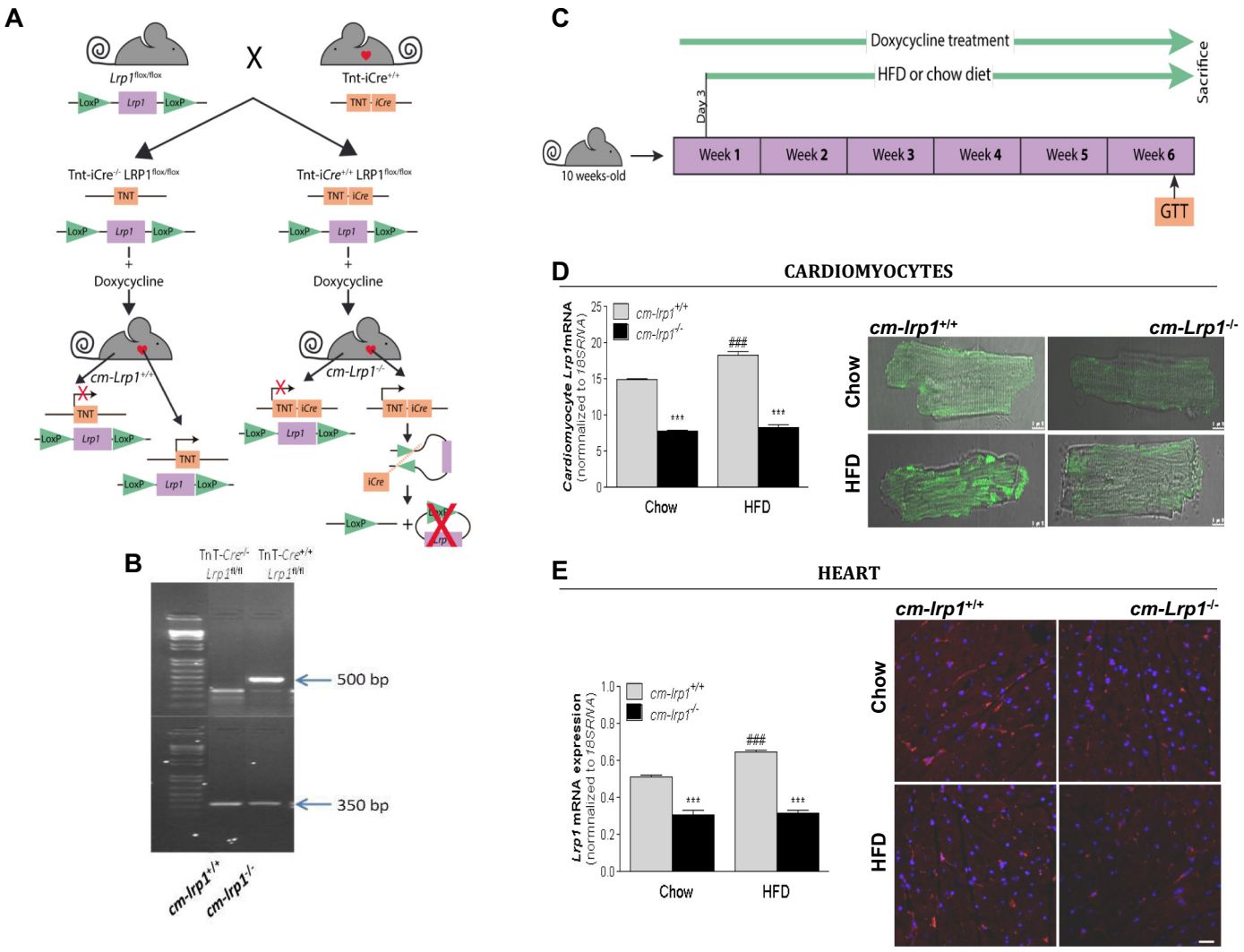

Fig. 1. *cm-Lrp1*$^{-/-}$ transgenic mice generation and validation. (A) Generation schedule of an *in vivo* model with a doxycycline-inducible attenuation of *Lrp1* expression selectively in cardiomyocytes. In *cm-Lrp1*$^{-/-}$ mice with the genotype TnTCre+/+ Lrp1$^{flox/flox}$, the activation of Cre recombinase by doxycycline converts the Lrp1 floxed alleles to KO (−) alleles. (B) Cre and Flox transgens were detected by PCR. A fragment of 500 bp was amplified from mouse tail genomic DNA when the Cre transgene driven by the TnT promoter was present. A fragment of 350 bp was amplified when flox sequences flank lrp1 gen. (C) Ten-week-old male mice were treated daily with doxycycline cyclate through their drinking water during the procedure to assess the conditional inhibition of LRP1 levels in cardiomyocytes. After three days of treatment, both *cm-Lrp1*$^{+/+}$ and *cm-Lrp1*$^{-/-}$ mice were randomized and fed a chow diet or high fat diet for six weeks. (D) *Lrp1* mRNA expression and LRP1 protein levels (in green) in isolated cardiomyocytes from hearts of *cm-Lrp1*$^{-/-}$ and control mice (E) *Lrp1* mRNA expression and LRP1 protein levels (LRP1 staining in red, nuclei in blue, Bar = 20 μm) in the heart. Data represent the mean ± SEM for 9 mice per group. *** $p < .005$ *versus* *cm-Lrp1*$^{+/+}$ mice; ### $p < .005$ *versus* chow diet. Differences between groups were analyzed using one-way analysis of variance (ANOVA) followed by a post-hoc Tukey-b test.

2.3. Analysis of ventricular function

Transthoracic echocardiography was conducted under light sedation (1% isoflurane in oxygen) three days after starting doxycycline treatment (baseline). A second echocardiography was conducted six weeks later, at the end of the experimental procedure [23]. Standard functional parameters were measured, including left ventricle (LV) internal diameter diastole (LVIDd) and LV internal diameter systole (LVIDs), LV end-diastolic volume (LVEDV), LV end-systolic volume (LVESV), LV ejection fraction (LVEF), LV fractional shortening (LVFS), LV anterior wall at end cardiac diastole (LVAWd), LV posterior wall at end cardiac diastole (LVPWd), and heart rate.

2.4. Glucose tolerance test (GTT)

The glucose tolerance test (GTT) was performed at week six of the dietetic intervention in fasting conditions. Basal blood glucose levels were measured from a tail nick through ACCU-CHEK® Aviva glucometer (Roche Molecular Systems). The mice were then intraperitoneally injected with glucose (1.3 mg/g BW). Blood glucose was measured at 15, 30, 60, 120 and 180 min after glucose injection. The area under the curve (AUC) of the response curve was then calculated using the software Prism 4.0 [24].

2.5. Distribution of intragastrically-administered [^{3}H]-TG

Mice were given an oral fat gavage (OFG) consisting of 20 μCi [^{3}H]-labeled triolein (glycerol tri[9, 10(n)-3H]oleate, 21.0 Ci/mmol; Amersham Biosciences, Buckinghamshire, UK) in 150 μL of olive oil [24]. Mice were bled by cardiac puncture at 1.5 h. Serum and target tissues (liver, eWAT, heart, leg muscle and BAT) were collected after perfusion with NaCl solution 0.9%. Radiolabeled serum and tissue TG were separated from the FA using methanol:chloroform:heptane 1.4:1.25:1 (v:v:v) and 0.1 mol/L H_3BO_3-KCO_3 at pH 10.5. The

radioactivity in the TG and FA fraction, in total serum and target tissues was determined by scintillation counting.

2.6. Cardiomyocyte isolation

Cardiomyocytes were obtained from the heart of our *in vivo* animal model by the Langendorff method. First, the heart was surgically removed and washed with a Ca^{2+} free Tyrode solution at 4 °C and oxygenated. The aorta was suspended in the Langendorff apparatus and the heart was perfused *via* the aorta with Ca^{2+} free Tyrode solution at 37 °C to clean blood remnants. The Ca^{2+} free Tyrode solution was then carefully removed, and the enzyme solution composed of Ca^{2+} free Tyrode solution with bovine serum albumin, collagenases and proteinases was added. Two reperfusion cycles (3 mL/min during 6 min) were performed to add the stop solution (Ca^{2+} free Tyrode solution without collagenases and proteinases). Once the perfusion was finished, the heart was removed from the Langendorff system and treated with an enzymatic solution for 5 min at 37 °C under shaking. The pieces of tissue were extracted with tweezers and, with shaking, submerged into stop solution to continue disaggregation. Tissue pieces were then removed and the solution containing the cardiomyocytes was centrifuged for 5 min at 450 rpm. The cell pellet was resuspended in stop solution or Tripure™ Isolation Reagent®, depending on the further methodology used.

2.7. Tissue homogenization

Frozen tissues (25 mg) (heart, liver, skeletal muscle, eWAT and BAT) were pulverized in liquid nitrogen using a mortar and a pestle. Samples were then homogenized in TriPure™ isolation reagent (Roche Molecular Systems) for total RNA and protein extraction according to the manufacturer's instructions. Total RNA from skeletal muscle was extracted using the RNeasy mini kit (Qiagen) according to the manufacturer's instructions after the previous addition of Proteinase K. For RNA extraction from eWAT, the tissue was processed with the kit RNeasy Mini Kit (Qiagen). DNA was digested with DNase I (Invitrogen). Extracted RNA was eluted in 25 μL of nuclease-free water. The yield and quality of RNA was tested by agarose electrophoresis and spectrophotometry. Isolated RNA was stored at −80 °C until use.

2.8. LRP1-deficient cardiomyocyte cell culture

Murine LRP1-deficient HL-1 cells were generated and kept in culture as previously described [9,10,25,26].

2.9. Hepatocyte (Hepa 1–6) cell culture

Hepa 1–6 cells were cultured in DMEM supplemented with 10% FCS, 2 mmol/L L-glutamine, 100 U/mL penicillin G, and 100 μg/mL streptomycin. Quiescent cells were used for two different experimental approaches. First, quiescent Hepa 1–6 were exposed to supernatants from LRP1- and LRP1- HL-1 cells. Second, quiescent Hepa 1–6 were exposed to increasing dose of ANP (0 to 10 nM).

2.10. Gene expression analyses by RT-PCR

Total RNA (1 μg) was used for cDNA synthesis according to the protocol provided with the High Capacity cDNA Reverse Transcription kit (Applied Biosystems). cDNA was stored at −20C until its use. Gene expression analyses of *Lrp1* (Mm00464608_m1), *Vldlr* (Rn01498166_m1), *Ldlr* (Mm01151339_m1), *Cd36* (Mm01135198-m1), *Nppa* (Mm01255747_g1), *Nppb* (Mm01255770_g1), *Cpt1* (Mm00550438), *Fasn* (Mm00662319_m1), *Acaca* (Mm01304257_m1), *Acsl3* (Mm01255804_m1), *Cav1* (Mm00483057_m1), *Slc27a2* (Mm00449517_m1) and *Slc27a4* (Mm01327405_m1) were performed by quantitative real-time reverse transcriptase-polymerase chain reaction (q-RT-PCR) in the Applied Biosystems 7300 Real Time PCR System (Applied Biosystems; Foster City, CA, USA). *18srRNA* (4319413E) was used as a housekeeping gene. The mRNA expression levels were measured in triplicate. The threshold cycle (Ct) values were normalized to the housekeeping gene.

2.11. Proteomic studies

Proteomic studies were performed as previously described with small modifications [27,28]. The mass spectrometry proteomics data have been deposited to the ProteomeXchange Consortium *via* the PRIDE partner repository with the dataset identifier PXD011564. The protein was digested with Sequencing Grade Modified Trypsin (Promega, Madison, WI, USA) using the FASP (Filter Aided Sample Preparation) digestion protocol as described [27]. A detailed description of the experimental procedures has been included in supplemental material.

2.12. Immunoprecipitation Assays

Dynabeads protein G was bound to the polyclonal anti-corin antibody (abcam ab125254) for 1 h at room temperature. The protein extract was incubated with the Dynabeads Protein G-anti-corin complex overnight at 4 °C. After incubation, the protein immune-complex beads were washed 3 times with the wash buffer and eluted with 50 mM glycine. Samples were separated by SDS-PAGE and transferred blots were incubated with Ab against Serpin 1 (biorbyt orb319062).

2.13. Corin catalytic activity assay

Protease corin activity was measured as previously described [29]. Corin activity was presented as V_{max}.

2.14. Immunoassays

ANP (ab108797, Abcam), GDF-15 (MGD150, R&D Systems) and adrenalin/epinephrine (abx257158, Abbexa) plasma levels were measured by commercially available-enzyme-linked immunosorbent assays (ELISA), according to the manufacturer's recommendations.

2.15. Western blotting analysis

Blots were incubated with antibodies against mouse LRP1 (β-chain, clone 5A6 RDI-PRO61066), AMPK (Cell Signaling Technology, Inc., # 2532), pAMPK (Cell Signaling Technology, Inc., Thr172, 40H9, # 2535), pVASP (Santa Cruz Biotechnology, Inc., sc-101,439), BNP (Santa Cruz Biotechnology, Inc., sc-67,455), ANP (Everest Biotech, EB11166), Serpin A1 (Biorbyt, orb319062), pACC (Cell Signaling Technology, 1673661S, total ACC (Cell Signaling Technology, 1673662S), pAkt (Cell Signaling Technology, #4060), total Akt (Cell Signaling Technology, #4685), UCP3 (Abcam, ab10985) and OXPHOS mitochondrial complexes (Abcam, ab110413). CPT1 from mitochondrial-enriched fractions in liver was determined [30] using the antibodies described by Herrero *et al* [31] and registered in antibodyregistry.org (Dolors Serra/Universitat de Barcelona Cat# CPT1A, RRID:AB_2636894). Protein extracts (10 μg) were loaded, resolved on 12% SDS-PAGE and transferred to nitrocellulose membranes (BioRad). Signal detection was carried out with the ECL immunoblotting detection system (GE Healthcare) and the results were quantitatively analyzed using Chemidoc (BioRad). Equal protein loading in each lane was verified by incubating blots with monoclonal antibodies against troponin T (TnT) (Thermo Scientific #MS-295-P) or β-tubulin (Cell Signaling Technology, Inc., #2146).

2.16. Measurement of cyclic GMP levels in tissues

The cyclic guanosine monophosphate (cGMP) levels in heart, liver and skeletal muscle were measured using an ELISA kit according to the manufacturer's instructions for non-acetylated methodology (ADI-900-014, Enzo Life Sciences).

2.17. Confocal microscopy

Mouse heart cryosections were subjected to target retrieval (10 mM Tris-HCl, pH = 6) and permeabilized with Triton X-100 (0.5%). Isolated cardiomyocytes were fixed with paraformaldehyde and preserved in PBS with sodium acid 0.2%. Cells were permeabilized with glycine (0.1 M) and Triton X-100 (0.2%). Samples were blocked with PBS, Tween-20 (0.2%) and BSA (1%) and incubated with primary antibody LRP1 (2 μg/mL Abcam). Secondary antibodies conjugated with Alexa488 and Cy3 (1 μg/mL) (Jackson ImmunoResearch) were used for detection. Cell nuclei were counterstained with 4′,6-diamidino-2-phenylindole (DAPI). Results were analyzed with an Axio-Observer Z1 (Zeiss) laser confocal microscope.

2.18. Histological staining

Tissue samples were frozen and sectioned (5 μm). Sections were stained with Hematoxilin/Eosin, Herxheimer, Oil red O and Sirius red stains. Herxheimer and oil red O stainings were used for the detection of lipids. A polarized light microscope was used to measure collagen types I and III on randomly selected Sirius red-stained sections.

2.19. Lipid extraction and semi-quantitative analysis of cholesteryl ester, free cholesterol, TG and FFA content in target tissues

Frozen pulverized tissue (10 mg) were homogenized in NaOH 0.1 M. Lipids were extracted and cholesteryl esters (CE), free cholesterol (FC) and TG content was analyzed by thin layer chromatography [9,10]. The FFA level was determined enzymatically using commercial kits adapted to a COBAS 6000 autoanalyzer.

2.20. Determination of fatty acid β-oxidation (FAO) activity in target tissues

Aliquots from heart and liver were homogenized in a buffer composed of 150 mM NaCl, 1 mM dithiothreitol, 30 mM EDTA and 50 mM KH_2PO_4. Tissue fatty acid oxidation (FAO) was determined with 30 μg of post nuclear supernatant by determining the conversion of palmitoyl CoA-1-[^{14}C] into acetyl-CoA [32].

2.21. Indirect calorymetry system

Measurements of oxygen consumption (VO_2) and CO_2 production (VCO_2) were performed using a comprehensive lab animal monitoring system (Oxymax-CLAMS, Columbus Instruments). Mice were acclimated in metabolic chambers for 1 day before the start of the recordings. Animals were continuously recorded for 2 days with measurements of their locomotor activity (in the xy and z axes) and gas exchange (O_2 and CO_2) taken every 20 min. Energy expenditure was calculated according to manufacturer's guidelines (Columbus Instruments). The respiratory quotient was estimated by calculating the ratio of CO_2 production to O_2 consumption.

2.22. Statistical analysis

Results are expressed as mean ± SEM. Differences between study groups were analyzed using one-way analysis of variance (ANOVA) followed by a *post-hoc Tukey-b* test, Student's *t*-test for independent samples and Student's *t*-test for paired samples. The statistical software R (www.r-project.org) was used for all statistical analyses. Differences were considered statistically significant when $P < .050$.

3. Results

3.1. Cardiomyocyte Lrp1 deficiency prevents diet-induced overweight and glucose intolerance by facilitating increased energy expenditure

Cardiomyocyte *Lrp1* deficient (*cm-Lrp1*$^{-/-}$) mice were generated as explained in Section 2.1 using the *TnT-iCre* transgenic mice provided by Zhou and Bu [20]. These authors showed that the transgenic method they used to generate *TNT-iCre* transgenic mice guarantees the deletion of genes exclusively in cardiomyocytes through all the states of heart development. Here, we investigated the effects of *Lrp1* specific deletion in cardiomyocytes by crossing *TnT-iCre* transgenic mice with *Lrp1*$^{flox/flox}$ that generated *cm-lrp1*$^{-/-}$ mice. A schematic representation of *cm-Lrp1*$^{-/-}$ generation and genotyping is shown in Fig. 1A,B. *cm-Lrp1*$^{-/-}$ mice fed either chow or HFD diet showed decreased *Lrp1* levels in isolated cardiomyocytes and in the heart (Fig. 1C-E). However, not differences were found in other lipoprotein receptors including *vldlr* or *ldlr* in the heart of *cm-Lrp1*$^{-/-}$ and control mice (*online* Fig. S2A). *Lrp1* levels in liver, skeletal muscle and eWAT did not show differences between *cm-Lrp1*$^{-/-}$ and control mice (*online* Fig. S2B-D).

First, we evaluated the effects of cardiomyocyte-specific Cre deletor on Lrp1 expression in chow-fed animals treated with doxycycline. These mice usually exhibit moderate increases in weight and IR when fed a chow diet, but sharp increases when fed a Western-type diet [22]. Surprisingly, the body weight of *cm-Lrp1*$^{-/-}$ mice was lower than that of the controls when the animals were fed a chow diet for a period of 6 weeks and this was concomitant with lower insulin levels and improved glucose tolerance as well as lower hepatic fat accumulation and eWAT weight (*online* Fig. S3A–F). Thus, we used western diet-fed *cm-Lrp1*$^{-/-}$ mice to evaluate a putative role of cardiomyocyte *Lrp1* deficiency on metabolic phenotype and the potential mechanisms involved. *Lrp1* deficiency did not cause significant alterations in functional or structural properties of the heart (*online* Fig. S4 and S5) or in serum lipid profile (*online* Table S2).

The body weight of *cm-Lrp1*$^{-/-}$ mice was lower than that of the controls at all tested times (Fig. 2A) while the average weekly food intake was similar between both groups (*online* Fig. S6). This suggests that the reduction in body weight gain was not due to differences of weekly food consumption. The weight-reducing effect of *Lrp1* deficiency was associated to decreased eWAT weight and eWAT/BAT adipocyte size (Fig. 2A-C). While TG/FA content was reduced in the liver of *cm-Lrp1*$^{-/-}$ mice (Fig. 2D), no differences were found in the heart and skeletal muscle of both groups (*online* Fig. S7). To know whether these phenotypic changes elicit a favorable metabolic profile, we conducted a TTG test. Compared with controls, *cm-Lrp1*$^{-/-}$ mice had lower glucose intolerance and lower AUC values (Fig. 2E). Glucose, insulin and IR index (HOMA-IR) were reduced in *cm-Lrp1*$^{-/-}$ compared to control mice (Table 1).

To determine whether cardiomyocyte *Lrp1* deficiency reduces body weight and adiposity by regulating energy expenditure, we performed Comprehensive Lab Animal Monitoring System (CLAMS) experiments. These experiments showed that the ambulation activity was higher during the dark period than during the light period. There were, however, no differences between *cm-Lrp1*$^{-/-}$ and control mice (*online* Fig. S8), indicating that the protection against weight gain of *cm-Lrp1*$^{-/-}$ mice was not caused by increased physical activity. *cm-Lrp1*$^{-/-}$ mice showed higher lipid oxidation during the light phase (Fig. 3A) and higher glucose oxidation during the dark phase (Fig. 3B). *cm-Lrp1*$^{-/-}$ mice showed higher VO_2 and energy expenditure than controls during both phases (Fig. 3C & D).

3.2. Hearts with Lrp1 deficiency show enhanced corin activity that favors higher ANP release to the plasma

To identify cardiac proteins potentially involved in the favorable metabolic phenotype of *cm-Lrp1*$^{-/-}$ mice, we performed proteomic analysis of hearts from both *cm-Lrp1*$^{-/-}$ and *cm-Lrp1*$^{+/+}$ mice groups.

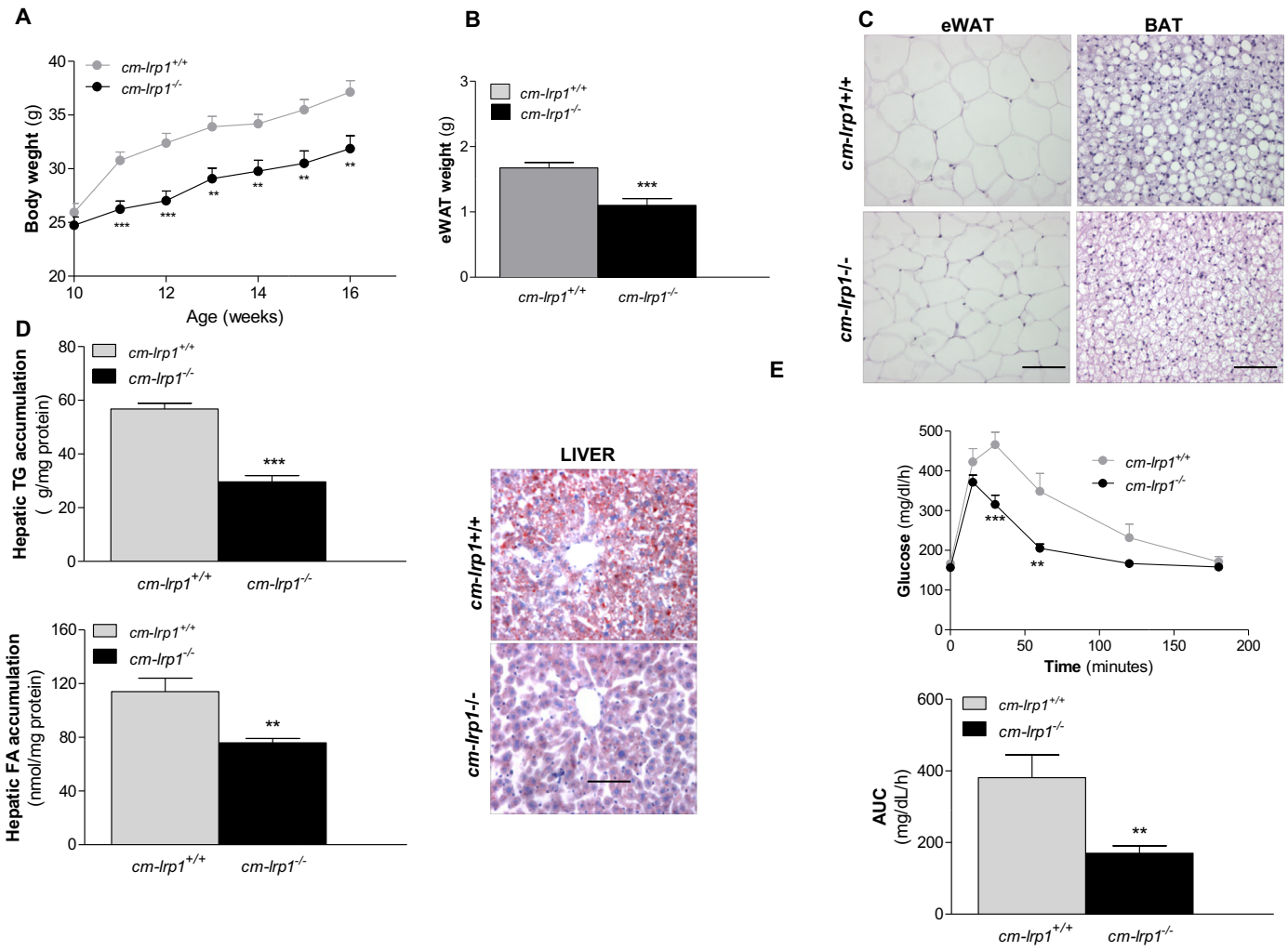

Fig. 2. *Lrp1* deficiency in cardiomyocytes improves diet-induced glucose intolerance and reduces weight gain. *cm-Lrp1*$^{+/+}$ and *cm-Lrp1*$^{-/-}$ mice (control) mice were treated for 6 weeks with doxycycline cyclate in their drinking water. (A) Body weight changes over 6 weeks of HFD diet. (B) Epididymal white adipose tissue (eWAT) tissue mass at necropsy. (C) Representative H&E stained sections from eWAT and brown adipose tissue (BAT) (Bar = 100 μm). (D) Triglyceride and FA content in the liver and representative Herxheimer stained liver sections (Bar =100 μm). (E) Glucose tolerance test in mice (1.3 mg/g body weight) and Area under the curve (AUC). The data represents the mean ± SEM. $n = 9$ mice per condition. $^{**}p < .01$ or *** $p < .005$ *versus* control mice. Differences between groups were analyzed using Student's *t*-test for independent samples.

We processed three biological replicates from each group. Each replicate was a pool from three animals. We identified 24,358 spectra corresponding to 6334 non-redundant peptides through a database search (1% FDR) (Data is available *via* the ProteomeXchange with the identifier PXD011564). For quantitative analysis, only peptides identified as unique (*i.e.* peptides sequences belonging to one single protein in the database) were considered. Overall, a total of 1213 proteins were quantified from 5735 non-redundant unique peptides. Quantified proteins were compared between groups and we found a total of 34 differential expressed proteins. These 34 proteins included 11 which have the potential to be secreted (Table 2). Among the differential secreted proteins, we found atrial natriuretic peptide (ANP) (ratio = 0.58; p = 2.1E-04) and serine protease inhibitors including serpin1a (ratio = 0.71; p = 2.0E-12), serpin 1b (ratio = 0.54; p = 6.0E-05), serpin 1d (ratio = 0.33; p = 1.7-E-03) and serpin 3 K (ratio = 0.71; p = 4.0E-09). To validate the Proteomics results, Western blot and immunoprecipitation experiments were performed.

Table 1
Comparison of serum glucose levels, serum insulin levels and Homeostatic Model Assessment for Insulin Resistance (HOMA-IR) between *cm-Lrp1*$^{-/-}$ and control mice. The data is shown as mean ± SEM. $N = 8$ per group. Differences between groups were analyzed using the Student's *t*-test for independent samples.

	cm-Lrp1$^{+/+}$	cm-Lrp1$^{-/-}$	P
GLUCOSE (mM)	11.09 ± 0.37	9.49 ± 0.84	0.072
INSULIN (μg/L)	1.23 ± 0.17	0.48 ± 0.04	0.003
HOMA-IR	13.06 ± 1.55	4.59 ± 0.74	0.003

As shown in Fig. 4A, ANP is generated from the precursor form proANP through the activation of corin, a convertase that facilitates the release of ANP (28 aa) from the C-terminal end of proANP [33]. Western blot analysis performed with Abs that bind to the sequence RIGAQSGLGCNSFR at the C-terminal end of precursor form showed that proANP (14 kDa) levels were strongly decreased in *cm-Lrp1*$^{-/-}$ compared to control mice. This same test also showed preproANP (17 kDa) to be similar among the groups (Fig. 4B). These results confirm proteomic differences (decreased levels of proANP in hearts from *cm-Lrp1*$^{-/-}$ mice) and suggest that there is higher release of ANP from LRP1- hearts.

Immunoprecipitation studies evidenced that serpins form complexes with corin. The number of SerpinA1/Corin complexes were higher in the heart of *cm-Lrp1*$^{-/-}$ mice compared to that of controls (Fig. 4C). The molecular weight of these complexes in the heart of our murine model was 45–50 KDa and 30–35 KDa, which lines up with what was previously described of cultured cardiomyocytes [34].

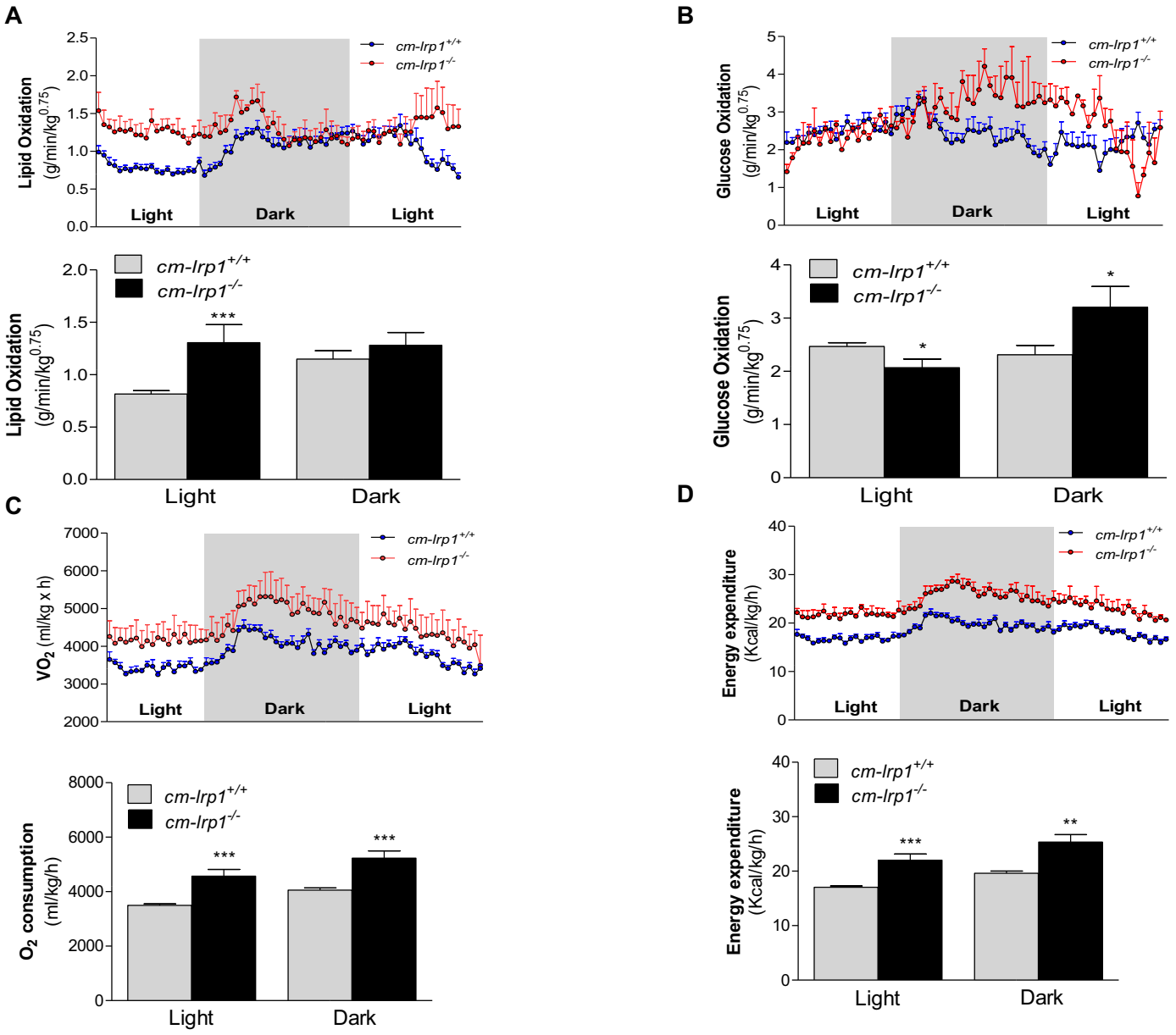

Fig. 3. Cardiomyocyte *Lrp1* deficiency increases whole-body energy consumption. *cm-Lrp1*$^{+/+}$ and *cm-Lrp1*$^{-/-}$ mice (control) mice were treated for 6 weeks with doxycycline cyclate in their drinking water and then submitted to CLAMS experiments. Oxymax respirometer measurements of lipid oxidation (A), glucose oxidation (B), VO_2 (C) and whole-body oxygen consumption (D) during the light and dark periods in mice over 6 weeks on HFD. $n = 8$ mice per condition. $^{*}p < .05$, $^{**}p < .01$ or $^{***}p < .005$ *versus cm-Lrp1*$^{+/+}$ mice. Differences between groups were analyzed using Student's *t*-test for independent samples.

Gladysheva IP *et al* reported that serpin1 binding to corin creates steric impediments to the union of effective inhibitors and allows prolonged corin activation [34].

Fluorogenic assays performed in this study revealed that protease enzymatic activities were higher in the cardiac membranes of *Lrp1*$^{-/-}$ mice with or without hirudin (Fig. 4D). Hirudin, a highly specific thrombin inhibitor, was added to the assay to exclude clotting enzymes in the membrane fraction. It did not show a significant effect on protease activity, suggesting that corin could be one of the main proteases contributing to the higher protease activity in cardiac membranes of *Lrp1*$^{-/-}$ mice.

Circulating ANP levels were higher (about 4-fold) in the plasma of *cm-Lrp1*$^{-/-}$ than in that of *cm-lrp1*$^{+/+}$ mice (Fig. 4E). Our results suggest that cardiac *Lrp1* deficiency facilitates corin activation and ANP release. There were no differences in cardiac *Nppa* between groups, whereas a modest downregulation in *Nppb* mRNA expression was found in *cm-lrp1*$^{-/-}$ mice (*online* Fig. S9). No differences were found in the circulating levels of other metabolic factors including adrenalin/epinephrine and GFD15 (Fig. 4F,G).

3.3. The ANP-NPR-A signaling activation is linked to AMPK phosphorylation and increased FA oxidation in the liver of cm-Lrp1$^{-/-}$ mice

To ascertain whether increased circulating ANP levels were associated with the activation of NPR-A signaling in peripheral tissues, we determined the levels of crucial mediators such as cGMP and pVASP in the liver, skeletal muscle and heart of *cm-Lrp1*$^{+/+}$ and *cm-Lrp1*$^{-/-}$ mice whether treated with the NPR-A antagonist A71915 or not (*online* Fig. S1B). cGMP and VASP were increased in the liver (Fig. 5A,B) and skeletal muscle (*online* Fig. S10A,B) but not the heart (*online* Fig. S11A,B) of untreated *cm-Lrp1*$^{-/-}$ mice. The treatment of *cm-Lrp1*$^{-/-}$ mice with A71915 completely blocked the increase of cGMP and pVASP levels in liver and partially blocked it in skeletal muscle. We found that cGMP/pVASP signaling was linked to increased AMPK phosphorylation in the

Table 2
Differential cardiac secreted proteins between *cm-Lrp1*$^{-/-}$ and *cm-lrp1*$^{+/+}$ mice. This table shows mass spectromic proteomic data concerning differential cardiac secreted proteins. Three biological replicates for each condition were processed. Each replicate was a pool of tissue obtained from three different animals. Differences between groups were analyzed using Student's *t*-test for independent samples.

Protein ID	Protein name	Gene name	*cm-Lrp1*$^{-/-}$ *vs* *cm-Lrp1*$^{+/+}$	
			Ratio	*P*
E9PV24	Fibrinogen alpha chain	Fga	0.64	1.8E-12
P05125	Natriuretic peptides A (ANP)	Nppa Pnd	0.57	4.8E-04
P07759	Serine protease inhibitor A3K	Serpina3k Mcm2 Spi2	0.63	1.6E-12
P22599	Alpha-1-antitrypsin 1–2	Serpina1b Aat2 Dom2 Spi1–2	0.44	1.2E-05
Q00897	Alpha-1-antitrypsin 1–4	Serpina1d Dom4 Spi1–4	0.30	9.4E-04
Q3TFQ8	Alpha-1,4 glucan phosphorylase	Pygb	0.72	8.1E-16
Q6S9I0	Kininogen	Kng2	0.77	1.1E-03
P01942	Hemoglobin subunit alpha	Hba	0.74	9.6E-05
Q8K0E8	Fibrinogen beta chain	Fgb	0.66	6.6E-14
Q8VCM7	Fibrinogen gamma chain	Fgg	0.65	5.5E-08
Q91X72	Hemopexin	Hpx Hpxn	0.70	5.0E-09

liver. Increased levels of hepatic pAMPK, like those of cGMP and pVASP, were abolished by the NPR-A antagonist (Fig. 5A,B). There were no differences in pAMPK levels in the skeletal muscle (*online* Fig. S10B) or the heart (*online* Fig. S11B) between groups. To know whether AMPK phosphorylation was linked to AMPK activity, we measured the phosphorylation of ACC, the downstream target of pAMPK. ACC mRNA expression levels in the liver of mice fed HFD were extremely low (reduced by aprox. 90% in HFD fed mice). Despite this, we detected an increased ratio pACC/total ACC in the liver of untreated *cm-Lrp1*$^{-/-}$ compared to the control mice (Fig. 5A). In addition, the increase in the phosphorylation of ACC was not observed in A91915-treated mice, supporting the activation of AMPK by ANP in the liver of KO mice. To explore the

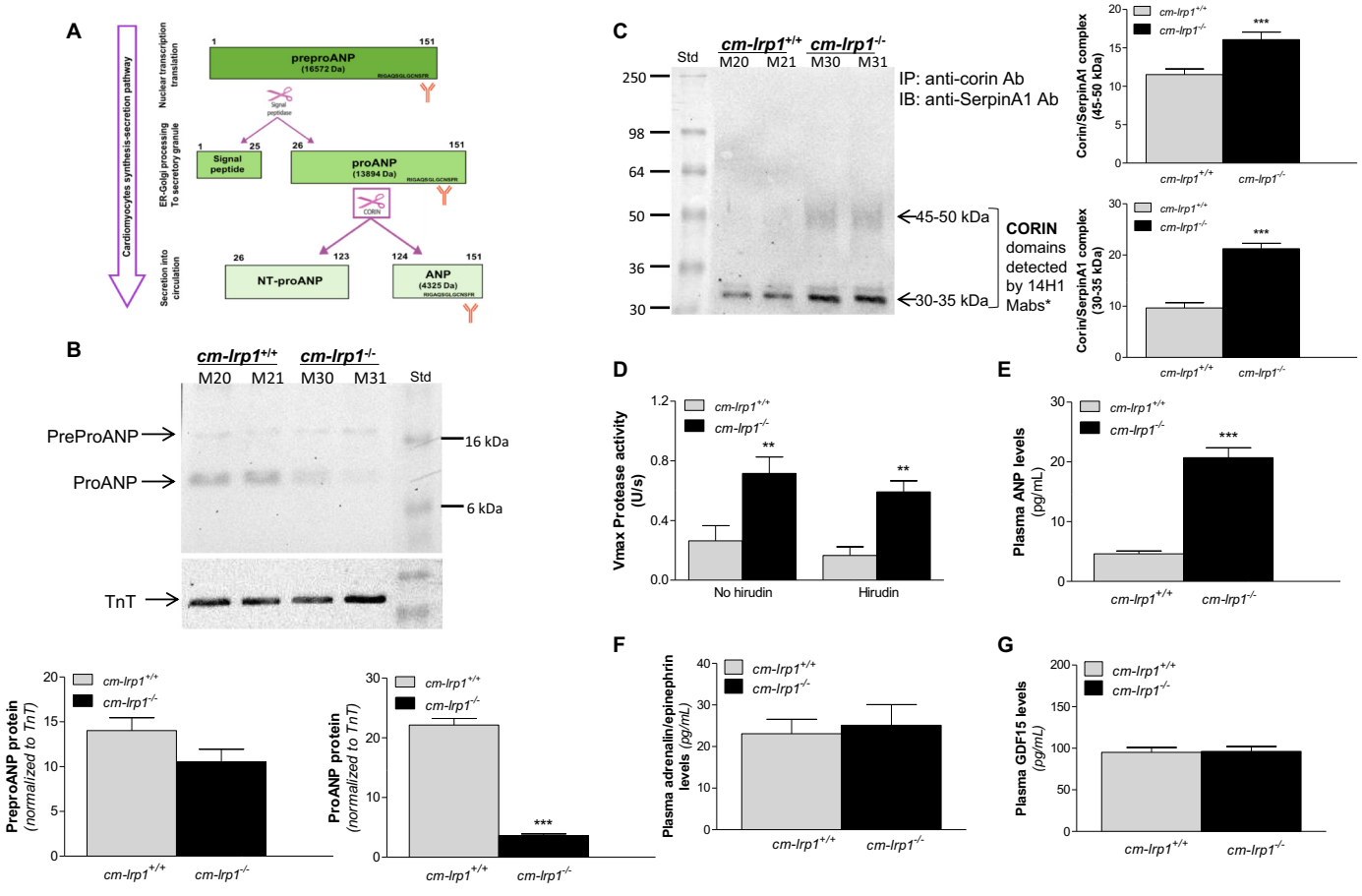

Fig. 4. Cardiomyocyte *Lrp1* deficiency favors higher corin activity and ANP release. (A) Schematic representation for the secretion of preproANP-derived peptides modified from Pemberton et al. [33]. The AA sequence RIGAQSGLGCNSFR that is recognized by the antibody (Ab) is localized at the extreme C-terminal of the protein. *cm-Lrp1*$^{+/+}$ and *cm-Lrp1*$^{-/-}$ mice (control) mice were treated for 6 weeks with doxycycline cyclate in their drinking water. After sacrifice, one aliquote of frozen heart tissue was used for protein extraction. (B) Representative Western blot analysis showing cardiac preproANP (16 kDa), proANP (13 kDa) and troponin (TnT) (endogenous control) protein bands and bar graphs showing the quantification of preproANP and proANP protein bands normalized to TnT. One aliquot of cardiac membranes (5 mg) was used for immunoprecipitation with anti-corin Abs. (C) Immunoblots performed with anti-SerpinA1 Abs showing two different molecular weight corin/serpinA1 complexes and bar graphs showing the quantification of 45–50 kDa complex and 30–35 kDa complex. (D) Other aliquot of cardiac membranes (25 μg) was used for membrane protease catalytic activity measurements (Vmax) in absence or presence of the thrombin inhibitor hirudin (2 μM). (*E*-G) Circulating levels of ANP, adrenalin/epinephrine and GDF15 measured by ELISA. $n = 6$ mice per condition. Data represent the mean ± SEM. $^{**}p < .01$ or $^{***}p < .005$ *versus* *cm-Lrp1*$^{+/+}$ mice. Differences between groups were analyzed using Student's *t*-test for independent samples.

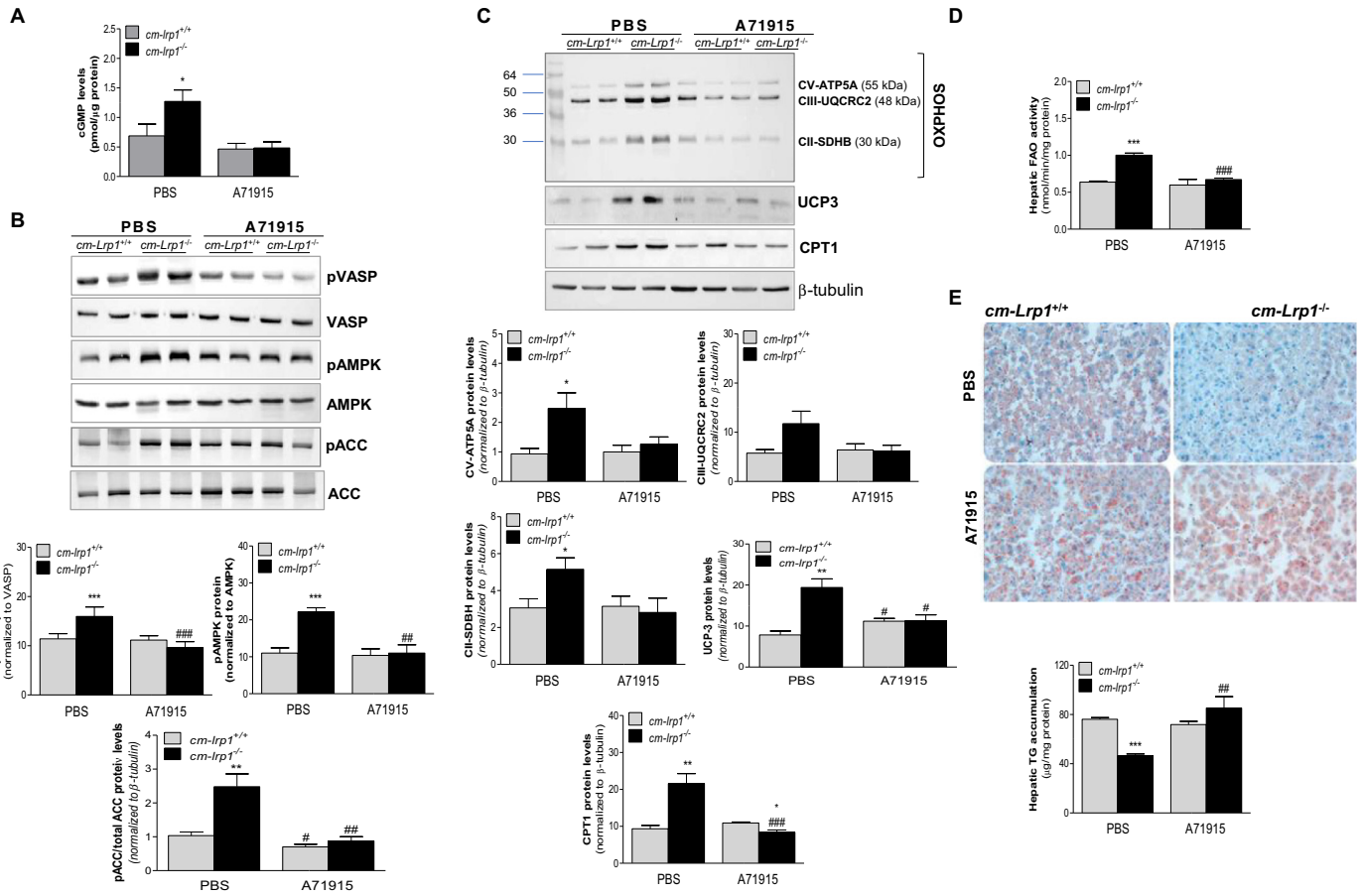

Fig. 5. High plasma ANP levels in *cm-Lrp1*$^{-/-}$ mice induce NPR-A-dependent signaling linked to AMPK phosphorylation and increased fatty acid oxidation in the liver. *cm-Lrp1*$^{+/+}$ and *cm-Lrp1*$^{-/-}$ mice (control) mice were treated for 6 weeks with doxycycline cyclate in their drinking water and then treated with either saline or the NPR-A antagonist A71915 (200 µg/kg in PBS in a final volume of 100 µL) for the last 4 weeks. (A) cGMP levels were detected by ELISA. Western blot analysis and bar graphs showing the quantification of pVASP, total VASP, pAMPK, total AMPK, pACC and total ACC (B) and OXPHOS, UCP3 and CPT1 (C) in the liver. (D) Rate of hepatic fatty acid oxidation (FAO). (E) Representative Herxheimer stained liver sections (Bar = 100 µm) and hepatic TG levels. n = 8–10 mice per condition. Data represent the mean ± SEM. *$p < .05$, ** $p < .01$ or *** $p < .005$ *versus cm-Lrp1*$^{+/+}$ mice; ## $p < .01$ or ### $p < .005$ *versus* PBS. Differences between groups were analyzed using one-way analysis of variance (ANOVA) followed by a post-hoc Tukey-b test.

potential impact of pAMPK activation on hepatic FA synthesis, we explored several genes involved in FA synthesis in the liver. We found that *Acsl3* mRNA expression was significantly lower in the liver of KO mice compared to the controls (*online* Fig. S12). There were no differences in the mRNA expression levels of *Fasn* or *Slc27a2* between groups.

To know the impact of pAMPK on FAO, we measured CPT1, a key mitochondrial enzyme responsible for FAO; the main components of the oxidative phosphorylation system (OXPHOS), responsible for mitochondrial respiration; and UCP3, an indicator of mitochondrial response to enhanced intracellular FA. Oxidative phosphorylation involves a flow of electrons through the electron transport chain (ETC), a series of proteins and electron carriers within the mitochondrial membrane. We used one OXPHOS cocktail antibody that contains 5 mouse Abs and detects one subunit of each (five) mitochondrial complexes of the *ETC*. The main subunits detected in whole hepatic and skeletal muscle tissue extracts of our murine model were CV-ATP5A (55 kDa), CIII-UQCRC2 (48 kDa) and CII-SDHB (30 kDa). The protein levels of CPT1, CII, and CV subunits of ETC were significantly higher in the liver (Fig. 5C) of untreated KO mice. The increase in these mitochondrial proteins was abolished in *cm-Lrp1*$^{-/-}$ mice treated with A71915, indicating that NPR-A-signaling is involved in the increase of OXPHOS protein subunits in mice. UCP-3, an indicator of FA supply to mitochondria, was also induced in the liver (Fig. 5C) but not in the skeletal muscle (*online* Fig. S10C) of KO mice. These results suggest that, despite the upregulatory effect of ANP signaling on OXPHOS subunits of the skeletal muscle, ANP signaling is not linked to FA oxidation in the skeletal muscle.

According to CPT1 upregulation, the hepatic FAO activity was higher in untreated KO mice than in control mice, but this increase was not observed in KO mice treated with A71915 (Fig. 5D). In addition, KO mice showed reduced hepatic TG accumulation in the untreated mice but not in the A71915–treated mice (Fig. 5E).

To explore whether these favorable changes may influence insulin signaling activation, we measured the activation state of Akt in different tissues. We found an increased ratio of pAkt/total Akt exclusively in the liver of KO mice (*online* Fig. S13).

3.4. Supernatants from LRP1 deficient HL-1 cells increased pAMPK and CPT1 levels in cultured hepatocytes

LRP1-deficient HL-1 cells (LRP1-) were generated in our group and previously used to test the impact of the cardiomyocyte LRP1 deficiency in several processes [9,10,25,26]. LRP1- cells show almost undetectable levels of LRP1 but similar morphologic characteristics to the control cells (Fig. 6A,B). Supernatants from LRP1- cells contain higher ANP levels than those from control cells (Fig. 6C), and, when added to hepatocytes, caused induced AMPK phosphorylation and increased CPT1 protein levels in cultured Hepa 1–6 cells (Fig. 6D,E). In parallel experiments, we also showed that ANP from 0 to 10 nM caused an increase in

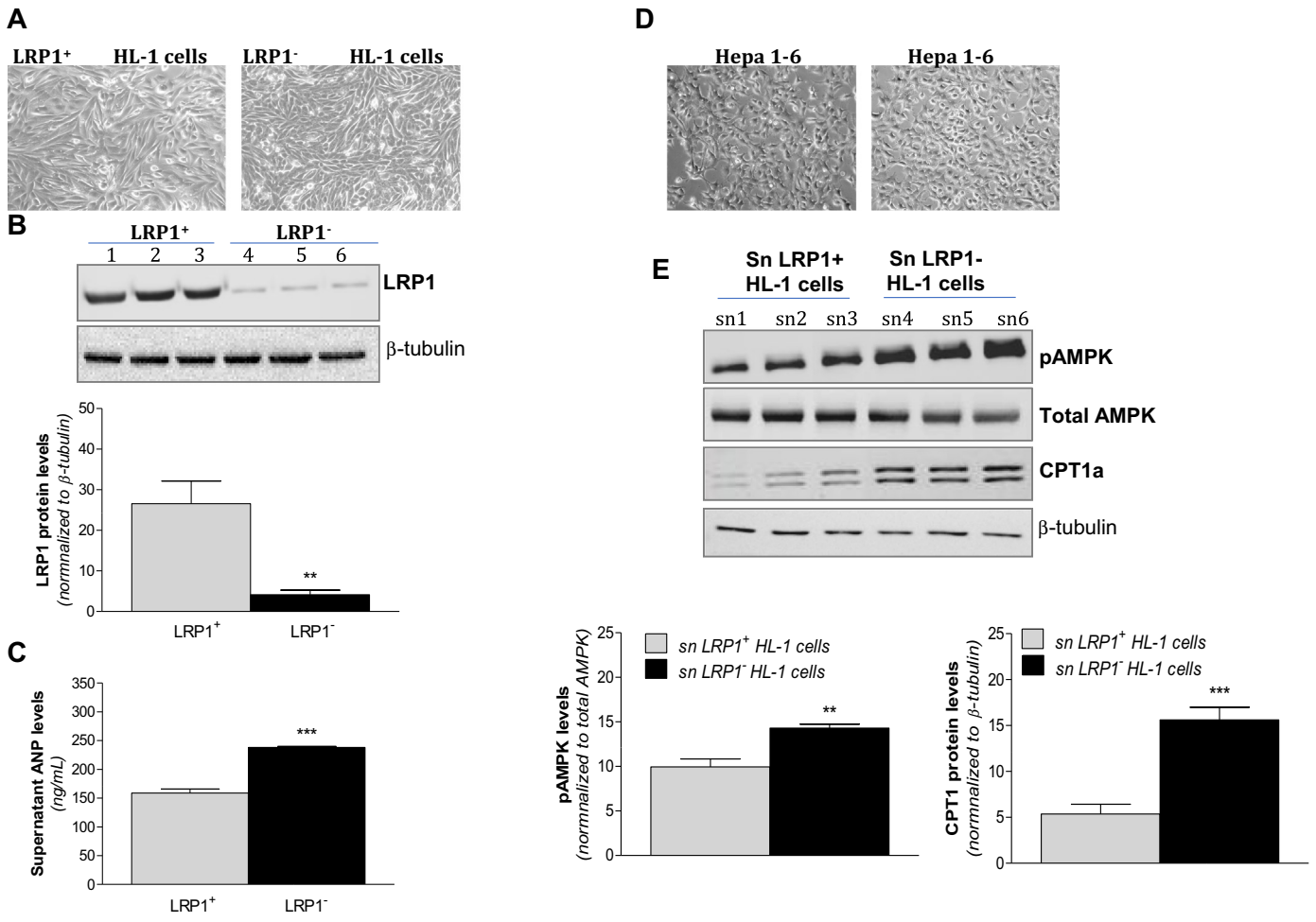

Fig. 6. Hepatocytes exposed to supernatants from LRP1-deficient (LRP1-) HL-1 cardiomyocytes exhibited increased levels of phosphorylated AMPK and CPT1. LRP1 deficient HL-1 (LRP1-) and control HL-1 cells (LRP1+) were grown in complete Claycomb medium from 48 h and supernatants were then collected. After determination of their ANP content by ELISA, supernatants were directly added to cultured hepatocytes (Hepa 1–6). Hepa 1–6 were exposed to HL-1 supernatants for 18 h and then collected in lysis buffer to perform Western blot analysis. (A) Representative optical microscopy image of LRP1+ and LRP1- HL-1 cells. (B) Western blot analysis and bar graphs showing LRP1 protein levels in LRP1- compared to LRP1+ HL-1 cells. (C) ANP levels in LRP1+ and LRP1- supernatants measured by ELISA. (D) Representative optical microscopy image of Hepa 1–6 cells exposed to supernatants from LRP1+ and LRP1- HL-1 cells. (E) Western blot analysis and bar graphs showing pAMPK/total AMPK ratio and CPT1 protein levels of Hepa 1–6. Data represent the mean ± SEM of three experiments performed in duplicate. ** $p < .01$ or *** $p < .005$ *versus* LRP1+ HL-1 cells or *versus* Hepa 1–6 cells exposed to supernatants from control HL-1 cells. Differences between groups were analyzed using Student's *t*-test for independent samples.

pAMPK/AMPK ratio and CPT1 protein levels in a dose-response manner without altering cell morphology (*online* Fig. S14A-C).

3.5. Activated ANP-NPR-A signaling is linked to increased FA uptake by the liver

AMPK phosphorylation has been previously reported to activate FA uptake in oxidative tissues [35,36]. Oral fat gavage (OFG) experiments showed an increase in [^{3}H]-TG and [^{3}H]-FFA uptake by the liver of *cm-Lrp1*$^{-/-}$ mice that was blocked by the NPR-A antagonist A71915 (Fig. 7A). Real-time PCR experiments showed an increased expression of hepatic *Vldlr* and *Cd36* mRNA in *cm-Lrp1*$^{-/-}$ mice (Fig. 7C) that were also efficiently blocked by the NPR-A antagonist. Unlike the liver, there were no differences between KO and control mice in [^{3}H]-TG and [^{3}H]-FFA uptake by the skeletal muscle, although a significant increase in [^{3}H]-TG and [^{3}H]-FFA uptake was detected in groups treated with A71915 (*online* Fig. S15). In contrast to liver, there was a reduced uptake of [^{3}H]-TG and [^{3}H]-FFA by eWAT of *cm-Lrp1*$^{-/-}$ mice (Fig. 7B). Reduced levels of *Vldlr* and *Cd36* mRNA expresion was detected in eWAT of KO *versus* control mice (Fig. 7D). As shown in Fig. 7E,F, A71915 equaled eWAT weight and eWAT adipocyte size between *cm-Lrp1*$^{-/-}$ and *cm-Lrp1*$^{+/+}$ mice.

CLAMS experiments showed that treatment of *cm-Lrp1*$^{-/-}$ mice with the NPR-A antagonist counteracted increased lipid oxidation during the light phase (Fig. 8A) and increased glucose oxidation during the dark phase (Fig. 8B). There were no differences in oxygen consumption (Fig. 8C) and energy expenditure (Fig. 8D) between *cm-Lrp1*$^{-/-}$ and control mice treated with the NPR-A antagonists.

4. Discussion

The main innovative findings of this study are that LRP1 receptor levels in cardiomyocytes regulate circulating levels of atrial natriuretic peptide and that through this mechanism control NPR-A dependent fatty acid metabolism in the liver and, consequently, the whole-body metabolism.

4.1. LRP1 Controls the systemic levels of atrial natriuretic peptide through modulation of Corin activity in cardiomyocytes

Here, we show that isolated cardiomyocytes from *cm-Lrp1*$^{-/-}$ mice are deficient in the receptor *Lrp1*. Previous studies have shown that LRP1 plays a crucial role in the degradation of serpin:protease complexes [37,38]. Results from the immunoprecipitation assays performed

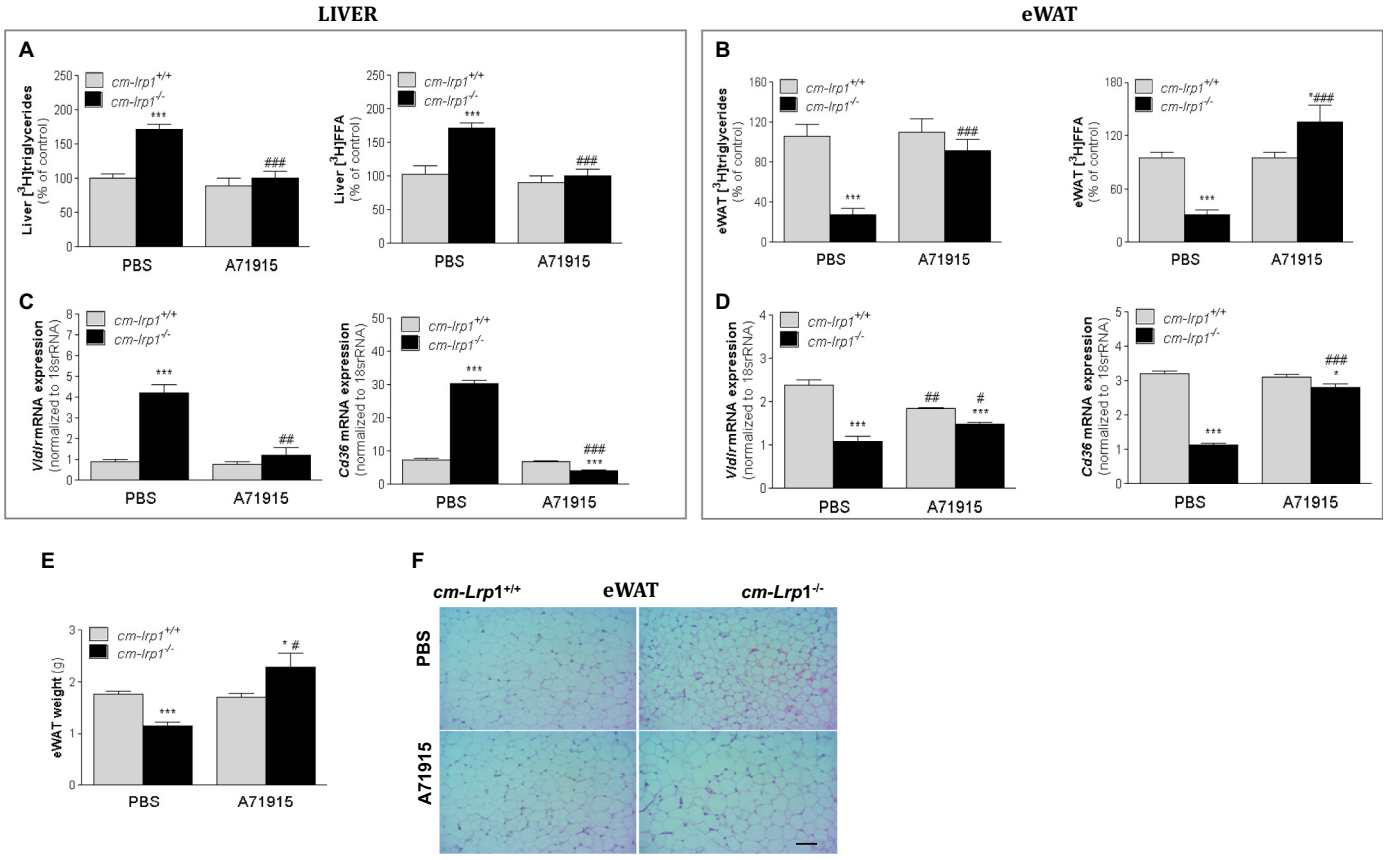

Fig. 7. TG and FA uptake increased in the liver while decreased in eWAT of *cm-Lrp1*$^{-/-}$ mice. *cm-Lrp1*$^{+/+}$ and *cm-Lrp1*$^{-/-}$ mice (control) mice were treated for 6 weeks with doxycycline cyclate in their drinking water and then treated with either saline or the NPRA antagonist A71915 for the last 4 weeks. Mice were then given an oral fat gavage (OFG) consisting of 20 μCi [^{3}H]-labeled triolein in 150 μL of olive oil as. Percentage of [^{3}H]-triglyceride and [^{3}H]-free fatty acid uptake by liver (A) and eWAT (B) in the different groups taking as reference the control group. Real-time PCR of *Vldlr* and *Cd36* mRNA expression levels in liver (C) and eWAT (D). (E) Representative Herxheimer stained eWAT sections (Bar = 100 μm). Data represent the mean ± SEM. $^*p < .05$, $^{**}p < .01$ or $^{***}p < .005$ *versus* control mice; ## $p < .01$ or ### $p < .005$ *versus* PBS. Differences between groups were analyzed using one-way analysis of variance (ANOVA) followed by a post-hoc Tukey-b test.

in this study indicated that corin, the main protease responsible for cardiac release of atrial natriuretic peptide [33], was mostly complexed with serpins in the heart of *cm-Lrp1*$^{-/-}$ mice, as it was previously shown in cultured cardiomyocytes [34]. In agreement with the capacity of LRP1 to modulate protease levels, we found that *Lrp1* deficiency in the cardiomyocyte, the most abundant and main ANP producing cell in the heart [39,40], directly impacts corin activity, cardiac ANP release and ANP circulating levels. A more direct proof of the capacity of LRP1 to modulate ANP release has been obtained from cell culture experiments performed with an LRP1-deficient HL-1 cell line (LRP1- HL-1 cells) previously generated in our group [9,10,25,26]. Our results evidenced the presence of higher ANP levels in the supernatants from LRP1- HL-1 cells compared to control cells.

The protease corin is also involved in the cleavage of pro-brain natriuretic peptide (BNP) to BNP [41]. Despite this, we did not observe alterations in cardiac or plasma BNP levels in *cm-Lrp1*$^{-/-}$ mice compared to the controls. The specific effect of the receptor deficiency on ANP release could be explained by the predominance of ANP (compared to the marginal presence of BNP) in hearts without ventricular dysfunction [42].

Several groups, including ours, have determined that the modulation of *Lrp1* receptor causes alterations of key signaling pathways in the heart. Our group reported that cardiac *Lrp1* overexpression contributes to enhanced cholesterol and triglyceride supply to the heart and is associated with serious calcium-handling alterations [25]. In the context of the myocardial infarction, LRP1 signaling activation has been reported to induce a cardioprotective signal, decreases infarct size, and preserves cardiac systolic function in young adult mice without comorbidities [43]. Elevated levels of *Lrp1* ligands, such as VLDL, can act as antagonists of *Lrp1* signaling [44]. Results from the present study show that cardiomyocyte *Lrp1* deficiency did not affect in cardiac function. This could be related to the absence of pathological stressors such as atherogenic dyslipemia or hypoxia. Further studies are required to know the optimal *Lrp1* threshold values in the presence of certain pathological ligands.

4.2. ANP activates NPR-A signaling that is linked to AMPK phosphorylation and increased FA oxidation/FA uptake in the liver of cm-Lrp1$^{-/-}$ *mice*

The systemic effects of ANP are well described, contributing to water-salt balance maintenance and blood pressure regulation through diuretic, natriuretic and vasodilatory effects. In addition, ANP displays important pleiotropic effects in the heart, acting as a main regulator of cardiovascular homeostasis in an autocrine and paracrine manner [45]. Besides the hemodynamic effects, ANP also is involved in lipolytic processes in white adipose tissue in primates [46]. Recently, it has been described as a potent lipolytic agent that exerts a great impact on the metabolism of patients with heart failure [47]. Interestingly, ANP induces anti-inflammatory effects in adipose tissue [48].

ANP has also been reported to promote oxidative metabolism in human skeletal muscle. In particular, ANP induces PGC-1α and mitochondrial OXPHOS gene expression in a cyclic GMP–dependent manner in human myotubes [49]. Results from the present study show that ANP increased NPR-A/cGMP/pVASP in the skeletal muscle of *cm-Lrp1*$^{-/-}$ mice. In our murine model, this upregulatory effect of ANP signaling was linked to mitochondrial OXPHOS upregulation, affecting CV-ATP5A and CII-SDHB subunit overexpression. However, there were no

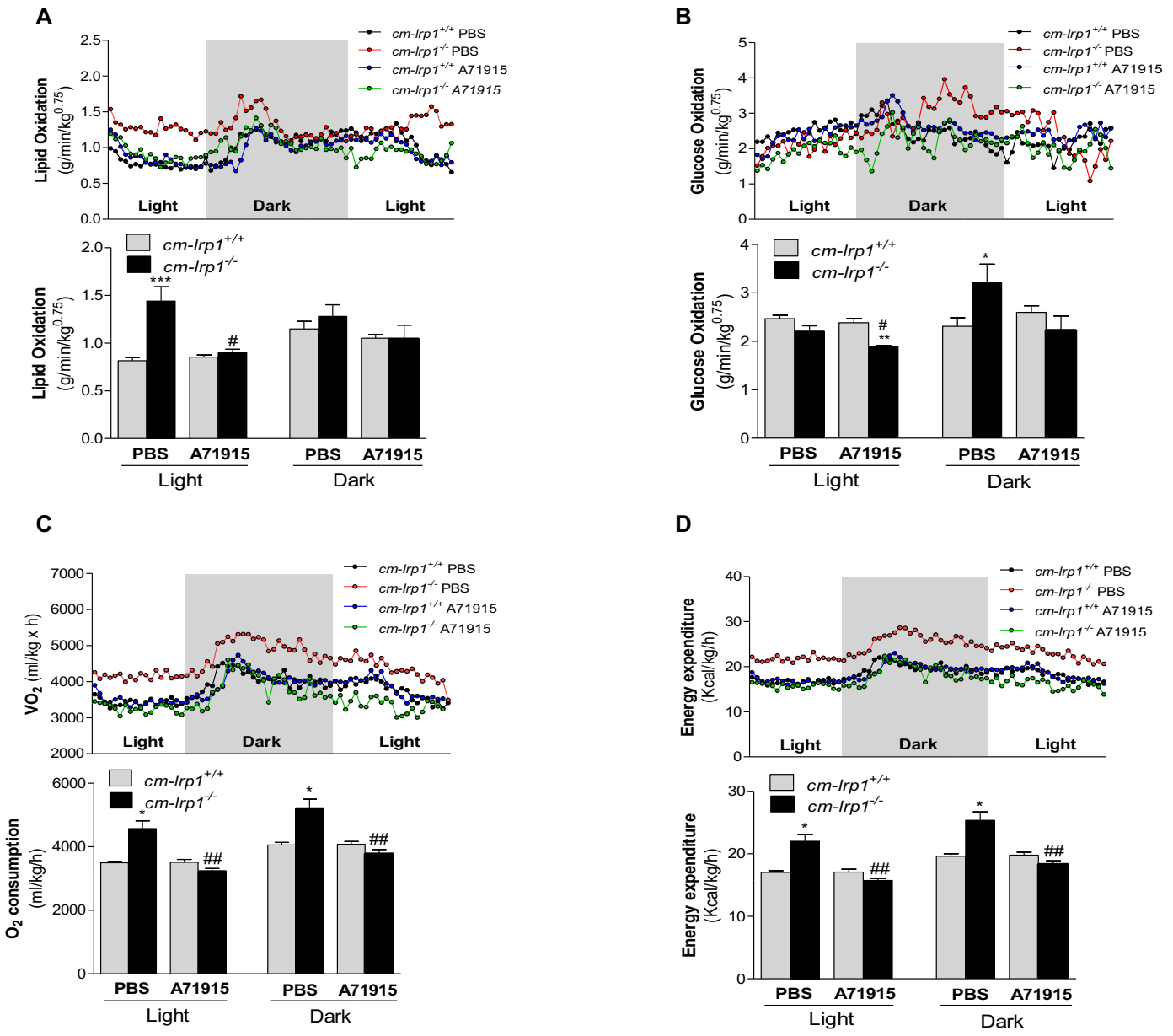

Fig. 8. Cardiomyocyte *Lrp1* deficiency increases whole-body energy consumption in an NPR-A dependent manner. *cm-Lrp1*$^{+/+}$ and *cm-Lrp1*$^{-/-}$ mice (control) mice were treated for 6 weeks with doxycycline cyclate in their drinking water and then treated with either saline or the NPR-A antagonist A71915 for the last 4 weeks. Oxymax respirometer measurements of lipid oxidation (A), glucose oxidation (B) VO_2 (C) and whole-body oxygen consumption (D) during the light and dark periods. $n = 8$–10 mice per condition. $^{*}p < .05$, $^{**}p < .01$ or $^{***}p < .005$ *versus* control mice; ## $p < .01$ or ### $p < .005$ *versus* PBS. Differences between groups were analyzed using one-way analysis of variance (ANOVA) followed by a *post-hoc Tukey-b* test.

differences in the levels of phosphorylated AMPK, the TG/FA uptake, the levels of CPT1 and UCP3, and TG accumulation in the skeletal muscle of *cm-Lrp1*$^{-/-}$ and control mice. These results indicate that FA uptake and FA oxidation were not significantly modulated by NPR-A/cGMP/pVASP signaling in the skeletal muscle of *cm-Lrp1*$^{-/-}$ mice.

In contrast, we found that NPR-A/cGMP/pVASP signaling was linked to AMPK phosphorylation in the liver of *cm-Lrp1*$^{-/-}$ mice. Our cell culture experiments evidenced that hepatocytes exposed to supernatants from LRP1- HL-1 cells or to ANP directly showed increased levels of phosphorylated AMPK. Previous studies have shown that pVASP, an ANP signaling mediator, phosphorylated specifically AMPK in the liver of a mouse model of diabetes [50]. AMPK is considered the master regulator of lipid metabolism and mitochondrial homeostasis [51–54]. One of the crucial functions of AMPK is the regulation of lipid metabolism through the phosphorylation of ACC. Upon activation of AMPK, phosphorylation of ACC results in ACC inactivation. Our results indicate that ACC phosphorylation is increased in the liver of KO mice and abolished by the treatment of KO mice with the NPR-A antagonist, indicating that the energy sensing AMPK/ACC pathway can be modulated by ANP in the liver. *Acsl3* mRNA expression levels were also decreased in the liver of *cm-Lrp1*$^{-/-}$ compared to control mice. *Acsl3* knockdown decreased total acyl-CoA synthetase activity in ob/ob mice and mice fed a high sucrose diet [55]. Together, these results support that ANP-induced AMPK phosphorylation is involved in the deactivation of FA synthesis in the liver of *cm-Lrp1*$^{-/-}$ mice.

The phosphorylation of ACC inhibits the production of malonyl-CoA, a substrate for fatty acid synthase (FAS) and a potent inhibitor of CPT1 [56]. CPT1 is the main mitochondrial enzyme responsible for fatty acid oxidation. Results from the present study showed increased levels of CPT1 in the liver *cm-Lrp1*$^{-/-}$ mice and in hepatocytes exposed to increased ANP levels. We also showed that this increase in dependent of NPR-A signaling. The link between AMPK phosphorylation and CPT1

activation has been previously shown in oxidative tissues of a mice model [36,51]. The upregulation of the mitochondrial OXPHOS subunits support an enhanced mitochondrial respiration in the liver of *cm-Lrp1*$^{-/-}$ mice. Further experiments are required to know the mechanism by which ANP signaling enhances the level of these OXPHOS protein subunits. This could be due to enhanced mitochondrial synthesis or enhanced amount of protein subunits per mitochondria. Together these results support an ANP-enhanced mitochondrial fatty acid oxidation in the liver of *cm-Lrp1*$^{-/-}$ mice.

Finally, UCP3, an indicator of mitochondrial response to intracellular FA, [^{3}H]-FA and [^{3}H]-TG uptake and FA/TG transporters such as Cd36 and VLDLR were upregulated in the liver of KO mice and the increase was abolished by the treatment of KO mice with the NPR-A antagonist. Previous studies have reported that pAMPK positively modulates *Cd36* in a mouse model of AMPK activation specifically in the liver [57].

Together, these results evidenced that ANP signaling promoted by cardiomyocyte LRP1 deficiency facilitates the repression of FA synthesis and the activation of FA uptake/FA mitochondrial oxidation in an AMPK-coordinated manner in the liver of *cm-Lrp1*$^{-/-}$ mice.

4.3. ANP-induced hepatic FAO confers a favorable metabolic profile to cm-Lrp1$^{-/-}$ *mice*

Here, we show that enhanced FA uptake and oxidation promoted by ANP reduces TG accumulation in the liver of KO mice. These results are in agreement with previous studies showing that moderate increases in *Cpt1a* activity are sufficient to reduce hepatic TG levels in CPT-1a-overexpressing animals [58] and even to modulate diabetes and obesity [30]. Interestingly, reduced hepatic triglyceride content in KO mice occurred in the context of enhanced supply of FA to the liver, and, by counteracting ANP-induced FA uptake by the liver, the NPR-A antagonist caused an increased FA uptake by eWAT. Although, a direct effect of ANP on adipose tissue of *cm-Lrp1*$^{-/-}$ cannot be discarded, data from the present study supports the secondary nature of cardiac *Lrp1* deficiency's benefits such as reducing diet-induced obesity and increasing energy expenditure. The liver is considered the main organ in the homeostasis of lipids and glucose and one of the highest contributors to whole-body lipid oxidation [59]. Moreover, previous studies have consistently demonstrated the link between the hepatic FAO and insulin-resistance [45,47,54]. Results from the present study show that phosphorylation of Akt, a crucial step in the insulin signaling pathway, is more active in the liver of *cm-Lrp1*$^{-/-}$ mice compared with controls. In addition, CLAMS experiments showed an ANP-induced glucose oxidation during the dark phase. However, further studies based on the analysis of signaling right after insulin administration are indeed required to obtain conclusions about the role of ANP on the modulation of diet-induced hepatic insulin resistance [60]. Similarly, it would be interesting to determine whether the response to leptin is altered in our model.

4.4. Main conclusions and translational potential of the work

Our results show that the favorable metabolic profile and increased energy expenditure in *cm-Lrp1*$^{-/-}$ mice mainly depends on ANP signaling involving hepatic AMPK activation (summarized in Fig. 9).

From the clinical point of view, our team has evaluated natriuretic peptide levels in patients with chronic heart failure. Recently, we described that patients with a low capacity to degrade active natriuretic

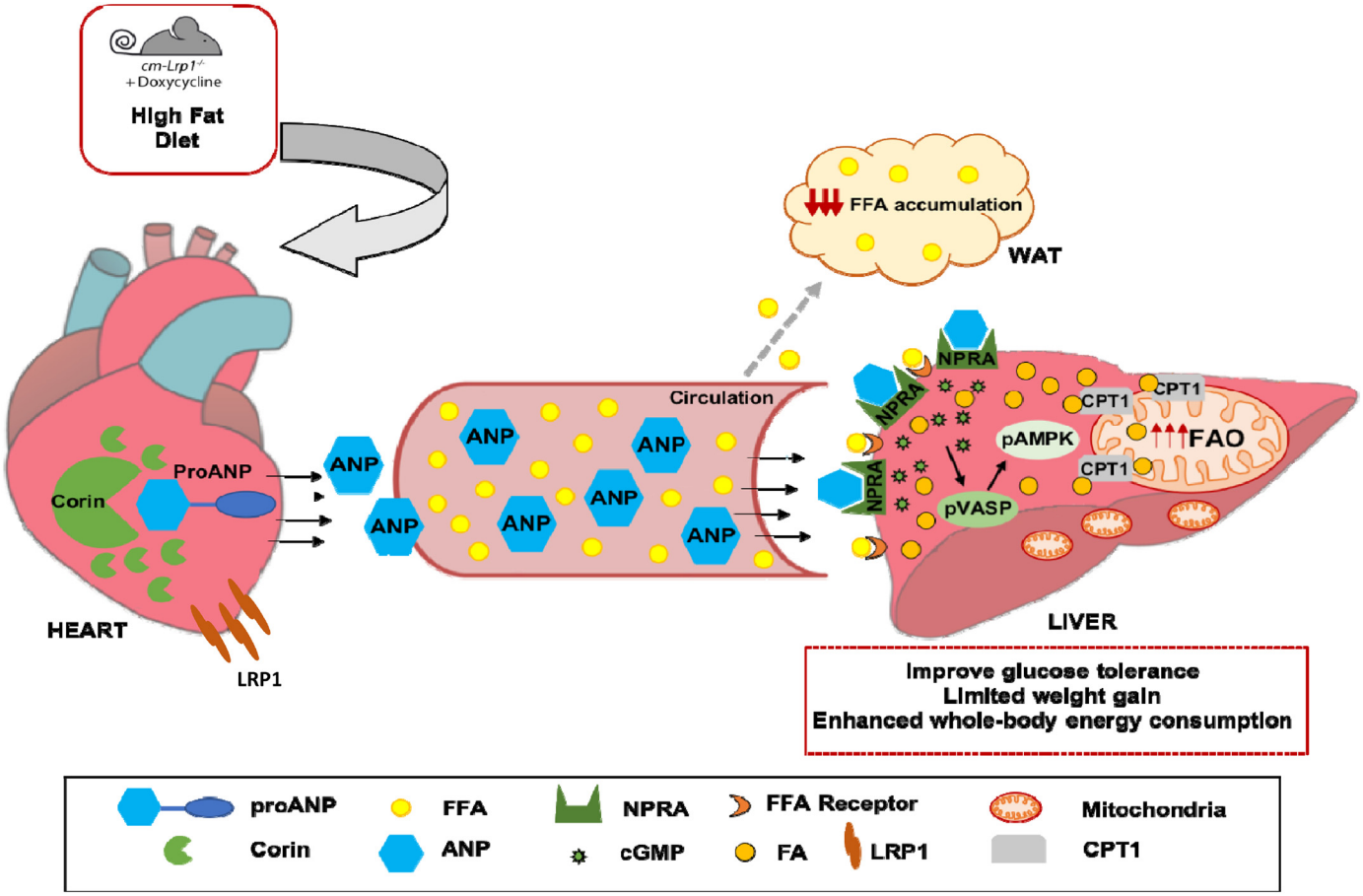

Fig. 9. Schematic main figure. Cardiomyocyte *Lrp1* deficiency facilitates corin activation and ANP release from the heart. NPR-A/cGMP/pVASP signaling activates AMPK/ACC pathway that coordinately inhibits FA synthesis and activates FA uptake and oxidation in the liver of *cm-Lrp1*$^{-/-}$ mice. The ANP-mediated activation of AMPK seems to underlie the decrease in hepatic TG content, the improved glucose tolerance, the limited weight gain and the enhanced whole-body energy consumption of cardiomyocyte-*lrp1* deficient mice.

peptides had better outcomes [61,62]. In humans, the main protective metabolic effects of ANP are related to ANP lipolytic effects in adipose tissue [46,63–67]. In fact, high levels of natriuretic peptides in plasma have been associated with weight loss in humans [66,67]. Here, treatment of *cm-Lrp1*$^{-/-}$ mice with the NPR-A antagonist restores energy expenditure to the levels of control mice, suggesting that ANP/NPR-A signaling is involved in the increased energy expenditure and reduced weight of *cm-Lrp1*$^{-/-}$ mice. It will be interesting to test in humans whether ANP-induced hepatic FA uptake/oxidation is an additional mechanism contributing to the impact of high circulating NP levels in weight loss. According to the present study, low levels of *Lrp1* expression in cardiomyocytes would contribute to the maintenance of elevated NP levels in circulation. This could be highly relevant in patients with metabolic disorders.

Acknowledgements

The authors thank Dr. Bin Zhou and Dr. Bingruo Wu (Department of Genetics, Albert Einstein College of Medicine, New York, USA) for kindly providing the Tnt2-Cre line, Dra. Montserrat Carrascal (CSIC Proteomics Unit) for her valuable help with the interpretation and representation of Proteomic data and Dr. Marta Casado (Instituto BioMedicina Valencia, CSIC) for help with line management and embryo preservation.

Funding

This work was funded by FIS PI14/01729 and FIS PI18/01584 (to VLl-C), FIS16/00139 (to JCE-G) grants from Instituto Salud Carlos III, co-financed by the European Fund for Regional Development (E.F.R.D.) and by the Ministry of Spain-MINECO (SAF2014-52223-C2-1-R to DS, co-financed by the European Fund for Regional Development (E.F.R.D.). Support was received from Ministerio de Economía y Competitividad to DdG-C (IJCI-2016-29393), Agència de Gestió d'Ajuts Universitaris i de Recerca Grant FI to ERL (FI-DGR 2013/00014), Fundació MARATÓ TV3 Project 201521-10 (to VLl-C) and Project 87/C/2016 to DS. CIBER Diabetes y Enfermedades Metabólicas Asociadas (CIBERDEM; CB07/08/0016 (FBV, JCE-G, LC); CB07/08/0017 (AZ), CIBER Fisiopatología de la Obesidad y la Nutrición (CIBEROBN; CB06/03/0001 (DS, LH); CB06/03/0017 (JCL, NR)) and CIBER Enfermedades Cardiovasculares (CIBERCV; CB16/1100403) (DdG-C, VLl-, CS, ERL and AB-G) are Instituto de Salud Carlos III (ISCIII) projects.

Author contribution section

Concept and design: Vicenta Llorente-Cortés and Joan Carles Escola-Gil.

Performed the experiments: Aleyda Benítez-Amaro, Elena Revuelta-López, Olga Bornachea, Lidia Cedo, Angela Vea, Laura Herrero, Nuria Roglans, Carolina Soler-Botija, Eduardo García, Laura Nasarre, Eugenia Mato, David Sebastian.

Data analysis and interpretation: Vicenta Llorente-Cortés, David de Gonzalo-Calvo, Sandra Camino-López, Francisco Blanco Vaca, Antoni Bayes Genis, Antonio Zorzano, Joan Carles Laguna, Dolors Serra, Joan Carles Escola-Gil, David Sebastian.

Writing and review of Manuscript: Elena Revuelta-López, Joan Carles Escola-Gil, Vicenta Llorente-Cortés.

Declaration of competing interest

The authors have declared no potential conflicts of interest.

Appendix A. Supplementary data

Supplementary data to this article can be found online at https://doi.org/10.1016/j.metabol.2020.154191.

References

[1] Grundy SM, Pasternak R, Greenland P, Smith S, Fuster V. Assessment of cardiovascular risk by use of multiple-risk-factor assessment equations: a statement for healthcare professionals from the American Heart Association and the American College of Cardiology. Circulation 1999;100:1481–92. https://doi.org/10.1161/01.CIR.100.13.1481.

[2] Goldberg IJ. Diabetic dyslipidemia: causes and consequences. J Clin Endocrinol Metab 2014;86:965–71. https://doi.org/10.1210/jcem.86.3.7304.

[3] Kankaanpää M, Lehto HR, Pärkkä JP, Komu M, Viljanen A, Ferrannini E, et al. Myocardial triglyceride content and epicardial fat mass in human obesity: relationship to left ventricular function and serum free fatty acid levels. J Clin Endocrinol Metab 2006;91:4689–95. https://doi.org/10.1210/jc.2006-0584.

[4] Pillutla P, Hwang YC, Augustus A, Yokoyama M, Yagyu H, Johnston TP, et al. Perfusion of hearts with triglyceride-rich particles reproduces the metabolic abnormalities in lipotoxic cardiomyopathy. Am J Physiol Metab 2005;288:E1229–35. https://doi.org/10.1152/ajpendo.00273.2004.

[5] Moon JH, Kang SB, Park JS, Lee BW, Kang ES, Ahn CW, et al. Up-regulation of hepatic low-density lipoprotein receptor-related protein 1: a possible novel mechanism of antiatherogenic activity of hydroxymethylglutaryl-coenzyme A reductase inhibitor: atorvastatin and hepatic LRP1 expression. Metabolism 2011;60:930–40. https://doi.org/10.1016/j.metabol.2010.08.013.

[6] Dato VA, Chiabrando GA. The role of low-density lipoprotein receptor-related protein 1 in lipid metabolism, glucose homeostasis and inflammation. Int J Mol Sci 2018. https://doi.org/10.3390/ijms19061780.

[7] Llorente-Cortés V, Martínez-González J, Badimon L. LDL receptor-related protein mediates uptake of aggregated LDL in human vascular smooth muscle cells. Arterioscler Thromb Vasc Biol 2000;20:1572–9. https://doi.org/10.1161/01.ATV.20.6.1572.

[8] Llorente-Cortés V, Otero-Viñas M, Badimon L. Differential role of heparan sulfate proteoglycans on aggregated LDL uptake in human vascular smooth muscle cells and mouse embryonic fibroblasts. Arterioscler Thromb Vasc Biol 2002;22:1905.

[9] Cal R, Juan-Babot O, Brossa V, Roura S, Gálvez-Montón C, Portoles M, et al. Low density lipoprotein receptor-related protein 1 expression correlates with cholesteryl ester accumulation in the myocardium of ischemic cardiomyopathy patients. J Transl Med 2012;10. https://doi.org/10.1186/1479-5876-10-160.

[10] Cal R, Castellano J, Revuelta-Lpez E, Aledo R, Barriga M, Farr J, et al. Low-density lipoprotein receptor-related protein 1 mediates hypoxia-induced very low density lipoprotein-cholesteryl ester uptake and accumulation in cardiomyocytes. Cardiovasc Res 2012;94:469–79. https://doi.org/10.1093/cvr/cvs136.

[11] Hofmann SM, Zhou L, Perez-Tilve D, Greer T, Grant E, Wancata L, et al. Adipocyte LDL receptor–related protein–1 expression modulates postprandial lipid transport and glucose homeostasis in mice. J Clin Invest 2007;117:3271–82. https://doi.org/10.1172/JCI31929.

[12] Bogan JS. Regulation of glucose transporter translocation in health and diabetes. Annu Rev Biochem 2012. https://doi.org/10.1146/annurev-biochem-060109-094246.

[13] Ding Y, Xian X, Holland WL, Tsai S, Herz J. Low-density lipoprotein receptor-related protein-1 protects against hepatic insulin resistance and hepatic steatosis. EBioMedicine 2016;7:135–45. https://doi.org/10.1016/j.ebiom.2016.04.002.

[14] Laatsch A, Merkel M, Talmud PJ, Grewal T, Beisiegel U, Heeren J. Insulin stimulates hepatic low density lipoprotein receptor-related protein 1 (LRP1) to increase postprandial lipoprotein clearance. Atherosclerosis 2009;204:105–11. https://doi.org/10.1016/j.atherosclerosis.2008.07.046.

[15] Jeon BH, Lee YH, Yun MR, Kim SH, Lee BW, Kang ES, et al. Increased expression of ATP-binding cassette transporter A1 (ABCA1) as a possible mechanism for the protective effect of cilostazol against hepatic steatosis. Metabolism 2015. https://doi.org/10.1016/j.metabol.2015.07.014.

[16] Bergman RN, Piccinini F, Kabir M, Ader M. Novel aspects of the role of the liver in carbohydrate metabolism. Metabolism 2019. https://doi.org/10.1016/j.metabol.2019.05.011.

[17] Nakamura M, Sadoshima J. Heart over mind: metabolic control of white adipose tissue and liver. EMBO Mol Med 2014;6:1521–4. https://doi.org/10.15252/emmm.201404749.

[18] Shimano M, Ouchi N, Walsh K. Cardiokines: recent progress in elucidating the cardiac secretome. Circulation 2012;126. https://doi.org/10.1161/CIRCULATIONAHA.112.150656.

[19] Planavila A, Fernández-Solà J, Villarroya F. Cardiokines as modulators of stress-induced cardiac disorders. Adv Protein Chem Struct Biol 2017;108:227–56. https://doi.org/10.1016/bs.apcsb.2017.01.002.

[20] Wu B, Zhou B, Wang Y, Cheng HL, Hang CT, Pu WT, et al. Inducible cardiomyocyte-specific gene disruption directed by the rat Tnnt2 promoter in the mouse. Genesis 2010;48:63–72. https://doi.org/10.1002/dvg.20573.

[21] Robertson A, Perea J, Tolmachova T, Thomas PK, Huxley C. Effects of mouse strain, position of integration and tetracycline analogue on the tetracycline conditional system in transgenic mice. Gene 2002;282:65–74. https://doi.org/10.1016/S0378-1119(01)00793-4.

[22] Escolà-Gil JC, Llaverias G, Julve J, Jauhiainen M, Méndez-González J, Blanco-Vaca F. The cholesterol content of western diets plays a major role in the paradoxical increase in high-density lipoprotein cholesterol and upregulates the macrophage reverse cholesterol transport pathway. Arterioscler Thromb Vasc Biol 2011;31:2493–9. https://doi.org/10.1161/ATVBAHA.111.236075.

[23] Llucià-Valldeperas A, Soler-Botija C, Gálvez-Montón C, Roura S, Prat-Vidal C, Perea-Gil I, et al. Electromechanical conditioning of adult progenitor cells improves recovery of cardiac function after myocardial infarction. Stem Cells Transl Med 2017. https://doi.org/10.5966/sctm.2016-0079.

[24] Julve J, Escolà-Gil JC, Rotllan N, Fiévet C, Vallez E, de la Torre C, et al. Human apolipoprotein A-II determines plasma triglycerides by regulating lipoprotein lipase activity and high-density lipoprotein proteome. Arterioscler Thromb Vasc Biol 2010;30 232 LP – 238.
[25] Revuelta-López E, Cal R, Herraiz-Martínez A, de Gonzalo-Calvo D, Nasarre L, Roura S, et al. Hypoxia-driven sarcoplasmic/endoplasmic reticulum calcium ATPase 2 (SERCA2) downregulation depends on low-density lipoprotein receptor-related protein 1 (LRP1)-signalling in cardiomyocytes. J Mol Cell Cardiol 2015;85. https://doi.org/10.1016/j.yjmcc.2015.04.028.
[26] Samouillan V, Revuelta-López E, Dandurand J, Nasarre L, Badimon L, Lacabanne C, et al. Cardiomyocyte intracellular cholesteryl ester accumulation promotes tropoelastin physical alteration and degradation: role of LRP1 and cathepsin S. Int J Biochem Cell Biol 2014;55. https://doi.org/10.1016/j.biocel.2014.09.005.
[27] Nguyen TD, Carrascal M, Vidal-Cortes O, Gallardo O, Casas V, Gay M, et al. The phosphoproteome of human Jurkat T cell clones upon costimulation with anti-CD3/anti-CD28 antibodies. J Proteomics 2016;131:190–8. https://doi.org/10.1016/j.jprot.2015.10.029.
[28] Óscar G, David O, Marina G, Montserrat C, Joaquin A. A collection of open source applications for mass spectrometry data mining. Proteomics 2014;14:2275–9. https://doi.org/10.1002/pmic.201400124.
[29] Chen S, Sen S, Young D, Wang W, Moravec CS, Wu Q. Protease corin expression and activity in failing hearts. Am J Physiol Hear Circ Physiol 2010;299:H1687–92. https://doi.org/10.1152/ajpheart.00399.2010.
[30] Orellana-Gavaldà JM, Herrero L, Malandrino Maria I, Pañeda A, Sol Rodríguez-Peña M, Petry H, et al. Molecular therapy for obesity and diabetes based on a long-term increase in hepatic fatty-acid oxidation. Hepatology 2010;53:821–32. https://doi.org/10.1002/hep.24140.
[31] Herrero L, Rubí B, Sebastián D, Serra D, Asins G, Maechler P, et al. Alteration of the malonyl-CoA/carnitine palmitoyltransferase I interaction in the β-cell impairs glucose-induced insulin secretion. Diabetes 2005;54:462–71. https://doi.org/10.2337/diabetes.54.2.462.
[32] Rebollo A, Roglans N, Baena M, Sánchez RM, Merlos M, Alegret M, et al. Liquid fructose downregulates Sirt1 expression and activity and impairs the oxidation of fatty acids in rat and human liver cells. Biochim Biophys Acta - Mol Cell Biol Lipids 1841;2014:514–24. https://doi.org/10.1016/j.bbalip.2014.01.002.
[33] Pemberton CJ, Siriwardena M, Kleffmann T, Ruygrok P, Palmer SC, Yandle TG, et al. First identification of circulating prepro-A-type natriuretic peptide (preproANP) signal peptide fragments in humans: initial assessment as cardiovascular biomarkers. Clin Chem 2012;58:757–67. https://doi.org/10.1373/clinchem.2011.176990.
[34] Gladysheva IP, Robinson BR, Houng AK, Kováts T, King SM. Corin is co-expressed with pro-ANP and localized on the cardiomyocyte surface in both zymogen and catalytically active forms. J Mol Cell Cardiol 2008;44:131–42. https://doi.org/10.1016/j.yjmcc.2007.10.002.
[35] Schönke M, Massart J, Zierath JR. Effects of high-fat diet and AMP-activated protein kinase modulation on the regulation of whole-body lipid metabolism. J Lipid Res 2018;59:1276–82. https://doi.org/10.1194/jlr.d082370.
[36] Viollet B. AMPK: Lessons from transgenic and knockout animals. Front Biosci 2009; Volume:19. doi:https://doi.org/10.2741/3229.
[37] Strickland DK, Muratoglu SC, Antalis TM. Serpin–enzyme receptors: LDL receptor-related protein 1. Methods Enzymol 2011;499:17–31. https://doi.org/10.1016/B978-0-12-386471-0.00002-X.
[38] Gettins PGW, Dolmer K. The high affinity binding site on plasminogen activator inhibitor-1 (PAI-1) for the low density lipoprotein receptorrelated protein (LRP1) is composed of four basic residues. J Biol Chem 2016;291:800–12. https://doi.org/10.1074/jbc.M115.688820.
[39] Ogawa Y, Nakao K, Mukoyama M, Hosoda K, Shirakami G, Arai H, et al. Natriuretic peptides as cardiac hormones in normotensive and spontaneously hypertensive rats: the ventricle is a major site of synthesis and secretion of brain natriuretic peptide. Circ Res 1991. https://doi.org/10.1161/01.RES.69.2.491.
[40] Nakao K, Ogawa Y, Suga SI, Imura H. Molecular biology and biochemistry of the natriuretic peptide system. I: Natriuretic peptides J Hypertens 1992. https://doi.org/10.1097/00004872-199210000-00002.
[41] Zhou Y, Wu Q. Corin in natriuretic peptide processing and hypertension. Curr Hypertens Rep 2014;16:415. https://doi.org/10.1007/s11906-013-0415-7.
[42] Luchner A, Muders F, Dietl O, Friedrich E, Blumberg F, Protter AA, et al. Differential expression of cardiac ANP and BNP in a rabbit model of progressive left ventricular dysfunction. Cardiovasc Res 2001;51:601–7.
[43] Toldo S, Austin D, Mauro AG, Mezzaroma E, Van Tassell BW, Marchetti C, et al. Low-density lipoprotein receptor–related protein-1 is a therapeutic target in acute myocardial infarction. JACC Basic to Transl Sci 2017;2:561–74. https://doi.org/10.1016/j.jacbts.2017.05.007.
[44] Boucher P, Liu P, Gotthardt M, Hiesberger T, Anderson RGW, Herz J. Platelet-derived growth factor mediates tyrosine phosphorylation of the cytoplasmic domain of the low density lipoprotein receptor-related protein in caveolae. J Biol Chem 2002. https://doi.org/10.1074/jbc.M200428200.
[45] Forte M, Madonna M, Schiavon S, Valenti V, Versaci F, Zoccai GB, et al. Cardiovascular pleiotropic effects of natriuretic peptides. Int J Mol Sci 2019. https://doi.org/10.3390/ijms20163874.
[46] Sengenès C, Zakaroff-Girard A, Moulin A, Berlan M, Bouloumié A, Lafontan M, et al. Natriuretic peptide-dependent lipolysis in fat cells is a primate specificity. Am J Physiol Integr Comp Physiol 2002;283:R257–65. https://doi.org/10.1152/ajpregu.00453.2001.
[47] Bartels ED, Guo S, Kousholt BS, Larsen JR, Hasenkam JM, Burnett J, et al. High doses of ANP and BNP exacerbate lipolysis in humans and the lipolytic effect of BNP is associated with cardiac triglyceride content in pigs. Peptides 2019. https://doi.org/10.1016/j.peptides.2018.11.003.
[48] Moro C, Klimcakova E, Lolmède K, Berlan M, Lafontan M, Stich V, et al. Atrial natriuretic peptide inhibits the production of adipokines and cytokines linked to inflammation and insulin resistance in human subcutaneous adipose tissue. Diabetologia 2007. https://doi.org/10.1007/s00125-007-0614-3.
[49] Engeli S, Birkenfeld AL, Badin PM, Bourlier V, Louche K, Viguerie N, et al. Natriuretic peptides enhance the oxidative capacity of human skeletal muscle. J Clin Invest 2012. https://doi.org/10.1172/JCI64526.
[50] Tateya S, Rizzo-De Leon N, Handa P, Cheng AM, Morgan-Stevenson V, Ogimoto K, et al. VASP increases hepatic fatty acid oxidation by activating AMPK in mice. Diabetes 2013;62:1913–22. https://doi.org/10.2337/db12-0325.
[51] Schonke M, Massart J, Zierath JR. Effects of high-fat diet and AMPK modulation on the regulation of whole-body lipid metabolism. J Lipid Res 2018. https://doi.org/10.1194/jlr.D082370.
[52] Carling D. AMPK signalling in health and disease. Curr Opin Cell Biol 2017;45:31–7. https://doi.org/10.1016/j.ceb.2017.01.005.
[53] Lyons CL, Roche HM. Nutritional modulation of AMPK-impact upon metabolic-inflammation. Int J Mol Sci 2018;19. https://doi.org/10.3390/ijms19103092.
[54] Herzig S, Shaw RJ. AMPK: Guardian of metabolism and mitochondrial homeostasis. Nat Rev Mol Cell Biol 2018. https://doi.org/10.1038/nrm.2017.95.
[55] Bu SY, Mashek MT, Mashek DG. Suppression of long chain acyl-CoA synthetase 3 decreases hepatic de novo fatty acid synthesis through decreased transcriptional activity. J Biol Chem 2009. https://doi.org/10.1074/jbc.M109.036665.
[56] Foster DW. The role of the carnitine system in human metabolism. Ann N Y Acad Sci 2004. https://doi.org/10.1196/annals.1320.001.
[57] Foretz M, Even PC, Viollet B. AMPK activation reduces hepatic lipid content by increasing fat oxidation in vivo. Int J Mol Sci 2018. https://doi.org/10.3390/ijms19092826.
[58] Stefanovic-Racic M, Perdomo G, Mantell BS, Sipula IJ, Brown NF, O'Doherty RM. A moderate increase in carnitine palmitoyltransferase 1a activity is sufficient to substantially reduce hepatic triglyceride levels. Am J Physiol Metab 2008;294:E969–77. https://doi.org/10.1152/ajpendo.00497.2007.
[59] Postic C, Dentin R, Girard J. Role of the liver in the control of carbohydrate and lipid homeostasis. Diabetes & Metab 2004;858:398 YP – 477. doi:http://dx.doi.org/DM-11-2004-30-5-1262-3636-101019-ART1.
[60] Sebastián D, Hernández-Alvarez MI, Segalés J, Sorianello E, Muñoz JP, Sala D, et al. Mitofusin 2 (Mfn2) links mitochondrial and endoplasmic reticulum function with insulin signaling and is essential for normal glucose homeostasis. Proc Natl Acad Sci U S A 2012. https://doi.org/10.1073/pnas.1108220109.
[61] Bayés-Genís A, Barallat J, Galán A, De Antonio M, Domingo M, Zamora E, et al. Soluble neprilysin is predictive of cardiovascular death and heart failure hospitalization in heart failure patients. J Am Coll Cardiol 2015;65:657–65. https://doi.org/10.1016/j.jacc.2014.11.048.
[62] Bayés-Genís A, Barallat J, Pascual D, Nuñez J, Miñana G, Sánchez-Mas J, et al. Prognostic value and kinetics of soluble neprilysin in acute heart failure. A Pilot Study JACC Hear Fail 2015;3:641–4. https://doi.org/10.1016/j.jchf.2015.03.006.
[63] Sengenès C, Bouloumié A, Hauner H, Berlan M, Busse R, Lafontan M, et al. Involvement of a cGMP-dependent pathway in the natriuretic peptide-mediated hormone-sensitive lipase phosphorylation in human adipocytes. J Biol Chem 2003;278:48617–26. https://doi.org/10.1074/jbc.M303713200.
[64] Birkenfeld AL, Budziarek P, Boschmann M, Moro C, Adams F, Franke G, et al. Atrial natriuretic peptide induces postprandial lipid oxidation in humans. Diabetes 2008;57:3199–204. https://doi.org/10.2337/db08-0649.
[65] Moro C, Crampes F, Sengenes C, De glisezinski I, Galitzky J, Thalamas C, et al.. Atrial natriuretic peptide contributes to physiological control of lipid mobilization in humans. FASEB J 2004;18:908–10. https://doi.org/10.1096/fj.03-1086fje.
[66] Chainani-Wu N, Weidner G, Purnell DM, Frenda S, Merritt-Worden T, Kemp C, et al. Relation of B-type natriuretic peptide levels to body mass index after comprehensive lifestyle changes. Am J Cardiol 2010;105:1570–6. https://doi.org/10.1016/j.amjcard.2010.01.016.
[67] Chen-Tournoux A, Khan AM, Baggish AL, Castro VM, Semigran MJ, McCabe EL, et al. Impact of weight loss following weight loss surgery on levels of plasma N-terminal pro-B-type natriuretic peptide. Am J Cardiol 2010;106:1450–5. https://doi.org/10.1016/j.amjcard.2010.06.076.

13.1 Article 1 supplemental material

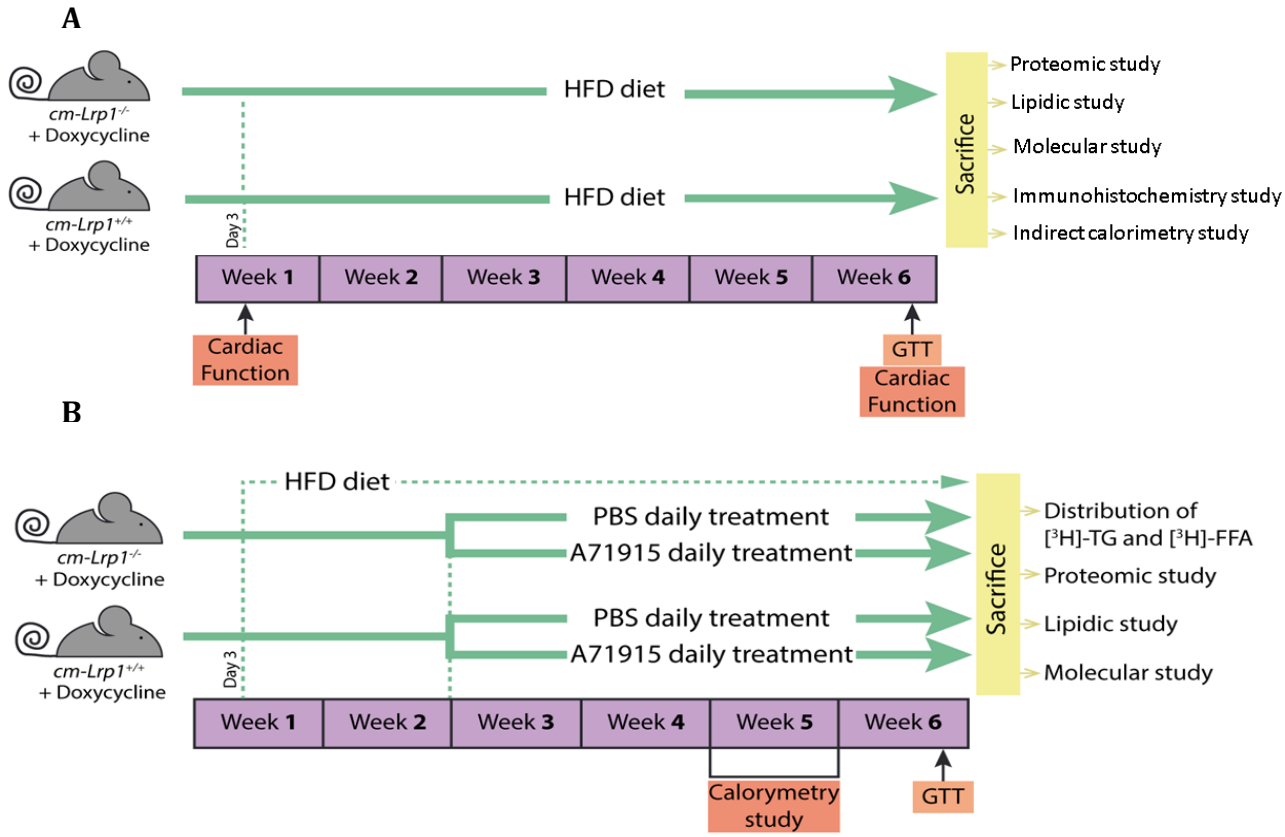

Figure S1. Scheme of experimental procedure and mice groups. (A) Study I: cm-*Lrp1*$^{-/-}$ (deficient) and cm-*Lrp1*$^{+/+}$ (control) mice (10-week old) were fed high fat diet for six week. Both cm-*Lrp1*$^{-/-}$ and control groups were daily treated with doxycycline cyclate administered in their drinking water to assess Lrp1 deficiency in cardiomyocytes. (B) Study II. Male cm-*Lrp1*$^{-/-}$ and cm-*Lrp1*$^{+/+}$ (control) mice (10-week old) were fed with HFD and daily treated with doxycycline cyclate administered in their drinking water to assess the attenuation of Lrp1 levels in cardiomyocytes. After two weeks of diet, mice were randomly assigned to either untreated (PBS) or treated with the NPRA inhibitor A71915 (200 µg/kg in PBS in a final volum of 100 µl) for the last four weeks. Calorimetry study was performed at week 5. The glucose tolerance test (GGT) was carried out during the last week of treatment. Animals were sacrificed at the end of the study.

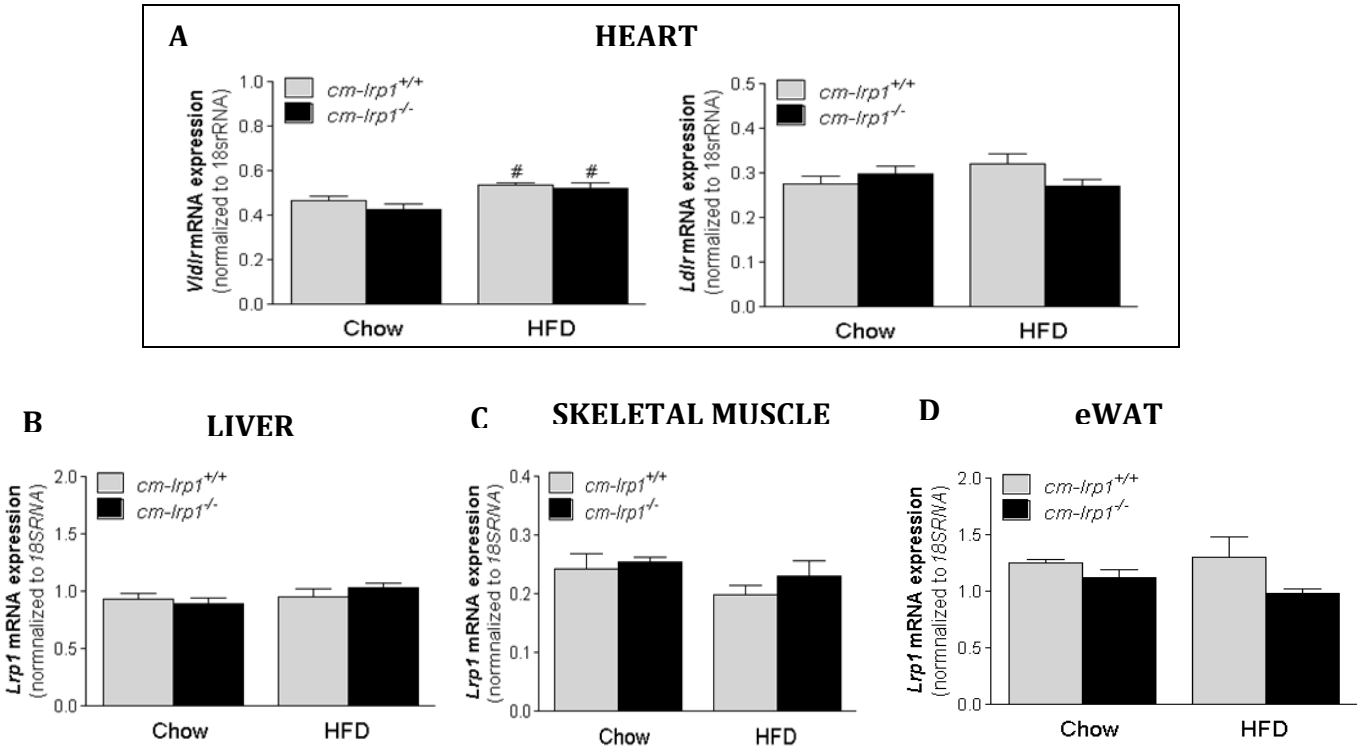

Figure S2. Hearts from cm-*Lrp1*$^{-/-}$ mice showed specific deletion of Lrp1 but not of other receptors of the same family. Ten week old male mice were treated daily with doxycycline cyclate administered in their drinking water during all the procedure to assess the conditional inhibition of Lrp1 levels in cardiomyocytes. After three days of treatment, both cm-*Lrp1*$^{+/+}$ and cm-*Lrp1*$^{-/-}$ mice were randomized and fed a chow diet or HFD for six weeks. (A) Real-time PCR measurements of Vldlr and Ldlr mRNA expression levels in the heart and of Lrp1 mRNA expression in liver (B), skeletal muscle (C) and eWAT (D). Data represent the mean±SEM for 9 mice per group. # $p<0.05$ versus chow diet. Differences between groups were analysed using one-way analysis of variance (ANOVA) followed by a post-hoc Tukey-b test.

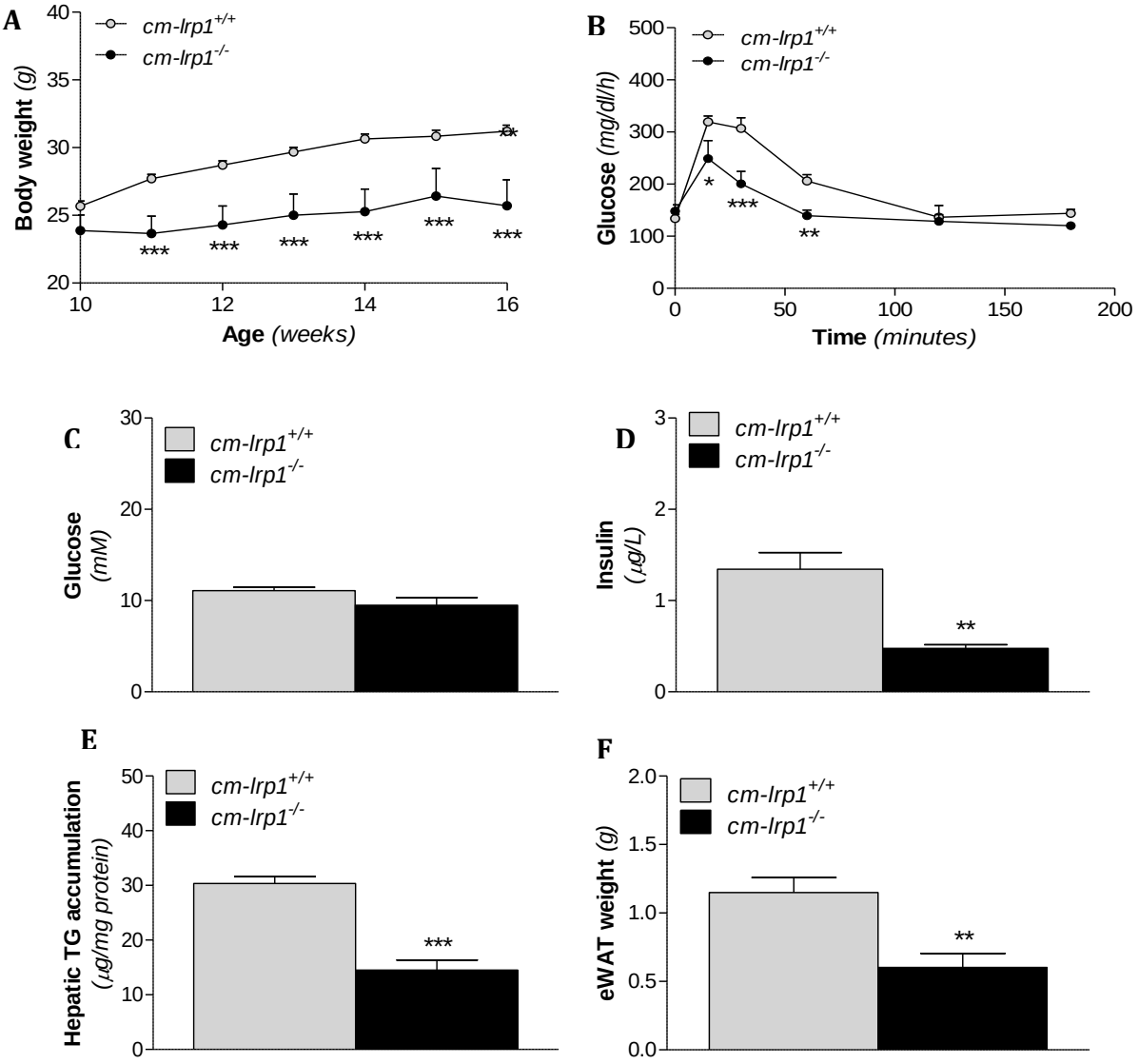

Figure S3. Lrp1 deficiency in cardiomyocytes improves diet-induced glucose tolerance and reduces weight gain. cm-*Lrp1*$^{-/-}$ and cm-*Lrp1*$^{+/+}$ (control) mice were treated for 6 weeks with doxycycline cyclate in their drinking water. (A) Body weight changes over 6 weeks of HFD diet. Glucose tolerance test in mice (1.3 mg/g of body mass) (B), glucose (C) and insulin (D) circulating levels. (E) Hepatic TG levels and (F) eWAT weight. Data represent the mean±SEM. n=9 mice per condition.*p<0.05, **p<0.01 or *** p<0.005 vs control mice. Differences between groups were analysed using Student's t test for independent samples.

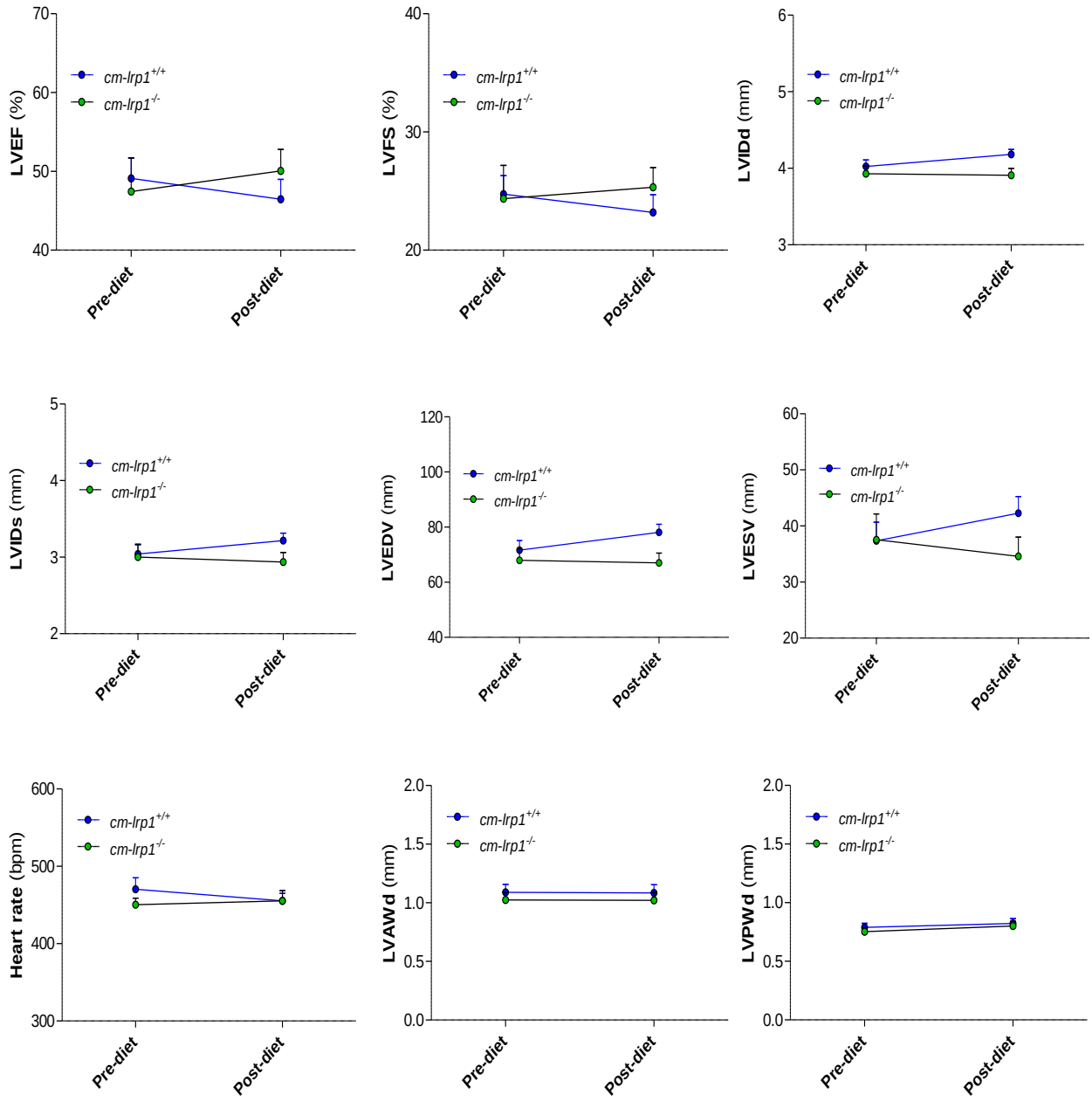

Figure S4. Cardiomyocyte Lrp1 deficiency did not alter cardiac functional parameters. Mice were subjected to a transthoracic echocardiography pre- and post-diet. LVEF, left ventricle ejection fraction; LVFS, left ventricle fractional shortening; LVIDd, left ventricle internal diameter diastole; LVIDs, left ventricle internal diameter systole; LVEDV, left ventricle end-diastolic volume; LVESV, left ventricle end-systolic volume; LVAWd, LV anterior wall at end cardiac diastole; LVPWd, LV posterior wall at end cardiac diastole. n=6-9 mice per condition. Data represent the mean±SEM. Differences between groups were analysed using Student's t test for paired samples.

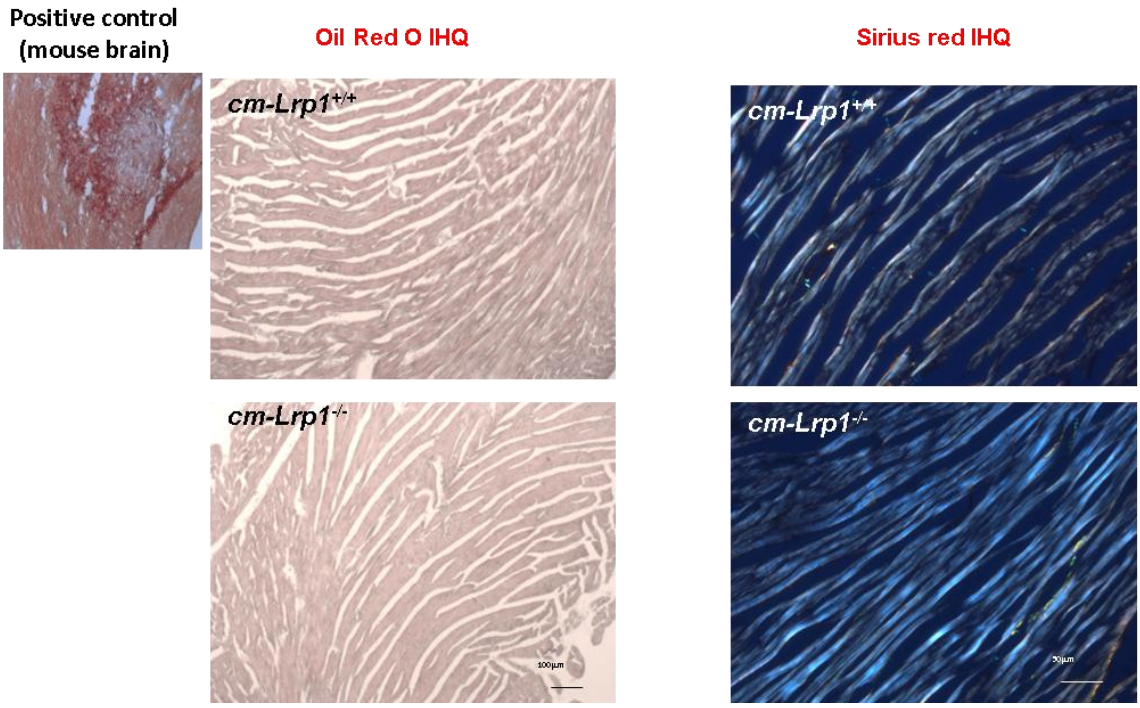

Figure S5. Cardiomyocyte Lrp1 deficiency did not alter cardiac structural parameters. Heart sections stained with Oil Red O to detect lipids (left panels). A polarized light microscope was used to measure collagen types I and III (right panels) on randomly selected Sirius red-stained sections.

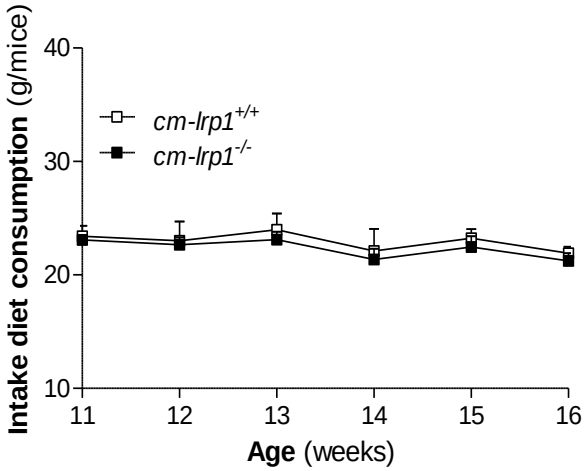

Figure S6. Food intake was similar in both cm-Lrp1$^{+/+}$ and cm-Lrp1$^{-/-}$ mice. Data represent the mean±SEM of 3 independent cages per group. Differences between groups were analysed using Student's t test for independent samples.

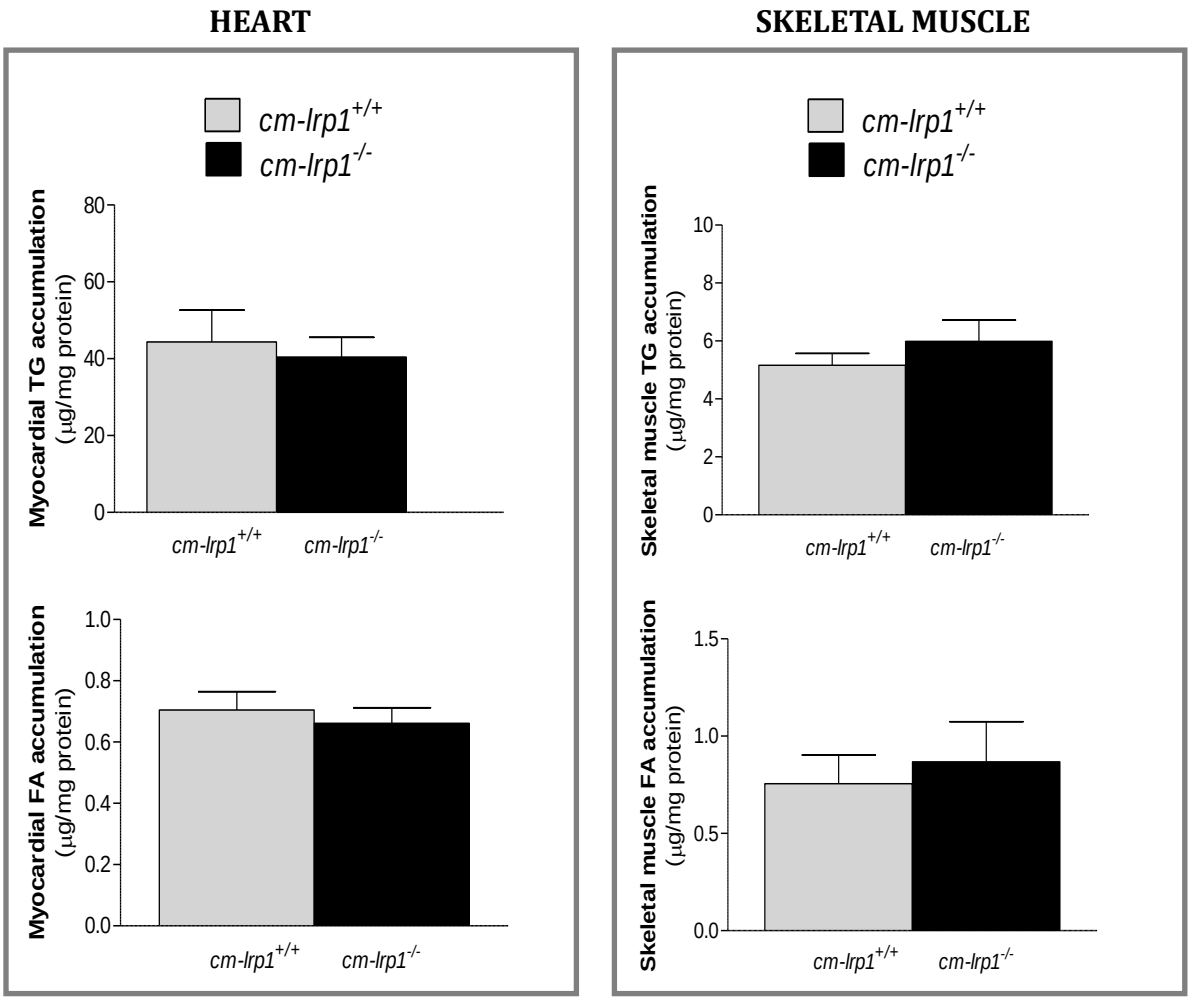

Figure S7. Lack of differences in triglyceride and fatty acid content of heart and skeletal muscle between cm-*lrp1*$^{-/-}$ and control mice. Heart and skeletal muscle were subjected to lipid extraction and used to lipid partitioning by Thin Layer Chromatography to quantify triglyceride content using a standard triglyceride (TG) curve and to measure FA content by a COBAS autoanalyzer. n=9-11 mice per condition. Data represent the mean±SEM. Differences between groups were analysed using Student's t test for independent samples.

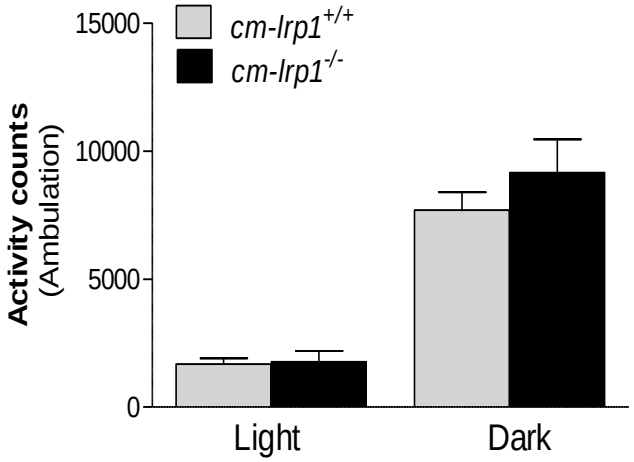

Figure S8. Ambulation activity was higher during the dark without differences between cm-*Lrp1*$^{-/-}$ and control mice. n=8 mice per condition. Data represent the mean±SEM. Differences between groups were analysed using Student's t test for independent samples.

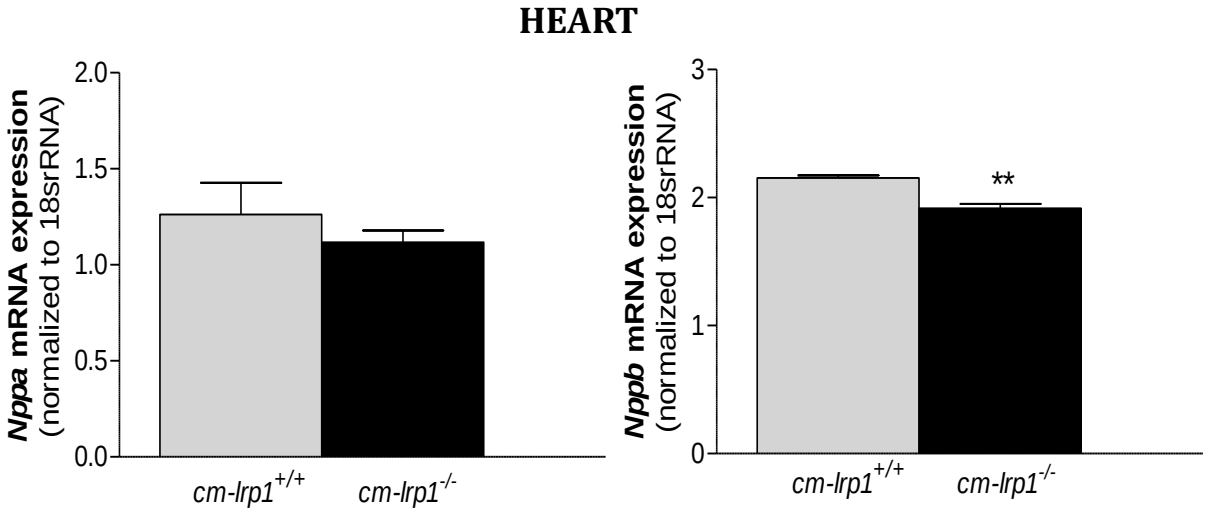

Figure S9. Cardiac Lrp1 deficiency does not upregulate natriuretic peptide A (Nppa) and natriuretic peptide B (Nppb) mRNA expression. Ten week old male mice were treated with Doxycycline Cyclate in drinking *ad libitum* water to assess the conditional inhibition of LRP1 in cardiomyocytes (cm-*Lrp1*$^{-/-}$) and HFD fed for 6 weeks. Real-time PCR measurements of cardiac Nppa and Nppb mRNA levels. Data represent the mean±SEM for 4 to 8 mice per group. ** $p<0.01$ vs cm-*Lrp1*$^{+/+}$ mice. Differences between groups were analysed using Student's t test for independent samples.

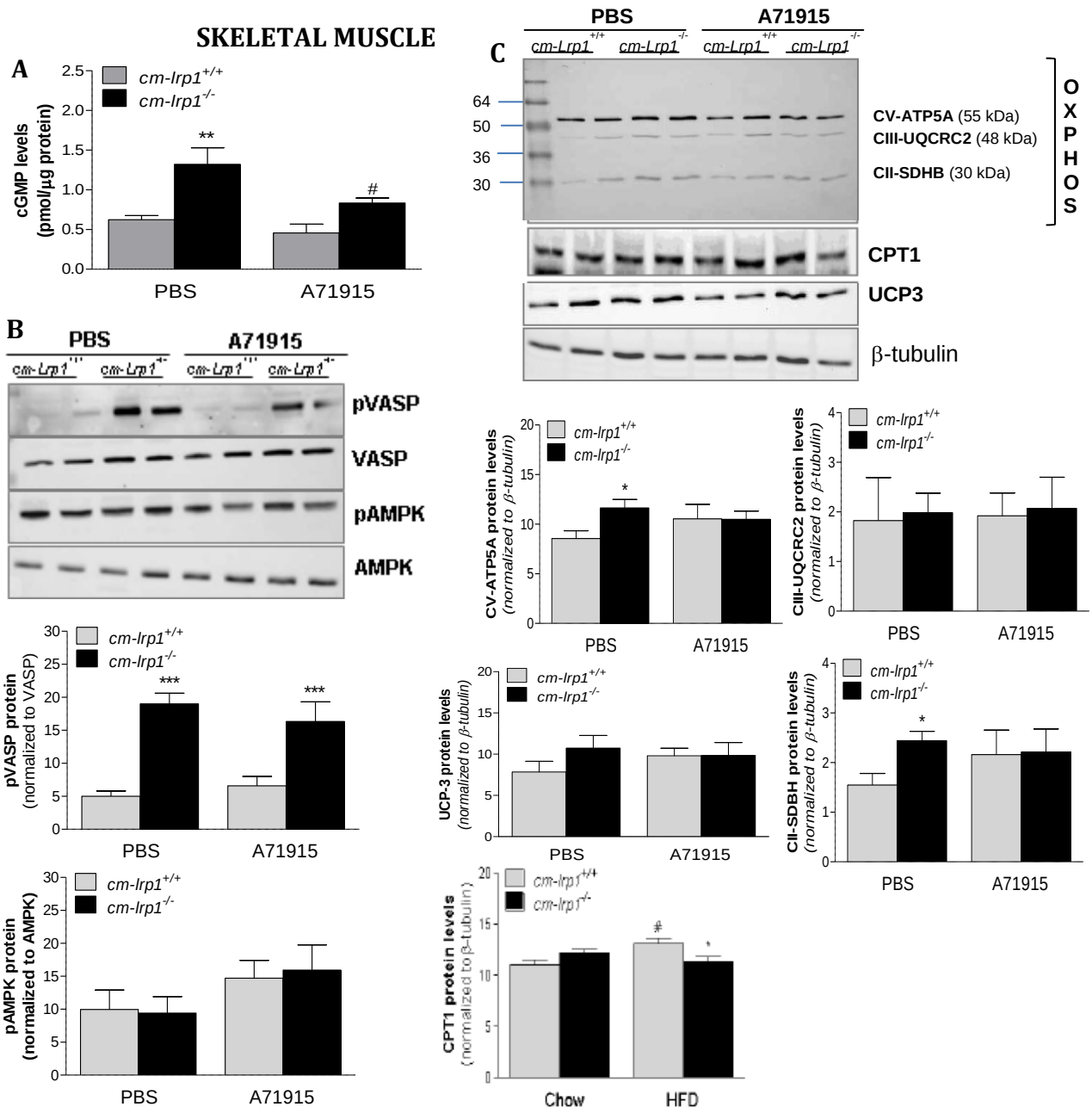

Figure S10. High plasma ANP levels in cm-*Lrp1*$^{-/-}$ mice induce NPRA signaling but not AMPK phosphorylation in the skeletal muscle. Male cm-*Lrp1*$^{-/-}$ and cm-*Lrp1*$^{+/+}$ (control) mice were treated for 6 weeks with Doxycycline Cyclate in their drinking water and then treated with either PBS or the NPRA antagonist A71915 (200 µg/kg in PBS in a final volum of 100 µl) for the last 4 weeks. (A) Levels of cGMP detected by ELISA. (B) Western blot analysis and bar graphs showing the quantification of pVASP, total VASP, pAMPK, total AMPK, and (C) OXPHOS, UCP3 and CPT1 in the skeletal muscle. n=8-10 mice per condition. Data represent the mean±SEM. *p<0.05, ** p<0.01 or *** p<0.005 vs cm-*Lrp1*$^{+/+}$ mica, # p<0.5 vs PBS. Differences between groups were analysed using one-way analysis of variance (ANOVA) followed by a post-hoc Tukey-b test.

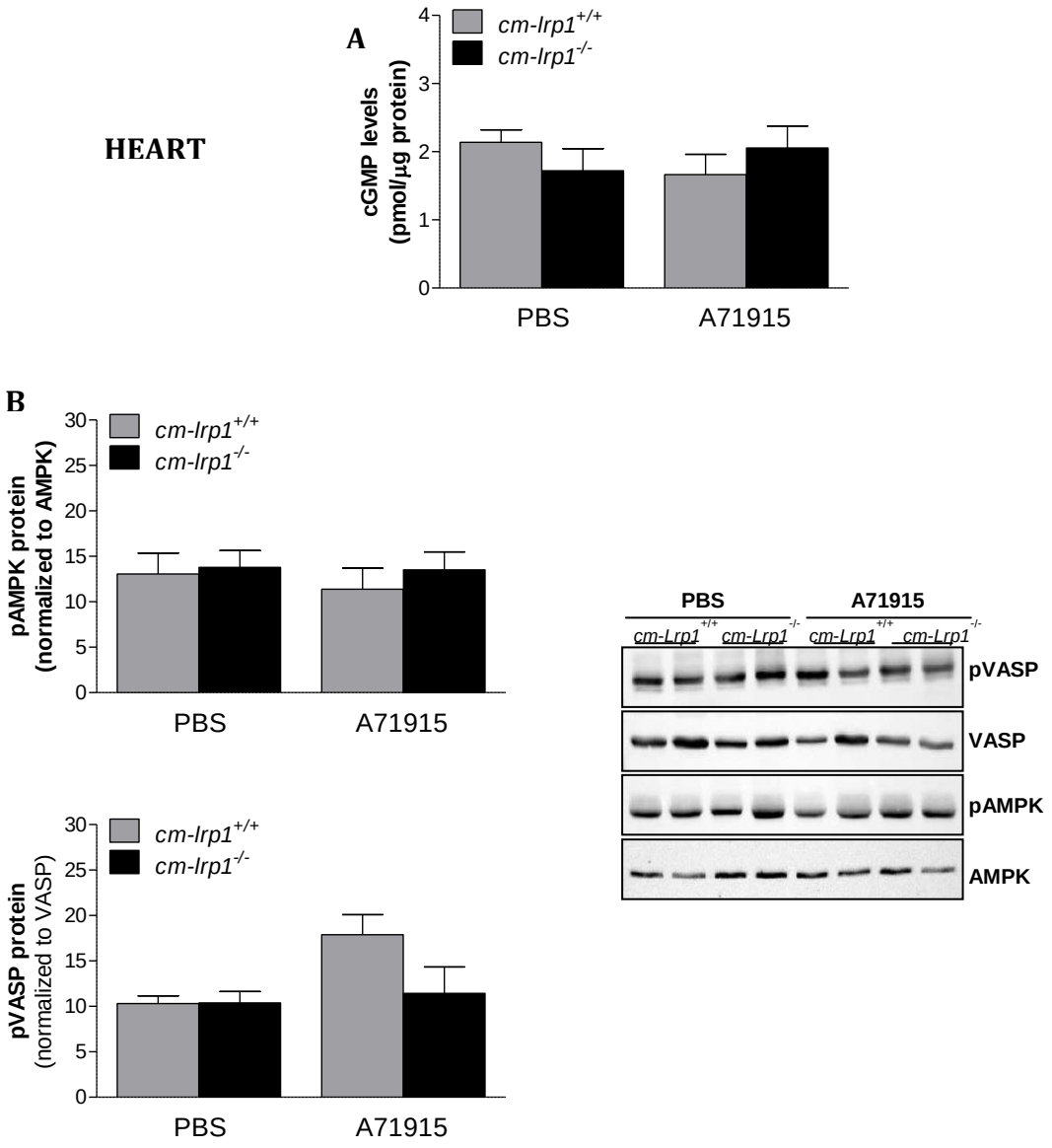

Figure S11. High plasma ANP levels did not induce NPRA signaling in the heart of cm-*Lrp1*$^{-/-}$ mice. Male cm-*Lrp1*$^{-/-}$ and cm-*Lrp1*$^{+/+}$ (control) mice were treated for 6 weeks with doxycycline cyclate in drinking *ad libitum* water and then treated with either PBS or the NPRA antagonist A71915 (200 µg/kg in PBS in a final volum of 100 µl) for the last 4 weeks. (A)Tissue cGMP levels detected by ELISA. (B) Western blot analysis and bar graphs showing the quantification of pVASP, total VASP, pAMPK, total AMPK in the heart. n=8-10 mice per condition. Data represent the mean±SEM.

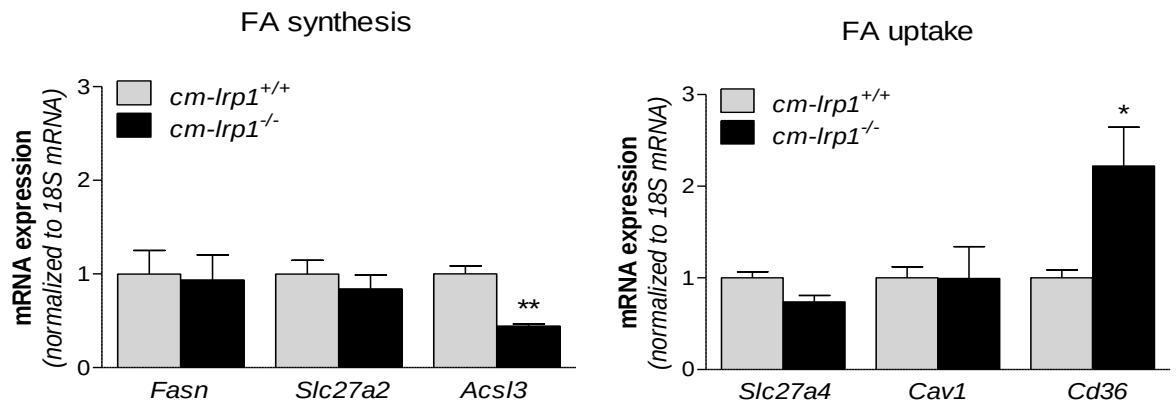

Figure S12. The expression of genes involved in FA uptake was increased in the liver of cm-*Lrp1*$^{-/-}$ mice. Male cm-*Lrp1*$^{-/-}$ and cm-*Lrp1*$^{+/+}$ (control) mice were treated for 6 weeks with Doxycycline Cyclate in drinking *ad libitum* water. After sacrifice, one aliquote of frozen liver was used for RNA extraction and real time PCR analysis. The expression of genes involved in FA uptake and FA synthesis were analyzed. Data represent the mean±SEM. *p<0.05 or ** p<0.01 vs cm-*Lrp1*$^{+/+}$ mice. Differences between groups were analysed using Student's t test for independent samples.

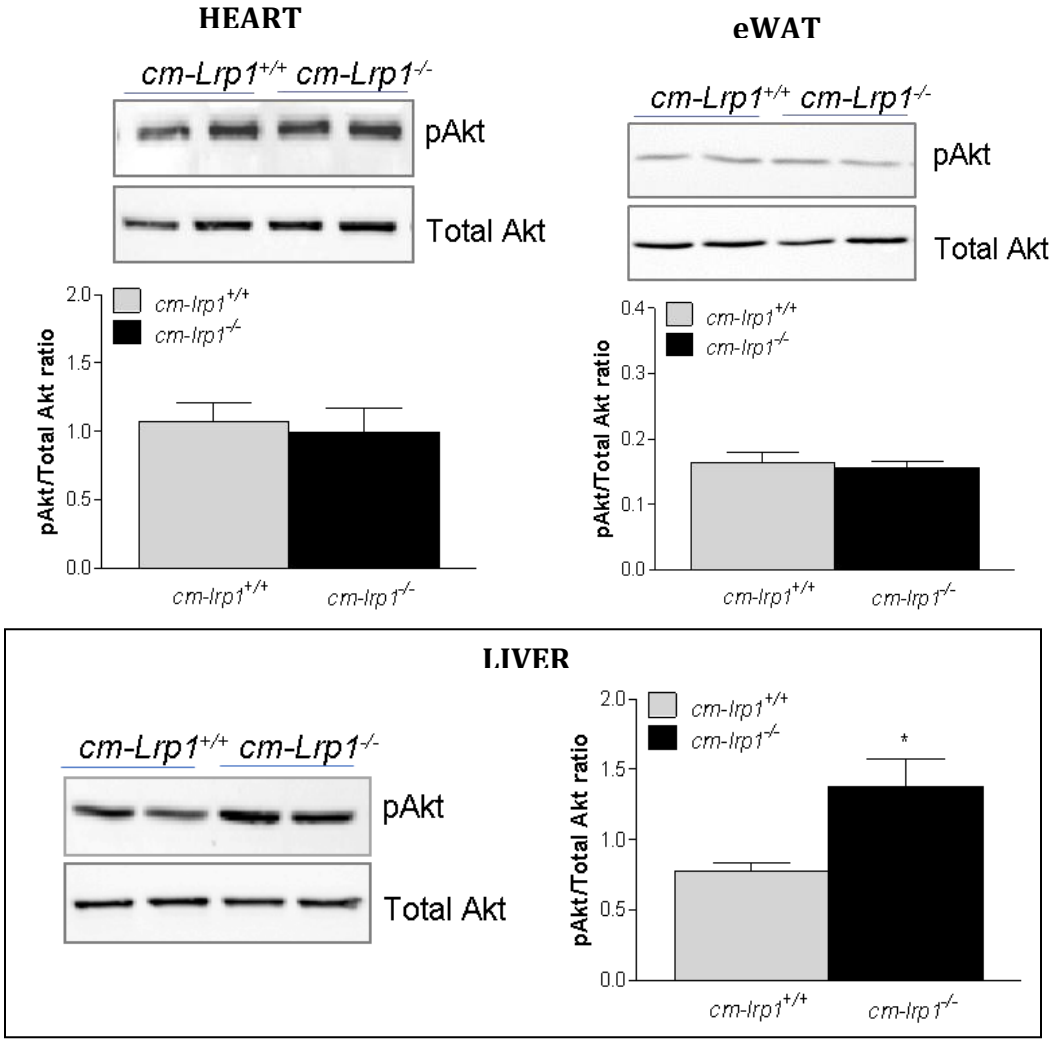

Figure S13. The ratio pAkt/total Akt is increased in the liver of cm-*Lrp1*$^{-/-}$ mice. Male cm-*Lrp1*$^{-/-}$ and cm-*Lrp1*$^{+/+}$ (control) mice were treated for 6 weeks with doxycycline cyclate in drinking *ad libitum* water. After sacrifice, one aliquote of frozen heart, eWAT and liver tissues were used for protein extraction. Representative Western blot analysis showing protein bands and bar graphs for the quantification of pAkt normalized to total Akt. Data represent the mean±SEM. *p<0.05 vs cm-*Lrp1*$^{+/+}$ mice. Differences between groups were analysed using Student's t test for independent samples.

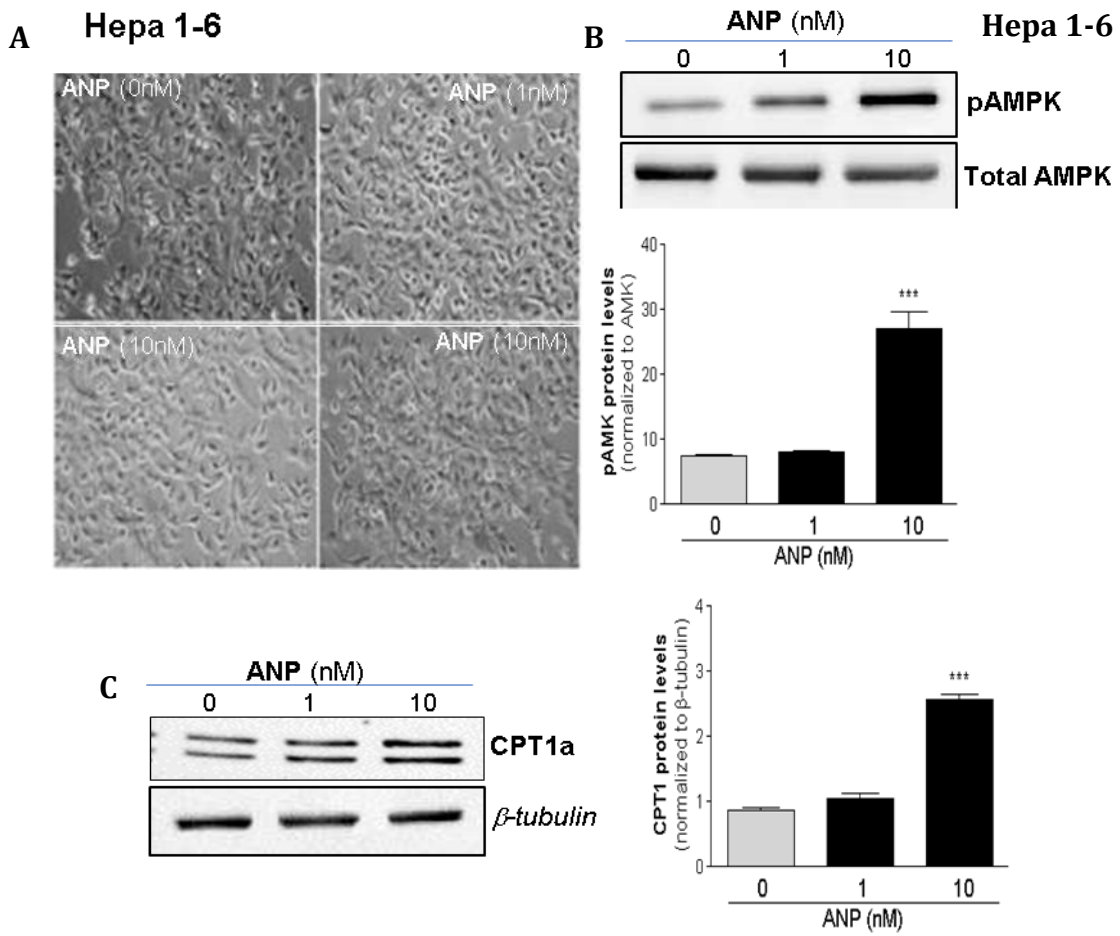

Figure S14. ANP increased the oxidative capacity of hepatocytes. Hepa 1-6 were exposed to increasing ANP concentrations (0, 1, and 10 nM) for 18 hours and then collected in lysis buffer to perform Western blot analysis. (A) Representative optical microscopy image of Hepa 1-6 exposed to different concentrations of ANP. (B) Western blot analysis and bar graphs showing pAMPK/total AMPK ratio and (C) CPT1a protein levels in Hepa 1-6 cells. Data represent the mean±SEM of three experiments performed in duplicate. *** $p<0.005$ vs cells unexposed to ANP. Differences between groups were analysed using Student's t test for independent samples.

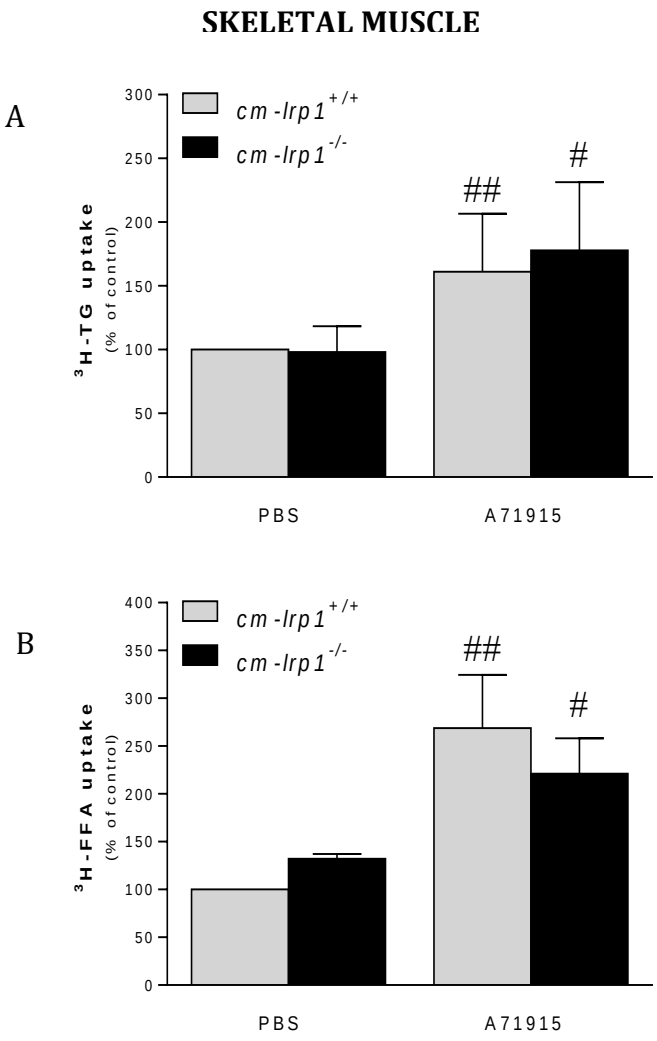

Figure S15. Treatment of control and cm-Lrp1$^{-/-}$ mice with the NPRA antagonist A71915 increases [^{3}H]-triglycerides and [^{3}H]-FFA uptake by skeletal muscle. Mice were treated with doxycycline cyclate in *ad libitum* drinking water to assess the conditional inhibition of Lrp1 in cardiomyocytes (cm-*Lrp1*$^{-/-}$) and were treated with either PBS or the NPRA antagonist A71915 ((200 µg/kg in PBS in a final volum of 100 µl) in conjunction with the HFD diet for 4 weeks. (A) [^{3}H]-triglycerides and (B) [^{3}H]-FFA content of skeletal muscle after 1.5h of injecting mice with a single bolus of 150µL of radiolabeled [^{3}H] olive oil based emulsion. # $p<0.05$ or ## $p<0.01$ versus PBS. Differences between groups were analysed using one-way analysis of variance (ANOVA) followed by a post-hoc Tukey-b test.

Table S1. Oligonucleotides used for mice genotyping (Table 9 of materials and methods section)

	cm-*lrp1*$^{+/+}$	cm-*lrp1*$^{-/-}$	*P*
Cholesterol (mM)	6.69±0.30	7.08±0.28	0.720
Phospholipids (mM)	5.15±0.23	5.52±0.28	0.631
Triglycerides (mM)	0.75±0.08	0.81±0.10	0.958
HDL-cholesterol (mM)	5.71±0.31	5.88±0.21	0.958
HDL-phospholipids (mM)	5.02±0.27	5.17±0.29	0.965

Table S2. Plasma biochemical parameters in cm-*Lrp1*$^{+/+}$ and cm-*Lrp1*$^{-/-}$. Cholesterol, total phospholipids, triglycerides, High Density Lipoprotein (HDL)-cholesterol and HDL- phospholipids were determined as explained in Material & Methods. N=8 per group. Differences between groups were analysed using Student's t test for independent samples.

14 RESULTS: Article 2

IVYSPRING INTERNATIONAL PUBLISHER

Theranostics

2020; 10(7): 3263-3280. doi: 10.7150/thno.37305

Research Paper

Immunization with the Gly[1127]-Cys[1140] amino acid sequence of the LRP1 receptor reduces atherosclerosis in rabbits. Molecular, immunohistochemical and nuclear imaging studies

Olga Bornachea[1,2], Aleyda Benitez-Amaro[1,2], Angela Vea[1], Laura Nasarre[1], David de Gonzalo-Calvo[1,2,3], Juan Carlos Escola-Gil[4], Lidia Cedo[4], Antoni Iborra[5], Laura Martínez-Martínez[6], Candido Juarez[6], Juan Antonio Camara[7], Carina Espinet[8], Maria Borrell-Pages[3,9], Lina Badimon[3,9,10], Joan Castell[8], Vicenta Llorente-Cortés[1,2,3]✉

1. Institute of Biomedical Research of Barcelona (IIBB). Spanish National Research Council (CSIC), Barcelona, Spain.
2. Lipids and Cardiovascular Pathology. Biomedical Research Institute Sant Pau (IIB Sant Pau), Hospital de la Santa Creu i Sant Pau. Barcelona. Spain.
3. CIBER enfermedades cardiovasculares (CIBERcv).
4. Metabolic Basis of Cardiovascular Risk, Biomedical Research Institute Sant Pau (IIB Sant Pau), Hospital de la Santa Creu i Sant Pau. CIBER de Diabetes y enfermedades Metabólicas Asociadas (CIBERDEM), Barcelona. Spain.
5. SCAC, Universitat Autònoma de Barcelona (UAB), Bellaterra, Spain
6. Department of Immunology, Institut de Recerca and Hospital Santa Creu i Sant Pau, Barcelona, Spain.
7. Preclinical Imaging Flatform. Vall dHebron Institute of Research. Barcelona, Spain.
8. Department of Nuclear Medicine, Institut de Diagnòstic per la Imatge (IDI), Hospital General Universitari Vall d'Hebrón, Universitat Autònoma de Barcelona, Barcelona, Spain.
9. Cardiovascular Program ICCC, Institut de Recerca Hospital de la Santa Creu i Sant Pau, Barcelona, Spain
10. Cardiovascular Research Chair, UAB, Barcelona, Spain

✉ Corresponding author: Vicenta Llorente-Cortés, Lipids and Cardiovascular Pathology group leader, IIBB-CSIC,IIB-Sant Pau, Hospital de la Santa Creu i Sant Pau, Sant Antoni Mª Claret, 167, 08025 Barcelona. Phone: +34 935565888, Fax: +34 935565559, E-mail: Cllorente@santpau.cat

Received: 2019.06.04; Accepted: 2019.12.31; Published: 2020.02.10

Abstract

Background: The LRP1 (CR9) domain and, in particular, the sequence Gly[1127]-Cys[1140] (P3) plays a critical role in the binding and internalization of aggregated LDL (agLDL). We aimed to evaluate whether immunization with P3 reduces high-fat diet (HFD)-induced atherosclerosis.

Methods: Female New Zealand White (NZW) rabbits were immunized with a primary injection and four reminder doses (R1-R4) of IrP (irrelevant peptide) or P3 conjugated to the carrier. IrP and P3-immunized rabbits were randomly divided into a normal diet group and a HFD-fed group. Anti-P3 antibody levels were determined by ELISA. Lipoprotein profile, circulating and tissue lipids, and vascular pro-inflammatory mediators were determined using standardized methods while atherosclerosis was determined by confocal microscopy studies and non-invasive imaging (PET/CT and Doppler ultrasonography). Studies treating human macrophages (hMΦ) and coronary vascular smooth muscle cells (hcVSMC) with rabbit serums were performed to ascertain the potential impact of anti-P3 Abs on the functionality of these crucial cells.

Results: P3 immunization specifically induced the production of anti-P3 antibodies (Abs) and did not alter the lipoprotein profile. HFD strongly induced cholesteryl ester (CE) accumulation in the aorta of both the control and IrP groups, and their serum dose-dependently raised the intracellular CE of hMΦ and hcVSMC, promoting TNFR1 and phospho-NF-kB (p65) overexpression. These HFD pro-inflammatory effects were dramatically decreased in the aorta of P3-immunized rabbits and in hMΦ and hcVSMC exposed to the P3 rabbit serums. Microscopy studies revealed that P3 immunization reduced the percentage of lipids, macrophages, and SMCs in the arterial intima, as well as the atherosclerotic extent and lesion area in the aorta. PET/CT and Doppler ultrasonography studies showed that the average standardized uptake value (SUV_{mean}) of the aorta and the arterial resistance index (ARI) of the carotids were more upregulated by HFD in the control and IrP groups than the P3 group.

Conclusions: P3 immunization counteracts HFD-induced fatty streak formation in rabbits. The specific blockade of the LRP1 (CR9) domain with Anti-P3 Abs dramatically reduces HFD-induced intracellular CE loading and harmful coupling to pro-inflammatory signaling in the vasculature.

Key words: LRP1 (CR9), atherosclerosis, LDL, vascular cholesteryl esters, NF-kB, TNFR1, ^{18}F-FDG-PET/CT, Doppler ultrasonography, inflammation

Introduction

Cardiovascular disease (CVD) is the leading cause of death, the dominant cause of which is atherosclerosis, which mainly occurs in the intima of several middle-sized and large arteries. Intimal thickening, occurring during the first step of atherosclerosis, is majorly associated with low density lipoprotein (LDL) retention by the proteoglycans of the arterial intima. Intimal retained LDLs undergo LDL aggregation (agLDL) and fusion which is a key event in the progression of atherosclerosis. [1–3]. AgLDL interacts with the receptor low-density lipoprotein receptor-related protein 1 (LRP1), and LRP1-mediated agLDL uptake causes intracellular cholesteryl ester (CE) loading and foam cell formation in human coronary vascular smooth muscle cells [4–6] and macrophages [7,8].

LRP1 receptor is a signaling mediator that exerts essential cytoprotective and anti-inflammatory functions. Therefore, its potential pathological functions could not be overcome by LRP1 silencing. This strategy will indeed cause deleterious effects in macrophage and VSMC functionality, which both depend on proper LRP1 β-chain signaling [9–11]. LRP1 β-chain is phosphorylated on the distal NPxY motif of the by PDGF-BB mitogenic signaling, and this modulates VSMC proliferation[12,13]. LRP1 signaling is also essential to limit lesional apoptosis and inflammation through the regulation of monocyte recruitment, macrophage apoptosis susceptibility, and efferocytosis [14,15]. In line, it has been thoroughly shown that disabling LRP1 tyrosine phosphorylation causes macrophage intracellular lipid accumulation and the anomalous clearance of apoptotic cells, resulting in accelerated atherosclerosis [16]. In addition to signaling mediated by the LRP1 b chain, signaling induced through the binding of its a-chain to extracellular ligands also seems to be essential for optimal vascular function. The atheroprotective induction of Wnt5a mediated by extracellular TGF-β in macrophages requires LRP1 α chain [17]. Apolipoprotein E-mediated interleukin-1 receptor associated kinase-1 (IRAK-1) signaling that downregulates NF-κB-induced inflammation requires the binding of Apolipoprotein E to LRP1 α chain [18]. The binding of protease-inhibitor complexes to LRP1 α chain inhibit the NF-kB inflammatory response, and induce a cytoprotective effect through phosphorylation of Akt and ERK1/2 protein kinases [19–21]. NF-kB is a key player involved in the development and progression of inflammation in different tissues, including the vasculature [22]. A vascular mediator in NF-kB activation is tumor necrosis factor-alpha receptor -1 (TNFR1), which enhances arterial wall chemokine and adhesion molecule expression, as well as smooth muscle cell proliferation and migration in atherosclerosis [23].

We have previously identified one peptide sequence (P3: H-GDNDSEDNSDEENC-NH2) (Gly 1127–Cys1140) in the CR9 domain of LRP1 that is crucial for its interaction with aggregated LDL [24]. We showed that polyclonal antibodies generated against P3 sequence (Anti-P3 Abs), located in the CR9 domain, efficiently blocked hcVSMC-foam cell formation. It is important to note that the CR8/CR9 tandem is the only pair of consecutive CR modules from the LRP1 cluster II that shows only negligible affinity for serpins such as plasminogen activator inhibitor-1 (PAI-1) and protease nexin 1 (PN1) [25]. This makes CR9 an ideal target to counteract LRP1-AgLDL interactions without altering the binding of other essential ligands, such as protease-inhibitor complexes, which are key inhibitors of pro-inflammatory signals.

On the basis of these previous results, we considered a challenge within the cardiovascular field to study the anti-atherosclerotic efficacy of anti-P3 antibodies in a translational *in vivo* model, similar to humans in the cholesterol-carried lipoprotein profile. In the rabbit model of HFD-induced atherosclerosis, cholesteryl esters are mainly carried by ApoB-100 lipoproteins and there is an elevated participation of SMCs in fatty streak lesions [26]. In addition, this model has been previously validated to study the effects of HDL on fatty streak formation and evolution [27] as well as to study vascular inflammation by the mainstay imaging technique ^{18}F-FDG/PET [28].

The aim of this work was to study the potential therapeutic relevance of a LRP1 (CR9)-specific blockade with anti-P3 Ab to counteract HFD-induced atherosclerosis. Our results showed that anti-P3 antibodies reduced HFD-induced cholesteryl ester accumulation and pro-inflammatory signaling in the aorta. The potent anti-inflammatory efficacy of anti-P3 Abs allowed for the corroboration of the treatment's efficacy via non-invasive imaging techniques, such as ^{18}F-FDG/PET and Doppler ultrasonography, which provided a high translational impulse to this innovative, anti-atherosclerotic, potentially therapeutic tool.

Methods

Peptide Synthesis and conjugation

The P3 peptide used to immunize rabbits contained the following sequence GDNDSEDNSDEENC corresponding to the amino acids 1127 to 1140 located in LRP1 cluster II (domain CR9) [24]. The P3 sequence corresponds to an area of high homology

between human and rabbit LRP1, with the difference that the asparagine (N) in humans was replaced by a serine (S) in the rabbit protein. In addition, the amino acid C^{1148} in the rabbit sequence (GDNDCEDNSDEE-NC) was replaced by S to achieve greater peptide immunogenic effectiveness. The irrelevant peptide (IrP) has the same sequence than P3 but with amino acids in D-enantiomer configuration. Both peptides were synthesized by the Laboratory of Proteomics & Protein Chemistry, Department of Experimental & Health Sciences, Pompeu Fabra University, by the solid-phase method using a Prelude peptide synthesizer (Protein Technologies, Inc.). Peptides were purified by high-performance liquid chromatography (HPLC, Waters 600) using UV detection at 254 nanometers (Waters 2487) and characterized by mass spectrometry (Applied Biosystems 4700 Proteomics Analyser).

Peptides were conjugated to the transporter molecule Keyhole limpet haemocyanin (KLH) for immunizations and with bovine serum albumin (BSA) for ELISAs. The conjugation of peptide to KLH and BSA (Sigma, St. Louis, MO) was performed as previously described [29]. Peptide–KLH conjugates were used for rabbit immunization and peptide-BSA conjugates for substrate in the immunoassay ELISA to detect specific anti-P3 Abs in the rabbit serum.

Animal model

Thirty New Zealand White (NZW) rabbits from the San Bernardo Farm animal centre (Navarra, Spain) weighing 1.8-2 kg (6-7 months-age) were used in this study. Rabbits were housed in a Tecniplast R-Suite cage with a surface area of 4.264 cm2. Housing temperature was maintained at 21°C, relative humidity ranged between 40-60%, and the light period was 12 hours a day. All animals had food and water *ad libitum*. Experimental procedures were approved by the Ethics Committee of Animal Experimentation of the Vall d'Hebrón Institute of Research with registration number 46/17, and performed in accordance with Spanish legislation and also with the European Union directives (2010/63/ EU).

Animals were fed the "chow" R-01 diet from Granja San Bernardo with the following formulation: 17.3% protein, 16.7% fibre and 3% fat; or HFD TD.88137 (42% from fat) from ENVIGO. Animals were acclimated for one week before the first immunization and immunized with a primary injection and four reminder doses (R1-R4) of IrP (irrelevant peptide) (IrP group; N=12) or P3 (P3 group; N=15) conjugated to the carrier every 21 days. An additional group of rabbits was injected with carrier alone (control group; N=3). The four doses of IrP or P3 antigen conjugated with KLH (or carrier) were administered subcutaneously (138 μg/kg, maximum volume 150 μL) every 21 days. For the first immunization, IrP or P3-KLH peptides were emulsified in Freund's Adjuvant Complete, and the rest of the immunizations were done using IrP or P3-KLH conjugated in Freund's Incomplete Adjuvant (both from Sigma Aldrich). During the immunization period, the animals were fed a chow diet.

Starting at the R4 time point, IrP and P3-immunized rabbits were randomly divided into normal diet group and high-fat diet (HFD)-fed group. Twelve rabbits (N=6 Irp-injected and N=6 P3-injected) continued fed on the chow diet, whereas fifteen rabbits (N=6 IrP-injected and N=9 P3-injected) and one rabbit control group (N=3 injected with carrier alone) received HFD for 30 days (supplemental Figure S1). In pre- and post-diet time points, animals were weighed, serum levels of specific anti-P3 Abs were determined by ELISA, and animals were submitted to PET-CT and carotid Doppler ultrasonography imaging studies. After imaging studies, animals were euthanized and aortas, carotids and liver were dissected and processed for molecular, confocal and immunohistochemical studies.

Determination of circulating lipids and the lipid content in lipoproteins

Total plasma cholesterol, choline-containing phospholipid, triglyceride and NEFA levels were enzymatically determined using commercial kits adapted to a COBAS 501 autoanalyzer (Roche Diagnostics, Rotkreuz, Switzerland). VLDL, LDL and HDL lipoproteins were isolated by sequential ultracentrifugation at 100,000 g for 24 h at a density of 1.006, 1.019-1.063 and 1.063-1.21 g/ml, respectively, using an analytical fixed angle rotor (50.3, Beckman Coulter) [30]. The composition of each lipoprotein, including total and free cholesterol, triglycerides and phospholipids, was determined by commercial methods adapted to the COBAS 501 autoanalyzer. Lipoprotein protein concentrations were determined by the bicinchoninic acid method (Termo Scientific, Rockford, IL). Lipoprotein composition was used to calculate the total mass of each lipoprotein.

Detection of specific antibodies

We standardized immunoELISAs to detect specific antibodies against P3 peptides. Briefly, all sera were analysed using 96-well polystyrene plates (Ref 442404 Maxisorp, NUNC, Labclinics, Spain) coated with peptide-BSA and BSA as a control for the detection of unspecific antibodies. ELISA plates were incubated with several serum dilutions for 90 minutes, and after washes, anti-rabbit IgGs conjugated to peroxidase (Ref 170-6515, BioRad,

Spain) was added to detect the antigen-antibody complexes. ELISA was revealed using OPD substrate (Ref P9187, Sigma Aldrich, Spain), and the absorbance was read in a Multilabel reader Victor3 (Perkin Elmer, Turku, Finland) at 450 nm. The absorbances obtained were adjusted to a 4PL curve to calculate the IC50. The parameter 1/IC50 was taken as the antibody titer.

Isolation of Rabbit Aortic Smooth Muscle Cells

Rabbit aortic smooth muscle cells **(**rSMCs) were obtained by gentle scraping of the medial layer of New Zealand White rabbit aortas after endothelial layer removal. Cells were incubated at 37°C in a humidified atmosphere of 5% CO^2 in Ham's F12-DMEM (8:2) supplemented with 20% foetal calf serum, 100 U/mL penicillin and 0.1 mg/mL streptomycin. To maintain exponential growth, cells were subcultured by trypsinization and seeded at a density of 10 000 cells/cm^2. rSMCs were identified by their growth behaviour, morphology, and immunofluorescence. Immunocytochemical identification of cells was performed by specific monoclonal antibodies for α-smooth muscle cell and von Willebrand factor. Cells were fixed with ice-cold methanol at 20°C for 5 minutes. A solution of BSA at 1% in PBS was used as a blocking agent. Monoclonal antibodies against LRP1 (Fitzgerald, 10R-L107c) and polyclonal antibodies obtained from P3-immunized rabbits were diluted in PBS/1% BSA/0.01% Triton X-100. Finally, FITC-conjugated goat anti-mouse IgG and FITC-conjugated goat anti-rabbit IgG were used as secondary antibodies. Images were captured and analysed on a Leica inverted fluorescence confocal microscope (Leica TCS SP2-AOBS).

Isolation of human macrophages primary cultures

Human macrophages (hMΦ) were obtained from buffy coats of healthy blood donors. Cells were applied on 15 ml of Ficoll-Hypaque and centrifuged at 300 g for 1 hour at 22°C, with no brake. Mononuclear cells were obtained from the central white band of the gradient, exhaustively washed in Dulbecco's phosphate buffer saline, and suspended in RPMI medium (Gibco) supplemented with 10% human serum AB (Sigma). Cells were left 7 days in culture and allowed to differentiate into macrophages by changing the cell culture media (RPMI supplemented with 10% human serum AB, 100 units/ml penicillin and 100 µg/ml streptomycin) every 3 days.

Culture of coronary human vascular smooth muscle cells

Human coronary vascular smooth muscle cells (hVSMC) were obtained from the medium layer isolated from macroscopically healthy coronary artery segments collected from patients undergoing cardiac transplantation at Hospital de la Santa Creu i Sant Pau (Barcelona, Spain). hVSMCs were isolated by a modification of the explant technique, as described previously [4–6]. The explants were incubated at 37 °C in a humidified atmosphere of 5% CO2. After 1week, the cells start to migrate from the explants and proliferate, covering the floor of the culture well. The medium was exchanged every 3 days after the onset of cell outgrowth; a significant outgrowth was reached after 10 days. Tissue fragments were collected with forceps and placed in a new dish with fresh medium. The cells that remained in the dish were cultured until confluence. For characterization, cells were seeded in cover-slips and grown to confluence. Cell quiescence was induced by maintaining the cell culture for 24 h in a medium with 0.2% FCS or for 48 h in a medium with 0.4% serum. All experiments used serum-deprived cells between passages 4 and 6; VSMCs at these passages appeared as a relatively homogeneous population, showing a hill-and-valley pattern at confluence. Western blot analysis for specific differentiation markers revealed high levels of-actin (45 kDa) and calponin (33 kDa). Cell monolayers were grown in medium 199 supplemented with 20% FBS, 2% human serum, 2 mmol/literL-glutamine, 100 units/ml penicillin G, and 100g/ml streptomycin. The study was approved by the Institutional Ethics Committee at Hospital de la Santa Creu i Sant Pau and conducted in accordance with the Declaration of Helsinki.

Treatment of hMΦ and hcVSMC with rabbit serums

Quiescent hMΦ and hcVSMC were exposed to increasing concentrations of serum (0.25%, 0.5% and 1%) from the different rabbit groups for two hours. In some experiments, quiescent hMΦ were exposed to aggregated LDL (100 µg/mL, 2 hours), generated as previously described [4–6] in the presence of increasing concentrations (1%, 5% and 10%) of chow serum from the different group of rabbits. Following the serum incubation period, cells were exhaustively washed and harvested in NaOH 0.1 M or lysis buffer for lipidic and Western blot analysis.

^{18}F-FDG PET/CT and image analysis

An injection of ^{18}F-FDG (0.5 mCi/kg) was administered through a catheter in the marginal vein of the ear of each animal. The image study was performed on a Siemens Biograph mCT S64 hybrid PET/CT instrument. We carried out an angiographic PET/CT study at 120 and 180 minutes, which allowed the anatomical and metabolic localization of the

studied structures. The CT and PET studies were recorded for 5-6 seconds and 15 minutes, respectively.

Acquisition parameters

Thoracic-abdominal imaging studies of the heart, great vessels and abdominal aorta in only one bed position (15 minutes) were performed at the maximum resolution of the PET/CT equipment (1.5 mm in the PET and 0.5 mm in the CT).

CT characteristics (attenuation correction)

AngioCT characteristics: An angiographic study was performed before PET acquisition. VISIPAQUE™ (iodixanol) contrast was used and injected at 0.7ml/sec.

Image analyses

The co-registration of both studies (PET and CT) was automatically carried out by the Software of the Siemens Biograph mCT S64 hybrid PET/CT equipment. PET/CT data were displayed in axial planes on a Syngovia (Siemens) workstation. Mean standard uptake value (SUV)s were recorded on contiguous axial slices of the aorta superior, central and inferior (one ROI in each area).

The corresponding SUV units were calculated in each animal. These units allow the comparison and standardization of the emission values of each structure studied, including decay correction between dual time-point images. PET/CT outcome variables were the maximum and averaged SUVs.

Ultrasonography

Ultrasonography was performed with a Mindray M7 device (Shenzen Mindray Bio-medical Electronics, Shenzen, PRC) and a 7.5 MHz central frequency lineal probe. All animals were anaesthetized with propofol and maintained with iIsofluorane (2-3% in fresh air) to respect their welfare and to avoid tachycardia or stress-induced pulse frequency.

Ultrasonographic exams were performed for carotid arteries. The morphology of carotid arteries was measured using B mode images, followed by colour and pulsed wave Doppler analysis to check the blood flow. The specific location at the internal and external carotid division was selected following previously published reference [31], assuming that this location is a target for lipid deposits.

The parameters included were systolic and diastolic velocities, as well as arterial resistance index (ARI). ARI=(Systolic velocity-Diastolic velocity)/ Systolic velocity). In all the ultrasonographic parameters, three different measurements were performed in each image, and the mean value was used for parameter calculation. The software used for measurements was that included in the ultrasound device, and mathematical calculations were obtained in Excel format.

Preparation of histological sections and immunohistochemistry

At necropsy, the aorta, carotids and liver were dissected. The aorta was cleaned from external fat and divided into two sections: thoracic aorta, from the aortic arc to the hepatic aorta, and abdominal aorta, from the hepatic aorta to the bifurcation of the iliac aortas (Supplemental Figure S2). As shown in Supplemental Figure 2, the first 2 cm section of the thoracic aorta was opened by a longitudinal incision. The rest of the aorta was divided into 1cm pieces. Alternatively, each piece was frozen and sectioned for histological and molecular studies. Carotids were frozen and kept at -80 ^{o}C for further analysis of lipid composition.

Longitudinally open sections of aorta were fixed in 4% paraformaldehyde-PBS solution for fatty streak detection and quantification using Herxheimer's staining method. Samples for immunohistochemistry were transversally cut with a cryostat in serial sections of 5 μm and mounted in gelatinized slides. Transversally cut sections were also stained with Herxheimer's staining method to detect lipids. Images were captured with an Olympus Vanox AHBT3 microscope, and digitalized using a Sony 3CCD camera.

Confocal microscopy studies

Arteries were dissected, immersed in cell maintenance media, examined under low magnification with a zoom stereo microscope and classified according to the criteria of the American Heart Association (AHA). At this point, samples were used for immunohistochemistry or were stained with Masson's trichromic to identify vascular structures. Serial sections (5 μm thick) were immunostained with Phalloidin-488 (to identify smooth muscle cells), and RAM11 (Dako M063301-8), NF-kB p65 (C22B4) (Cell Signalling; #4764) and TNFR1 (MyBiosource MBS8409 39) with secondary antibody Alexa Fluor 633 IgG). Images were recorded on a Leica inverted fluorescence confocal microscope (Leica TCS SP2-AOBS, Germany). Arteries were viewed with HCX PL APO 20x/0,75 IMM Corr CS2 objective. Fluorescent images were acquired in a scan format of 1024 x 1024 pixels and were processed with the Leica Standard Software TCS-AOBS. Controls without primary antibody showed no fluorescence labelling.

Image analysis

Image analysis was performed using Visilog 5.4 software (Noesis, France) to quantify the extent of the

lesions, and the results were given as the percentage of the total aortic area covered by lipid. Images were captured with a Vanox AHBT3 microscope (Olympus) and digitized using a DXC-S500 camera (Sony) at x200 magnification. Six different sections were analysed per animal, and six animals were analysed per group. The results were shown as the mean ± SD.

Western blotting analysis

Blots were incubated with antibodies against mouse LRP1 (β-chain, clone 5A6 RDI-PRO61066), SREBP-2 (Santa Cruz Biotechnology; sc-13552), phospho-NF-kB p65 (Cell Signaling; #3039), NF-kB p65 (C22B4) (Cell Signalling; #4764) and TNFR1 (My-Biosource MBS840939) Protein extracts (10 µg) were loaded, resolved on 12% SDS-PAGE and transferred to nitrocellulose membranes (BioRad). Signal detection was carried out with the ECL immunoblotting detection system (GE Healthcare) and the results were quantitatively analyzed using Chemidoc (BioRad). Equal protein loading in each lane was verified by incubating blots with monoclonal antibodies against β-actine (Cell Signaling Technology, Inc, #3700S).

Lipid analyses and determination of aortic, carotid and hepatic neutral lipid content Aorta (10 mg), liver (2.5 mg) and the whole extracted carotid were homogenized in NaOH 0.1 M. Lipids were extracted and quantified as previously described [4–6]. Cholesteryl esters (CE) triglycerides (TG) and free cholesterol (FC) were analysed by thin-layer chromatography (TLC). The organic solvent was removed under an N_2 stream, the lipid extract was redissolved in dichloromethane, and one aliquot was partitioned by TLC which was performed on silica G-24 plates. Different concentrations of standard (a mixture of cholesterol, triglycerides and cholesterol palmitate) were applied to each plate. The chromatographic developing solution was heptane/diethylether/acetic acid (74:21:4, vol/vol/vol). Spots corresponding to CE and FC were quantified by densitometry against the standard curve of cholesterol palmitate and cholesterol, respectively, using a computing densitometer.

Statistical analysis

The results were expressed as the mean ± SD. Differences between study groups were analysed using one-way analysis of variance (ANOVA) followed by a *post-hoc Tukey b*-test. In the image analysis, Student's *t*-test for paired samples was used to compare differences between baseline and HFD feeding PET/CT parameters in each experimental group. The statistical software R (www.r-project.org) was used for all statistical analyses. Differences were considered statistically significant when $P < 0.05$.

Results

P3- Immunization induces the production of anti-P3 antibodies in rabbits

ELISA analyses showed the absence of specific antibodies against P3 in the serum of both the control (Figure 1A) and IrP-injected groups (Figure 1B) as well as its presence in P3-immunized rabbits serum (Figure 1C). Anti-P3 Abs levels were maintained in P3-immunized rabbits serum throughout the entire diet period. Previous studies focusing on the functional evaluation of anti-P3 Abs showed their efficacy in reducing foam cell formation through the blockade of the LRP1/agLDL interaction [24]. Here, confocal microscopy studies revealed that Abs in the P3-immunized rabbits serum hybridized with the LRP1 with a similar efficiency as commercial anti-LRP1 Abs in rabbit aortic vascular smooth muscle cells (rSMCs) (Figure 1D). None of the sera showed an unspecific response when only BSA without a conjugated peptide, was used as an antigenic source in ELISA (data not shown).

Anti-P3 Abs counteract HFD-induced atherosclerosis in rabbits

En face preparations of the thoracic aorta showed that HFD feeding in rabbits induced a high percentage of occupation of the aortic vasculature with fatty streak lesions in the control and IrP groups but not in the P3-immunized group (Figure 2A and 2B). Immunohistochemistry studies revealed a high percentage of lipids and macrophages in the arterial intima of control and IrP-immunized rabbits that was strongly reduced in P3-immunized rabbits (Figure 2C). Finally, confocal microscopy studies showed an elevated presence of α-actin positive cells in the intima of the initial lesions in control and IrP groups that was almost completely absent in the P3 group (Figure 3A). Both VSMC (falloidin positive cells in red) and macrophages (RAM11 positive cells in green) coexist in the intimal thickening of initial atherosclerotic lesions (Figure 3B). Taken together, these results demonstrate that anti-P3 Abs limit monocyte recruitment and VSMC migration, thus preventing early atherosclerotic formation in rabbits.

Anti-P3 Abs reduce cholesteryl ester accumulation and pro-inflammatory signals induced by HFD in the vasculature of rabbits without altering serum lipid levels or the lipoprotein profile

Circulating levels of cholesterol, phospholipid and NEFAs, but not triglycerides, were strongly higher in HFD- compared to chow fed rabbits, but there were no differences in P3 compared to control

groups (Suplemental Figure S3). VLDL, LDL, or HDL lipoprotein masses and triglyceride (TG), phospholipid (Ph), free cholesterol (FC), cholesteryl esters (CE) and protein levels in lipoprotein fractions were similar among the three groups (Figure 4). These results clearly indicate that P3 immunization did not alter the plasma lipid levels and that, in rabbits, cholesteryl esters are mainly carried by LDL and VLDL lipoproteins in all rabbit groups. There were no differences on weight gain according to diet or between groups (supplemental Figure S4).

Consistent with the high impact of HFD on the VLDL and LDL cholesteryl ester content, HFD increased CE accumulation to a much higher extent in the aorta of control and IrP groups than in the P3-immunized group (Figure 5A). There were no differences in the low TG or FC content in the vasculature between groups. In the liver, HFD strongly increased CE, TG and FC content with no differences between the groups (Figure 5B).

Molecular studies have shown that HFD increased LRP1 levels in the aorta (Figure 6A,B), as previously shown in this and other models by the group [4,32]. The upregulatory effect of HFD on LRP1 was not observed in the aorta of P3-immunized rabbits, confirming the vascular LRP1 upregulation by cholesteryl esters in this particular experimental setting.

Molecular studies combined with confocal studies have shown that HFD raises TNFR1 (Figure 6A,C,D)and NF-kB (p65) (Figure 6A,E,F) protein levels in the aorta of the control and IrP groups but not in the P3-immunized group. These results indicate that anti-P3 are highly efficient inhibiting cholesteryl ester accumulation and pro-infammatory signaling in the vasculature of rabbits.

HFD serum from the P3-immunized rabbits, different from that of the control and IrP-immunized rabbits, failed to induce intracellular cholesteryl ester accumulation and pro-inflammatory signaling in human macrophages and human coronary vascular smooth muscle cells

The treatment of human macrophage **(**hMΦ**)** and human coronary vascular smooth muscle cell

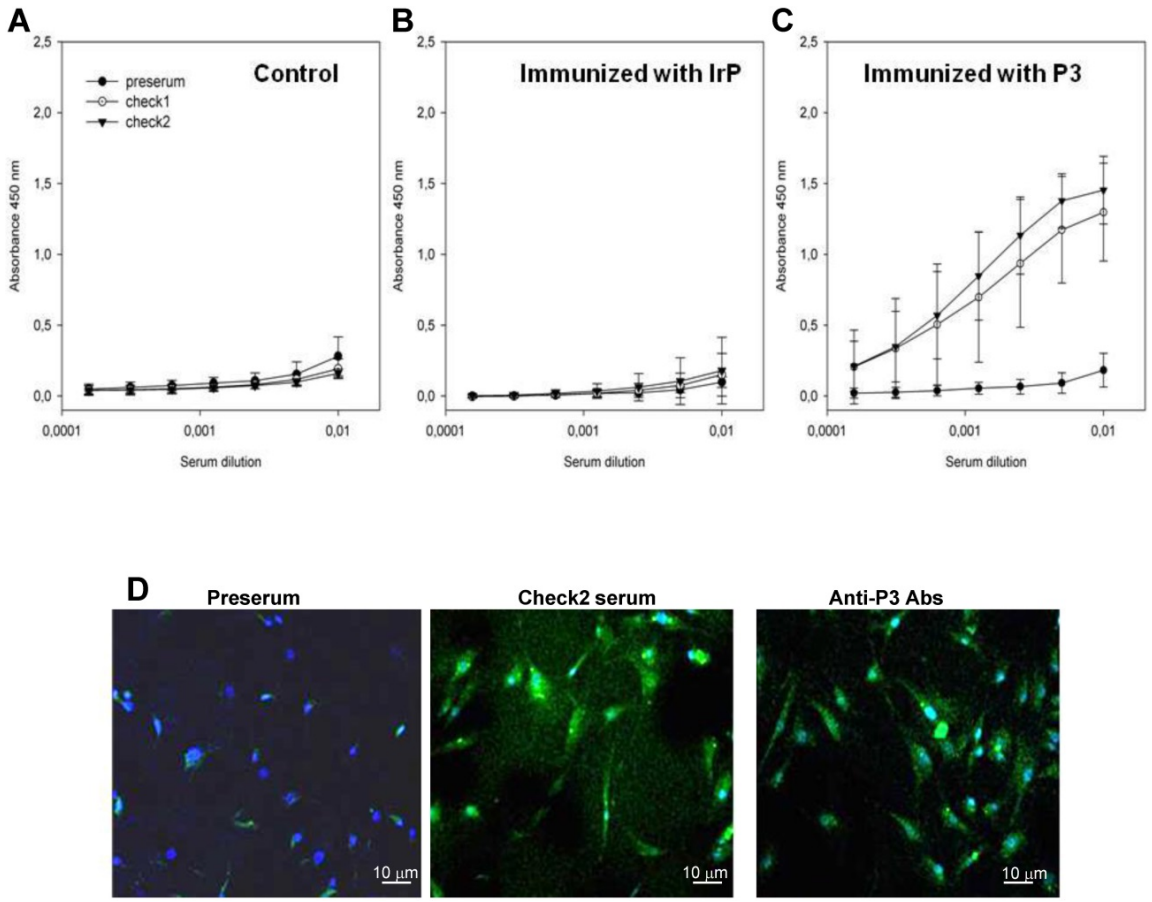

Figure 1. P3 immunization raises serum levels of specific anti-P3 antibodies. (**A**) Graphs showing the results of standardized enzyme-linked immunosorbent assay (ELISA) in pre-serum and serum at the check points (Check1 and Check2) from control (**A**), IrP- (**B**) and P3-treated rabbits (**C**) against P3-BSA used as antigenic source. Results are shown as mean±SD. Control (N=3); IrP (N=12); P3 (N=15) (**D**) Confocal images of rabbit SMCs exposed to serum from P3-treated rabbits (middle panel) or to commercial anti-LRP1 (right panel).

(hcVSMC) with chow serum from the control, IrP or P3 groups (1%, 2 hours) failed to increase intracellular cholesteryl ester content in hMΦ (Figure 7A) and hcVSMC (Figure 8A). In contrast, treatment of cells with HFD serum (1%, 2 hours) from the control and IrP groups (but not the P3 group) dramatically raised the intracellular CE content in hMΦ (Figure 7A) and hcVSMC (Figure 8A). HFD serum from control and IrP groups (but not the P3 group) dose-dependently raised the intracellular CE content of both hMΦ and hcVSMC (supplemental Figure S5). Treatment with chow serum from P3-immunized rabbits but not from control or IrP-injected rabbits dose-dependently reduced intracellular CE accumulation in hMΦ exposed to aggregated LDL (100 µg/mL, 2 hours) (supplemental Figure S6).

Concurrently with HFD serum-induced intracellular CE accumulation, LRP1 protein levels were augmented while those of sterol regulatory element binding protein 2 (SREBP-2) decayed in hMΦ and hcVSMC exposed to (control and IrP)-HFD serums (1%, 2 hours) but not in cells exposed to P3 serum under the same experimental conditions (Figure 7B,C,D and 8B,C,D respectively). These results are in line with the capacity of intracellular cholesteryl esters to stimulate LRP1 transcription through SREBP-2 downregulation previously described by our group [4,33,34]. There were no differences in LRP1 and SREBP-2 protein levels between cells exposed to chow serum from the different groups.

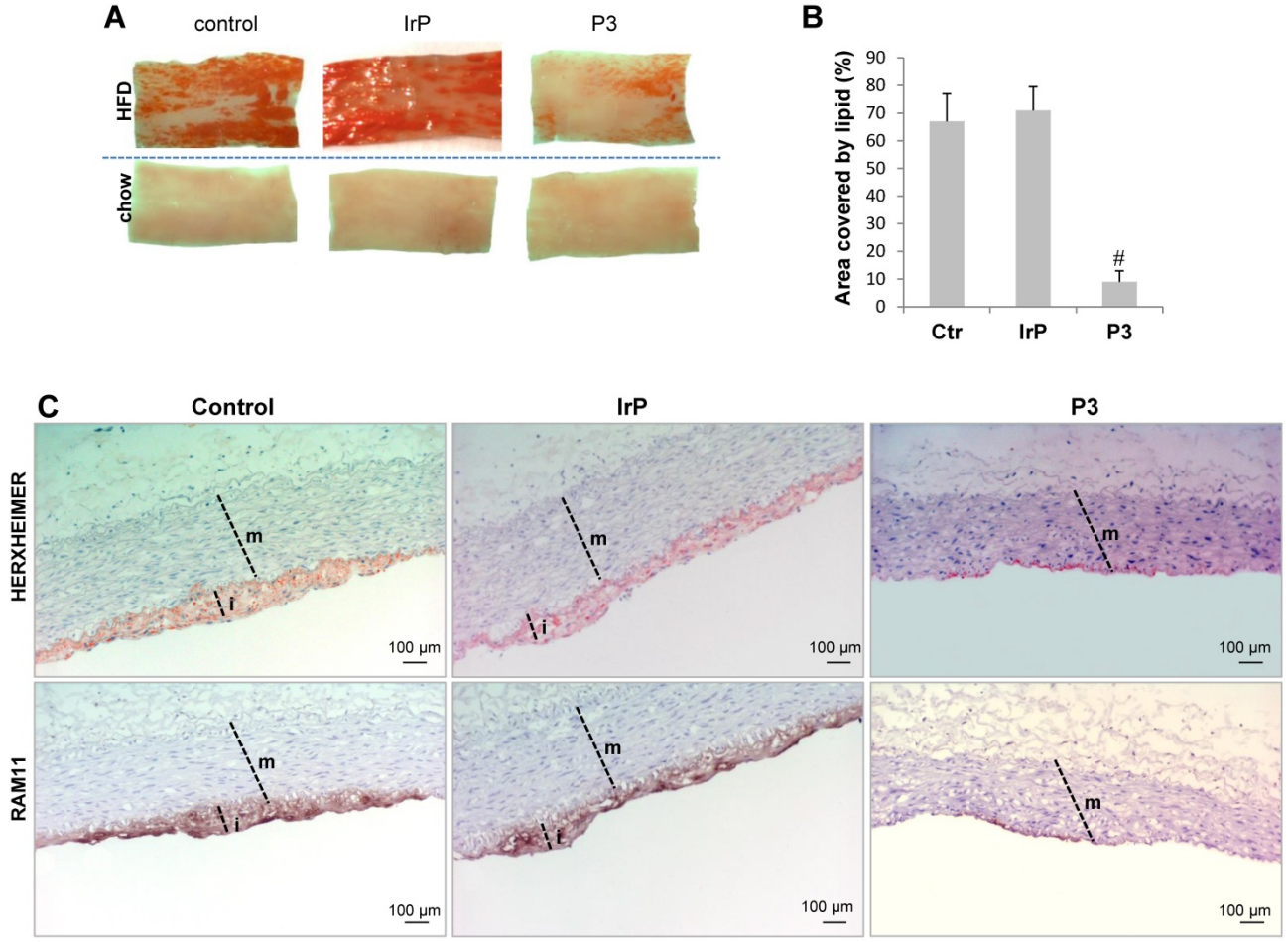

Figure 2. P3 immunization reduces HFD-induced atherosclerotic burden. (**A**) Representative images of longitudinally open sections of aorta stained with Herxheimer in control, IrP and P3-immunized rabbits fed either chow or HFD. (**B**) Graph showing quantification of atherosclerotic burden in HFD-fed rabbits from control (N=3), IrP (N=6) and P3 (N=9). Results are shown as mean±SD of 8 aortic sections/rabbit. #P<0.005, P3 *versus* control and IrP groups. (**C**) Representative immunohistochemical images of lipid and macrophage staining in cross-sections of aortas from control and P3-immunized rabbits, both on HFD m: media; i: intima.

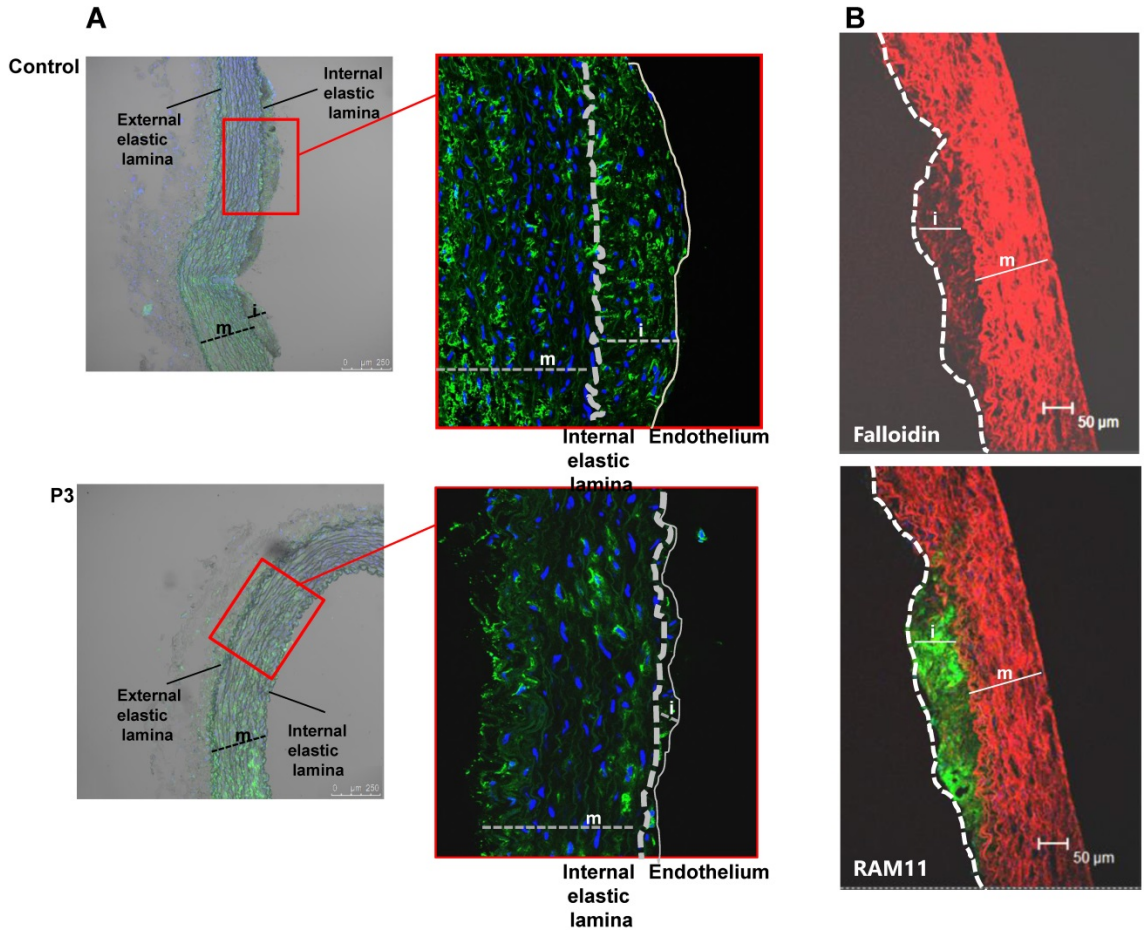

Figure 3. P3 immunization reduces HFD-induced SMC accumulation in the arterial intima. Representative confocal microscopy images of SMCs detected with anti-a-actin antibodies in cross-sections of aortas from control and P3- immunized rabbits (**A**) and of SMC detected with falloidin and macrophages detected with anti-RAM antibodies (**B**). Fluorescent images were acquired in a scan format of 1024 x 1024 pixels and were processed with the Leica Standard Software TCS-AOBS. m: media; i: intima.

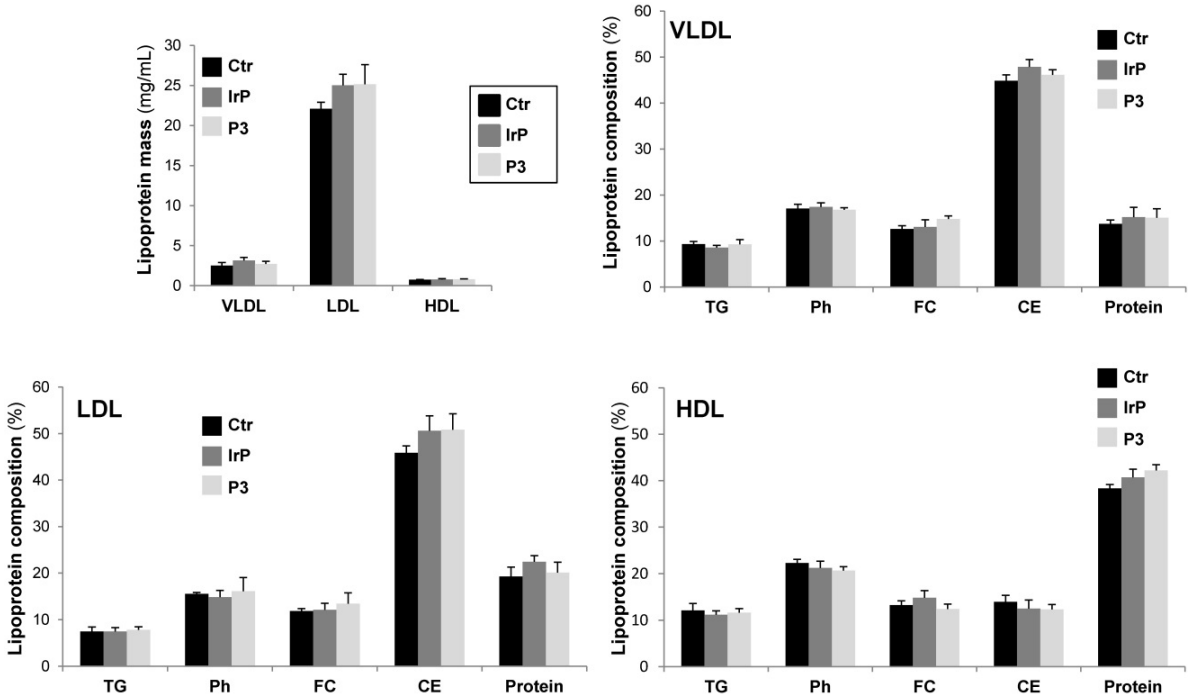

Figure 4. P3 immunization did not induce alterations in lipoprotein mass subclasses or lipoprotein profile of HFD fed rabbits. VLDL, LDL and HDL were isolated by sequential ultracentrifugation and their composition in terms of total, free cholesterol, triglycerides, phospholipids and protein were determined as explained in methods. Lipoprotein composition was used to calculate the total mass of each lipoprotein. Results are shown as mean±SD of control (N=3), IrP (N=6) and P3-immunized rabbits (N=9).

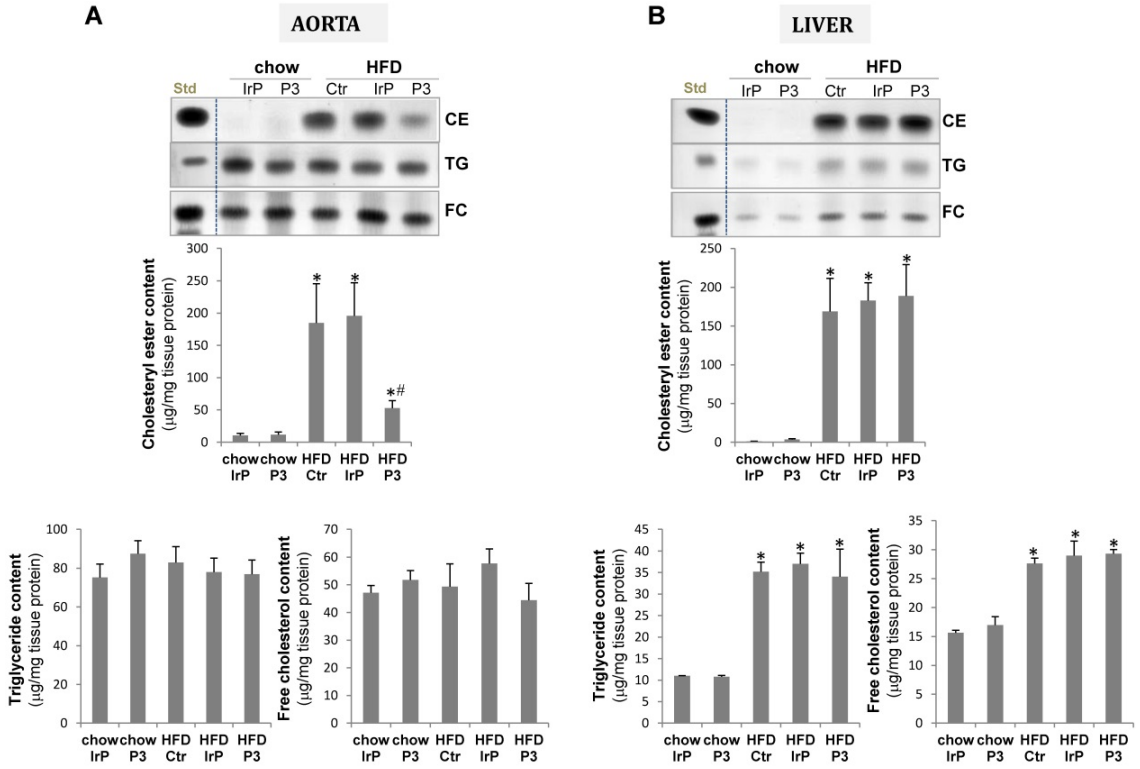

Figure 5. P3 immunization reduces HFD-induced cholesterol accumulation in the aorta but not in the liver. Representative thin-layer chromatography of aorta (**A**) and liver (**B**). Bar graphs showing the quantification of cholesteryl ester (CE), triglycerides and free cholesterol content of aorta and liver. Results are expressed as µg cholesterol per mg protein and shown as mean ± SD in chow IrP (N=6), chow P3 (N=6), HFD Ctr (N=3), HFD IrP (N=6) and HFD P3 (N=9). *P<0.005 versus chow diet; #P<0.005 versus control or IrP-rabbits.

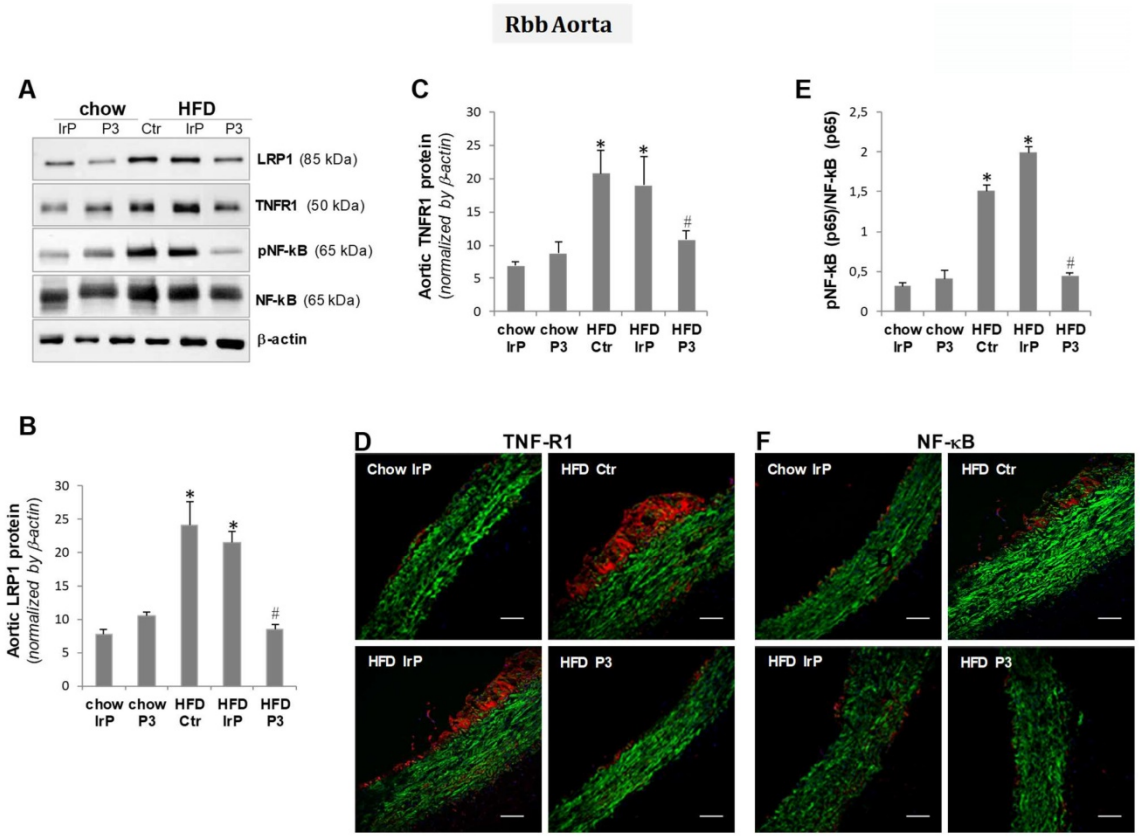

Figure 6. P3 immunization reduces aortic pro-inflammatory mediators in the aorta. Representative Western blot analysis of LRP1, TNFR1, pNF-kB (p65), total NF-kB (p65), and β-actin bands (**A**) and bar graphs showing band quantification of LRP1 and TNFR1 normalized by a-actin (**B,C**) and pNF-kB (p65)/total NF-kB (p65) ratio (**E**). Results are shown as mean ± SD in chow IrP (N=6), chow P3 (N=6), HFD Ctr (N=3), HFD IrP (N=6) and HFD P3 (N=9). *P<0.005 versus chow diet; #P<0.005 versus control or IrP-rabbits. Representative confocal microscopy images of TNFR1 (**D**) and NF-kB levels (**F**) in aortic samples from the different groups. Scale bar = 50 µm.

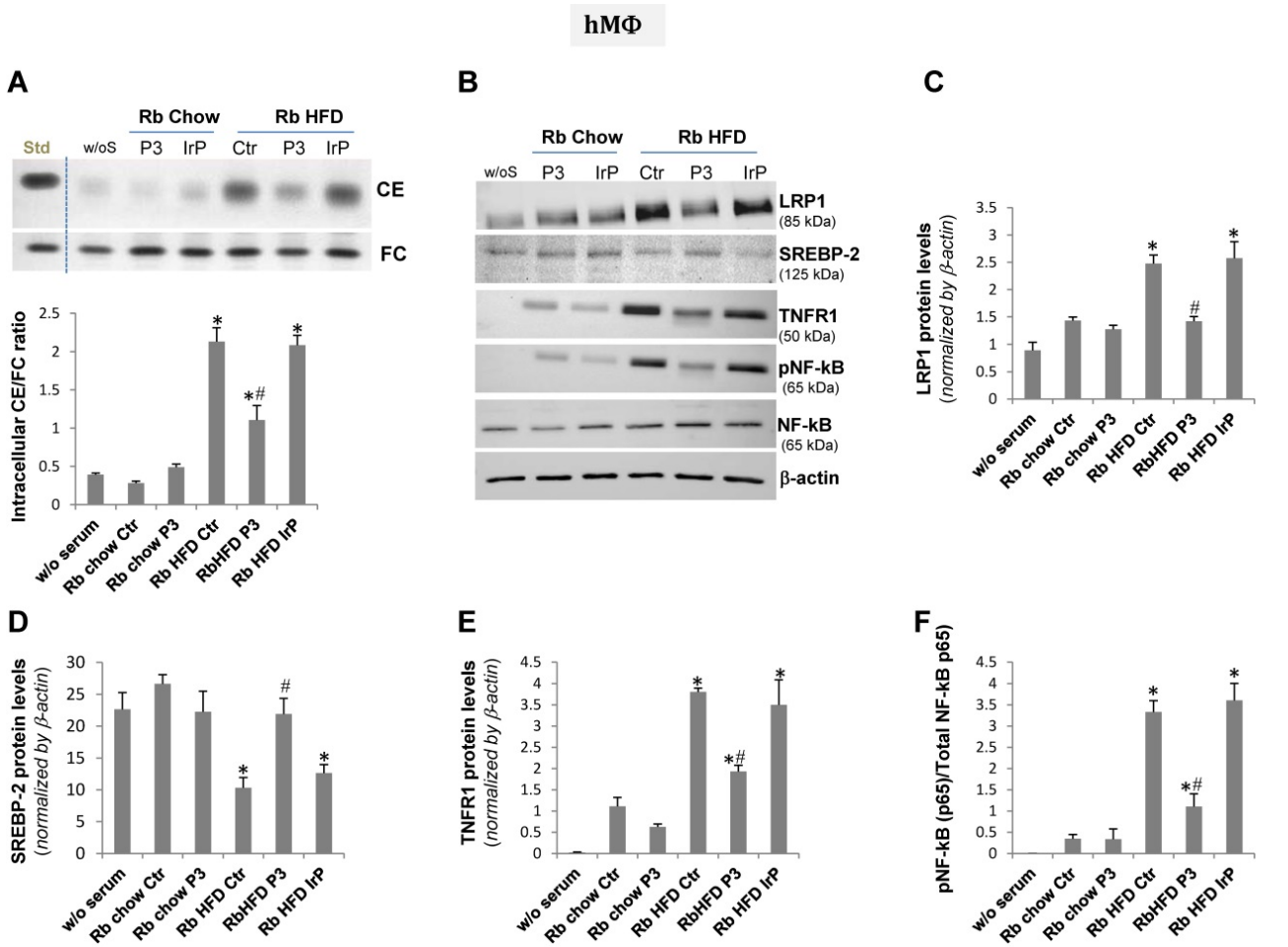

Figure 7. HFD serum from control and IrP serum, but not P3 serum, dramatically increased intracellular CE and pro-inflammatory mediators in human macrophages. Quiescent human macrophages (hMΦ) were exposed to serum from the different groups (0.5%, 2 hours). Cells were then exhaustively washed and collected in NaoH 0.1N for lipid extraction or in lysis buffer for Western blot analysis. **A**) Representative TLC and bar graphs showing the cholesteryl ester (CE) /free cholesterol ratio. Representative Western blot analysis of LRP1, SREBP-2, TNFR1, pNF-kB (p65), total NF-kB (p65), and a-actin bands (**B**) and bar graphs showing band quantification of LRP1, SREBP-2 and TNFR1 normalized by a-actin (**C,D,E**) and pNF-kB (p65)/total NF-kB (p65) ratio (**F**). Results are shown as mean ± SD of three experiments performed in duplicate. *P<0.005 versus chow serum; #P<0.005 versus control or IrP-serums.

Our molecular studies showed that HFD serum (from the control and IrP groups) promote a much higher induction of crucial inflammatory mediators, such as TNFR1 and pNF-kB (p65), than a chow diet in hMΦ (Figure 7B,E,F) and hcVSMC (Figure 8B,E,F). However, P3 immunization efficiently restricted the HFD serum pro-inflammatory effects in cells to the levels found in cells exposed to chow serums. These results highlight the crucial role of Anti-P3 Abs in counteracting HFD-induced pro-inflammatory signaling coupled with the intracellular cholesteryl ester loading of human macrophages and human coronary vascular smooth muscle cells.

PET/CT imaging studies show that Anti-P3 Abs reduce ^{18}F-FDG uptake in the aorta of rabbits

PET-CT metabolic images were performed and analyzed at 120 and 180 minutes after the intravenous administration of 18-FDG in the three groups before their submission to a specific diet. After 31 days of specific diet feeding, subsequent new metabolic images were obtained and analyzed at 120 and 180 minutes. Maximal-intensity projections (MIP) and orthogonal slices were analyzed in fused morpho-metabolic images to identify the aortic tract, and, in the axial plane, three sections were selected for SUV measurements: upper, middle and lower. A circular region of interest (ROI) was drawn following anatomical limits in each section, from which SUV_{mean} was obtained. A progressive decrease in aortic activity was observed as a function of time, which was attributed to the clearance of the vascular background activity. The acquisition that best separated the groups was that performed at 120 minutes. The measurements in the three segments of the aorta showed that the highest ^{18}F-FDG uptake activity occurred in the upper region while it decreased in the middle region and practically disappeared in the lower region. HFD significantly increased SUV_{mean} in

the upper and middle regions of the aorta of control groups, as previously shown [35]. In contrast, in the P3-immunized rabbits, HFD only slightly induced SUV_{mean} in these aortic regions (Figure 9). Moreover, rabbits on the chow diet did not show alterations in post-diet *versus* pre-diet SUV_{mean} values (supplemental Figure S7). The high impact of Anti-P3 Abs on aortic ^{18}F-FDG uptake confirmed molecular, confocal and immunohistochemical results obtained in the present study showing an elevated anti-inflammatory potential of anti-P3 Abs in macrophages and smooth muscle cells in the vasculature.

Doppler ultrasonography imaging reveals that anti-P3 Abs prevent the HFD-induced arterial resistance index in the carotids of rabbits

B-mode ultrasound images of rabbit carotid arteries did not show thickening or calcification indicative of the presence of atherosclerotic lesions. Our available technology was not suitable for performing high-resolution studies (40-50 MHz) capable of detecting early atherosclerotic lesions in carotids. Doppler measurements were used to obtain the arterial resistance index (ARI), an indirect hemodynamic parameter that indicates the resistance to blood flow in a vascular bed distal to the points of measurement: the systolic (1, 3, and 5), diastolic (2, 4, and 6), and pulse frequency measurement points (vertical dotted lines) (marked in Figure 10A). ARI was measured at baseline (pre-diet) and after one month of feeding rabbits HFD (post-diet) into the external and internal carotids from the IrP and P3-immunized rabbits. There were no differences in terms of the basal measurements between the groups. HFD increased ARI in both the external and internal carotid arteries of the IrP rabbits. However, in the P3-immunized rabbits, HFD only slightly induced ARI in the internal carotid artery (Figure 10B). As in the aorta, HFD dramatically induced cholesteryl ester accumulation in the carotids of IrP rabbits and anti-P3 Abs significantly reduced CE accumulation in the external but not in the internal carotid artery (Figure 10C).

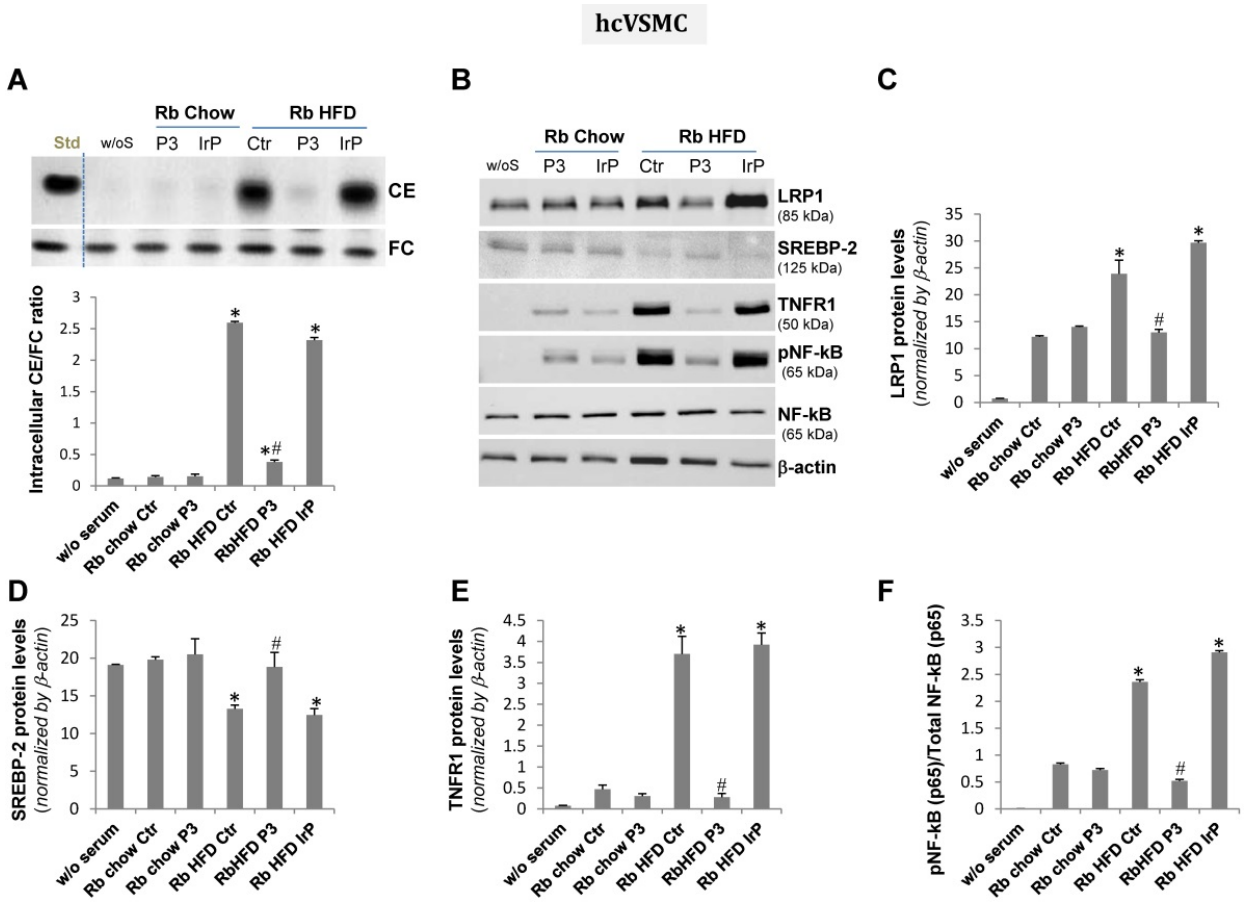

Figure 8. HFD serum from control and IrP serum, but not P3 serum, dramatically increased intracellular CE and pro-inflammatory mediators in human coronary vascular smooth muscle cells. Quiescent human coronary vascular smooth muscle cells (hcVSMC) were exposed to serum from the different groups (0.5%, 2 hours). Cells were then exhaustively washed and collected in NaoH 0.1N for lipid extraction or in lysis buffer for Western blot analysis. **A**) Representative TLC and bar graphs showing the cholesteryl ester (CE) /free cholesterol ratio. Representative Western blot analysis of LRP1, SREBP-2, TNFR1, pNF-kB (p65), total NF-kB (p65), and a-actin bands (**B**) and bar graphs showing band quantification of LRP1, SREBP-2 and TNFR1 normalized by a-actin (**C,D,E**) and pNF-kB (p65)/total NF-kB (p65) ratio (**F**). Results are shown as mean ± SD of three experiments performed in duplicate. *P<0.005 versus chow serum; #P<0.005 versus control or IrP-serums.

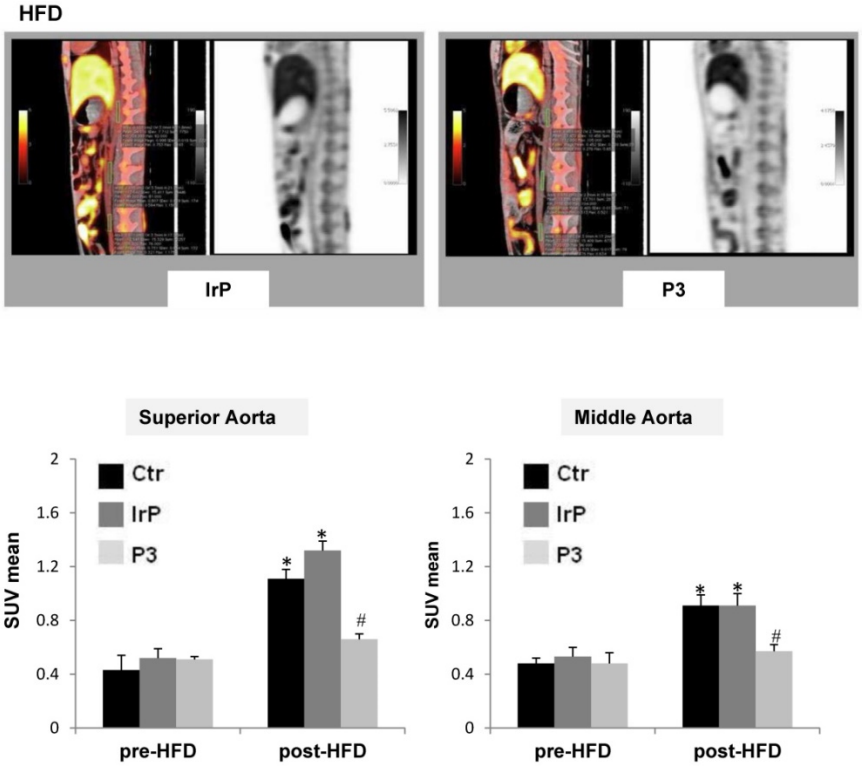

Figure 9. P3 immunization counteracts aortic ^{18}F-FDG uptake induced by HFD in rabbits. (**A**) Representative PET/CT longitudinal images of the aorta in control and P3 immunized rabbits fed HFD. (**B**) Graphs showing the SUV_{mean} progression from pre-diet to post-diet time points in the upper and middle parts of the aorta in HFD-fed rabbits (IrP and P3 groups) (N=6/group). *P<0.005 versus pred-diet; #P<0.005 versus IrP-rabbits.

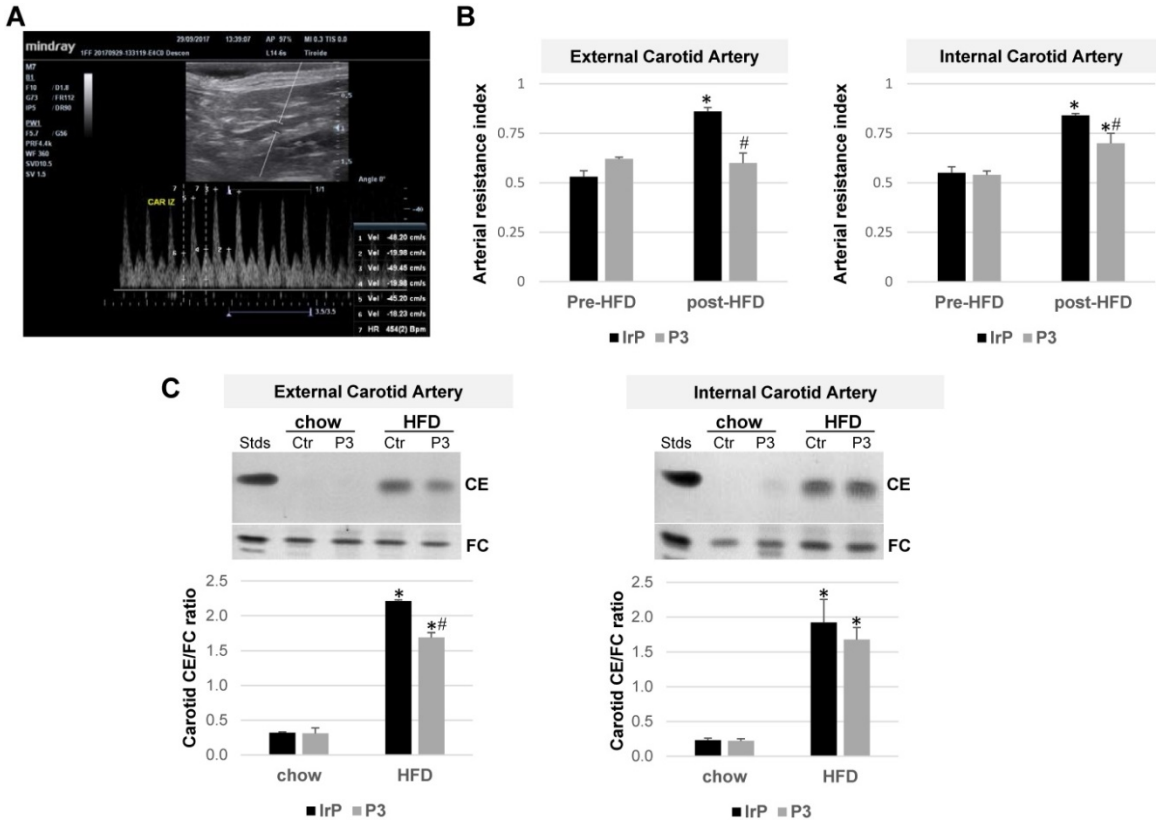

Figure 10. P3 immunization reduces the HFD-induced arterial resistance index (RI) and cholesteryl ester content in the carotids of rabbits. (**A**) Representative image of Eco Pulsed-Wave Doppler in the external carotid of rabbits. The systolic (1, 3 and 5), diastolic (2, 4 and 6), and pulse frequency measurement points (vertical dotted lines) are marked. (**B**) Arterial resistance index (ARI) was measured at baseline (pre-diet) and after 1 month of HFD feeding (post-diet) in external and internal carotids by Doppler ultrasonography in IrP and P3 groups (N=4/group). (**C**) Representative thin-layer chromatography of external and internal carotids and bar graphs showing the cholesteryl ester (CE)/free cholesterol (FC) ratio in carotids. Results are shown as mean ± SD. ***P<0.001, P3 *versus* control. *P<0.005 versus pred-diet; #P<0.005 versus IrP-rabbits.

Discussion

In this study, we revealed the significant reduction of two surrogate markers of atherosclerosis, aortic ^{18}F-FDG cellular metabolism and carotid resistance index, upon the P3 immunization of rabbits. Immunohistochemical, confocal, and molecular studies showed that P3 immunization efficiently counteracted the formation of fatty streaks due to the high efficacy of Anti-P3 Abs in preventing foam cell formation and their coupled pro-inflammatory signaling involved in monocyte recruitment and VSMC migration (summarized in the graphical abstract, Fig. 11).

Previous studies have consistently shown that LRP1 plays a crucial role in the maintenance of the vascular function and in atheroprotection due to its participation in signaling pathways that limit the vascular smooth muscle cell proliferative activity [12,13], apoptosis/efferocytosis and the pro-inflammatory signal of macrophages [14–16].The essential LRP1's role in signaling prompted us to develop antibodies with capacity to specifically block the binding of aggregated LDL. In the present study, we show that Anti-P3 Abs normalized aortic LRP1 levels until the levels found in the aorta of chow fed rabbits. Therefore, this strategy to modulate LRP1 function should not alter the binding of essential LRP1 ligands and coactivators.

HFD is known to promote atherosclerosis. Here, we found that, in agreement with previous studies [32,36], one month of HFD strongly promoted hypercholesterolemia and led to early atherosclerotic lesions or fatty streaks in NZW rabbits. In our rabbit experimental model, HFD increased circulating CE levels to aproximately 55 mM (2115 mg/dL), mainly transported by VLDL and LDL in the rabbit serum. Considering that the percentage of the protein in lipoproteins is similar to humans, LDL and VLDL in HFD-fed rabbits are extremely enriched in cholesteryl esters compared to human LDLs. In fact, the exposure of hMΦ and hcVSMC to HFD serum (0.5%) for only 2 hours caused a tremendous intracellular CE accumulation, in agreement with the high CE accumulation that we observed in the aorta of this rabbit model. In line with our results in rabbits, an increased atherogenicity of large CE-enriched ApoB-100 lipoproteins has been previously reported in monkeys and pigs [37,38]. Remarkably, large LDLs have been associated with increased coronary artery disease in humans [39,40]. The excessive cholesteryl ester load of these lipoproteins *per se* seems not to be a primary factor determining their increased atherogenicity. Core cholesteryl ester and triglyceride seem to cause serious alterations in ApoB-100 conformation, a key determinant of the LDL affinity by the LDLR [41,42]. Here, the high capacity of rabbit CE-enriched ApoB-100 lipoproteins to cause intracellular CE accumulation in human macrophages

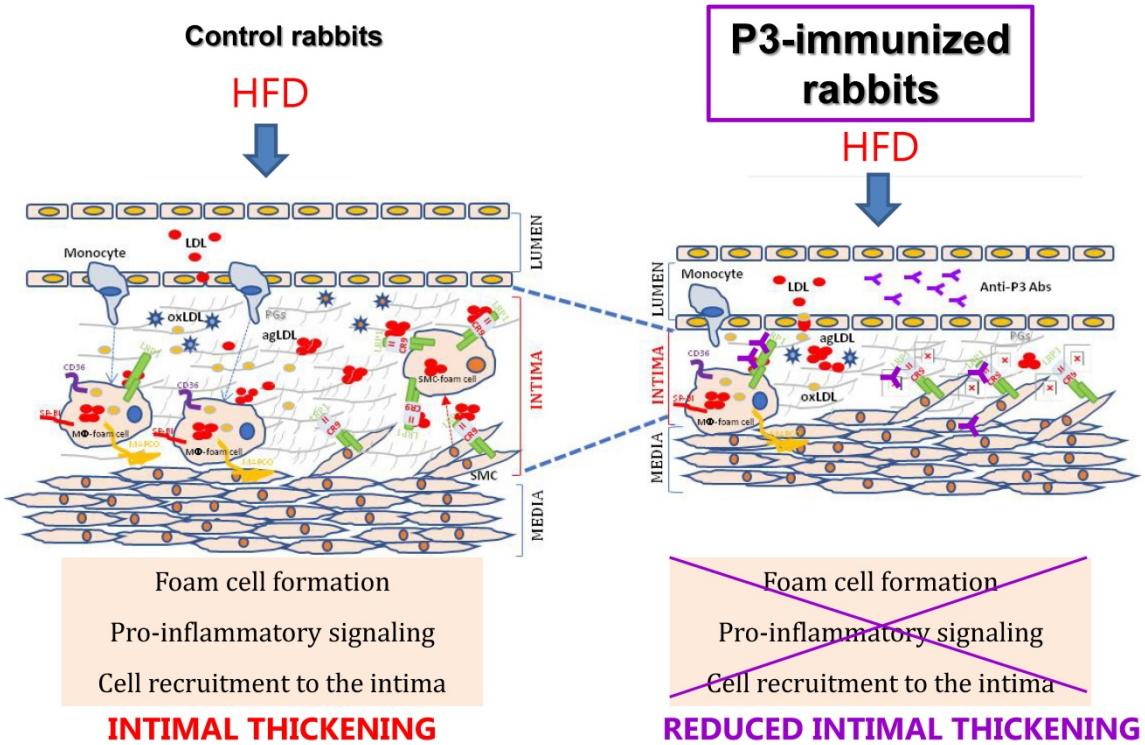

Fig. 11. Graphical Abstract

and VSMC suggest that they are not taken up through the LDLR, a receptor downregulated by intracellular CE levels. Unexpectedly, anti-P3 Abs, designed to inhibit agLDL, not only counteracted CE accumulation in the rabbit vasculature, where LDL aggregation could have been facilitated by proteoglycans of the arterial intima, but also in hMΦ and hcVSMC that have been directly exposed to VLDL and LDL of the rabbit serum. The high efficacy of Anti-P3 Abs to block serum-induced hMΦ and hcVSMC cholesteryl ester loading suggest that rabbit large VLDL and/or LDL (CE-enriched ApoB-100 lipoproteins) could be interacting with the human LRP1, probably through the same domain than aggregated LDL. Futher molecular studies are indeed required to know how CE-enriched large VLDLs and/or LDLs influence ApoB-100 conformation and whether the epitope of ApoB-100 generated in these lipoproteins share structural similarities with that generated in aggregated LDL. An important challenge for future research will be to design molecular tools suitable to reduce the vascular impact of the majority of atherogenic lipoproteins.

Differently to aorta, where HFD only upregulates vascular cholesteryl ester content, HFD increased both hepatic cholesteryl esters and triglycerides. The differential impact of HFD serum in the neutral lipid content of aorta and liver could be associated to the particular lipoproteins that mainly interact with vascular and hepatic tissues. In vascular cells (macrophages and VSMC), LRP1 supposedly interacts greatly with agLDL [4–6]. In hepatic cells, LRP1 mainly interacts with ApoE-enriched lipoproteins such as chylomicrons [43]. It is known that ApoB-100 and ApoE interact with LRP1 receptor through different clusters. The new epitope generated in ApoB-100 during LDL aggregation interacts with cluster II (CR9 domain) [24] while ApoE interacts with cluster III (domain CR17) [44,45]. The different lipoproteins that reach aortas and livers may explain why P3 immunization reduces cholesteryl ester accumulation in the vasculature (aorta and carotids) but not in liver. The CR9 and CR17 domains are so spatially distant that it is structurally impossible for anti-P3 antibodies to cause any effect on the binding of ApoE-enriched lipoproteins. This could explain why P3 immunization did not exert any effect on the HFD-induced neutral lipid accumulation in the liver. The liver is a key organ that modulates whole-body lipid and lipoprotein metabolism and consequently circulating lipid and lipoprotein profile [46]. Therefore, the lack of impact of the Anti-P3 Abs in the hepatic neutral lipid content could be a determinant of the similar lipoprotein profile between groups.

Molecular, immunohistochemical and confocal microscopy experiments showed that Anti-P3 Abs decreased HFD-induced TNFR1 overexpression in vasculature and cells. Macrophage-foam cells have been reported to secrete extracellular vesicles that determine the proliferative and migratory capacity of SMC [47]. Moreover, TNFR1 promotes monocyte recruitment and SMC proliferation in the pro-atherosclerotic arterial wall [23]. Therefore, the reduced TNFR1 levels that we observed in Anti-P3 treated macrophages and VSMCs could indeed contribute to limit the recruitment of monocytes and VSMCs into the arterial intima.

The impact of HFD on NF-kB (p65) phosphorylation reported in this study is in line with previous results showing that an excessive input of nutrition activates NF-kB signaling in macrophages [48]. Similar HFD effects were observed in the phosphorylation of NF-kB (p65) phosphorylation in VSMC. The high efficiency of Anti-P3 Abs to counteract HFD-induced NF-kB (p65) phosphorylation in hMΦ and hcVSMC, suggest a high potential of these Abs to modulate atherosclerosis. Abbate's group has elegantly shown that, by counteracting NF-kB pro-inflammatory signaling, LRP1 activation with SP16 agonist leads to a cardioprotective signal that reduces infarct size [20,21]. SP16 has been designed on the basis of the motif present in protease-inhibitor complexes, which have been reported not to be recognized by the consecutive CR8/CR9 modules of cluster II [25]. The specific interaction of anti-P3 Abs with CR9 domains ensures high specificity of effects, and importantly, guarantees zero interference with the agonists of the LRP1 anti-inflammatory signaling. Of note that anti-P3 Abs did not exert any effect on these basal LRP1 levels, suggesting that Anti-P3 Abs reduced HFD-induced pro-inflammatory signaling without disturbing the atheroprotective LRP1 signaling in the vasculature.

Taken together, our results highlight the strategic therapeutic value of Anti-P3 Antibodies to inhibit diet-induced cellular cholesteryl ester loading and coupled inflammation in the vasculature.

In line with previous studies showing that ^{18}F-FDG uptake reaches maximal values during early foam cell formation [35], in the current study, we also showed that the anti-atherosclerotic efficiency of P3 immunization on early lesions can be tracked by PET/CT. Complementary confocal microscopy analysis showed that reduced ^{18}F-FDG uptake in the aorta of P3-immunized rabbits occurred concomitantly with a reduced presence of macrophages and SMCs in the arterial intima. Although cellular metabolic activity in PET/CT has been assumed to be mainly caused by the high number of macrophages in atherosclerotic plaques [28], more recent studies have demonstrated

that SMCs also play a crucial role in plaque PET/CT activity due to their high capacity to take up glucose when exposed to pro-inflammatory cytokines [49].

While imaging for the detection of atherosclerotic lesions at different stages has been extensively used for rabbit aortas, less investigated has been the impact of HFD on the development of atherosclerosis in carotids of this animal model, and especially through imaging techniques. Here, we showed that one month of HFD increased the resistance index (RI) of both external and internal carotids despite the lack of direct evidence of atherosclerotic plaques in carotids. In carotid arteries, a significant correlation between RI and the degree of generalized atherosclerosis has been previously shown in humans [50]. Here, we demonstrated the efficacy of P3-immunization in reducing carotid RI, although the effect was different between the external and internal carotids (higher for the external carotids). In fact, further carotid lipidic analysis showed that P3 immunization reduced cholesteryl ester accumulation on the external but not on the internal carotid. Differential anatomy and hemodynamics could likely explain the differential impact of P3 immunization on these carotids. On the basis of aortic PET/CT and carotid Doppler ultrasonography, our results revealed that P3 immunization efficiently reduces HFD-induced atherosclerosis in rabbits, at least in the early stages. Moreover, these results suggested that PET/CT and ultrasonography are imaging techniques that can track the effect of potential therapeutic P3 immunizations in other translational *in vivo* models and in humans.

Limitations of the study

The main limitations of this study were that the efficacy of P3 immunization was not analyzed in the endothelium despite the crucial role of endothelial *lrp1* in atherosclerosis, glucose sensitivity and lipid profiles [51]. Recently, it has been reported the feasibility of a surface-enhanced Raman scattering-antibody-functionalized gold nanoprobes (SERS-BFNP) molecular imaging platform for non-invasive detection of adhesion molecules in the endothelium of atherosclerotic lesions in *in vivo* models [52]. In addition, the efficacy of P3 immunization was only tested in early atherosclerotic lesions despite the high relevance of the interaction of VSMC with LDL for the vulnerability of the atherosclerotic plaques [53]. Finally, the technology used in the present study to detect the presence of atherosclerotic plaques in carotids has certain limitations.

Conclusions

In conclusion, our study demonstrates that, by specifically blocking LRP1-mediated intracellular CE accumulation in vascular cells, Anti-P3 Abs counteract cellular pro-inflammatory signals that allow for the recruitment of monocytes and VSMC into the arterial intima of a rabbit model of HFD-induced atherosclerosis. Moreover, anti-P3 Abs are extremely effective to stop foam cell formation from human macrophages and human coronary vascular smooth muscle cells and the efficacy of P3 immunization can be tracked using non-invasive imaging techniques such as PET/CT and Doppler ultrasonography. These both aspects confer an enormous translational potential to Anti-P3 Abs.

Abbreviations

AgLDL: aggregated LDL; ANOVA: analysis of variance; ApoA-I: apolipoprotein A-I; apoB-100: apolipoprotein B-100; ApoJ: apolipoprotein J; ARI: arterial resistance index; BSA: bovine serum albumin; CE: cholesteryl esters; CVD: cardiovascular disease; ELISA: enzyme-linked immunosorbent assay; FDG: 2-fluoro-2-deoxy-D-glucose; HFD: high-fat diet; IMT: intima-media thickness; KLH: Keyhole limpet haemocyanin; LDL: low-density lipoprotein; LRP1: low-density lipoprotein receptor-related protein 1; NF-kB: nuclear factor kB; NZW: New Zealand White; PET/CT: positron emission tomography/computed tomography; RI: resistance index; rSMC: rabbit smooth muscle cells; SMC: smooth muscle cells; SUV: standard uptake value; TNFR1: tumor necrosis factor receptor 1.

Supplementary Material

Supplementary figures.
http://www.thno.org/v10p3263s1.pdf

Acknowledgments

We thank Joan Repulles (IR-SantPau PSCT Confocal microscopy) and Esther Peña for their help in configuring confocal microscopy images.

Sources of Funding

The main support to develop this project was received from Fundació MARATÓ TV3 Project 201521-10 (to VLl-C) and FIS PI18/01584 (to VLl-C), FIS16/00139 (to JCE-G) from the Instituto de Salud Carlos III (ISCIII) and co-financed with ERDFs. Support was received from Fundació Marató TV3 (Project 201521-10) for post-doctoral funding to OB and from Ministerio de Economía y Competitividad to DdG-C (IJCI-2016-29393). CIBER Diabetes y Enfermedades Metabólicas Asociadas (CIBERDEM; CB07/08/0016 to JCE-G) and CIBER Enfermedades Cardiovasculares (CIBERCV; CB16/1100403 to DdG-C, VLl-C and CB16/11/00411 to LB and MB-P) are projects run by the Instituto de Salud Carlos III

(ISCIII). We also acknowledge support from "Secretaria d'Universitats i Recerca del Departament d'Economia I Coneixement de la Generalitat de Catalunya" [2017SGR946 to VLl-C and 2017SGR1480 to LB]. DdG-C, VL-C and JCE-G are members of the Group of Vascular Biology of the Spanish Society of Atherosclerosis (SEA).

Competing Interests

The authors have declared that no competing interest exists.

References

1. Lu M, Gursky O. Aggregation and fusion of low-density lipoproteins *in vivo* and *in vitro*. Biomol Concepts. 2013; 4: 501-18.
2. Öörni K, Posio P, Ala-Korpela M, Jauhiainen M, Kovanen PT. Sphingomyelinase induces aggregation and fusion of small very low-density lipoprotein and intermediate-density lipoprotein particles and increases their retention to human arterial proteoglycans. Arterioscler Thromb Vasc Biol. 2005; 25: 1678–83.
3. Öörni K, Pentikäinen MO, Ala-Korpela M, Kovanen PT. Aggregation, fusion, and vesicle formation of modified low density lipoprotein particles: molecular mechanisms and effects on matrix interactions. J Lipid Res. 2000; 41: 1703–14.
4. Llorente-Cortés V, Otero-Viñas M, Sánchez S, Rodríguez C, Badimon L. Low-Density Lipoprotein Upregulates Low-Density Lipoprotein Receptor-Related Protein Expression in Vascular Smooth Muscle Cells. Circulation. 2002; 106: 3104-10.
5. Llorente-Cortés V, Martínez-González J, Badimon L. LDL Receptor–Related Protein Mediates Uptake of Aggregated LDL in Human Vascular Smooth Muscle Cells. Arterioscler Thromb Vasc Biol. 2000; 20: 1572-9.
6. Llorente-Cortés V, Otero-Viñas M, Badimon L. Differential Role of Heparan Sulfate Proteoglycans on Aggregated LDL Uptake in Human Vascular Smooth Muscle Cells and Mouse Embryonic Fibroblasts. Arterioscler Thromb Vasc Biol. 2002; 22: 1905-11.
7. Sakr SW, Eddy RJ, Barth H, Wang F, Greenberg S, Maxfield FR, et al. The Uptake and Degradation of Matrix-bound Lipoproteins by Macrophages Require an Intact Actin Cytoskeleton, Rho Family GTPases, and Myosin ATPase Activity. J Biol Chem. 2001; 276: 37649–58.
8. Llorente-Cortés V, Royo T, Juan-Babot O, Badimon L. Adipocyte differentiation-related protein is induced by LRP1-mediated aggregated LDL internalization in human vascular smooth muscle cells and macrophages. J Lipid Res. 2007; 48: 2133–40.
9. Lillis AP, Muratoglu SC, Au DT, Migliorini M, Lee MJ, Fried SK, et al. LDL receptor-related protein-1 (LRP1) regulates cholesterol accumulation in macrophages. PLoS One. 2015; 11: e0147457.
10. Zhou L, Takayama Y, Boucher P, Tallquist MD, Herz J. LRP1 regulates architecture of the vascular wall by controlling PDGFRβ-dependent phosphatidylinositol 3-kinase activation. PLoS One. 2009; 4: e6922.
11. Boucher P, Gotthardt M, Li WP, Anderson RGW, Herz J. LRP: Role in vascular wall integrity and protection from atherosclerosis. Science. 2003; 300: 329–32.
12. Boucher P, Liu P, Gotthardt M, Hiesberger T, Anderson RGW, Herz J. Platelet-derived growth factor mediates tyrosine phosphorylation of the cytoplasmic domain of the low density lipoprotein receptor-related protein in caveolae. J Biol Chem. 2002; 277: 15507–13.
13. Loukinova E, Ranganathan S, Kuznetsov S, Gorlatova N, Migliorini M, Loukinov D, et al. Platelet-derived Growth Factor (PDGF)-induced Tyrosine Phosphorylation of the Low Density Lipoprotein Receptor-related Protein (LRP): Evidence for integrated co-receptor function between LRP and the PDGF. J Biol Chem. 2002; 277: 15499–506.
14. Yancey PG, Blakemore J, Ding L, Fan D, Overton CD, Zhang Y, et al. Macrophage LRP-1 controls plaque cellularity by regulating efferocytosis and Akt activation. Arterioscler Thromb Vasc Biol. 2010; 30: 787–95.
15. Yancey PG, Ding Y, Fan D, Blakemore JL, Zhang Y, Ding L, et al. Low-density lipoprotein receptor-related protein 1 prevents early atherosclerosis by limiting lesional apoptosis and inflammatory Ly-6C high monocytosis: Evidence that the effects are not apolipoprotein e dependent. Circulation. 2011; 124: 454–64.
16. Xian X, Ding Y, Dieckmann M, Zhou L, Plattner F, Liu M, et al. LRP1 integrates murine macrophage cholesterol homeostasis and inflammatory responses in atherosclerosis. Elife. 2017; 6. pii: e29292.
17. El Asmar Z, Terrand J, Jenty M, Host L, Mlih M, Zerr A, et al. Convergent signaling pathways controlled by LRP1 (Receptor-related Protein 1) cytoplasmic and extracellular domains limit cellular cholesterol accumulation. J Biol Chem. 2016; 291: 5116–27.
18. Kawamura A, Baitsch D, Telgmann R, Feuerborn R, Weissen-Plenz G, Hagedorn C, et al. Apolipoprotein E interrupts interleukin-1β signaling in vascular smooth muscle cells. Arterioscler Thromb Vasc Biol. 2007; 27: 1610–7.
19. Gaultier A, Arandjelovic S, Li X, Janes J, Dragojlovic N, Zhou GP, et al. A shed form of LDL receptor-related protein-1 regulates peripheral nerve injury and neuropathic pain in rodents. J Clin Invest. 2008; 118: 161–72.
20. Toldo S, Austin D, Mauro AG, Mezzaroma E, van Tassell BW, Maechetti C, et al. Low-Density Lipoprotein Receptor-Related Protein-1 Is a Therapeutic Target in Acute Myocardial Infarction. JACC Basic to Transl Sci. 2017; 2: 561–74.
21. Potere N, Del Buono MG, Mauro AG, Abbate A, Toldo S. Low Density Lipoprotein Receptor-Related Protein-1 in Cardiac Inflammation and Infarct Healing. Front Cardiovasc Med. 2019; 6:51.
22. Fiordelisi A, Iaccarino G, Morisco C, Coscioni E, Sorriento D. NFkappaB is a key player in the crosstalk between inflammation and cardiovascular diseases. International Journal of Molecular Sciences. 2019; 20. pii: E1599.
23. Zhang L, Zhang ZG, Liu XS, Hozeska-Solgot A, Chopp M. The PI3K/Akt pathway mediates the neuroprotective effect of atorvastatin in extending thrombolytic therapy after embolic stroke in the rat. Arterioscler Thromb Vasc Biol. 2007; 27: 2470–5.
24. Costales P, Fuentes-Prior P, Castellano J, Revuelta-Lopez E, Corral-Rodríguez MA, Nasarre L, et al. Domain CR9 of Low Density Lipoprotein (LDL) Receptor-related Protein 1 (LRP1) Is Critical for Aggregated LDL-induced Foam Cell Formation from Human Vascular Smooth Muscle Cells. J Biol Chem. 2015; 290: 14852–65.
25. Jensen JK, Dolmer K, Gettins PGW. Specificity of binding of the low density lipoprotein receptor-related protein to different conformational states of the clade E serpins plasminogen activator inhibitor-1 and proteinase nexin-1. J Biol Chem. 2009; 284: 17989–97.
26. Bocan TMA, Bak Mueller S, Mazur MJ, Uhlendorf PD, Quenby Brown E, Kieft KA. The relationship between the degree of dietary-induced hypercholesterolemia in the rabbit and atherosclerotic lesion formation. Atherosclerosis. 1993; 102: 9–22.
27. Badimon JJ, Badimon L, Fuster V. Regression of atherosclerotic lesions by high density lipoprotein plasma fraction in the cholesterol-fed rabbit. J Clin Invest. 1990; 85: 1234–41.
28. Hyafil F, Cornily J-C, Rudd JHF, Machac J, Feldman LJ, Fayad ZA. Quantification of Inflammation Within Rabbit Atherosclerotic Plaques Using the Macrophage-Specific CT Contrast Agent N1177: A Comparison with 18F-FDG PET/CT and Histology. J Nucl Med. 2009; 50: 959–65.
29. Avrameas S. Coupling of enzymes to proteins with glutaraldehyde. Use of the conjugates for the detection of antigens and antibodies. Immunochemistry. 1969; 6: 43–52.
30. Julve J, Escolà-Gil JC, Rotllan N, Fiévet C, Vallez E, de la Torre C, et al. Human Apolipoprotein A-II Determines Plasma Triglycerides by Regulating Lipoprotein Lipase Activity and High-Density Lipoprotein Proteome. Arterioscler Thromb Vasc Biol. 2010; 30: 232-8.
31. Casadei A, Floreani M, Catalini R, Serra C, Assanti AP, Conci P. Sonographic characteristics of carotid artery plaques: Implications for follow-up planning? J Ultrasound. 2012; 15: 151–7.
32. Llorente-Cortes V, Casani L, Cal R, LLenas A, Juan-Babot O, Camino-López S, et al. Cholesterol-lowering strategies reduce vascular LRP1 overexpression induced by hypercholesterolaemia. Eur J Clin Invest. 2011; 41: 1087–97.
33. Llorente-Cortés V, Costales P, Bernués J, Camino-Lopez S, Badimon L. Sterol Regulatory Element-binding Protein-2 Negatively Regulates Low Density Lipoprotein Receptor-related Protein Transcription. J Mol Biol. 2006; 359: 950–60.
34. Costales P, Aledo R, Vérnia S, Das A, Shah VH, Casado M, et al. Selective role of sterol regulatory element binding protein isoforms in aggregated LDL-induced vascular low density lipoprotein receptor-related protein-1 expression. Atherosclerosis. 2010; 213: 458–68.
35. Zhao QM, Feng TT, Zhao X, Xu ZM, Liu Y, Li DP, et al. Imaging of atherosclerotic aorta of rabbit model by detection of plaque inflammation with fluorine-18 fluorodeoxyglucose positron emission tomography/computed tomography. Chin Med J (Engl). 2011; 124: 911–7.
36. Phinikaridou A, Hallock KJ, Qiao Y, Hamilton JA. A robust rabbit model of human atherosclerosis and atherothrombosis. J Lipid Res. 2009; 50: 787–97.

37. Rudel LL, Parks JS, Hedrick CC, Thomas M, Williford K. Lipoprotein and cholesterol metabolism in diet-induced coronary artery atherosclerosis in primates. Role of cholesterol and fatty acids. Vol. 37, Progress in Lipid Research. 1998.
38. Checovich WJ, Fitch WL, Krauss RM, Smith MP, Rapacz J, Smith CL, et al. Defective Catabolism and Abnormal Composition of Low-Density Lipoproteins from Mutant Pigs with Hypercholesterolemia. Biochemistry. 1988; 27: 1934–41.
39. Campos H, López-Miranda J, Rodríguez C, Albajar M, Schaefer EJ, Ordovás JM. Urbanization elicits a more atherogenic lipoprotein profile in carriers of the apolipoprotein A-IV-2 allele than in A-IV-1 homozygotes. Arterioscler Thromb Vasc Biol. 1997; 17: 1074–81.
40. Gray RS, Robbins DC, Wang W, Yeh JL, Fabsitz RR, Cowan LD, et al. Relation of LDL size to the insulin resistance syndrome and coronary heart disease in American Indians: The strong heart study. Arterioscler Thromb Vasc Biol. 1997; 17: 2713–20.
41. Nigon F, Lesnik P, Rouis M, Chapman MJ. Discrete subspecies of human low density lipoproteins are heterogeneous in their interaction with the cellular LDL receptor. J Lipid Res. 1991; 32: 1741–53.
42. McNamara JR, Small DM, Li Z, Schaefer EJ. Differences in LDL subspecies involve alterations in lipid composition and conformational changes in apolipoprotein B. J Lipid Res. 1996; 37: 1924–35.
43. Rohlmann A, Gotthardt M, Hammer RE, Herz J. Inducible inactivation of hepatic LRP gene by Cre-mediated recombination confirms role of LRP in clearance of chylomicron remnants. J Clin Invest. 1998; 101: 689–95.
44. Guttman M, Prieto JH, Handel TM, Domaille PJ, Komives EA. Structure of the minimal interface between ApoE and LRP. J Mol Biol. 2010; 398: 306–19.
45. Guttman M, Prieto JH, Croy JE, Komives EA. Decoding of lipoprotein-receptor interactions: Properties of ligand binding modules governing interactions with apolipoprotein E. Biochemistry. 2010; 49: 1207–16.
46. Dietschy JM, Turley SD, Spady DK. Role of liver in the maintenance of cholesterol and low density lipoprotein homeostasis in different animal species, including humans. Vol. 34, Journal of Lipid Research. 1993; 34: 1637-59.
47. Niu C, Wang X, Zhao M, Cai T, Liu P, Li J, et al. Macrophage foam cell-derived extracellular vesicles promote vascular smooth muscle cell migration and adhesion. J Am Heart Assoc. 2016; 5. pii: e004099.
48. Ben J, Jiang B, Wang D, Liu Q, Zhang Y, Qi Y, et al. Major vault protein suppresses obesity and atherosclerosis through inhibiting IKK–NF-κB signaling mediated inflammation. Nat Commun. 2019; 10: 1801.
49. Folco EJ, Sheikine Y, Rocha VZ, Christen T, Shvartz E, Sukhova GK, et al. Hypoxia but not inflammation augments glucose uptake in human macrophages: Implications for imaging atherosclerosis with 18fluorine-labeled 2-deoxy-D-glucose positron emission tomography. J Am Coll Cardiol. 2011; 58: 603–14.
50. Frauchiger B, Peter Schmid H, Roedel C, Moosmann P, Staub D. Comparison of carotid arterial resistive indices with intima-media thickness as sonographic markers of atherosclerosis. Stroke. 2001; 32: 836–41.
51. Mao H, Lockyer P, Li L, Ballantyne CM, Patterson C, Xie L, et al. Endothelial LRP1 regulates metabolic responses by acting as a co-activator of PPARγ. Nat Commun. 2017; 8: 14960.
52. Noonan J, Asiala SM, Grassia G, MacRitchie N, Gracie K, Carson J, et al. In vivo multiplex molecular imaging of vascular inflammation using surface-enhanced Raman spectroscopy. Theranostics. 2018; 8: 6195-209.
53. Ma S, Motevalli SM, Chen J, Xu MQ, Wang Y, Feng J, et al. Precise theranostics nanomedicines for inhibiting vulnerable atherosclerotic plaque progression through regulation of vascular smooth muscle cell phenotype switching. Theranostics. 2018; 8: 3693-706.

14.1 Article 2 supplemental material

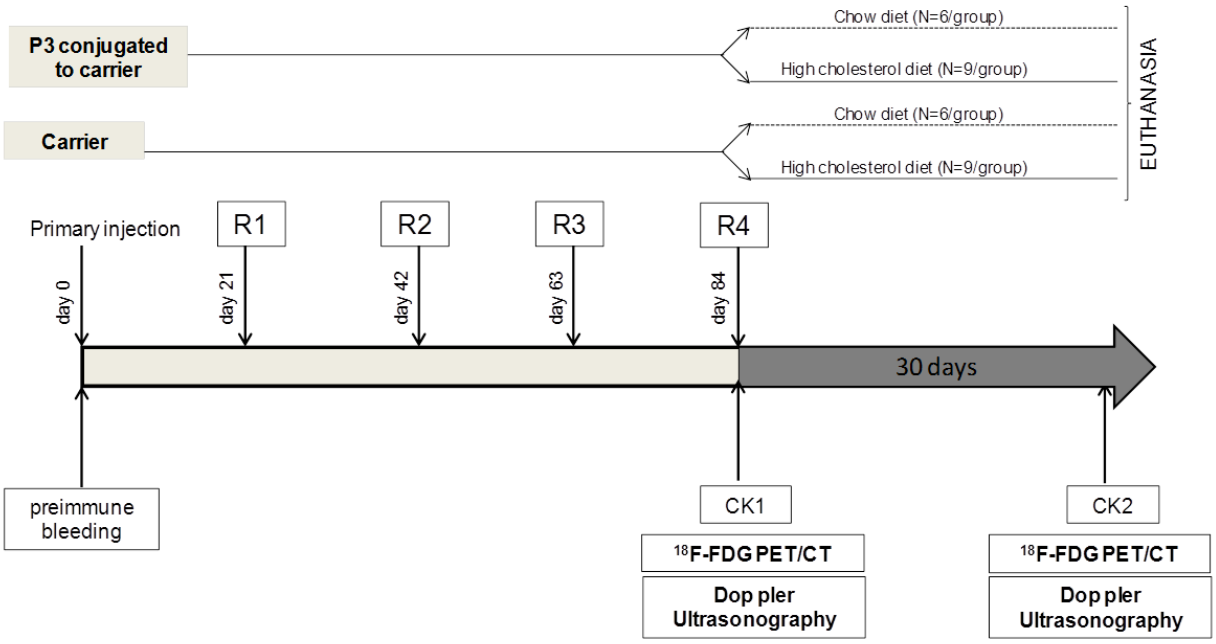

Figure S1. Study Design. Animals were acclimated for one week before the first immunization and immunized with a primary injection and four reminder doses (R1-R4) of IrP (irrelevant peptide) (IrP group; N=12) or P3 (P3 group; N=15) conjugated to the carrier every 21 days. An additional group of rabbits was injected with carrier alone (control group; N=3). At day 84, 18F-FDG PET/CT image scans, Doppler ultrasonography and circulating anti-P3 specific antibody determinations (CK1) were performed and considered as a reference of basal levels. Starting at the R4 time point, IrP and P3-immunized rabbits were randomly divided into normal diet group and high-fat diet (HFD)-fed group. Twelve rabbits (N=6 Irp-injected and N=6 P3-injected) continued fed on the chow diet, whereas fifteen rabbits (N=6 IrP-injected and N=9 P3-injected) and one rabbit control group (N=3 injected with carrier alone) received HFD for 30 days. After one month, final imaging PET/CT scans, Doppler measurements and circulating anti-P3 specific antibody determinations (CK2) were performed. At day 114, animals were then euthanized, and tissues (aorta, carotids and liver) were processed for immunohistochemistry, confocal microscopy and molecular studies. CK1: check point 1 (pre-diet); CK2: check point 2 (post-diet)

Figure S2. Representative image of isolated aorta indicating the consecutive sections (1 cm) used for immunohistochemistry (IHQ) and molecular studies (mol). IA: Iliac bifurcation (Figure 15 of materials and methods section)

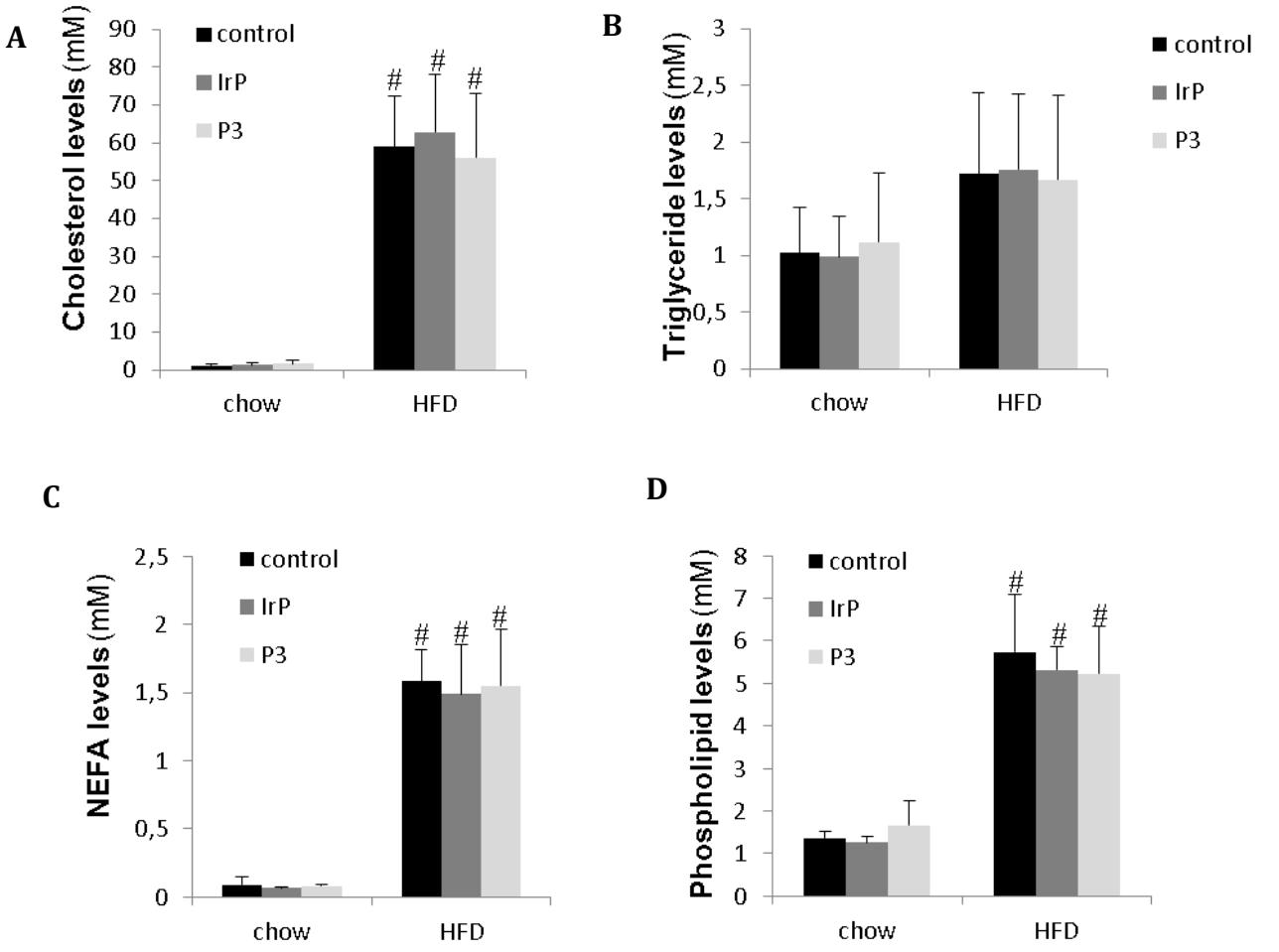

Figure S3. Circulating lipid levels in controls and P3-immunized rabbits. Bar graphs showing (A) cholesterol, (B) triglycerides, (C) non-esterified fatty acids (NEFA) and (D) phospholipid levels in serum from control, IrP and P3-immunized rabbits. # P<0.005 versus chow diet.

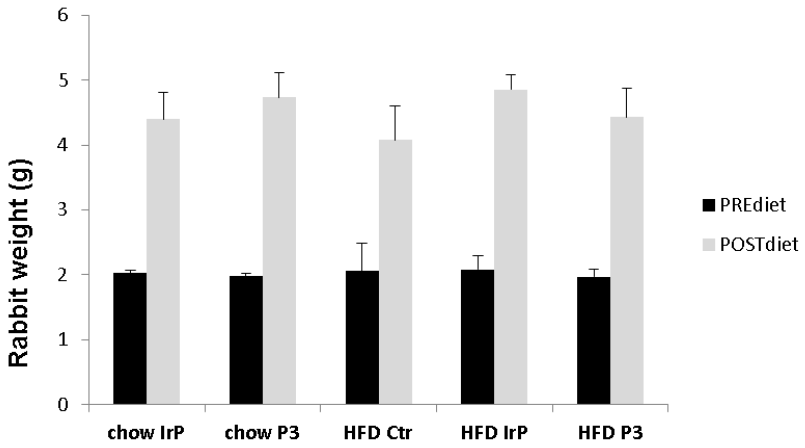

Figure S4. Rabbit weight gain in pre- and post-diet time points in the different studied groups.

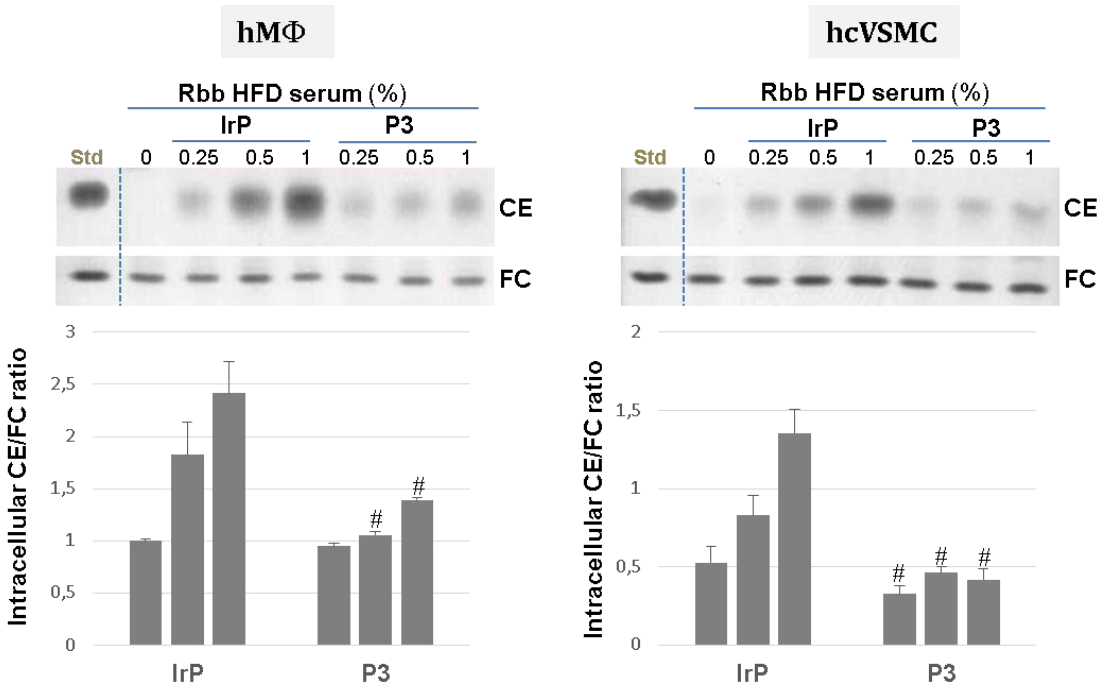

Figure S5. Effect of HFD serum from IrP and P3-immunized rabbits in the intracellular CE/FC ratio of human macrophages (hMΦ) and human coronary vascular smooth muscle cells (hcVSMC). Quiescent hMΦ and hcVSMC were exposed for increasing serum dose (0.25%, 0.5% and 1%) for two hours. Cells were then exhaustively washed and collected in NaoH 0.1N for lipid extraction followed by TLC. Bar graphs show the cholesteryl ester (CE) /free cholesterol (FC) ratio. Data are shown as mean ± SEM of three experiments performed in duplicate. # P<0.005 versus IrP.

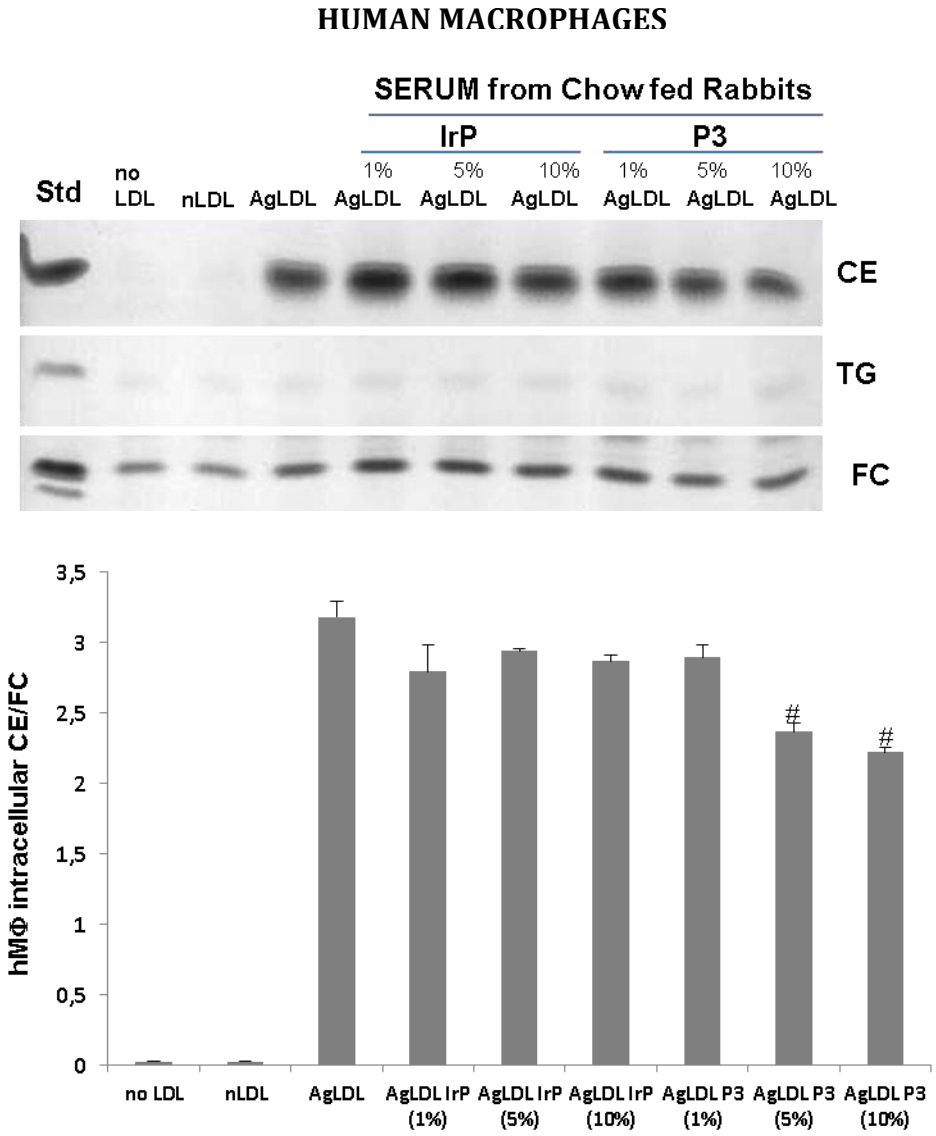

Figure S6. Effect of chow serum from IrP and P3-immunized rabbits in the intracellular CE/FC ratio induced by aggregated LDL in human macrophages (hMΦ). Quiescent hMΦ were exposed to aggregated LDL (100 μg/mL, 2 hours) in the presence of increasing dose of chow serum from IrP or P3 rabbits (1%, 5% and 10%). Cells were then exhaustively washed and collected in NaoH 0.1N for lipid extraction followed by TLC. Bar graphs show the cholesteryl ester (CE) /free cholesterol (FC) ratio. Data are shown as mean ± SEM of three experiments performed in duplicate. # P<0.005 versus IrP.

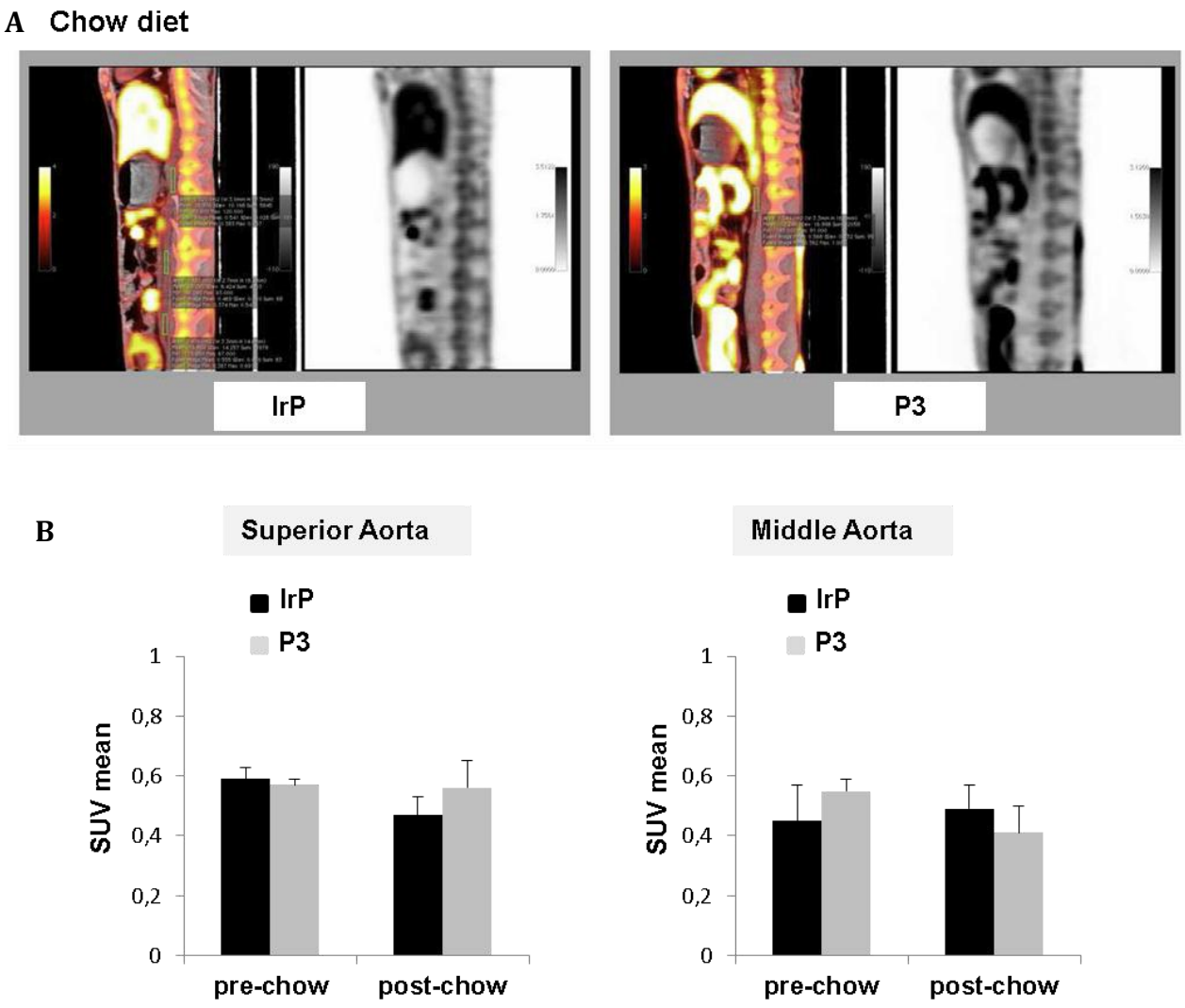

Figure S7. P3 immunization did not exert any effect on basal aortic ^{18}F-FDG uptake. (A) Representative PET/CT longitudinal images of the aorta in control and P3 immunized rabbits fed chow diet. (B) Graphs showing the SUVmean values at pre-diet and post-diet time points in the upper and middle parts of the aorta in chow-fed rabbits (IrP and P3 groups) (N=3/group).

15 RESULTS: Article 3

Biomedicine & Pharmacotherapy 152 (2022) 113270

Contents lists available at ScienceDirect

Biomedicine & Pharmacotherapy

journal homepage: www.elsevier.com/locate/biopha

Targeting cholesteryl ester accumulation in the heart improves cardiac insulin response

Virginia Actis Dato [a,b,1], Aleyda Benitez-Amaro [c,d,1], Eduardo Garcia [c,d,1], Lene Claudi [c,d], Maria Teresa LaChica Lhoëst [c,d], Antoni Iborra [e], Joan Carles Escola-Gil [f], Jose Maria Guerra [g,h], Valerie Samouillan [i], Carlos Enrich [j,k], Gustavo Chiabrando [a,b,*,2], Vicenta Llorente-Cortés [c,d,h,**,3]

[a] Departamento de Bioquímica Clínica, Facultad de Ciencias Químicas, Universidad Nacional de Córdoba, Argentina
[b] Consejo Nacional de Investigaciones Científicas y Técnicas (CONICET), Centro de Investigaciones en Bioquímica Clínica e Inmunología (CIBICI), Córdoba, Argentina
[c] Institute of Biomedical Research of Barcelona (IIBB)-Spanish National Research Council (CSIC), Barcelona, Spain
[d] Biomedical Research Institute Sant Pau (IIB Sant Pau), Barcelona, Spain
[e] SCAC, Universitat Autònoma de Barcelona (UAB), Bellaterra, Spain
[f] Metabolic Basis of Cardiovascular Risk, Biomedical Research Institute Sant Pau (IIB Sant Pau), Hospital de la Santa Creu i Sant Pau. CIBER de Diabetes y enfermedades Metabólicas Asociadas (CIBERDEM), Barcelona. Spain
[g] Department of Cardiology, Hospital de la Santa Creu i Sant Pau, Biomedical Research Institute Sant Pau (IIB Sant Pau), Universitat Autonoma de Barcelona, Barcelona, Spain
[h] CIBERCV, Institute of Health Carlos III, 28029 Madrid, Spain
[i] CIRIMAT, Université de Toulouse, Université Paul Sabatier, Equipe PHYPOL, 31062 Toulouse, France
[j] Unitat de Biologia Cel·lular, Departament de Biomedicina, Facultat de Medicina i Ciències de la Salut, Universitat de Barcelona, Barcelona, Spain
[k] Centre de Recerca Biomèdica CELLEX, Institut d'Investigacions Biomèdiques August Pi i Sunyer (IDIBAPS), Barcelona, Spain

ARTICLE INFO

Keywords:
High-fat diet
Lipid droplets
Cholesteryl esters
Heart
Lipoprotein
Insulin
LRP1

ABSTRACT

Background: Antibodies against the P3 sequence (Gly1127-Cys1140) of LRP1 (anti-P3 Abs) specifically block cholesteryl ester (CE) accumulation in vascular cells. LRP1 is a key regulator of insulin receptor (InsR) trafficking in different cell types. The link between CE accumulation and the insulin response are largely unknown. Here, the effects of P3 peptide immunization on the alterations induced by a high-fat diet (HFD) in cardiac insulin response were evaluated.

Methods: Irrelevant (IrP)- or P3 peptide-immunized rabbits were randomized into groups fed either HFD or normal chow. Cardiac lipid content was characterized by thin-layer chromatography, confocal microscopy, and electron microscopy. LRP1, InsR and glucose transporter type 4 (GLUT4) levels were determined in membranes and total lysates from rabbit heart. The interaction between InsR and LRP1 was analyzed by immunoprecipitation and confocal microscopy. Insulin signaling activity and glucose uptake were evaluated in HL-1 cells exposed to rabbit serum from the different groups.

Findings: HFD reduces cardiac InsR and GLUT4 membrane levels and the interactions between LRP1/InsR. Targeting the P3 sequence on LRP1 through anti-P3 Abs specifically reduces CE accumulation in the heart independently of changes in the circulating lipid profile. This restores InsR and GLUT4 levels in cardiac membranes as well as the LRP1/InsR interactions of HFD-fed rabbits. In addition, anti-P3 Abs restores the insulin signaling cascade and glucose uptake in HL-1 cells exposed to hypercholesterolemic rabbit serum.

* Correspondence to: Departamento de Bioquímica Clínica, Facultad de Ciencias Químicas, Universidad Nacional de Córdoba, Haya de la Torre s/n, Ciudad Universitaria, 5000 Córdoba, Argentina.
** Correspondence to: Institute of Biomedical Research of Barcelona (IIBB)-Spanish National Research Council (CSIC), Biomedical Research Institute Sant Pau (IIB Sant Pau), Sant Quintí 77-79, 08041 Barcelona, Spain.
E-mail addresses: gustavo.chiabrando@unc.edu.ar (G. Chiabrando), vicenta.llorente@iibb.csic.es, cllorente@santpau.cat (V. Llorente-Cortés).
[1] These authors equally contributed to this work
[2] ORCID: 0000-0001-8902-6693
[3] ORCID: 0000-0001-8591-7632

https://doi.org/10.1016/j.biopha.2022.113270
Received 4 May 2022; Received in revised form 2 June 2022; Accepted 6 June 2022
Available online 13 June 2022

Interpretation: LRP1-immunotargeting can block CE accumulation within the heart with specificity, selectivity, and efficacy, thereby improving the cardiac insulin response; this has important therapeutic implications for a wide range of cardiac diseases.
Funding: Fundació MARATÓ TV3: grant 101521-10, Instiuto de Salud Carlos III (ISCIII) and ERDF PI18/01584, Fundación BBVA Ayudas a Equipos de Investigación 2019. SECyT-UNC grants PROYECTOS CONSOLIDAR 2018-2021; FONCyT, Préstamo BID PICT grant 2015-0807 and grant 2017-4497.

1. Introduction

Cardiovascular disease (CVD) is the leading cause of death worldwide and is frequently associated with metabolic syndrome (MS) and type 2 diabetes mellitus (T2DM)[1–4]. Individuals with MS or T2DM have a 2.5-times higher risk of developing heart failure than healthy individuals [5], and frequently present myocardium steatosis, which is associated with alterations in insulin signaling [6–8] and precedes diastolic dysfunction and loss of metabolic flexibility [9–11]. Further, insulin resistance is associated with pathological remodeling of the heart, which is characterized by concentric hypertrophy of the left ventricle, interstitial fibrosis, and extracellular matrix (ECM) remodeling that leads to diastolic dysfunction [12–14]. Recently, left ventricle myocardial remodeling has been linked to high levels of cholesteryl ester (CE)-enriched lipoproteins, such as low-density lipoprotein (LDL), using paired lipid and cardiovascular magnetic resonance data, in a one-sample Mendelian randomization study that included 17 311 individuals [15]. However, the molecular mechanisms underlying the link between lipoprotein-derived cardiac lipid accumulation, insulin action, and cardiac dysfunction are largely unknown.

The susceptibility of LDL particles to aggregate is associated with increased cardiovascular mortality [16]. The small, dense LDL particles (prevalent in MS and T2DM patients) have a higher tendency to be retained and aggregated (agLDL) in the extracellular spaces of several tissues, including the arterial intima [17–19]. AgLDL, in contrast to native LDL, is taken up by the LDL receptor-related protein 1 (LRP1), a receptor that is upregulated by hypercholesterolemic conditions in cells of the cardiovascular system (including smooth muscle cells, macrophages, and cardiomyocytes) [20–22]. The interaction of LRP1 with agLDL facilitates the selective uptake and transfer of CEs from agLDL to intracellular lipid droplets of vascular and cardiac cells [21,22]. Of note, LRP1-mediated agLDL uptake decreases insulin-induced intracellular signaling, glucose transporter type 4 (GLUT4) translocation to the plasma membrane, and glucose uptake by HL-1 cells [6]. In fat and muscle cells, LRP1 regulates the intracellular trafficking of insulin-responsive GLUT4 storage vesicles (GSV) [23]. Under insulin stimulation, GSVs are trafficked and fused with the plasma membrane by a mechanism that is dependent on the activation of the phosphatidylinositol-3-kinase (PI3K)/protein kinase B (Akt)/AS160 (Akt substrate of 160 kDa) pathway [24]. LRP1 interacts with insulin receptor (InsR) to regulate InsR-associated intracellular signaling in neurons, hepatocytes, and cardiomyocytes [6,25,26]. In addition, in retinal Müller glial cells, blocking LRP1 exocytosis towards the plasma membrane disturbs intracellular signaling induced by insulin[27]. These data suggest that LRP1 is critical for the link between lipid accumulation and insulin signaling in different cell types.

The LRP1 P3 peptide sequence of H-GDNDSEDNSDEENC-NH2 (Gly1127–Cys1140) is located on the CR9 domain of the extracellular alpha chain, cluster II and is crucial for the interaction of this receptor with CE-enriched lipoproteins [28]. We previously showed that polyclonal antibodies against the P3 sequence (anti-P3 Abs) efficiently reduced foam cell formation and atherosclerosis in *in vitro*, *ex vivo,* and *in vivo* models [28,29]. In particular, purified anti-P3 Abs have a higher affinity for the P3 epitope than agLDL, blocking the binding of this atherogenic LDL to LRP1 and its subsequent uptake by vascular cells [28]. In *in vivo* studies, immunization against LRP1 prevents intracellular CE accumulation in the vasculature and harmful coupling of pro-inflammatory signaling in rabbits, as well as in *ex vivo* human macrophages or human coronary vascular smooth muscle cells exposed to rabbit hypercholesterolemic sera [29]. The CR9 domain (which binds anti-P3 Abs) show scarce affinity for serpins, such as plasminogen activator inhibitor-1 and protease nexin 1, which induce a protective signal in the heart [30]. This makes CR9 an ideal target for blocking LRP1 interactions with pathological ligands (atherogenic lipoproteins) but without altering interactions with protective ligands (protease-inhibitor complexes) [31]. On the basis of these previous results, the main objectives of the present study were i) to evaluate the impact of CE-enriched lipoproteins on cardiac lipid accumulation, and ii) to study the consequences of CE accumulation on cardiac insulin response. For this, we specifically blocked the interaction of CE-enriched lipoproteins with LRP1 receptor *via* immunization with the peptide P3.

2. Methods

2.1. Animal model

Experimental procedures were approved by the Ethics Committee of Animal Experimentation of the Vall d'Hebron Institute of Research with registration number 46/17, and performed in accordance with Spanish legislation and also with the European Union directives (2010/63/ EU). Female rabbits (thirty New Zealand White [NZW]) were fed i) a chow R-01 diet from Granja San Bernardo with the following formulation: 17.3 % protein, 16.7 % fiber, and 3 % fat, or ii) a high-fat diet (HFD) TD.88 137 (42 % fat, 0.2 % cholesterol) from ENVIGO, for 1 month (Fig. S1a). Animals were acclimated for one week before the first immunization and immunized with a primary injection and four reminder doses (R1-R4) every 21 days of irrelevant peptide (IrP group; $n = 10$) or P3 peptide (P3 group; $n = 10$) conjugated to the carrier. The four doses of IrP or P3 antigen conjugated with keyhole limpet hemocyanin (KLH) were administered subcutaneously (138 μg/kg, maximum volume 150 μl). For the first immunization, IrP or P3-KLH peptides were emulsified in complete Freund's adjuvant; the rest of the immunizations were done using IrP or P3-KLH conjugated in incomplete Freund's adjuvant (both from Sigma Aldrich). During the immunization period, the animals were fed a normal chow diet. Starting at the R4 time point, IrP- and P3-immunized rabbits were randomly divided into a chow-fed or a HFD-fed group. Ten rabbits ($n = 5$ IrP-injected, $n = 5$ P3-injected) continued the chow diet, whereas ten rabbits ($n = 5$ IrP-injected, $n = 5$ P3-injected) received HFD for 30 days. Four groups of rabbits were included in this study: i) chow IrP-immunized, ii) chow P3-immunized, iii) HFD IrP-immunized, and iv) HFD P3-immunized (Fig. S1a). Animals were weighed at pre- and post-diet time points, and serum levels of specific anti-P3 antibodies were determined by ELISA. At the end of the study, animals were euthanized, and the hearts and livers were removed aseptically and processed for molecular, confocal, electron microscopy, biophysical, and immunohistochemical studies.

2.2. Peptide synthesis and conjugation

The P3 peptide used to immunize rabbits contained the sequence GDNDSEDNSDEENC, which corresponds to the amino acids 1127–1140 located in LRP1 cluster II (domain CR9) [28,29]. The P3 sequence corresponds to an area of high homology between human and rabbit LRP1, with the difference that the asparagine (N) in humans was replaced by a

serine (S) in the rabbit protein. In addition, the amino acid C1140 in the rabbit sequence (GDNDCEDNSDEENC) was replaced by S to achieve greater peptide immunogenic effectiveness. The irrelevant peptide (IrP) has the same sequence than P3 but with amino acids in D-enantiomer configuration. Both peptides were synthesized by the Laboratory of Proteomics & Protein Chemistry, Department of Experimental & Health Sciences, Pompeu Fabra University, by the solid-phase method using a Prelude peptide synthesizer (Protein Technologies, Inc.). Peptides were purified by high-performance liquid chromatography (HPLC, Waters 600) using UV detection at 254 nanometers (Waters 2487) and characterized by mass spectrometry (Applied Biosystems 4700 Proteomics Analyser). Peptide conjugation to KLH or BSA (Sigma, St. Louis, MO) was performed as previously described [32]. Peptide–KLH conjugates were used for rabbit immunization, and peptide-BSA conjugates were used as a substrate in the immunoassay ELISA to detect specific anti-P3 Abs in the rabbit serum.

2.3. Detection of specific antibodies

ELISAs were standardized to detect specific antibodies against P3 peptides. Briefly, all sera were analyzed using 96-well polystyrene plates (442 404 Maxisorp, NUNC, Labclinics, Spain) coated with peptide-BSA or BSA as a control to detect unspecific antibodies. ELISA plates were incubated with several serum dilutions for 90 min; after washes, anti-rabbit IgGs conjugated to peroxidase (170–6515, BioRad, Spain) were added to detect the antigen–antibody complexes. ELISA was revealed using OPD substrate (P9187, Sigma Aldrich, Spain), and the absorbance was read in a Multilabel reader Victor3 (Perkin Elmer, Turku, Finland) at 450 nm. The measured absorbances were adjusted to a 4PL curve to calculate the IC50. The parameter 1/IC50 was used as the antibody titer.

2.4. Biochemical analysis of serum and isolated lipoproteins

Serum lipids and lipoproteins, including cholesterol and triglyceride (TG) (corrected from free glycerol), were enzymatically determined using commercial kits adapted to a COBAS 6000 autoanalyzer (Roche Diagnostics) [33]. VLDL, LDL, and HDL lipoproteins were isolated by sequential ultracentrifugation at 100,000*g* for 24 h at a density of 1.006, 1.019–1.063 and 1.063–1.21 g/ml, respectively, using an analytical fixed angle rotor (50.3, Beckman Coulter). The composition of each lipoprotein, including total and free cholesterol, triglycerides and phospholipids, was determined by commercial methods adapted to the COBAS 501 autoanalyzer. Lipoprotein protein concentrations were determined by the bicinchoninic acid method (Termo Scientific, Rockford, IL). Lipid and protein concentrations were used to calculate the total mass of each lipoprotein.

2.5. Glucose tolerance test (GTT)

The glucose tolerance test (GTT) was performed at week four of the dietetic intervention under fasting conditions. Basal blood glucose levels were measured from an ear nick through ACCU-CHEK® Aviva glucometer (Roche Molecular Systems). Rabbits were then intraperitoneally injected with glucose (1.3 mg/g BW). Blood glucose was measured at 15 min, 30 min, 60 min, 120 min and 180 min after glucose injection. The area under the curve (AUC) of the response curve was then calculated using the software Prism 4.0 [34].

2.6. Cell culture

The murine HL-1 cardiomyocyte-derived cell line was generated by Dr. W.C. Claycomb (Louisiana State University Medical Centre, New Orleans, Louisiana, USA). HL-1 cells were maintained in Claycomb medium (Sigma-Aldrich) in plastic dishes [6], coated with 12.5 g/ml fibronectin (Sigma-Aldrich) and 0.02 % gelatin, in a 5% CO2 atmosphere at 37 °C. HL-1 cells were fasted with 0.2 % FBS for 24 h and then were incubated with serum (0.25 %, 1.5 h) from the different rabbit groups i) chow IrP-immunized, ii) chow P3-immunized, iii) HFD IrP-immunized, and iv) HFD P3-immunized-rabbits.

2.7. Determination of neutral lipid content in heart and liver

Myocardial, hepatic, and cellular lipids were extracted and partitioned by thin-layer chromatography. Lipids were extracted with dichloromethane/methanol [1:2] and cholesteryl esters (CE), free cholesterol (FC), and triglycerides (TG) were analyzed by thin-layer chromatography (TLC) on silica G-24 plates as previously described [35,36]. Different concentrations of standards (a mixture of cholesterol, cholesterol palmitate and triglycerides) were applied to each plate. The spots corresponding to CE, TG, and FC were quantified by densitometry against the standard curve of cholesterol palmitate, triglycerides and cholesterol, respectively, using a computing densitometer.

2.8. Assessment of lipid droplet morphology and size

2.8.1. Electron microscopy

Cells growing in 60 mm plates were washed in PBS 1X and then fixed with 2.5 % glutaraldehyde in 0.1 M phosphate buffer at room temperature for 1 h. Next, cells were gently scraped and then pelleted in 1.5 ml tubes. Cardiac tissue was cut into small pieces, extensively washed in PBS 1X and fixed with 2.5 % glutaraldehyde, 2 % PFA in 0.1 M phosphate buffer overnight. Samples were dehydrated, embedded in Spurr and sectioned using Leica ultramicrotome (Leica Microsystems). Ultrathin sections (50–70 nm) were stained with 2 % uranyl acetate for 10 min, a lead-staining solution for 5 min and then analyzed with a transmission electron microscope, JEOL JEM-1010 fitted with a Gatan Orius SC1000 (model 832) digital camera at the Unit of Electron Microscopy, Scientific and Technological Centers of the University of Barcelona, School of Medicine and Health Sciences (Barcelona, Spain).

2.8.2. Confocal microscopy

A stock solution of the fluorescent dye boron-dipyrromethene (BODIPY) was diluted to a final concentration of 1 mg/ml in DMSO. To study lipid droplets, heart slides were incubated for 30 min with 100 μl of BODIPY (1 mg/ml in DMSO). Images of immunostained cells were analyzed on a Leica inverted fluorescence confocal microscope (Leica TCS SP2-AOBS; excitation wavelength 480 nm, emission maximum 515 nm).

2.9. FTIR, freeze-dried state

Fourier transform infrared spectroscopy/attenuated total reflectance (FTIR/ATR) spectra of the freeze-dried lipoproteins and tissues were acquired using a Nicolet 5700 FTIR instrument (Thermo Fisher Scientific, Waltham, MA) equipped with an ATR device with a KBr beam splitter and a MCT/B detector as previously described [37,38]. The ATR accessory used was a Smart Orbit with a type IIA diamond crystal (refractive index 2.4). Freeze-dried samples (1 mg) were directly deposited on the entire active surface of the crystal and gently pressed with a Teflon tip to assure good contact. For each sample, 80 interferograms were recorded in the 4000–450/cm-1 region, co-added and Fourier transformed to generate an average spectrum of the segmented heart part with a nominal resolution of 1 cm-1 using Omnic 8.0 (Thermo Fisher Scientific, Waltham, MA). A single-beam background spectrum was collected from the clean diamond crystal before each experiment, and this background was subtracted from the spectra. Spectra were then subjected to ATR and baseline corrections and normalized using the maximum of the Amide II peak. Second derivatives were used to enhance the chemical information present in overlapping infrared absorption bands of spectra.

2.10. Determination of InsR and LRP1 levels in membranes and total cardiac lysates

2.10.1. Tissue subfractionation

Tissue was washed with PBS 1X and homogenized using a POLYTRON® Immersion Dispersers PT 2500 as previously described [35,38]. In brief, to obtain membrane protein fraction, the homogenized tissue was filtered using QIAshredder spin columns (79 656, QIAGEN), incubated with lysis buffer A (NaCl 150 mM, HEPES 50 mM, digitonin 25 μg/ml, 1 M hexylene glycol, protease inhibitor cocktail 1 % v-v) using an end-over-end rotator. After centrifugation, the supernatant containing mainly cytosolic proteins was removed and the the pellet was incubated with lysis buffer B (NaCl 150 mM, HEPES 50 mM, igepal 1 % v-v, 1 M hexylene glycol, protease inhibitor cocktail 1 % v-v). After centrifugation, the supernatant containing mainly plasma membrane proteins was collected. Proteins were analyzed by Western blot with antibodies against rabbit LRP1 (ab92544 Abcam) or InsR (LS-C63091, LSBio) or GLUT4 (LS-C123618, LSBio). Total cardiac lysates were obtained using RIPA buffer (50 mM Tris-HCl pH 8.0, 150 mM NaCl, 1 % Triton X-100, 0.5 % sodium deoxycholate, 0.1 % SDS, 1 mM PMSF, 10 mM sodium ortho-vanadate, and protease inhibitor cocktails (Sigma-Aldrich, St. Louis, MO, USA), and proteins were analyzed by Western blot. Anti-ATP1A1 (MA3–928, Invitrogen) and anti-GAPDH (sc-81 545, Santa Cruz Biotechnology) were used as total and plasma membrane loading controls, respectively.

2.10.2. Biotin-labeling of cell surface proteins

HL-1 cells were exposed to rabbit's serum (0.25 %) for 1.5 h and then treated with insulin (100 nM) for 30 min. Biotin-labeling protein assay (EZ-Link Sulfo-NHS-SS-Biotin (21 331,Thermo Scientific) was used to determine the protein levels of GLUT4 at the cell surface. Briefly, cells were incubated first with a biotin solution 0.12 mg/ml for 2 h at 4 °C and, then with 0.1 mM glycine solution for 30 min at 4 °C and then washed three times with PBS 1X. Biotinylated proteins were pulled down by streptavidin-conjugated agarose beads (Pierce Streptavidin Agarose (20 353, Thermo Scientific) for 2 h at room temperature. Biotinylated and total proteins (10 % of proteins incubated with agarose beads) were analyzed by Western blot after incubated with rabbit anti-GLUT4 (sc-7938; Santa Cruz Biotechnology), mouse monoclonal anti-ATP1A1 (MA3–928, Invitrogen), or mouse monoclonal anti-β-actin (A2228; Sigma-Aldrich) antibodies overnight at 4 °C, following by incubation with secondary antibodies (goat anti-mouse and goat anti-rabbit; Dako) diluted 1/10 000 for 1 h at room temperature. Signals were detected with the ECL immunoblotting detection system (GE Healthcare) and results were quantitatively analyzed using Chemidoc (BioRad). Biotinylated-ATP1A1 and β-actin were used as loading control of plasma membrane protein and total protein extracts, respectively.

2.11. Western blot analysis

Protein extracts were obtained using RIPA buffer (50 mM Tris-HCl pH 8.0, 150 mM NaCl, 1 % Triton X-100, 0.5 % sodium deoxycholate, 0.1 % SDS, 1 mM PMSF, 10 mM sodium ortho-vanadate, and protease inhibitor cocktails) (Sigma-Aldrich, St. Louis, MO, USA). Cell protein extracts (40 μg) were diluted in 5 × sample buffer with dithiothreitol (DTT) and heated for 5 min at 95 °C. Electrophoresis on 10 % SDS-polyacrylamide gels was performed, and proteins were transferred to nitrocellulose membrane (GE Healthcare Life Science, Amsterdam, The Netherlands). Nonspecific binding was blocked with 5 % non-fat dry milk in a Tris-HCl buffer containing 0.01 % Tween 20 (TBS-T) for 60 min at room temperature. Membranes were incubated overnight at 4 °C with primary antibodies and then with secondary antibodies (goat anti-mouse and goat anti-rabbit; Dako) diluted 1/10 000 for 1 h at room temperature. For signaling activation analysis, the following primary antibodies were used: rabbit anti-Akt (9272, Cell Signaling Technology), rabbit anti-pAkt (Ser473, 07–789, Merck), rabbit anti-AS160 (ab24469, Abcam), rabbit anti-pAS160 (Thr642, ab65753, Abcam), and mouse monoclonal anti-β-actin (A2228; Sigma-Aldrich). Signals were detected with the ECL immunoblotting detection system (GE Healthcare), and the results were quantitatively analyzed using Chemidoc (BioRad).

2.12. Confocal microscopy

The procedures were followed as previously described [6]. HL-1 cardiomyocyte were washed with PBS 1 × , fixed with 4 % paraformaldehyde (PFA), permeabilized for 30 min with 0.5 % (v/v) saponin and blocked with 2 % bovine serum albumin (BSA). Primary antibodies were used for 1 h, using rabbit anti-LRP1 monoclonal antibody (ab92544, Abcam) or mouse anti-InsR antibody (ab69508; Abcam), and secondary antibodies conjugated with Alexa Fluor (1/800) and Hoechst 33 258 (1/2000) were used for 1 h. Finally, cells were mounted with Mowiol 4–88 (Calbiochem (Merck, Darmstadt). Images were obtained with an Olympus FluoView FV1200 confocal microscope (Olympus), processed using the FV10-ASW Viewer 3.1 (Olympus) and quantified by ImageJ software. Quantification of the colocalization level was analyzed by JACoP plug-in from ImageJ software [6].

Heart slides were washed with PBS 1 × , permeabilized for 5 min with PBS 1 × with 1 % Tween and blocked with PBS 1 × with 1 % BSA. Primary antibodies were used for 1 h (mouse anti-GLUT4 monoclonal antibody LS-C123618. LS-Bio) (1/50) and secondary antibody conjugated with alexa fluor (1/100) and Hoechst 33 258 (1/1000) were used for 1 h. Slides were then mounted with ProLong™ Gold Antifade Mountant (P10144, Thermoscientific). Images were obtained with an Olympus FluoView FV1200 confocal microscope (Olympus), processed using the FV10-ASW Viewer 3.1 (Olympus) and quantified by ImageJ software.

2.13. Immunoprecipitation (IP) assay

Cardiac tissue from the rabbit groups and HL-1 cells exposed to rabbit's serum from each of the four groups were subjected to immunoprecipitation (IP) assays as previously described [6]. Briefly, protein extracts were incubated with rabbit anti-LRP1 monoclonal antibody (ab92544, Abcam) or rabbit non-immune IgG as control (2 μg/200 μg of total proteins) for 2 h at 4 °C. Samples were then incubated with protein A–conjugated agarose agarose beads following the manufacturer's procedure (sc-2001; Santa Cruz Biotechnology) overnight at 4 °C. Immunoprecipitated proteins were characterized by Western blot using anti-InsR (ab69508; Abcam) and anti-LRP1 (ab92544; Abcam) monoclonal antibodies, and secondary antibodies (goat anti-mouse or goat anti-rabbit; Dako). Signals were detected using ECL immunoblotting detection system (GE Healthcare) and the results were quantitatively analyzed using Chemidoc (BioRad).

2.14. 2-NBDG uptake assay

HL-1 cells were exposed to rabbit's serum (0.25 %) for 1.5 h and then treated with insulin (100 nM) in the presence of 2-deoxy-2-[(7-nitro-2,1,3-benzoxadiazol-4-yl) amino]-D-glucose (2-NBDG solution; Sigma-Aldrich) (80 μM) for 30 min. Cells were then washed with 1X PBS, fixed with 4 % paraformaldehyde, blocked with 2 % BSA, and incubated with Hoechst 33 258 colorant (1/2000) for 1 h [6]. Fluorescence was detected with a Leica DMI8 biological microscope (Leica, Germany). Total fluorescence in the whole cell area was quantified by ImageJ software.

2.15. Statistical analysis

Differences between study groups were analyzed using two-way analysis of variance (ANOVA) followed by a Tukey *post-hoc* test. The statistical software R (www.r-project.org) was used for all statistical analyses. Differences were considered statistically significant when $p <$

0.05.

3. Results

3.1. Immunization with the P3 peptide produces anti-P3 Abs in rabbits

The experimental rabbit immunization procedure included the primary injection and four booster injections of either the P3 peptide or an irrelevant peptide (IrP), and two blood extractions at the checking points. Rabbits were either fed a high-fat diet (HFD) or a control diet (*i.e.*, normal chow) for 30 days (Fig. S1a). ELISA analysis showed a significant anti-P3 Abs production that was maintained throughout the entire dietetic intervention period in the serum of P3-immunized rabbits, based on the levels of antibodies at the two checkpoints, Chk1 and Chk2 (Fig. S1b, middle and left panel). Rabbits immunized with the IrP peptide did not show any response against P3 in ELISA (Fig. S1c).

3.2. Lipid profile and peripheral insulin resistance induced by HFD are not modified by anti-P3 Abs

Cholesterol levels (Fig. 1a) and triglyceride (TG) levels (Fig. 1b) were higher in the serum of HFD-fed rabbits than in serum of control diet rabbits, with no differences between P3- or IrP-immunized rabbits. Liver lipid extraction followed by TLC showed a significant upregulatory effect of HFD on levels of hepatic CE, TG, and free cholesterol (FC), also with no differences between P3- or IrP-immunized rabbits (Fig. 1c-f).

Rabbits in all four groups (*e.g.*, HFD P3, HFD IrP, chow P3, and chow IrP) exhibited a similar increase in body weight over the study period (30 days) (Fig. S2a). However, the glucose tolerance test (GTT) showed that HFD induced glucose intolerance in both IrP and P3 immunized groups (Fig. S2b, c), indicating that the impairment of peripheral insulin response induced by HFD was not affected by P3 immunization.

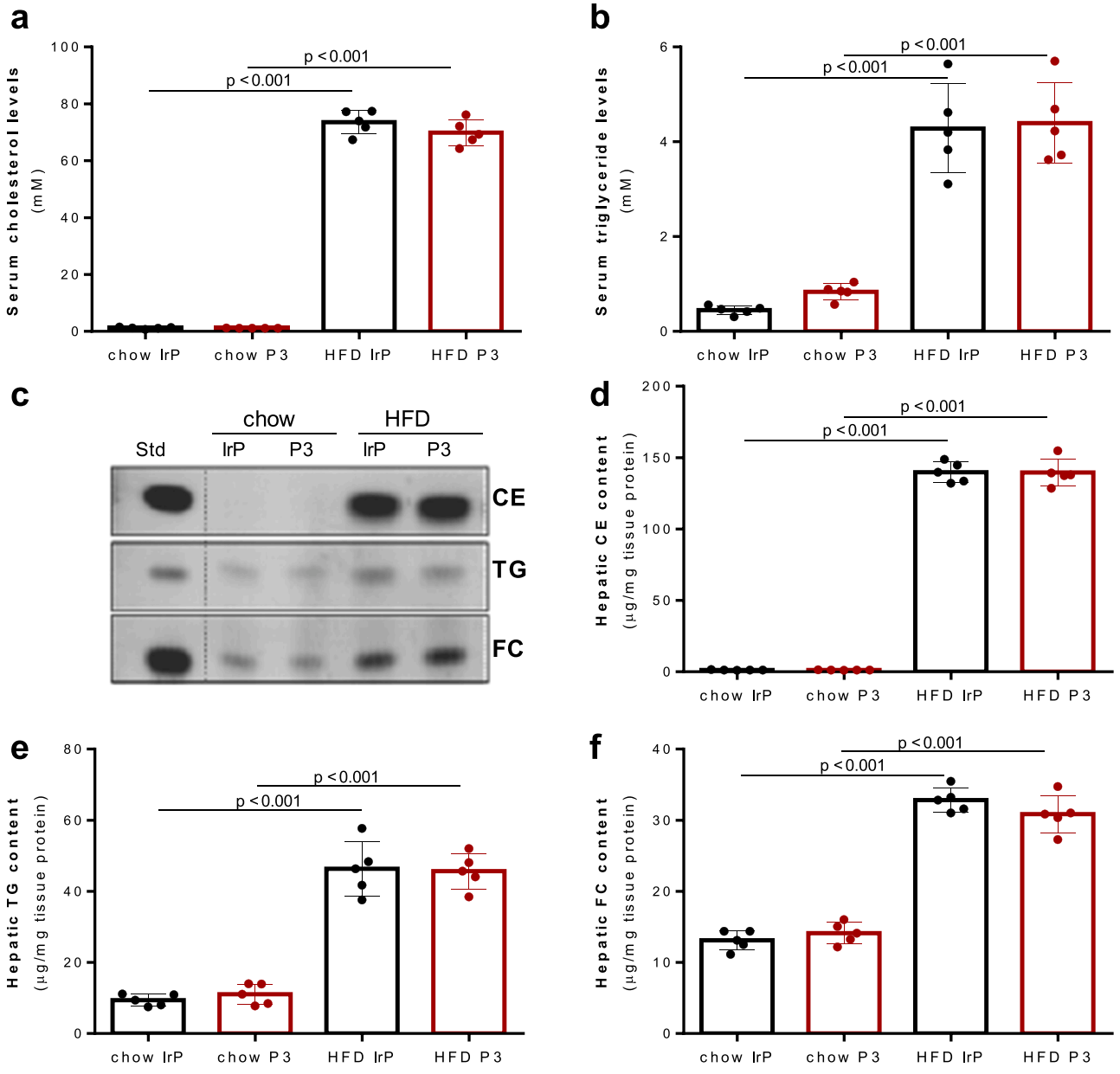

Fig. 1. Immunization with P3 peptides does not alter serum or liver lipid profiles in rabbits. (a, b) Bar graphs showing serum cholesterol and triglyceride (TG) levels. (c) Representative thin-layer chromatography (TLC) of cholesterol ester (CE), TG, and free cholesterol (FC) in the liver. The CE/TG/FC bands from the standards (Std) are shown. (d, e, f) Bar graphs showing results as mean ± SD of CE, TG, or FC, quantified as µg/mg tissue protein. Statistical significance was determined by 2-way ANOVA with Tukey's post-hoc test. $n = 5$/group.

3.3. Cholesteryl esters in HFD-fed rabbits are mainly carried by VLDL and LDL lipoproteins

The HFD-fed groups had much higher total mass of circulating LDL (IrP: 32.10 ± 3.53 *vs* 1.23 ± 0.68 g/L, $p < 0.001$) and, to a lesser extent, of VLDL (IrP: 5.90 ± 0.85 *vs* 0.35 ± 0.13 g/L, $p < 0.001$), than either of the chow-fed groups (Fig. S3), with most of HFD-increased plasma cholesterol carried by LDL and VLDL. Both VLDL and LDL had much higher CE content in HFD rabbits (Fig. S3c,d) than in control rabbits (Fig. S3a,b), with no differences in the lipid/protein profile of VLDL and LDL lipoproteins between IrP- and P3-injected rabbits, irrespective of diet. Despite the low total mass of circulating VLDL and LDL in serum from control groups, these lipoproteins had higher proportion of TG (Fig. S3a,b) than the HFD groups (Fig. S3c,d), irrespective of IrP- or P3-immunization. HDL was the minor lipoprotein class, with a similar composition in the four groups. Overall, the lipoprotein fraction content of VLDL, LDL, and HDL lipoprotein masses, as well as of TG, phospholipid (Ph), FC, CE, and protein levels, were similar between IrP- and P3-injected groups irrespective of diet. These results clearly indicate that P3 immunization did not significantly alter the lipid/protein profile of VLDL, LDL, or HDL in rabbits.

3.4. The spectral FTIR lipid signature of CE-enriched lipoproteins (VLDL and LDL) is evident in rabbit heart

FTIR spectroscopy is based upon the interaction between the IR radiation and the covalent bonds of molecules. IR spectroscopy exploits the fact that molecules have specific frequencies at which they vibrate corresponding to discrete energy levels (vibrational modes). C-H stretching vibrations arise essentially from lipids and lead to absorption bands in the 3050–2800 cm^{-1}. In this infrared zone [3050–2800 cm^{-1}] of the FTIR spectra, human and rabbit lipoproteins showed the specific absorption of asymmetric and symmetric (CH3) and (CH2) stretching, mainly associated with the vibrational answer of the different classes of lipids, as well as the (C═H) stretching at 3010 cm^{-1} that corresponds to unsaturated lipids (Fig. S4a). The band associated with unsaturated lipids as well as the specific bands of CE in the [2900–2880 cm^{-1}] zone were better detected on the second derivative spectra (Fig. S4b) that enhances resolution for both lipoproteins and rabbit hearts.

In the [3050–2800 cm^{-1}] zone, the spectral signatures of lipids from LDL and VLDL were identified in the FTIR profile of hearts from both chow and HFD rabbit groups (Fig. 4a, Fig. S4a,b). These absorption bands can be detected at the same position both in lipoproteins and heart tissues. This fact indicates that these lipoproteins are one of the main sources of neutral lipids to the heart.

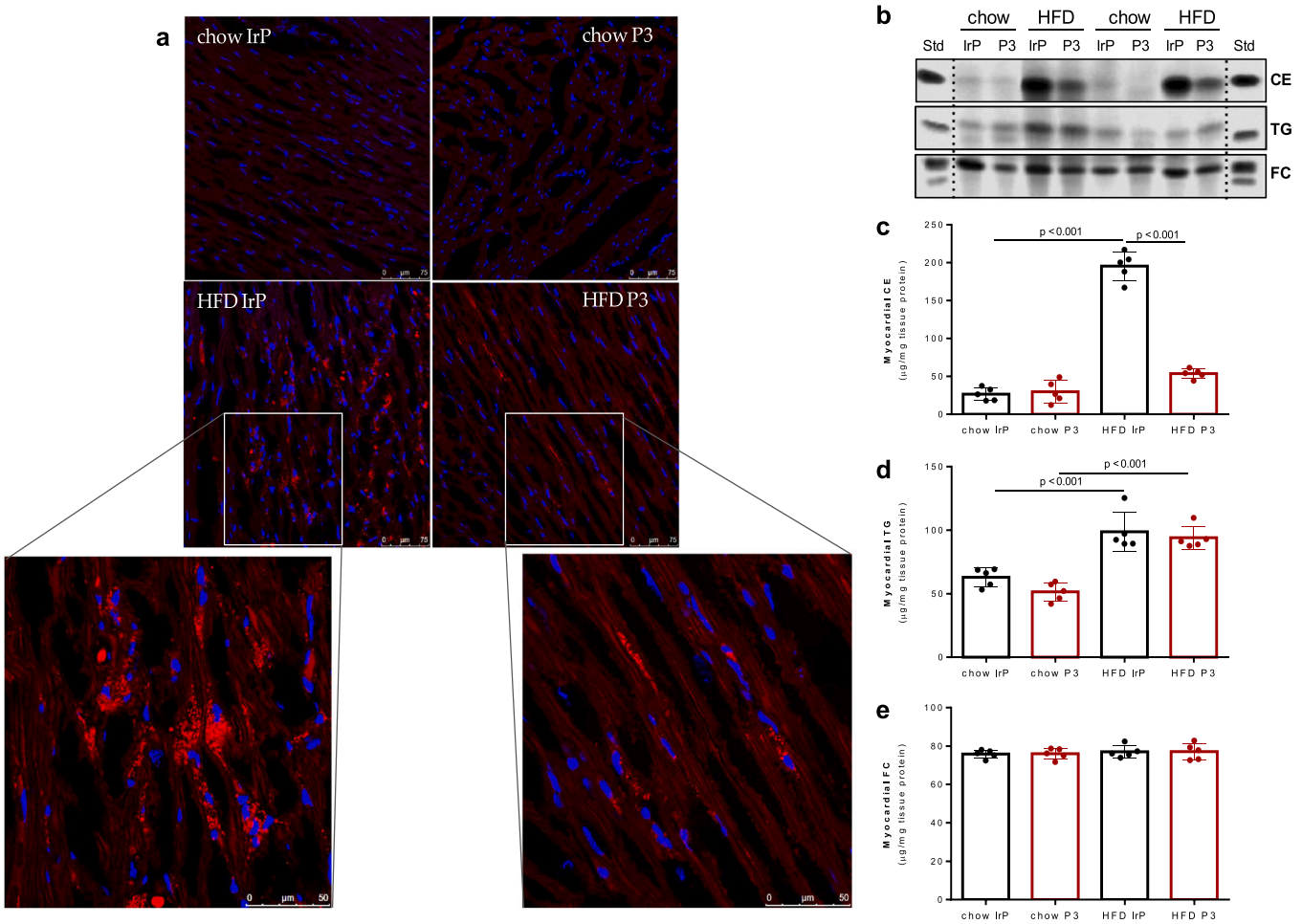

Fig. 2. Anti-P3 Abs specifically block the selective uptake of CE from lipoproteins in the heart. (a) Confocal microscopy images showing BODIPY-stained lipid droplets (*red dots*) in the hearts from the distinct rabbit groups. Cell nuclei are stained with DAPI (blue). (b) Representative TLC of heart lipid extracts and bands corresponding to the cardiac content of cholesteryl esters (CE), triglyceride (TG), and free cholesterol (FC). The CE/TG/FC bands of standards (Std) are shown in duplicate. Bar graph represents the mean ± SD of CE (c), TG (d), or FC (e), expressed as µg/mg tissue protein. Statistical significance was determined by 2-way ANOVA with Tukey's post-hoc test. $n = 5$/group. (For interpretation of the references to colour in this figure, the reader is referred to the web version of this article.)

3.5. Lipoprotein-derived CE accumulation in heart and HL-1 cardiomyocytes is reduced by anti-P3 Abs

Confocal microscopy analysis of BODIPY-stained transversal cross sections from the heart showed lower levels of lipid droplets in the HFD P3 group as compared to HFD IrP group (Fig. 2a). To further explore the impact of P3 immunization of cardiac lipid content, we performed thin-layer chromatography (TLC) of cardiac lipid extracts. TLC showed that HFD strongly increased intramyocardial CE and TG content as compared to chow diet (Fig. 2b–d). P3 immunization showed efficacy in reducing exclusively intramyocardial CE (Fig. 2b,c) but not TG content (Fig. 2b, d). Cardiac FC was similar for all four groups (Fig. 2b, e). Additionally, in *ex vivo* experiments, we explored the effect of increased percentages of serum (0.25–1 %; 1.5 h) from all four groups in the intracellular lipid content of the HL-1 cardiomyocytes. At 1.5 h, HFD serum induced intracellular CE/FC ratio in a dose-dependent manner but no changes in the TG/FC ratio. The anti-P3 Abs present in HFD P3 rabbit serum efficiently blocked the intracellular CE/FC ratio induced by the hypercholesterolemic serum in HL-1 cells at each tested dose (Fig. S5a,b).

3.6. P3 immunization changes the ultrastructure and bioenergetics of lipid droplets in the rabbit heart

Transmission electron microscopy (TEM) of ultrathin sections from heart of HFD-fed rabbits revealed the presence of neutral lipids forming lipid-filled vacuoles in cardiomyocytes of hearts from HFD groups (Fig. 3a,b and S6c,d). These lipid droplets were located between the sarcomere fibers and surrounded by a membrane that seems to be in close contact with mitochondria, as well as by the sarcoplasmic reticulum membrane. An important finding from electron microscopy studies was that lipid droplets in the heart of P3-immunized rabbits (Fig. 3b and S6d) were scarcer, more electrodense and bigger than those found in the heart of IrP injected rabbits (Fig. 3a and S6c). Another important finding was that the inter-sarcomere cytoplasm contained abundant glycogen in proximity with lipid droplets in the heart of HFD IrP (Fig. 3a and S6c) but not in that from HFD P3 rabbits (Fig. 3b and S6d). Similar or even higher abundance of glycogen drops were observed in the surroundings of lipid droplets formed in HL-1 cells exposed to rabbit HFD IrP serum (Fig. S7a, S7b). Lipid droplets were not detected in HL-1 cells exposed to rabbit serum from the other groups.

3.7. Anti-P3 Abs increase membrane InsR levels and restore InsR/LRP1 interaction and insulin signaling impaired by HFD in cardiomyocytes

We then evaluated InsR and LRP1 protein levels in the cardiac membranes and total extracts from the heart of the four different groups. Plasma membrane was disrupted by digitonin fractionation [36], and ATP1A1 (ATPaseNa/K) used as a specific marker for plasma membrane. As shown in Fig. 4a,b, membrane to total InsR ratio was significantly lower in the heart from HFD rabbits compared to than from chow rabbits, however, in the presence of anti-P3 Abs, membrane to total InsR ratio was restored and even exceeded those observed in chow rabbits. As shown in Fig. 4c,d, membrane to total LRP1 ratio was much higher in HFD than in control chow groups without differences between IrP and P3 groups. In addition, immunoprecipitation assays showed that InsR/LRP1 interaction complexes were reduced in the heart of HFD compared to chow groups; and that anti-P3 Abs not only restored but even surpassed the basal levels of InsR/LRP1 complexes observed in the heart of chow animals (Fig. 4e,f). Along the same line, *ex-vivo* experiments showed that treatment of HL-1 cardiomyocytes with HFD IrP serum reduced InsR/LRP1 complex levels in the absence or presence of insulin while HFD P3 serum restored and even increased the levels of InsR/LRP1 complex in these cells (Fig. S8a,b).

Confocal microscopy experiments showed that serum from HFD IrP animals, but not that from HFD P3 animals, reduced InsR and LRP1 colocalization in HL-1 cardiomyocytes (Fig. 5a,b). In addition, HFD IrP serum significantly reduced insulin-induced Akt and AS160 phosphorylation, while HFD P3 serum restored insulin-induced p-Akt and p-AS160 levels to those found in HL-1 cells exposed to chow serum (Fig. 5c-e). Taken together, these results indicate that anti-P3 Abs reduced the deleterious effect of HFD on the InsR/LRP1 association, InsR membrane translocation, and InsR signaling in cardiomyocytes.

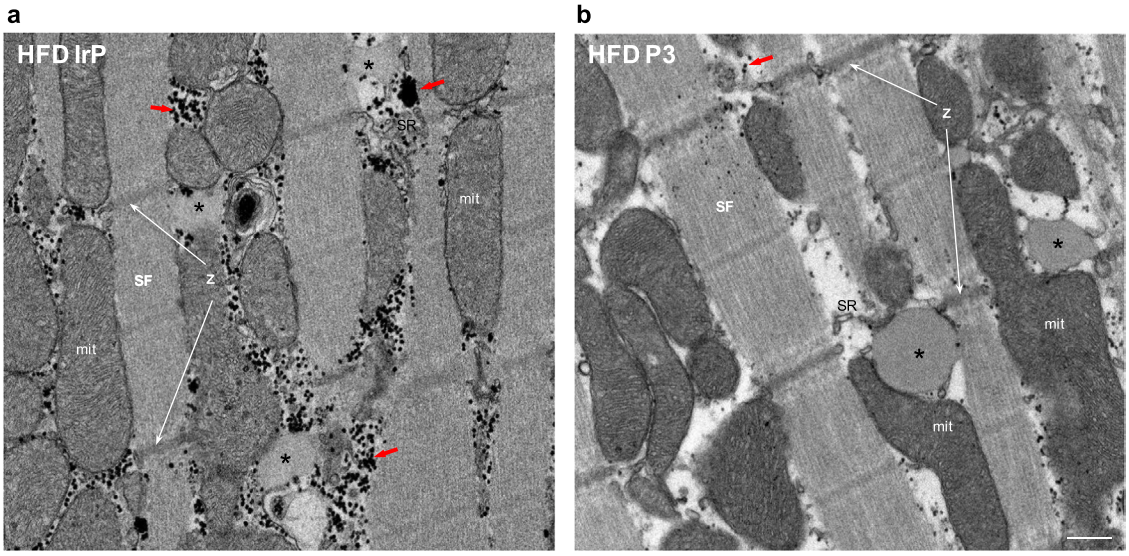

Fig. 3. Anti-P3 Abs alters lipid droplet size and electrodensity as well as the glycogen content induced by HDF. Representative electron microscopy of cardiomyocyte ultrastructure from the heart of HFD-fed rabbits showing differences between the size and electrodensity of lipid droplets (LD) (asterisks) in HFD IrP (a) and HFD P3 (b) rabbit groups. LD are located in the intersarcomeric cytoplasm between the sarcomeric fibers (SF) and in close connection with mitochondria (mit) and sarcoplasmic reticulum (SR). A high number of glycogen (electrodense granules, red arrows) surrounding the LD (asterisks) can also be observed in the heart of HFD IrP group. Representative Z-disc (Z) are indicated. Scale bar: 400 nm. (For interpretation of the references to colour in this figure, the reader is referred to the web version of this article.)

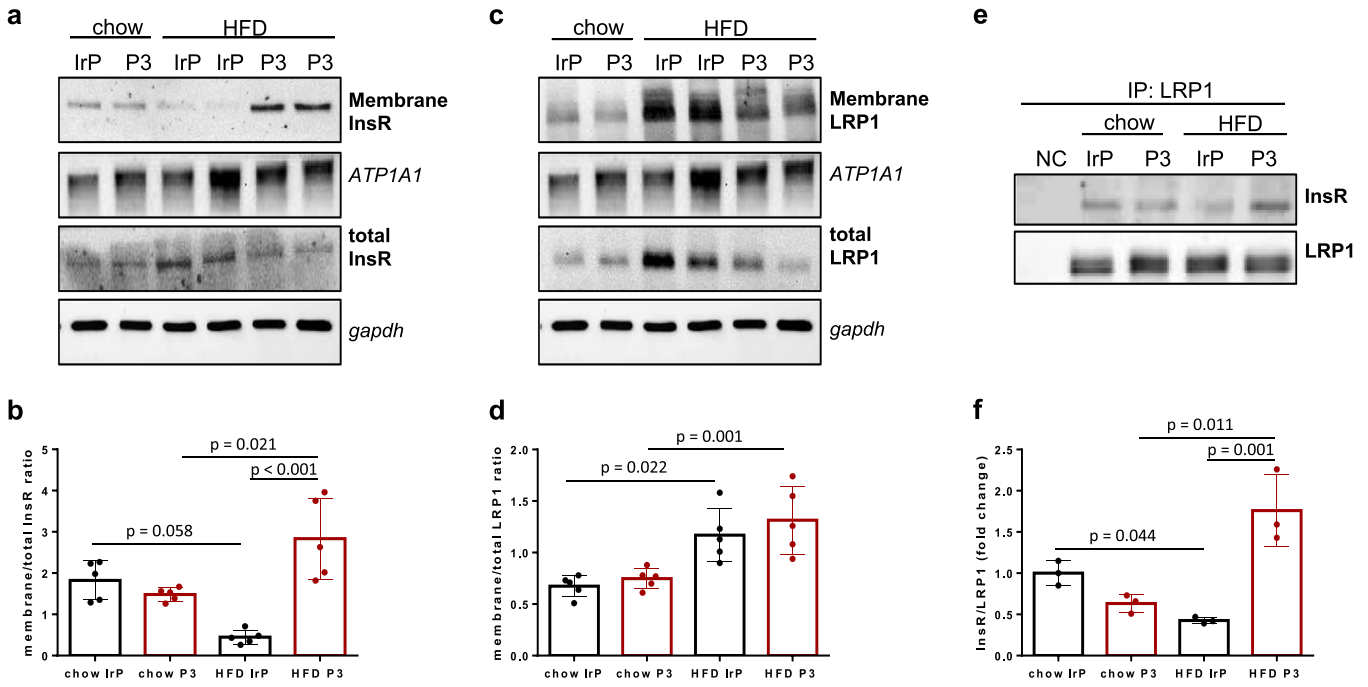

Fig. 4. Anti-P3 Abs prevent the deleterious effects of HFD on cardiac LRP1 and InsR membrane localization and interaction. Representative Western blot analysis of InsR (a) and LRP1 (c) in cardiac membranes and total cardiac lysates. Bar graph showing the InsR (b) and LRP1 (d) ratio between membrane and total levels normalized by ATP1A1 (membranes) or GAPDH (total extracts). $n = 5$/group. (e) Immunoprecipitation assay for LRP1. Myocardial lysates were immunoprecipitated with anti-LRP1 antibodies and analyzed by Western blot assays for InsR and total LRP1. NC, non-immune control without anti-LRP1 Ab. (f) Bar graph showing the densitometry quantification of Western blot bands. Values are expressed as mean ± SD of the relative intensity of LRP1 and InsR bands with respect to the endogenous control and are shown as a fold-change against the mean value of control IrP-immunized group. $n = 3$/group. Statistical significance was determined by 2-way ANOVA with Tukey's post-hoc test.

3.8. Anti-P3 Abs restore GLUT4 membrane levels in HFD hearts and the insulin response in HL-1 cardiomyocytes exposed to HFD serum

Western blot analysis (using ATP1A1 as a specific marker for plasma membrane) and confocal microscopy revealed that membrane to total GLUT4 ratio was much lower in the heart of HFD rabbits than in that of control chow rabbits, however, in the presence of anti-P3 Abs, GLUT4 membrane levels were restored to those observed in control chow rabbits (Fig. 6a-c). In addition, we evaluated whether anti-P3 Abs could restore GLUT4 trafficking to plasma membrane and glucose uptake in HL-1 cardiomyocytes exposed to HFD serum. Biotin-labeling cell surface protein assays showed that insulin failed to induce GLUT4 translocation to the plasma membrane in HL-1 cells exposed to HFD IrP but not in cells exposed to HFD P3 and chow serums (Fig. 6a,b). In line, insulin failed to induce 2-deoxyglucose (2-NBDG) uptake in HL-1 cells exposed to HFD IrP serum but not in cells exposed to HFD P3 and chow serums (Fig. 6c). These results suggest that anti-P3 Abs counteract the deleterious effect of HFD on GLUT4 trafficking to plasma membrane and glucose uptake in cardiomyocytes Fig. 7.

4. Discussion

Here we show that CE accumulation within the heart in response to HFD is driven by LRP1. Immunization of the rabbit model against the P3 sequence of LRP1 is able to reverse myocardial CE accumulation independently of changes in the circulating lipid profile. Here, we also show that intramyocardial CE accumulation is linked to a deficiency of InsR and GLUT4 in cardiac membranes as well as to impaired LRP1/InsR interaction, both of which were recovered in hypercholesterolemic rabbits by inhibition of myocardial CE accumulation. In line, *ex vivo* experiments showed that rabbit hypercholesterolemic serum strongly induces intracellular CE accumulation in HL-1 cardiomyocytes, decreasing InsR signaling, insulin-induced GLUT4 translocation to plasma membrane and insulin-induced glucose uptake in these cells. All these outputs were significantly reduced in HL-1 cells exposed to hypercholesterolemic serums containing anti-P3 Abs. These novel findings show that cardiomyocyte intracellular CE accumulation plays a crucial role in impaired cardiac insulin response induced by diet, and that these alterations are efficiently reduced by exposure to antibodies against the P3 sequence of LRP1 CR9 domain.

Intramyocardial CE accumulation in the heart is promoted by ischemia [35,37,39], hypercholesterolemia [40], and obesity [38]. However, the clinical impact of intramyocardial CE accumulation (independently of TG accumulation) has not yet been investigated, even though experimental studies have consistently shown that the causes and consequences of intracellular CE and TG accumulation involve differential mechanisms and pathological consequences. TG accumulation is mainly caused by an imbalance between the rates of fatty acid (FA) entry and FA oxidation, and it usually occurs in parallel to accumulation of detrimental lipid intermediates, such as long-chain acyl--CoA, ceramides, and diacylglycerol, all of which impair insulin signaling and glucose use in the heart [41]. We and others have proposed that intramyocardial CE accumulation is caused by the uptake of CE-enriched lipoproteins through lipoprotein receptors [22,35,39]. Here, molecular studies revealed that intramyocardial CE accumulation is mainly caused by LRP1-mediated uptake of CE-enriched lipoproteins, since it is blocked in rabbit heart by anti-P3 Abs, similar to our previous results in neonatal rat ventricular myocytes and cardiac-derived HL-1 cells by RNA silencing approaches [22,35]. CE-enriched VLDLs and LDLs are large lipoproteins in rabbits that display lower affinity for the LDL receptor [42,43] but increased affinity for the LRP1 receptor [29].

Our electron microscopy studies revealed that the lipid droplets in cardiomyocytes of P3- injected rabbits, although lower in number, are bigger and more electrodense than those found in the heart of IrP-injected rabbits. These imaging results combined with molecular and biophysical studies suggest that lipid droplets in the heart of P3-

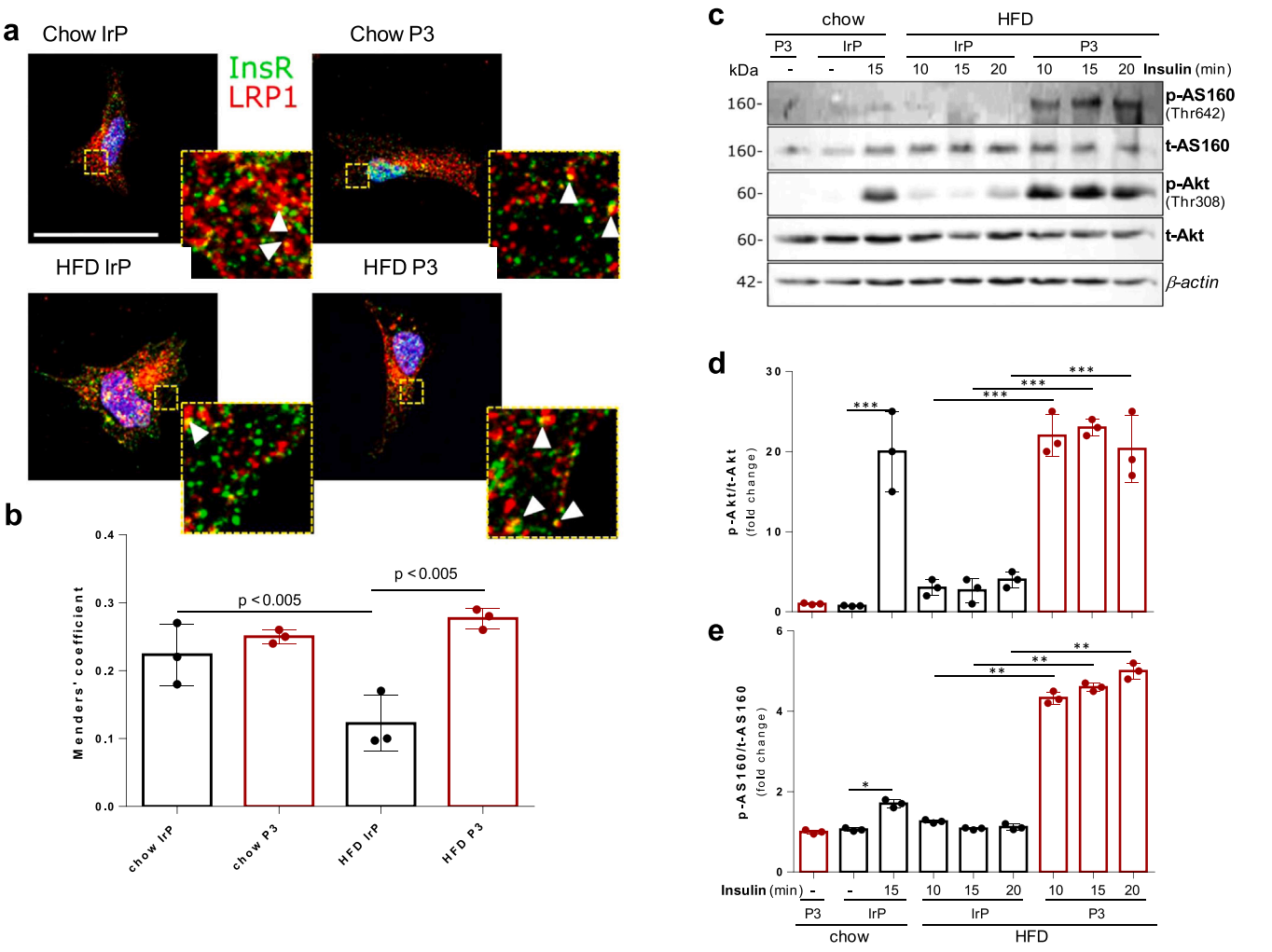

Fig. 5. Anti-P3 Abs block the down-regulatory effects of intracellular CE on InsR signaling in HL-1 cells. (a) Confocal microscopy of HL-1 cells exposed to rabbit serum (0.25 %, 1.5 h) from the different groups, showing the co-localization between LRP1 (red) and InsR (green). The inset represents the 4× magnification of the framed regions in the dotted lines. The white arrowheads indicate co-localization vesicles. Images are representative of three independent experiments ($n = 3$). Scale bar, 10 μm. (b) Bar graph showing the mean ± SD of Manders' coefficient of the co-localization between InsR and LRP1, obtained from the quantification performed in 30 cells per condition. (c) Western blot assays of phosphorylated Akt (p-Akt) and AS160 (p-AS160), and total Akt (t-Akt) and AS160 (t-AS160) in HL-1 cells exposed to serum (0.25 %, 1.5 h) from the different groups of rabbits and then stimulated with insulin (100 nM, 10–20 min). β-actin was used as a protein loading control. Bar graphs showing the densitometry quantification of p-Akt (d) and p-AS160 (e) normalized to t-Akt and t-AS160 bands respectively, and represented as a fold-change as compared to the mean of control IrP group. *** $p < 0.0001$ *versus* indicated conditions. ** $p < 0.001$ *versus* indicated conditions. Results are shown as mean ± SD of three independent experiments ($n = 3$). Statistical significance was determined by one-way ANOVA followed by a Dunnett's multiple comparison. (For interpretation of the references to colour in this figure, the reader is referred to the web version of this article.)

immunized rabbits contain almost exclusively TG, while those in the heart of IrP rabbits are mixed (cholesteryl esters and triglycerides). In line with our findings, lipid droplets containing exclusively CE have been observed to have a reduced size [44,45]. In addition, from the biophysical point of view, the liquid crystalline nature of CE mechanistically determines the intracellular phase behaviors of lipid droplets, and thus the structure and organization of a TG/CE lipid droplet, the lipid droplet nucleation, and the TG packaging [46,47]. These studies suggest that presence of CE limits lipid droplet growth, which would explain the smaller size of CE/TG lipid droplets present in the heart of the HFD IrP rabbits as compared to the TG-enriched lipid droplets present in the heart of HFD P3 rabbits. In addition, TLC results showed that P3- immunization had a strong efficacy in exclusively reducing intramyocardial CE content. Together, these results demonstrate that P3-immunization shows specificity for targeting CE accumulation in the heart.

Another key observation in this study is that mixed CE/TG lipid droplets formed in the heart of HFD rabbits and in HL-1 cells exposed to rabbit HFD IrP serum are surrounded by abundant glycogen drops, in contrast to TG-enriched lipid droplets in the heart of HFD P3 rabbits (which are not surrounded by glycogen). Our results suggest that P3-immunization counteracts the increased glycogen content induced by HFD in the heart of rabbits. Of note, previous studies have reported an increased glycogen content in the liver of fasted mice [48].

Our subfractionation studies combined with Western blot analysis showed that the membrane/total InsR ratio was lower in hearts from HFD rabbits than in those from normal chow rabbits. Coherently, LRP1 immunoprecipitation assays in rabbit heart tissue showed that HFD not only reduced cardiac membrane InsR levels but also disrupted InsR interaction with LRP1, suggesting that InsR/LRP1 interactions mainly occurs at the cardiac membrane. These results in the *in vivo* model are in line with previous studies from our group showing a reduction in the InsR/LRP1 association in aggregated LDL-loaded HL-1 cells [6]. It remains to be explored whether this interaction is direct or mediated by other intermediate proteins. A key result from the present study is that anti-P3 Abs, which blocked LRP1 interactions with CE-enriched

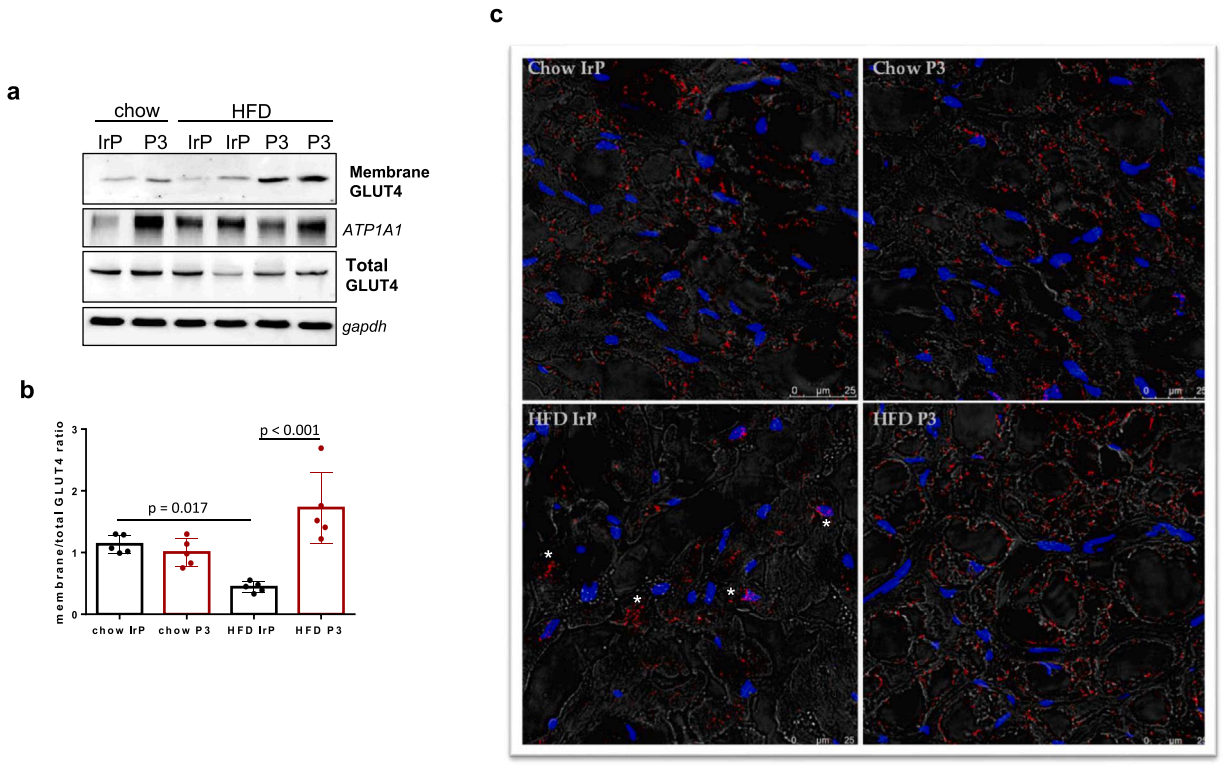

Fig. 6. Anti-P3 Abs block the deleterious effects of HFD on cardiac GLUT4 membrane localization. (a) Representative Western blot analysis of GLUT4 levels in cardiac membrane and total rabbit heart extracts. ATP1A1 and GADPH were used as protein loading controls for plasma membrane and total cardiac protein extracts, respectively. (b) Bar graphs showing the GLUT4 ratio between membrane and total levels normalized by ATP1A1 (membranes) or GADPH (total extracts), respectively. $n = 5$/group. (c) Confocal microscopy of slides from the heart of the four groups. Images show the localization of GLUT4 (in red) in cardiomyocytes. An overlay of confocal and transmission images helps to visualize GLUT4 localization in the boundary of cardiomyocytes in the hearts from the chow IrP, chow P3, and HFD P3 groups but not from HFD IrP rabbit group. Asteriks indicate GLUT4 in the cytoplasm of cardiomyocytes. Nuclei are shown in blue. (For interpretation of the references to colour in this figure, the reader is referred to the web version of this article.)

lipoproteins and intramyocardial CE accumulation, facilitated the recovery of InsR levels and InsR/LRP1 complex in membranes in the heart of rabbits and HL-1 cells exposed to HFD serum. Unexpectedly, we have also found that HFD increased total InsR levels in rabbit heart, and that anti-P3 Abs also blocked this effect. Interestingly, the presence of excessive InsR levels in muscle tissues has been proposed to contribute to dyslipemia and steatosis [49] and to be a compensatory mechanism in a situation of the HFD-generated insulin resistance [50].

In our model, both total and membrane LRP1 were higher in HFD-fed groups as compared to standard chow control groups, and anti-P3 Abs reduced the LRP1 levels to near that found in the control group, as expected by the positive transcriptional upregulation of LRP1 by hypercholesterolemia [51]. In the presence of anti-P3 Abs, the cardiac membrane InsR levels and the InsR/LRP1 interactions were even higher than those found in the control group, suggesting that blocking LRP1 interactions with lipoproteins could be a highly efficient process for recovering a correct cardiac insulin response. Our *ex vivo* studies showed that reducing the levels of the InsR/LRP1 complexes by a HFD was directly responsible for alterations in InsR signaling, in agreement with previous studies showing the pivotal role of LRP1 in insulin-induced InsR phosphorylation [6,25,26]. Further studies are now required to determine how intramyocardial CE accumulation impairs InsR/LRP1 complex formation and, how anti-P3 Abs overcome this effect.

Insulin and glucose metabolism are tightly related, and glucose transport across the cell membrane is strongly influenced by membrane fluidity [52] and, modulated by cholesterol [53]. Our current results from *ex vivo* studies showed that hypercholesterolemic serum reduced insulin response in terms of glucose uptake, and that anti-P3 Abs restored this response. In rabbit hearts, we showed that GLUT4 trafficking to cardiac membrane was reduced in HFD IrP rabbits but recovered in HFD P3 rabbits. In line with our results, HFD-mediated membrane cholesterol loading seems to promote the loss of cortical actin filaments required for GLUT4 trafficking to the membrane (a hallmark of skeletal muscle insulin resistance) [54]. We showed that blocking intramyocardial CE accumulation with anti-P3 Abs was sufficient to restore insulin-induced InsR signaling, GLUT4 trafficking to plasma membrane, and glucose uptake by HL-1 cardiomyocytes. Thus, LRP1-mediated CE accumulation is an early and reversible mechanism linking HFD to altered insulin response. Indeed, the multiple roles for LRP1 in mediating lipoprotein uptake [51,55], InsR signaling [6,25], and GLUT4 trafficking [6,23] also underpin the link between the cardiomyocyte intracellular CE accumulation and cardiac insulin signaling abnormalities. It is tempting to suggest that LRP1 binding to CE-enriched lipoproteins prevents the LRP1 receptor from interacting with other receptors or transporters, such as InsR or GLUT4, respectively, and this precludes their movement to plasma membrane. Further studies are required to explore these crucial mechanistic aspects connecting LRP1-mediated intramyocardial CE accumulation and insulin resistance in peripheral tissues. As glucose uptake in the heart is largely controlled by insulin-sensitive mechanisms, insulin resistance is an obstacle for enhanced myocardial glucose utilization. In recent studies, the use of insulin-sensitizing agents, such as metformin or SGLT2 (sodium-glucose cotransporter 2) inhibitors, was shown to reduce the risk of cardiovascular death or hospitalizations for heart failure in patients with T2DM [56,57].

A crucial question that remains open in this study is why anti-P3 Abs protected against HFD-induced cardiac but not peripheral insulin resistance. Peripheral insulin resistance is considered to be caused by hepatic steatosis [58], and HFD feeding dramatically increased accumulation of both CE and TG in the liver of this rabbit model. Of note,

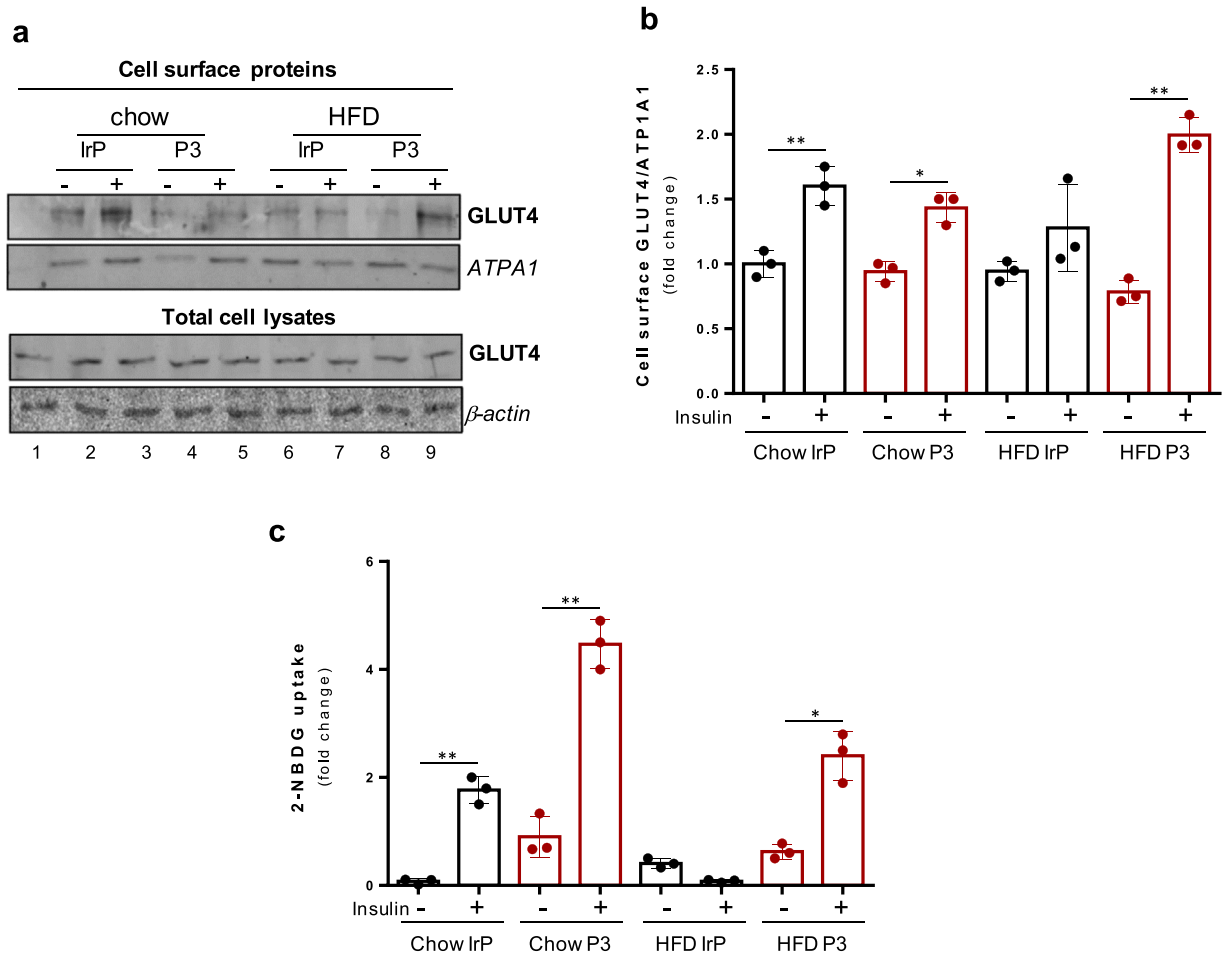

Fig. 7. Anti-P3 abs block the deleterious effects of hypercholesterolemic serum on GLUT4 traffic to the plasma membrane and glucose uptake by HL-1 cells. (a) Representative Western blot analysis from biotin-labeling protein assays of GLUT4 in the plasma membrane (upper panel) and in total cell extracts (lower panel) of HL-1 cells exposed to rabbit serum (0.25 %, 1.5 h) and stimulated with insulin (100 nM, 30 min). ATP1A1 and β-actin were used as protein loading controls for plasma membrane and total cell protein extracts, respectively. Line 1 represents control without biotin. (b) Bar graphs showing the quantification of Western blot bands for cell surface GLUT4 normalized to ATP1A1, and expressed as a fold-change as compared to the mean value of HL-1 exposed to serum from chow IrP group. Values are expressed as mean ± SD of three independent experiments ($n = 3$). (**c**) Bar graph showing the 2-NBDG uptake in HL-1 cells exposed to serum (0.25 %, 1.5 h) and then stimulated with insulin (100 nM, 30 min) in the presence of 2-NBDG (80 μM). The bar graph shows the mean ± SD of the fluorescence intensity of 2-NBDG per area of three independent experiments ($n = 3$), expressed as fold change as compared to the mean value of control IrP group. * $p < 0.05$; ** $p < 0.01$ insulin-stimulated *versus* basal. Statistical significance was determined by two-way ANOVA followed by a Student *t*-test.

hepatic TGs are the main regulators of VLDL secretion by the liver [59]. Controversially, insulin resistance has been reported to decrease membrane LRP1 levels in the liver, which could contribute to impaired hepatic clearance of triglyceride-rich lipoproteins. We now show that anti-P3 Abs had not protective effect against hepatic TG or CE accumulation induced by HFD. Importantly, anti-P3 Abs blocked the interaction of vascular LRP1 with ApoB100-enriched lipoproteins [29], the main lipoprotein ligand of LRP1 in the cardiovascular system. However, in liver, the main lipoprotein ligands of LRP1 are ApoE-enriched lipoproteins, such as chylomicrons [60]. It is known that ApoB100 and ApoE interact with the LRP1 receptor through domains localized in different clusters: CR9 in cluster II for ApoB100 [28] and CR17 in cluster IV for ApoE [61]. The inefficiency of anti-P3 Abs to block the interactions of LRP1 with ApoE-enriched lipoproteins could be the reason behind their lack of effect on HFD-induced systemic insulin resistance in rabbits.

In conclusion, our study now shows that i) diet-induced intramyocardial CE accumulation impaired cardiac insulin response, and that ii) anti-P3 Abs specifically and efficiently blocked intramyocardial CE accumulation, thereby normalizing the cardiac insulin response (summarized in Fig. 8). Further studies are required to determine the mechanisms underlying the link between reduced CE accumulation in the heart and restored insulin response. This aspect deserves to be investigated indepth given the potential role of myocardial CE accumulation on insulin resistance in a wide range of cardiac diseases. The innovative immunization-based approach that we took here, which differs from more traditional pharmacological or genetic techniques, showed both specificity and selectivity for targeting cardiovascular CE accumulation. These findings have important therapeutic implications in the management of CVD and shed new light on the complex role of LRP1 in regulating cardiac insulin response associated with hypercholesterolemia, obesity, and T2DM.

Research in context

Evidence before this study

Cardiovascular disease, the leading cause of death worldwide, is frequently associated with increased levels of atherogenic lipoproteins. Cholesteryl ester (CE)-enriched lipoproteins are an essential source of lipids to the heart; however, their dysregulated uptake and consequent lipid accumulation in the heart contributes to cardiac metabolic alterations and cardiac dysfunction. In particular, CE accumulation in the

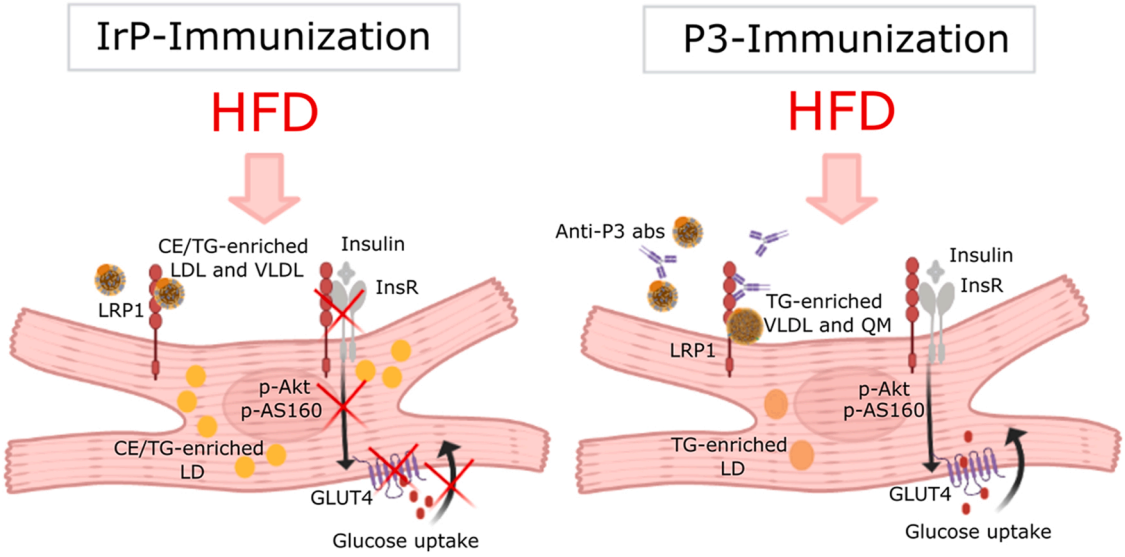

Fig. 8. Schematic summary of the main findings. A high-fat diet (HFD) causes a strong intramyocardial accumulation of cholesteryl ester (CE) associated with altered cardiac insulin response. By specifically blocking intramyocardial CE accumulation, P3 immunization restores insulin signaling and glucose uptake in cardiomyocytes.

heart causes calcium-handling alterations and cardiac remodeling in experimental models. Recently, a clinical study with more than 15,000 individuals has revealed the link between high levels of CE-enriched lipoproteins and left ventricle myocardial remodeling. Antibodies against the receptor LRP1 (the P3 sequence of CR9 domain of cluster II) specifically block intracellular CE accumulation in vascular cells by successful competition with aggregated LDL uptake. Moreover, P3 immunization of rabbits inhibits vascular CE accumulation and atherosclerosis.

Added value of this study

In this study, we used an innovative immunization-based approach to inhibit the CE uptake from lipoproteins into the heart. By complementary molecular, biophysical, and imaging approaches, we show that P3 immunization has specificity and selectivity for targeting intracellular CE accumulation within the heart of rabbits without modifying the circulating lipid profile or the myocardial triglyceride accumulation. In addition, we found that the selective inhibition of CE accumulation is enough to restore both the levels of InsR and GLUT4 levels in the cardiac membrane as well as the interaction between LRP1/InsR that is necessary for correct insulin signaling of hypercholesterolemic rabbits.

Implications of all the available evidence

This study provides new insight into lipid metabolism and its relationship to the insulin response in the heart and uncovers a novel and different approach to specifically modifying cholesterol metabolism and treat impaired cardiac insulin response. By providing a novel strategy of preventing the deleterious effect of hypercholesterolemia, it opens the possiblity for new therapeutical strategies of clinical management of impaired insulin response. Strikingly, reducing LRP1-mediated CE accumulation can restore insulin signaling in the myocardium. This is an important finding given the role of cardiac lipid accumulation and insulin response in a range of cardiac diseases and underscores the therapeutic potential/utility of antibody therapies.

Conflict of interest statement

The authors declare no conflict of interest.

Acknowledgements

The economic support to develop this project was received from Fundació MARATÓ TV3 with the grant 201521–10 (to V.Ll.-C), from the Instituto de Salud Carlos III (ISCIII) and co-financed with ERDFsFIS PI18/01584 (to V.Ll.-C), and from Fundación BBVA Ayudas a equipos de investigación 2019. This work was also funded by Secretaría de Ciencia y Tecnología de la Universidad Nacional de Córdoba (SECyT-UNC) grants PROYECTOS CONSOLIDAR 2018–2021 (to G.A.C); Fondo para la Investigación Científica y Tecnológica (FONCyT), Préstamo BID Proyecto de Investigación en Ciencia y Tecnología (PICT) grant 2015–0807 and grant 2017–4497 (to G.A.C). Support was received from Albert Renold Travel Fellowship Programme 2019 from the European Foundation of the study of Diabetes (EFSD) and the Wood-Whelan fellowship Programme 2019 from the International Union of Biochemistry and Molecular Biology (IUBMB) to cover the stay of V.A.D. in Institute of Biomedical Research of Barcelona (IIBB)-Spanish National Research Council (CSIC) and Biomedical Research Institute Sant Pau (IIB Sant Pau), Barcelona, Spain. V.A.D is a postdoctoral fellow of Consejo Nacional de Investigaciones Científicas y Técnicas (CONICET), Centro de Investigaciones en Bioquímica Clínica e Inmunología (CIBICI), Córdoba, Argentina. A.B.A. is a predoctoral fellow (FI19/00205) granted by the Programme _Contratos predoctorales de formación de investigación en salud_ from the Instituto de Salud Carlos III (ISCIII) and co-financed with ERDFs. Our group is part of CIBER Enfermedades Cardiovasculares (CIBERCV; CB16/11/00276 to J.M.G and VLl-C) and CIBER Diabetes y Enfermedades Metabólicas Asociadas (CIBERDEM; CB07/08/0016 to JCE-G), projects run by the Instituto de Salud Carlos III. Our group also participates in Redes de investigación (Enfermedades Metabóloicas y Cáncer RED2018–102799-T), a project run by MINECO. VLl-C group recognized by Generalitat de Catalunya (2017 SGR 946). We are thankful to Eva Prats and the staff from Centres Científics i Tecnològics de la Universitat de Barcelona (Campus Casanova) (CCiT/UB) for the processing of samples for electron microscopy. We also thank Veronica Raker for the scientitic and english editing of the manuscript.

Author contributions

V.A.D., and A.B.A contributed equally to this work. G.A.C. and V.Ll.-C. are both corresponding authors of this work. V.Ll.-C. and G.A.C. designed the research; V.A.D., A.B.A., E.G.,L.C; and M.T.L.C-H

performed most of the experimental research; A.I. contributed with the immunization procedure and ELISA design and setting to test anti-P3 Ab production in rabbits; JC.E.G contributed with biochemical determinations of lipoproteins; V.S. contributed with the biophysical analysis of lipoproteins and hearts; C.E. contributed with the electron microscopy experiments and images; V.A.D., A.B.A., J.M.G., G.A.C. and V.Ll.-C. analyzed the data; and V.A.D., G.A.C. and V.Ll.-C. wrote the paper.

Appendix A. Supporting information

Supplementary data associated with this article can be found in the online version at doi:10.1016/j.biopha.2022.113270.

References

[1] H. Bugger, E. Abel, Molecular mechanisms of diabetic cardiomyopathy, Diabetologia 57 (2014) 660–671, https://doi.org/10.1007/s00125-014-3171-6.

[2] C. Riehle, E. Abel, Insulin signaling and heart failure, Circ. Res. 118 (2016) 1151–1169, https://doi.org/10.1161/CIRCRESAHA.116.306206.

[3] M. Tadic, C. Cuspidi, D. Vasic, P.L.M. Kerkhof, Cardiovascular implications of diabetes, metabolic syndrome, thyroid disease, and cardio-oncology in women, Adv. Exp. Med. Biol. 1065 (2018) 471–488, https://doi.org/10.1007/978-3-319-77932-4_29.

[4] B. Bozkurt, D. Aguilar, A. Deswal, S.B. Dunbar, G.S. Francis, T. Horwich, et al., Contributory risk and management of comorbidities of hypertension, obesity, diabetes mellitus, hyperlipidemia, and metabolic syndrome in chronic heart failure: a scientific statement from the American Heart Association, Circulation 134 (2016) e535–e578, https://doi.org/10.1161/CIR.0000000000000450.

[5] W.B. Kannel, M. Hjortland, W.P. Castelli, Role of diabetes in congestive heart failure: the framingham study, Am. J. Cardiol. 34 (1974) 29–34, https://doi.org/10.1016/0002-9149(74)90089-7.

[6] V. Actis Dato, A. Benitez-Amaro, D. de Gonzalo-Calvo, M. Vazquez, G. Bonacci, V. Llorente-Cortés, et al., LRP1-mediated AggLDL endocytosis promotes cholesteryl ester accumulation and impairs insulin response in HL-1 Cells, Cells 9 (2020) 182, https://doi.org/10.3390/cells9010182.

[7] G. Jia, M.A. Hill, J.R. Sowers, Diabetic cardiomyopathy: an update of mechanisms contributing to this clinical entity, Circ. Res 122 (2018) 624–638, https://doi.org/10.1161/CIRCRESAHA.117.311586.

[8] Q. Hu, H. Zhang, N. Gutiérrez Cortés, D. Wu, P. Wang, J. Zhang, et al., Increased Drp1 Acetylation by Lipid Overload Induces Cardiomyocyte Death and Heart Dysfunction, Circ. Res 126 (2020) 456–470, https://doi.org/10.1161/CIRCRESAHA.119.315252.

[9] A. Ruiz-Ramírez, O. López-Acosta, M.A. Barrios-Maya, M. El-Hafidi, Cell death and heart failure in obesity: role of uncoupling proteins, Oxid. Med Cell Longev. 2016 (2016) 1–11, https://doi.org/10.1155/2016/9340654.

[10] G. Jia, V.G. DeMarco, J.R. Sowers, Insulin resistance and hyperinsulinaemia in diabetic cardiomyopathy, Nat. Rev. Endocrinol. 12 (2016) 144–153, https://doi.org/10.1038/nrendo.2015.216.

[11] N. Frangogiannis, Cardiac fibrosis, Cardiovasc Res 117 (2021) 1450–1488, https://doi.org/10.1093/cvr/cvaa324.

[12] M. Tate, D.J. Grieve, R.H. Ritchie, Are targeted therapies for diabetic cardiomyopathy on the horizon? Clin. Sci. (Lond.) 131 (2017) 897–915, https://doi.org/10.1042/CS20160491.

[13] N.G. Frangogiannis, The extracellular matrix in myocardial injury, repair, and remodeling, J. Clin. Invest 127 (2017) 1600–1612, https://doi.org/10.1172/JCI87491.

[14] M.R. Hayden, N. Chowdhury, G. Govindarajan, R. Poorna, P.R. Karuparthi, J. Habibi, et al., Myocardial myocyte remodeling and fibrosis in the cardiometabolic syndrome, J. Cardiometab Syndr. 1 (2007) 326–333, https://doi.org/10.1111/j.1559-4564.2006.05626.x.

[15] N. Aung, M.M. Sanghvi, S.K. Piechnik, S. Neubauer, P.B. Munroe, S.E. Petersen, The effect of blood lipids on the left ventricle, J. Am. Coll. Cardiol. 76 (2020) 2477–2488, https://doi.org/10.1016/j.jacc.2020.09.583.

[16] M. Ruuth, S.D. Nguyen, T. Vihervaara, M. Hilvo, T.D. Laajala, P.K. Kondadi, et al., Susceptibility of low-density lipoprotein particles to aggregate depends on particle lipidome, is modifiable, and associates with future cardiovascular deaths, Eur. Heart J. 39 (2018) 2562–2573, https://doi.org/10.1093/eurheartj/ehy319.

[17] C. Bancells, S. Villegas, F.J. Blanco, S. Benítez, I. Gállego, L. Beloki, et al., Aggregated electronegative low density lipoprotein in human plasma shows a high tendency toward phospholipolysis and particle fusion, J. Biol. Chem. 285 (2010) 32425–32435, https://doi.org/10.1074/jbc.M110.139691.

[18] E. Hurt-Camejo, G. Camejo, P. Sartipy, Phospholipase A2 and small, dense low-density lipoprotein, Curr. Opin. Lipido 11 (2000) 465–471, https://doi.org/10.1097/00041433-200010000-00004.

[19] G. Camejo, E. Hurt-Camejo, O. Wiklund, G. Bondjers, Association of apo B lipoproteins with arterial proteoglycans: pathological significance and molecular basis, Atherosclerosis 139 (1998) 205–222, https://doi.org/10.1016/S0021-9150(98)00107-5.

[20] V. Llorente-Cortés, M. Otero-Viñas, E. Hurt-Camejo, J. Martínez-González, L. Badimon, Human coronary smooth muscle cells internalize versican-modified LDL through LDL receptor–related protein and LDL receptors, Arterioscler. Thromb. Vasc. Biol. 22 (2002) 387–393, https://doi.org/10.1161/hq0302.105367.

[21] V. Llorente-Cortés, J. Martínez-González, L. Badimon, LDL receptor–related protein mediates uptake of aggregated LDL in human vascular smooth muscle cells, Arterioscler. Thromb. Vasc. Biol. 20 (2000) 1572–1579, https://doi.org/10.1161/01.ATV.20.6.1572.

[22] R. Cal, O. Juan-Babot, V. Brossa, S. Roura, C. Gálvez-Montón, M. Portoles, et al., Low density lipoprotein receptor-related protein 1 expression correlates with cholesteryl ester accumulation in the myocardium of ischemic cardiomyopathy patients, J. Transl. Med 10 (2012) 160, https://doi.org/10.1186/1479-5876-10-160.

[23] M.P. Jedrychowski, C.A. Gartner, S.P. Gygi, L. Zhou, J. Herz, K.V. Kandror, et al., Proteomic analysis of GLUT4 storage vesicles reveals LRP1 to Be an important vesicle component and target of insulin signaling, J. Biol. Chem. 285 (2010) 104–114, https://doi.org/10.1074/jbc.M109.040428.

[24] D. Leto, A.R. Saltiel, Regulation of glucose transport by insulin: traffic control of GLUT4, Nat. Rev. Mol. Cell Biol. 13 (2012) 383–396, https://doi.org/10.1038/nrm3351.

[25] C. Liu, J. Hu, C. Tsai, M. Yue, H.L. Melrose, T. Kanekiyo, et al., Neuronal LRP1 regulates glucose metabolism and insulin signaling in the brain, J. Neurosci. 35 (2015) 5851–5859, https://doi.org/10.1523/JNEUROSCI.5180-14.2015.

[26] Y. Ding, X. Xian, W. Holland, S. Tsai, J. Herz, Low-density lipoprotein receptor-related protein-1 protects against hepatic insulin resistance and hepatic steatosis, EBioMedicine 7 (2016) 135–145, https://doi.org/10.1016/j.ebiom.2016.04.002.

[27] V. Actis Dato, R. Grosso, M.C. Sánchez, C.F. Fader, G.A. Chiabrando, Insulin-induced exocytosis regulates the cell surface level of low-density lipoprotein-related protein-1 in Müller Glial cells, Biochem J. 475 (2018) 1669–1685, https://doi.org/10.1042/BCJ20170891.

[28] P. Costales, P. Fuentes-Prior, J. Castellano, E. Revuelta-Lopez, M.A. Corral-Rodríguez, L. Nasarre, et al., K domain CR9 of low density lipoprotein (LDL) receptor-related protein 1 (LRP1) is critical for aggregated LDL-induced foam cell formation from human vascular smooth muscle cells, J. Biol. Chem. 290 (2015) 14852–14865, https://doi.org/10.1074/jbc.M115.638361.

[29] O. Bornachea, A. Benitez-Amaro, A. Vea, L. Nasarre, D. de Gonzalo-Calvo, J. C. Escola-Gil, et al., Immunization with the Gly 1127 -Cys 1140 amino acid sequence of the LRP1 receptor reduces atherosclerosis in rabbits. Molecular, immunohistochemical and nuclear imaging studies, Theranostics 10 (2020) 3263–3280, https://doi.org/10.7150/thno.37305.

[30] S. Toldo, D. Austin, A.G. Mauro, E. Mezzaroma, B.W. Van Tassell, C. Marchetti, et al., Low-density lipoprotein receptor–related protein-1 Is a therapeutic target in acute myocardial infarction, JACC: Basic Transl. Sci. 2 (2017) 561–574, https://doi.org/10.1016/j.jacbts.2017.05.007.

[31] N. Potere, M.G. del Buono, G. Niccoli, F. Crea, S. Toldo, A. Abbate, Developing LRP1 agonists into a therapeutic strategy in acute myocardial infarction, Int J. Mol. Sci. 20 (2019) 544, https://doi.org/10.3390/ijms20030544.

[32] S. Avrameas, Coupling of enzymes to proteins with glutaraldehyde, Immunochemistry 6 (1969) 43–52, https://doi.org/10.1016/0019-2791(69)90177-3.

[33] J. Julve, J.C. Escolà-Gil, N. Rotllan, C. Fiévet, E. Vallez, C. de la Torre, et al., Human apolipoprotein A-II determines plasma triglycerides by regulating lipoprotein lipase activity and high-density lipoprotein proteome, Arterioscler. Thromb. Vasc. Biol. 30 (2010) 232–238, https://doi.org/10.1161/ATVBAHA.109.198226.

[34] J.C. Escolà-Gil, G. Llaverias, J. Julve, M. Jauhiainen, J. Méndez-González, F. Blanco-Vaca, The cholesterol content of western diets plays a major role in the paradoxical increase in high-density lipoprotein cholesterol and upregulates the macrophage reverse cholesterol transport pathway, Arterioscler. Thromb. Vasc. Biol. 31 (2011) 2493–2499, https://doi.org/10.1161/ATVBAHA.111.236075.

[35] R. Cal, J. Castellano, E. Revuelta-López, R. Aledo, M. Barriga, J. Farré, et al., Low-density lipoprotein receptor-related protein 1 mediates hypoxia-induced very low density lipoprotein-cholesteryl ester uptake and accumulation in cardiomyocytes, Cardiovasc Res 94 (2012) 469–479, https://doi.org/10.1093/cvr/cvs136.

[36] I. Schulz, [19] Permeabilizing cells: Some methods and applications for the study of intracellular processes, Methods Enzym. 192 (1990) 280–300, https://doi.org/10.1016/0076-6879(90)92077-Q.

[37] V. Samouillan, I.M. Martinez de Lejarza Samper, A. Benitez-Amaro, D. Vilades, J. Dandurand, J. Casas, et al., Biophysical and lipidomic biomarkers of cardiac remodeling post-myocardial infarction in humans, Biomolecules 10 (2020) 1471, https://doi.org/10.3390/biom10111471.

[38] V. Samouillan, E. Revuelta-López, J. Dandurand, L. Nasarre, L. Badimon, C. Lacabanne, et al., Cardiomyocyte intracellular cholesteryl ester accumulation promotes tropoelastin physical alteration and degradation, Int J. Biochem Cell Biol. 55 (2014) 209–219, https://doi.org/10.1016/j.biocel.2014.09.005.

[39] C. Drevinge, L.O. Karlsson, M. Ståhlman, T. Larsson, J. Perman Sundelin, L. Grip, et al., Cholesteryl esters accumulate in the heart in a porcine model of ischemia and reperfusion, PLoS One 8 (2013), e61942, https://doi.org/10.1371/journal.pone.0061942.

[40] Y. Huang, K.E. Walker, F. Hanley, J. Narula, S.R. Houser, T.N. Tulenko, Cardiac systolic and diastolic dysfunction after a cholesterol-rich diet, Circulation 109 (2004) 97–102, https://doi.org/10.1161/01.CIR.0000109213.10461.F6.

[41] A. Gastaldelli, M.A. Morales, P. Marraccini, R. Sicari, The role of cardiac fat in insulin resistance, Curr. Opin. Clin. Nutr. Metab. Care 15 (2012) 523–528, https://doi.org/10.1097/MCO.0b013e328358be7b.

[42] F. Nigon, P. Lesnik, M. Rouis, M.J. Chapman, Discrete subspecies of human low density lipoproteins are heterogeneous in their interaction with the cellular LDL

receptor, J. Lipid Res 32 (1991) 1741–1753, https://doi.org/10.1016/S0022-2275(20)41629-3.
[43] J.R. McNamara, D.M. Small, Z. Li, E.J. Schaefer, Differences in LDL subspecies involve alterations in lipid composition and conformational changes in apolipoprotein B, J. Lipid Res 37 (1996) 1924–1935, https://doi.org/10.1016/S0022-2275(20)37557-X.
[44] W. Shen, S. Azhar, F. Kraemer, Lipid droplets and steroidogenic cells, Exp. Cell Res. 340 (2016) 209–214, https://doi.org/10.1016/j.yexcr.2015.11.024.
[45] X. Zhou, Z. Mo, Y. Li, L. Huang, S. Yu, L. Ge, Y. Hu, S. Shi, L. Zhang, L. Wang, L. Gao, G. Yang, G. Chu, Oleic acid reduces steroidogenesis by changing the lipid type stored in lipid droplets of ovarian granulosa cells, J. Anim. Sci. Biotechnol. 13 (2022) 27, https://doi.org/10.1186/s40104-021-00660-5.
[46] V. Zoni, R. Khaddaj, P. Campomanes, A. Thiam, R. Schneiter, S. Vanni, Pre-existing bilayer stresses modulate triglyceride accumulation in the ER versus lipid droplets, eLife (2021) 10, https://doi.org/10.7554/eLife.62886.
[47] S.F. Shimobayashi, Y. Ohsaki, Universal phase behaviors of intracellular lipid droplets, PNAS 116 (2019) 25440–25445, https://doi.org/10.1073/pnas.1916248116.
[48] B. Lu, D. Bridges, Y. Yang, K. Fisher, A. Cheng, L. Chang, et al., Metabolic crosstalk: molecular links between glycogen and lipid metabolism in obesity, Diabetes 63 (2014) 2935–2948, https://doi.org/10.2337/db13-1531.
[49] R.K. Semple, A. Sleigh, P.R. Murgatroyd, C.A. Adams, L. Bluck, S. Jackson, et al., Postreceptor insulin resistance contributes to human dyslipidemia and hepatic steatosis, J. Clin. Invest 119 (2009) 315, https://doi.org/10.1172/JCI37432.
[50] G. Wang, Y. Yu, W. Cai, T.M. Batista, S. Suk, H.L. Noh, et al., Muscle-specific insulin receptor overexpression protects mice from diet-induced glucose intolerance but leads to postreceptor insulin resistance, Diabetes 69 (2020) 2294–2309, https://doi.org/10.2337/db20-0439.
[51] V. Llorente-Cortés, M. Otero-Viñas, S. Sánchez, C. Rodríguez, L. Badimon, Low-density lipoprotein upregulates low-density lipoprotein receptor-related protein expression in vascular smooth muscle cells, Circulation 106 (2002) 3104–3110, https://doi.org/10.1161/01.CIR.0000041434.28573.0B.
[52] N. Al-Makdissy, M. Younsi, S. Pierre, O. Ziegler, M. Donner, Sphingomyelin/cholesterol ratio: an important determinant of glucose transport mediated by GLUT-1 in 3T3-L1 preadipocytes, Cell Signal 15 (2003) 1019–1030, https://doi.org/10.1016/s0898-6568(03)00070-6.
[53] N. Saxena, N.C. Chandra, Cholesterol: a prelate in cell nucleus and its serendipity, Curr. Mol. Med. 20 (2021) 692–707, https://doi.org/10.2174/1566524020666200413112030.
[54] K.M. Habegger, B.A. Penque, W. Sealls, L. Tackett, L.N. Bell, E.K. Blue, et al., Fat-induced membrane cholesterol accrual provokes cortical filamentous actin destabilisation and glucose transport dysfunction in skeletal muscle, Diabetologia 55 (2012) 457–467, https://doi.org/10.1007/s00125-011-2334-y.
[55] V. Llorente-Cortés, M. Otero-Viñas, S. Camino-López, P. Costales, L. Badimon, Cholesteryl esters of aggregated LDL are internalized by selective uptake in human vascular smooth muscle cells, Arterioscler. Thromb. Vasc. Biol. 26 (2006) 117–123, https://doi.org/10.1161/01.ATV.0000193618.32611.8b.
[56] J.M.M. Evans, A.S.F. Doney, M.A. AlZadjali, S.A. Ogston, J.R. Petrie, A.D. Morris, et al., Effect of metformin on mortality in patients with heart failure and type 2 diabetes mellitus, Am. J. Cardiol. 106 (2010) 1006–1010, https://doi.org/10.1016/j.amjcard.2010.05.031.
[57] M. Packer, Reconceptualization of the molecular mechanism by which sodium-glucose cotransporter 2 inhibitors reduce the risk of heart failure events, Circulation 140 (2019) 443–445, https://doi.org/10.1161/CIRCULATIONAHA.119.040909.
[58] C. Postic, R. Dentin, J. Girard, Role of the liver in the control of carbohydrate and lipid homeostasis, Diabetes Metab. 30 (2004) 398–408, https://doi.org/10.1016/S1262-3636(07)70133-7.
[59] B.C. Moon, A. Hernandez-Ono, B. Stiles, H. Wu, H.N. Ginsberg, Apolipoprotein B secretion is regulated by hepatic triglyceride, and not insulin, in a model of increased hepatic insulin signaling, Arterioscler. Thromb. Vasc. Biol. 32 (2012) 236–246, https://doi.org/10.1161/ATVBAHA.111.241356.
[60] A. Rohlmann, M. Gotthardt, R.E. Hammer, J. Herz, Inducible inactivation of hepatic LRP gene by cre-mediated recombination confirms role of LRP in clearance of chylomicron remnants, J. Clin. Invest 101 (1998) 689–695, https://doi.org/10.1172/JCI1240.
[61] M. Guttman, J.H. Prieto, J.E. Croy, E.A. Komives, Decoding of lipoprotein−receptor interactions: properties of ligand binding modules governing interactions with apolipoprotein E, Biochemistry 49 (2010) 1207–1216, https://doi.org/10.1021/bi9017208.

15.1 Article 3 supplemental material

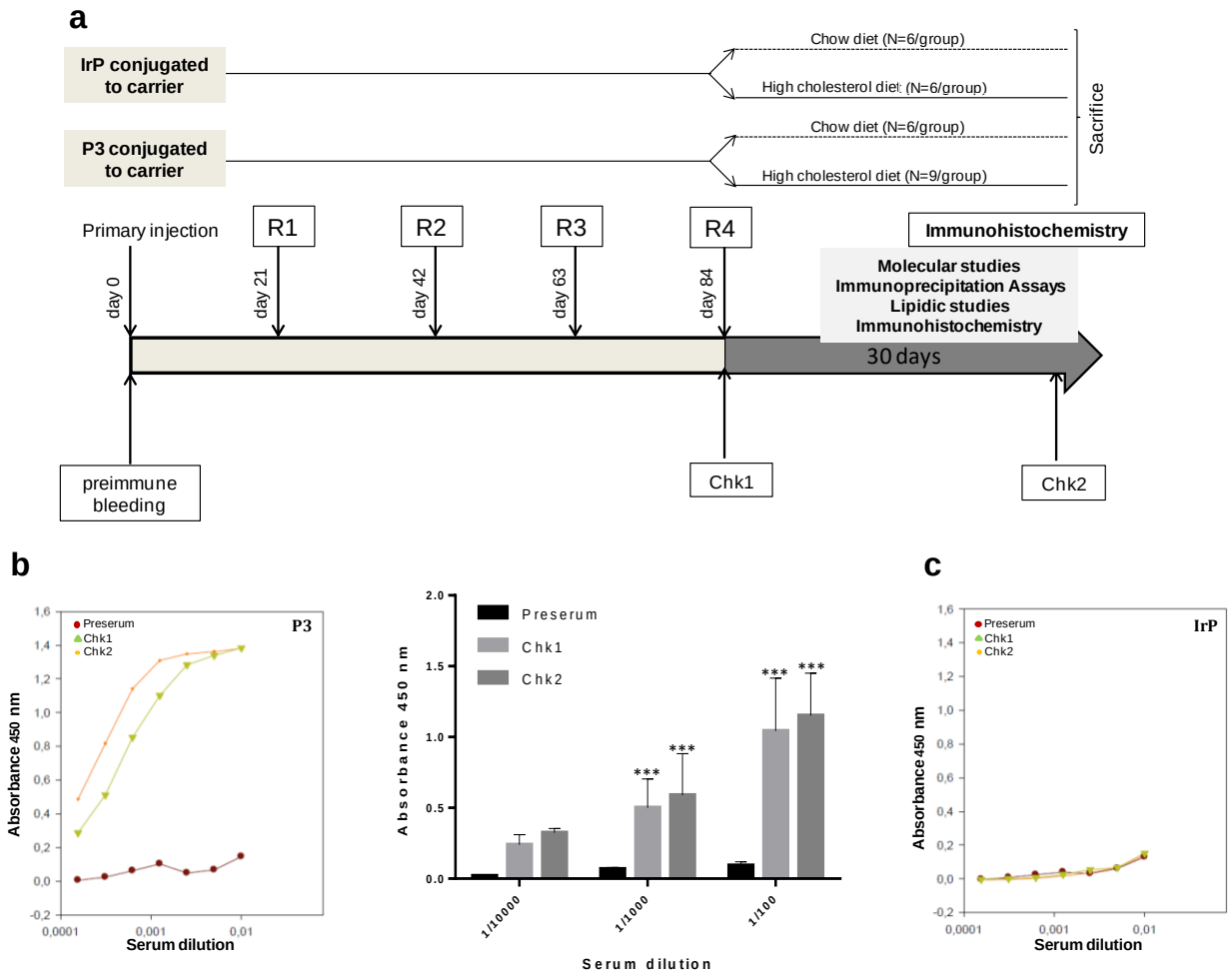

Figure S1. Immunization with P3 peptide raised anti-P3 antibodies in rabbits. (a) Rabbits were divided into two groups, one immunnized with P3 (immunized group) (n = 15) and the other injected with irrelevant peptide (IrP) (n = 12), both peptides conjugated to the carrier KLH. A primary injection and four remainder (R1-R4) dose (138 µg/Kg; volume max: 150 µL) were administered every 21 days. At day 84, circulating anti-P3 specific antibody determinations (Chk1) were performed and considered as reference of basal levels. Animals were then divided into two subgroups: chow diet and HFD diet subgroups. After 1 month, circulating anti-P3 specific antibody determinations (Chk2) were again quantified and animals were then euthanized, and tissue analysis performed. (b) Representative linear graphs showing the results of standardized ELISA in preserum and serum from the checkpoints (Chk1 and Chk2) and bar graphs showing the mean±SD of anti-P3 abs levels in serum from P3-inmmunized rabbits. (c) Representative graphs showing the lack of immune response in IrP injected rabbits. ***p < 0.001 vs. preserum. Statistical significance was determined by Two-Way ANOVA followed by a Tukey post-hoc test.

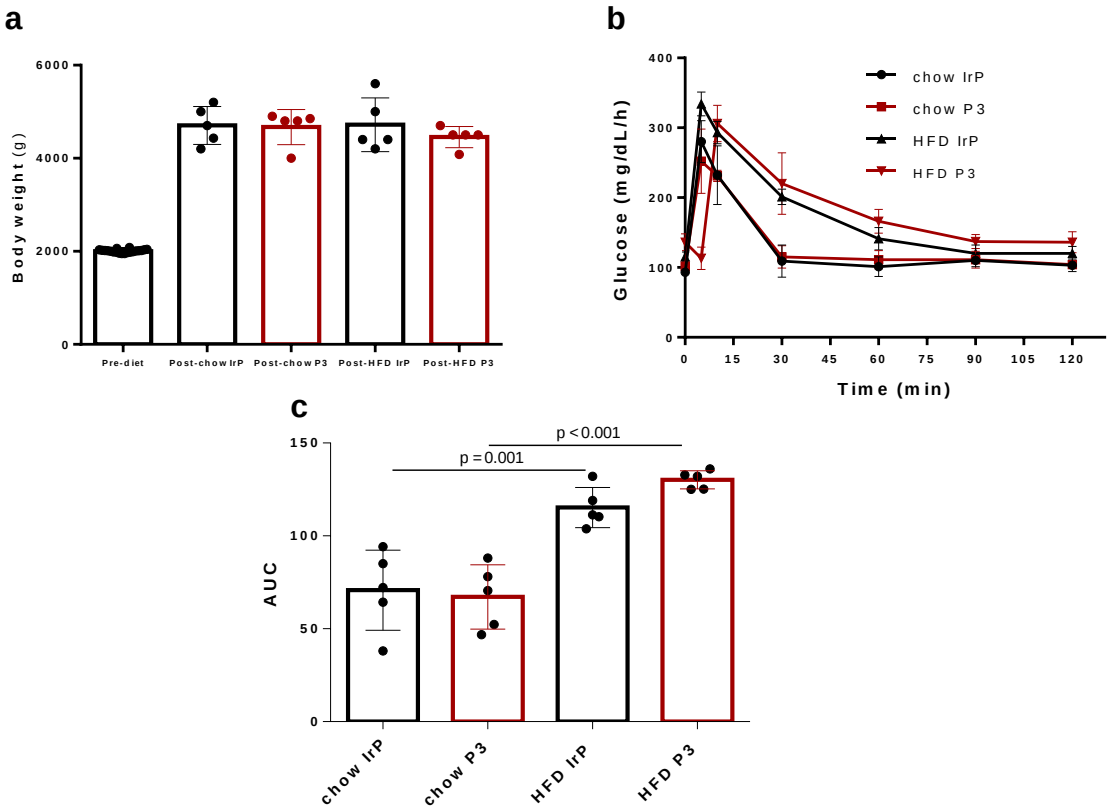

Figure S2. HFD induced glucose intolerance in rabbits. (a) Bar graphs showing body weight changes over 30 days of chow or HFD rabbit feeding. Results are shown as mean ± SD of body weight expressed in grams (gr). Pre-diet group (N=20). N = 5/group pre-diet (at R4). (b) Glucose tolerance test in rabbit (1.3 mg/g body weight). (c) Area under the curve (AUC). Results are shown as mean ± SD. Statistical significance was determined by 2-way ANOVAs with Tukey's post-hoc test.

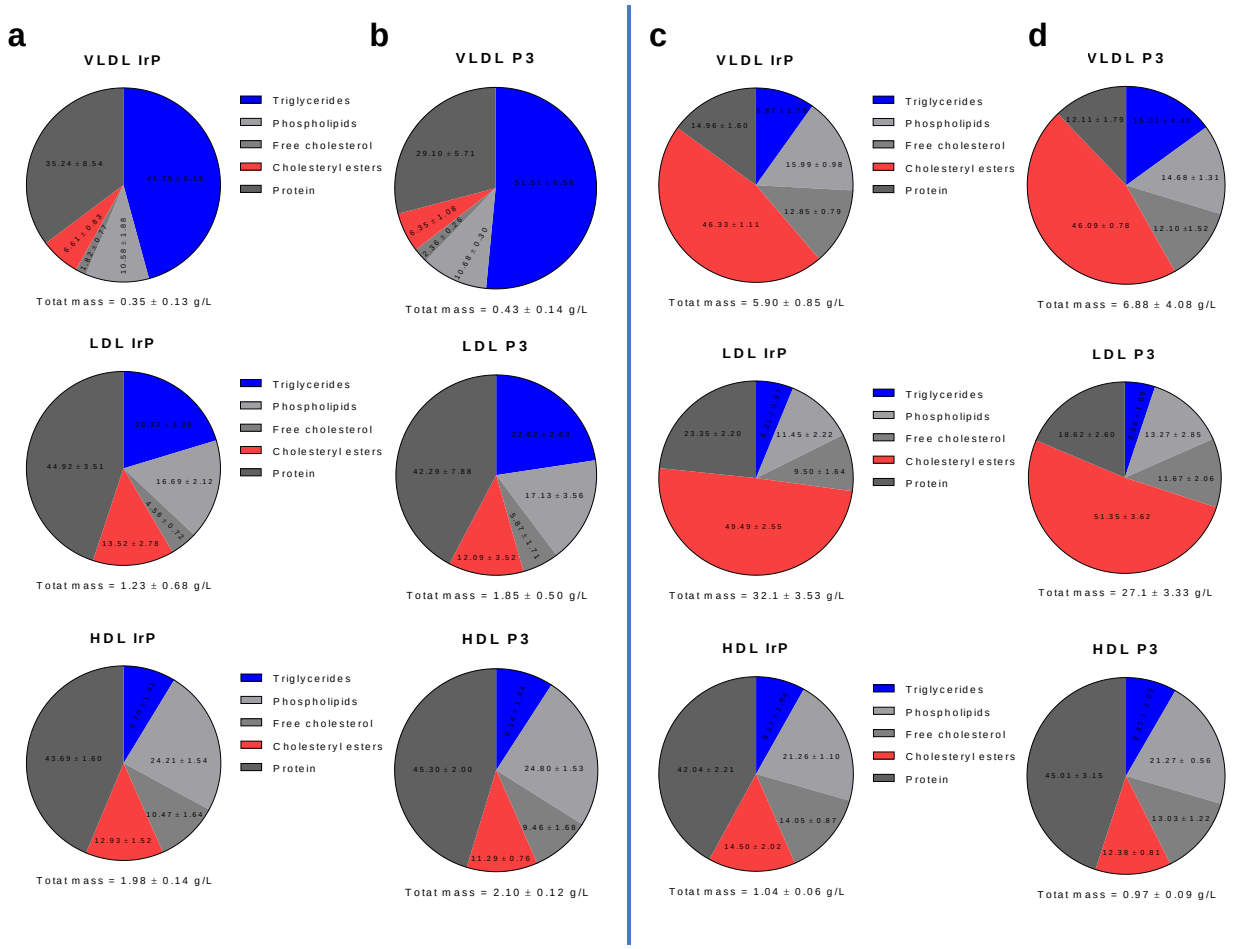

Figure S3. Immunization with P3 peptides does not alter total mass and VLDL, LDL and HDL composition in control and HFD rabbit groups. Chart graphs showing the total mass and lipid and protein composition of VLDL, LDL, and HDL in rabbits fed a chow (a,b) or HFD (c,d) diet and either injected with IrP (negative control) (a,c) or immunized with P3 peptides (b,d) . Results are shown as mean ± SD of the percentage of total mass. Chow IrP and chow P3 n = 4/group; HFD IrP (n = 5/group) and HFD P3 (n = 5/group). Cholesteryl esters, red color; triglycerides, blue color; phospholipids, light gray color; free cholesterol, intermediated gray color; protein, dark gray color.

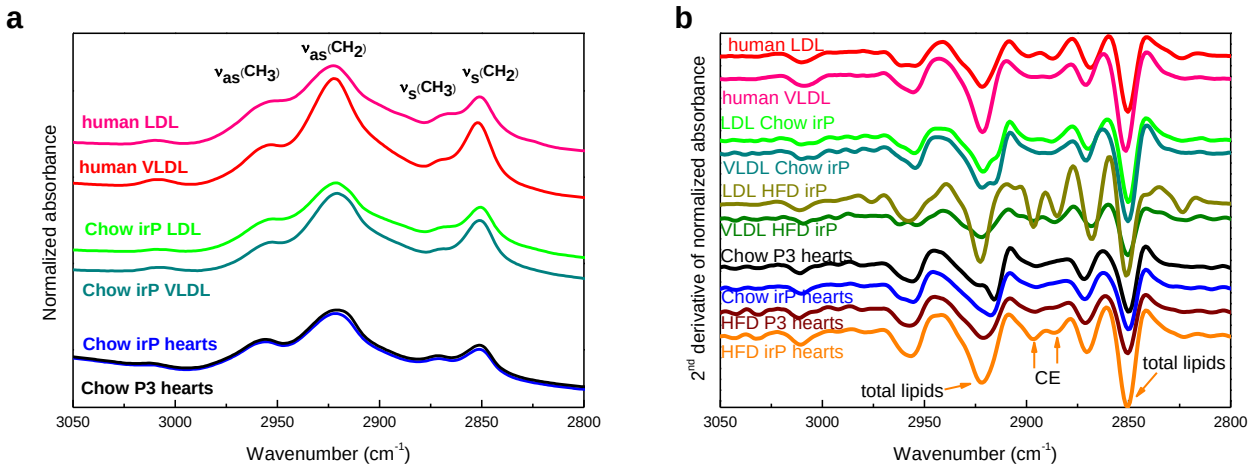

Figure S4. Infrared spectra and 2nd derivative spectra reflecting the similarity of human and rabbit lipoproteins signatures in the main lipid zone and the signature of lipids from LDL and VLDL in the hearts tissues. (a) Normalized mean FTIR-ATR spectra of rabbit lipoproteins, human lipoproteins and chow rabbit hearts (n = 5/group) in the (CHx) stretching zone. (b) FTIR-ATR 2nd derivative spectra in the same zone, with the superimposition of lipoproteins and hearts from HFD rabbits. Hearts FTIR spectra magnified 5X. Arrows indicate the intensification of absorption bands in HFD IrP rabbits.

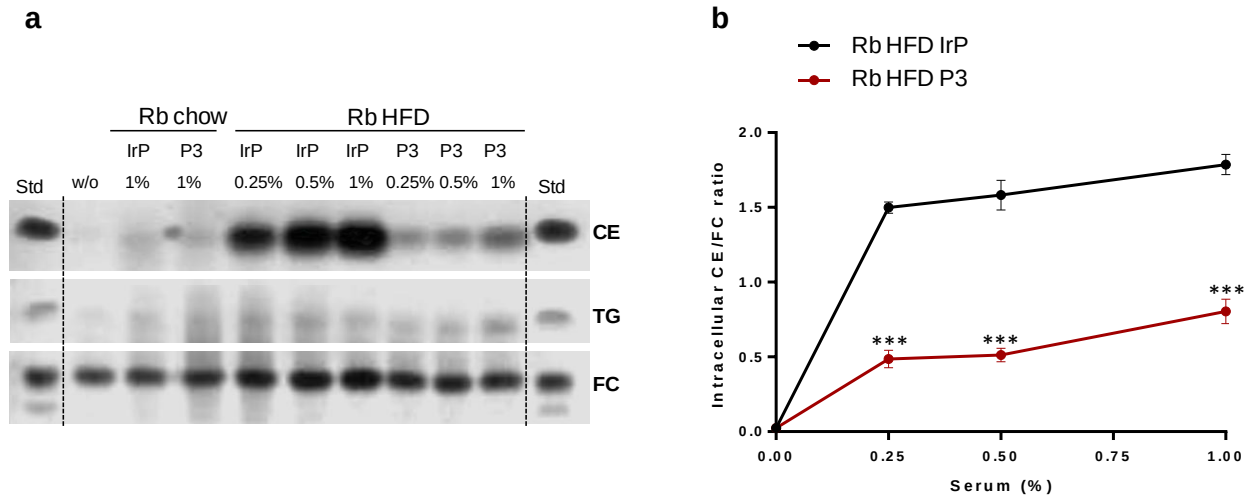

Figure S5. Anti-P3 Abs block intracellular cholesteryl ester accumulation in HL-1cells. (a) Representative thin-layer chromatography of HL-1 cell lipid extracts showing the bands corresponding to cholesteryl esters (CE), triglyceride (TG), and free cholesterol (FC) from HL-1 cells exposed to increased serum concentrations (0.25, 0.5 and 1%) from the different rabbit groups (n =3/group). The CE/TG/FC bands of standards (Std) are shown by duplicate. (b) Line graph showing the mean ± SD of intracellular CE/FC ratio in HL-1cells exposed to HFD IrP (black line) and HFD P3 (red line) rabbit serum (from 0.25% to 1% for 1.5h). ***p < 0.001 HFD P3 versus HFD IrP.

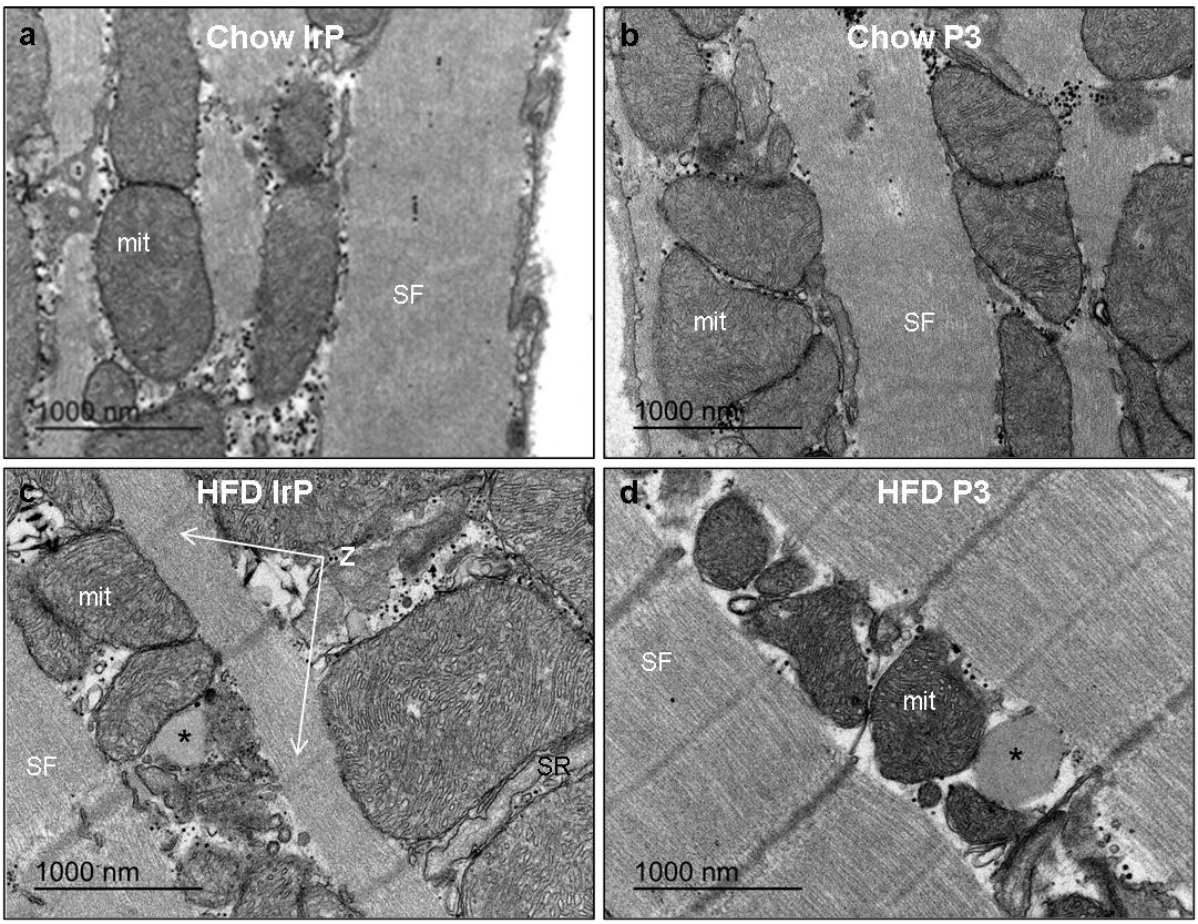

Figure S6. HFD induces lipid droplets formation in cardiomyocytes of rabbit heart. Representative electron micrographs of cardiomyocyte ultrastructure from the heart of the four rabbit groups. HFD IrP and HFD P3 hearts show prototypical lipid droplets (asterisks) that have different size and electrodensity in HFD IrP and HFD P3 hearts and that are located in the intersarcomeric cytoplasm between the sarcomeric fibers (SF) in close contact with mitochondria (mit).

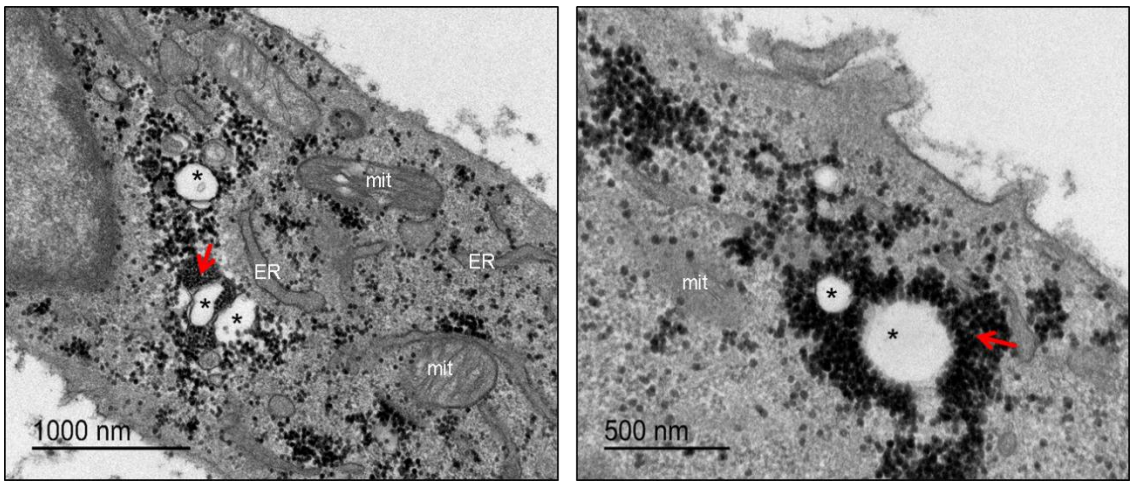

Figure S7. HFD induces lipid droplets formation in HL-1 cells. Thin-section electron micrographs of lipid droplets (asterisks) in HL-1 cells exposed to rabbit HFD IrP serum (1%, 2 h). LDs are surrounded by glycogen (red arrows) and are in close contact with mitochondria (mit) and endoplasmic reticulum (ER). Lipid droplets were not found in HL-1 cells exposed to HFD P3, chow IrP or chow P3 under similar conditions.

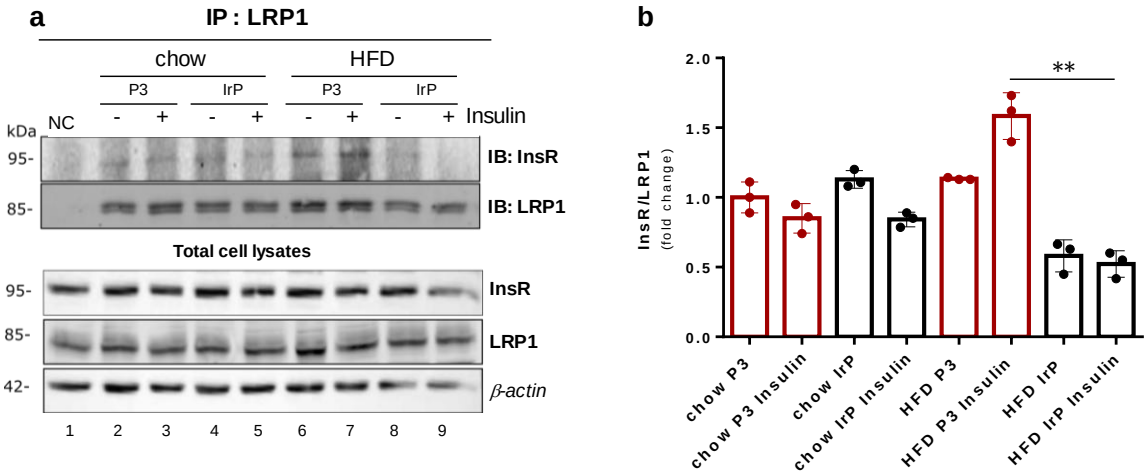

Figure S8. Anti-P3 Abs counteract the deleterious effect of hypercholesterolemic serum in the interaction between InsR and LRP1 in HL-1 cells. (a) Cell lysates were immunoprecipitated with anti-LRP1 antibodies and subjected to Western blot analysis for InsR and LRP1. (NC) non-immune control without anti-LRP1 ab. The detection of LRP1, InsR and β-actin in total lysates is shown in the lower panel. (b) Bar graphs showing the densitometric quantification of Western blot bands. Values are expressed as mean ± SD of the relative intensity of InsR bands normalized to LRP1 and shown as a fold against the mean value of chow P3 group, of three independent experiments (n = 3), **p<0.005 versus indicated conditions. Statistical significance was determined by One-Way ANOVA followed by a Dunnett´s multiple comparison test.

GLOBAL DISCUSSION

GLOBAL DISCUSSION

In this thesis project, we have generated two *in vivo* models using different approaches to modulate the LRP1 receptor. In the murine model, we used a genetic approach to induce LRP1 deficiency specifically and conditionally in cardiomyocytes. In the rabbit model, we used an LRP1-based immunotherapy to inhibit specifically the interactions of LRP1 with pro-atherogenic lipoproteins without altering LRP1 interaction with ligands involved in essential signaling pathways.

16 Study I

16.1 Validation of cm-*lrp1*$^{-/-}$ as a model of specific cardiomyocyte LRP1 deficiency

Real-time PCR and confocal microscopy analyses showed that cm-*Lrp1*$^{-/-}$ mice are characterized phenotypically by decreased Lrp1 levels in the heart, and specifically in cardiomyocytes. Cardiomyocytes isolated from the heart of cm-*Lrp1*$^{-/-}$ mice maintain a low expression of Lrp1 mRNA and LRP1 protein levels. Coherently, the cm-*Lrp1*$^{-/-}$ mice showed a low expression of Lrp1 mRNA and LRP1 protein levels in the heart but not in other tissues such as liver, skeletal muscle and eWAT. There were no differences in vldlr or ldlr mRNA expression levels in the heart of cm-*Lrp1*$^{-/-}$ and control mice.

16.2 Phenotypic changes induced by a high-fat diet in the murine model

Mice fed a HFD for 6 weeks generated a mouse model of diet-induced insulin resistance (IR). This was reflected, among other features, in increased body and eWAT weight, higher eWAT adipocyte size, increased glucose intolerance and AUC values. In addition, this model showed increased glucose, and insulin levels in plasma, and an elevation in the IR index (HOMA-IR).

This diet also induced hepatic steatosis due to an increased TG and FA uptake and accumulation in the liver. Our results in mice are in agreement with previous studies in HFD-fed rats, in which hepatic steatosis was observed after short times [243–245]. In our model, HFD-induced hepatic lipid accumulation was associated with decreased FAO oxidation due to reduced levels of proteins involved in FA oxidation and increased levels of proteins involved in FA synthesis. All these results agree with experiments *in vivo* using the Comprehensive Laboratory Animal Monitoring System (CLAMS), showing decreased whole-body lipid and glucose oxidation that result in lower systemic energy expenditure and oxygen consumption in HFD-fed compared to standard diet-fed mice.

However, this dietary intervention did not alter the accumulation of neutral lipids in the heart. In the murine model, most cholesterol is transported by HDL, and it was previously reported that the main lipoproteins supplying neutral lipids to the heart are TG-enriched lipoproteins[168].

16.3 Lrp1 cardiomyocyte deficiency prevents diet-induced overweight and glucose intolerance by facilitating increased energy expenditure.

Our results show that Lrp1 attenuation decreased blood glucose and insulin levels, insulin resistance, and weight gain without altering plasma lipid levels in HFD-fed mice. The weight-reducing effects of Lrp1 deficiency were associated to decreased eWAT weight and eWAT/BAT adipocyte size. These beneficial metabolic changes occur simultaneously with increased protein levels of carnitine palmitoyltransferase 1a (CPT1a) (a mitochondrial enzyme that plays a key role in FA oxidation) and a reduction in triglyceride levels in the liver. Our results are in line with a previous study showing that a moderate increase in CPT1a activity is sufficient to reduce hepatic TG levels [246].

CPT1a is the main isoform present in the liver, heart, and pancreas. This enzyme is in the outer mitochondria membrane and its main function is the transport of lipids to be metabolized in the organelle. An aberrant function of CPT1a and FAO favors the development of NAFLD and liver injury [247,248]. Along this line, short-term genetically induced hepatic FAO has been reported to mitigate insulin resistance in rodent models [249,250]. Together, these results suggest that the liver may play a central role in the favorable metabolic profile derived from *lrp1* attenuation in cardiomyocytes.

Indirect Calorimetry System or CLAMS experiments are widely used for the analysis of whole-body energy metabolism. These experiments allow the energy expenditure and substrate utilization to be calculated by measuring the rate of respiratory exchange [251]. In the present work, we demonstrate that cm-*Lrp1*$^{-/-}$ mice have a higher oxygen consumption and energy expenditure than HFD-fed control littermate. During the light period (starvation), the increased energy production of cm-*Lrp1*$^{-/-}$ mice is derived from lipid oxidation, while during the dark period (feeding), it is derived from glucose oxidation. We also found that there was no difference between cm-*Lrp1*$^{-/-}$ and control mice in terms of ambulation activity, indicating that the protection against weight gain of cm-*Lrp1*$^{-/-}$ mice was not caused by increased physical activity. These results demonstrate that all the favorable metabolic changes found in HFD-fed cm-*Lrp1*$^{-/-}$ mice are due to increased energy expenditure.

16.4 LRP1 controls systemic levels of atrial natriuretic peptide through modulation of Corin activity in cardiomyocytes

To determine the mechanism by which LRP1 deficiency produces an increase in energy expenditure, differential proteomics studies of hearts from lrp1 deficient mice and controls were performed. These studies revealed that ANP and serine protease inhibitors such as serpin1a, serpin3k, serpin1b, and serpin1d were differentially secreted proteins in the heart of cm-*Lrp1*$^{-/-}$ mice compared with control mice. Several peptides or proteins secreted by cardiac cells (e.g., cardiokines) may influence not only cardiac function but also mechanisms occurring in distal organ tissues [196,224]. Considering all this information,

we decided to study the ANP signaling pathway in liver and skeletal tissues, and the activity of corin, which is necessary for the cardiac release of ANP, in the heart.

In our murine model, the attenuation of cardiomyocyte lrp1 increased corin activity, enhancing ANP secretion. This corin-induced ANP release found in the heart of cm-*Lrp1*$^{-/-}$ mice is consistent with previous studies in rat and mouse models showing how the switch from ANP inactivation to activation depends exclusively on the action of corin [211,252]. Chan *et al.* reported elevated levels of proANP peptide (inactive form) and almost undetectable values of ANP (active form) in the heart of corin-deficient (*Cor*$^{-/-}$) mice. *Cor*$^{-/-}$ mice showed increased body weight, hypertension, and cardiac hypertrophy compared with control mice. ANP release in these mice was recovered only by injection of active recombinant soluble corin [252].

In our study, the corin catalytic activity assays revealed increased corin activity in hearts from *Lrp1*-deficient mice. Immunoprecipitation of corin followed by immunoblotting with anti-serpinA1 antibody showed increased complex formation between the protease domains of corin and serpinA1. Despite complex formation between serpinA1 and corin protease domains, it has been reported that these soybean trypsin inhibitors fail to efficiently inhibit cell-bound corin due to steric hindrance [253]. Furthermore, it has been proposed that the binding of soybean trypsin inhibitors to corin protects the enzyme from inhibition by its hitherto unknown physiological inhibitors. LRP1 binds to serpin:protease complexes and determines their degradation, with this process being very effective in controlling protease activity in various cell types [254,255]. It is tempting to speculate that cardiac LRP1 deficiency might facilitate an increased half-life of the corin/serpinA1 complex, with corin protease activity conserved through interactions with serpins. A more direct proof of the capacity of LRP1 to modulate ANP release has been obtained from cell culture experiments performed with an LRP1-deficient HL-1 cell line (LRP1-HL-1 cells) previously generated by our group [161,170,174,256]. Our results revealed the presence of higher ANP levels in the supernatants from LRP1- HL-1 cells as compared to those from control cells.

In contrast to the differential levels of plasma ANP between cm-*Lrp1*$^{-/-}$ and control mice, there were no alterations in cardiac or plasma BNP levels between groups. It has been previously reported that BNP activation depends on furin activity. A specific silencing of furin seems to decrease the cleavage of proBNP in both atrial and ventricular myocytes [211]. Furin is mainly localized in the Golgi apparatus where BNP activation occurs [211,257,258]. Further complementary experiments will be required to determine furin levels in the heart of cm-*Lrp1*$^{-/-}$ mice. Supporting our results, the specific silencing of corin has been previously shown to decrease proANP levels in both atrial and ventricular myocytes with no impact on proBNP cleavage [211].

In a previous study, we reported that LRP1 is upregulated in cardiomyocytes exposed to atherogenic lipoproteins and in the heart of diabetic rats [161,174]. It is therefore feasible that LRP1 overexpression in the heart could be associated with metabolic alterations. Further studies in *in vivo* experimental models of diabetes are indeed required to know whether cardiac LRP1 overexpression plays a role in the reduction of plasma ANP levels observed in with the context of type 2 diabetes [259–261].

16.5 ANP is the mediator that activates fatty acid oxidation in the liver of cm-*Lrp1*$^{-/-}$ mice

In previous sections, we found that proANP levels were decreased in cm-*Lrp1*$^{-/-}$ mice in association with the activation of corin, which promotes ANP release into the circulation. Here, we explain how increased circulating ANP levels are related to the activation of NPRA signaling. To find out whether the effects observed in the liver were caused by ANP, we included two additional groups treated with the NPRA antagonist (A71915). A71915 is an ANP-derived peptide composed of two non-native amino acids at locations 8 and 26 that efficiently inhibits binding of ANP to its receptor [262–264].

We found that the ANP/NPRA/cGMP/pVASP signaling pathway was activated in the liver of cm-*Lrp1*$^{-/-}$mice. In particular, pVASP specifically phosphorylates AMPK in the liver of a mouse model of diabetes [265], and AMPK regulates the phosphorylation of acetyl-CoA carboxylase (ACC), which results in its inactivation [266]. Results from the present study show that ACC phosphorylation is increased in the liver of deficient mice, and that this increase is abolished by treatment of deficient mice with the NPRA antagonist, indicating that the AMPK/ACC energy-sensing pathway may be modulated by ANP in the liver of our murine model. AMPK is recognized as the principal regulator of lipid metabolism and mitochondrial homeostasis [267,268]. One of the critical roles of AMPK is the regulation of lipid metabolism through ACC phosphorylation. ACC phosphorylation inhibits the production of malonyl-CoA, a substrate for fatty acid synthase (FAS) and a potent inhibitor of CPT1 [268]. We now show that cm-*Lrp1*$^{-/-}$ mice have increased levels of CPT1 in the liver, and that these increased levels depend on NPRA signaling. These results agree with our cell culture experiments that showed that hepatocytes exposed to ANP-enriched supernatant from LRP1-HL-1 cells, or to ANP directly, had increased levels of phosphorylated AMPK and CPT1. The link between AMPK phosphorylation and CPT1 activation has been previously demonstrated in oxidative tissues of a mouse model [267]. Upon AMPK activation, ACC phosphorylation leads to ACC inactivation, which promotes the reduction of malonyl-CoA, a substrate for fatty acid synthase and a potent inhibitor of CPT1 [269].

To understand the effects of pAMPK activation in FAO, we analyzed the main components of the oxidative phosphorylation system (OXPHOS) (responsible for mitochondrial respiration) and UCP3, an indicator of mitochondrial response to intracellular FA uptake.

Positive regulation of mitochondrial OXPHOS subunits supports and enhances mitochondrial respiration in the liver of cm-*Lrp1*$^{-/-}$ mice. The increase in these mitochondrial proteins was eliminated in cm-*Lrp1*$^{-/-}$ mice treated with A71915, indicating that NPRA signaling is involved in the increase of OXPHOS protein subunits in mice. Further experiments are required to elucidate the mechanism by which ANP signaling enhances the level of these OXPHOS protein subunits. This could be due to enhanced mitochondrial synthesis or an enhanced amount of protein subunits per mitochondrion. Together, these results support ANP-enhanced mitochondrial fatty acid oxidation in the liver of cm-*Lrp1*$^{-/-}$ mice. Finally, UCP3, [^{3}H]-TG and [^{3}H]-FFA and FA/TG transporters, such as Cd36 and Vldlr, are increased in the liver of *lrp1*-deficient mice, and the increase was abolished by treatment of *lrp1*-deficient mice with the antagonist NPRA. Previous studies reported that pAMPK positively modulates Cd36 in a mouse model of liver-specific AMPK activation (delivery of active AMPK using adenovirus) [270].

Here, we show that the enhanced FA uptake and oxidation promoted by ANP reduces TG accumulation in the liver of *lrp1*-deficient mice. These results are in agreement with previous studies showing that moderate increases in Cpt1a activity are sufficient to i) reduce hepatic TG levels in animals overexpressing CPT1a [246] and ii) modulate diabetes and obesity [227]. Interestingly, the reduction of hepatic triglyceride content in deficient mice occurs in the context of increased FA delivery to the liver due to a reduced [^{3}H]-TG and [^{3}H]-FFA uptake by eWAT. By counteracting ANP-induced FA uptake in the liver, the NPRA antagonist caused increased FA uptake by eWAT of cm-*Lrp1*$^{-/-}$ mice. Although a direct effect of ANP on cm-*Lrp1*$^{-/-}$ adipose tissue cannot be ruled out, our data support that the benefits of cardiac *Lrp1* deficiency on diet-induced obesity derive from its direct upregulatory effects on whole-body energy expenditure.

The liver is considered the major organ in lipid and glucose homeostasis and is a major contributor to whole-body lipid oxidation [271]. In addition, previous studies have consistently demonstrated the link between hepatic FAO and insulin resistance [272]. The results of the present study show that Akt phosphorylation, a crucial step in the insulin signaling pathway, is more active in the liver of cm-*Lrp1*$^{-/-}$ mice as compared to controls. Furthermore, CLAMS experiments showed glucose oxidation during the dark phase and fat oxidation during the light phase. Increased oxygen consumption, energy expenditure, and the shift from lipid oxidation to glucose were dependent on ANP signaling, as all these protective changes were abolished in cm-*Lrp1*$^{-/-}$ mice treated with the NPRA inhibitor. However, further studies based on the analysis of signaling immediately after insulin administration are required to draw conclusions about the role of ANP in modulating diet-induced hepatic insulin resistance [273].

All these favorable metabolic changes observed in deficient mice were abolished by treatment with the NPRA antagonist, indicating that the AMPK/ACC energy-sensing

pathway may be modulated by ANP in the liver. *Acsl3* mRNA expression levels were also reduced in the liver of cm-*Lrp1*$^{-/-}$ compared with control mice. Deletion of *Acsl3* has been reported to decrease total acyl-CoA synthase activity in ob/ob mice and high sucrose diet-fed mice [274]. Together, these results strongly suggest that ANP-induced AMPK phosphorylation is involved in increased FA oxidation and inactivation of FA synthesis in the liver of cm-*Lrp1*$^{-/-}$ mice.

16.6 The ANP signaling pathway is partially activated in skeletal muscle of cm-*Lrp1*$^{-/-}$ mice

Natriuretic peptides released by the heart has been shown to alter skeletal muscle metabolism. Of note, an increase of the NPRA receptor (involved in both ANP and BNP signaling) has been detected in the muscle of athletes [212]. In particular, ANP has been reported to promote oxidative metabolism in human skeletal muscle, and to induce gene expression of PGC-1α and mitochondrial OXPHOS in a cyclic GMP-dependent manner in human myotubes [201]. The results of the present study show that the ANP-induced increase of NPRA/cGMP/pVASP in skeletal muscle of cm-*Lrp1*$^{-/-}$ mice is abolished by treatment with the NPRA antagonist A71915. In our murine model, ANP signaling in skeletal muscle was also linked to positive regulation of mitochondrial OXPHOS, which affects CVATP5A and CII-SDHB subunit overexpression. However, there were no differences in phosphorylated AMPK, CPT1 or UCP3 levels in skeletal muscle of cm-*Lrp1*$^{-/-}$ and control mice. In contrast to the liver, there were no differences in [^{3}H]-TG and [^{3}H]-FFA uptake by skeletal muscle between cm-*Lrp1*$^{-/-}$ and control mice, although there was a significant increase in [^{3}H]-TG and [^{3}H]-FFA uptake detected in the A71915-treated groups. These results indicate that FA uptake and FA oxidation are not significantly modulated by NPRA/cGMP/pVASP signaling in skeletal muscle of cm-*Lrp1*$^{-/-}$ mice, and suggest that downstream mediators of VASP signaling are different in liver and skeletal muscle.

The differential ANP effects on liver and skeletal muscle might be due to the fact that the main effector of metabolism in skeletal muscle is BNP. Mice with induced overexpression of BNP showed improvement of obesity and glucose intolerance due to increased fat oxidation [275]. Other studies have shown that BNP can protect against mitochondrial dysfunction and oxidative stress in skeletal muscle after ischemia-reperfusion [276]. Different studies have also reported the participation of perosyxomel proliferator activated receptors (PPARs) in the effects of BNP on mitochondrial biogenesis and fat oxidation in skeletal muscle [275]. In addition, AMPK, a master enzyme in cellular energy homeostasis, has been identified as a novel PPARα-associated component in the promoters of activated metabolic genes [277]. Further studies are needed to determine the role of BNP in skeletal muscle metabolism in deficient mice.

17 Studies II and III

17.1 Impact of hypercholesterolemia in the cardiovascular system of rabbits

17.1.1 Impact of HFD on lipids and the lipoprotein profile

Biochemical studies have revealed that circulating levels of cholesterol and triglyceride are much higher in HFD-fed rabbits than in chow-fed control rabbits. Specifically, the HFD-fed groups had much higher total mass of circulating LDL and, to a lesser extent, of VLDL, than control group, with most of HFD CE mainly transported by ApoB-100 lipoproteins (LDL and VLDL). Considering that the percentage of the protein in lipoproteins is similar to that in humans, LDL and VLDL are extremely CE enriched particles in this rabbit model. In line with our results in rabbits, an increased atherogenicity of large CE-enriched ApoB100 lipoproteins has been previously reported in monkeys and pigs [278,279]. Both VLDL and LDL had much higher CE content in HFD rabbits than in control rabbits. Despite the low total mass of circulating VLDL and LDL in serum from control groups, these lipoproteins had higher proportion of TG than the HFD groups. These results are consistent with previous studies in which Japanese white rabbits were fed a diet containing 1% cholesterol for 8 weeks (chol-8w) or 12 weeks (chol-12w). Rabbits in the chol-8w group had higher circulating levels of total cholesterol, HDL-cholesterol, and LDL-cholesterol as compared to the control group (chow-fed rabbits), and this increase was more pronounced with a longer diet time (chol-12w fed rabbit) [280]. These HFD-induced changes in the lipoprotein profile occurred without differences in body weight among the three groups [280].

17.1.2 Impact of HFD on the accumulation of lipids in vasculature, heart, and liver in rabbits

17.1.2.1 HFD upregulated vascular cholesteryl ester accumulation and inflammation and causes atherosclerosis

In this study, we found a strong increase in vascular CE accumulation (but not free cholesterol) induced by HFD in the aorta and carotids in the rabbit model. This increase in vascular CE coincided with increased monocyte recruitment and VSMC migration to the arterial intima (as corroborated by confocal microscopy). HFD mainly increased CE content in rabbit LDL in agreement with previous studies in this model [158,281] as well as in humans [282,283] and promotes hypercholesterolemia, leading to early atherosclerotic lesions or fatty streaks (after only one month of dietetic intervention) in the vasculature. In addition, similar to previous studies using NZW rabbits [284], fatty streak lesions comprising SMC and macrophages were present in our rabbit model. *Ex vivo* studies in which we exposed cultured hcVSMC and hMΦ to rabbit HFD serum from control and IrP groups (0.5%, 2 h) showed a massive build-up of intracellular CE in these cells. Concurrently with HFD serum-induced intracellular CE accumulation, LRP1 protein levels were augmented while those of sterol regulatory element binding protein 2 (SREBP-2)

decayed in these cells. These results are in line with the capacity of intracellular CE to stimulate LRP1 transcription through SREBP-2 downregulation, as previously described by our group [151,157,285]. There were no differences in LRP1 and SREBP-2 protein levels between cells exposed to chow serum from IrP or P3-immunized rabbits. Besides LRP1, several pro-inflammatory markers, including TNFR1 and NFkB, were also upregulated by HFD in the rabbit vasculature and in human SMC and macrophages.

Like in other experimental models [286–288], our FDG-PET/CT imaging studies in our rabbit model confirmed that HFD increased the SUVmax (a surrogate marker of inflammation) and validated the vascular association between cholesterol accumulation and inflammation. In addition, Doppler ultrasonography imaging studies revealed that HFD increased the resistance index (RI) of the external and internal carotids, despite the lack of direct evidence of atherosclerotic plaques in this arterial territory. In carotid arteries, a significant correlation between RI and the degree of generalized atherosclerosis has been previously demonstrated in humans [289].

17.1.2.2 HFD upregulates myocardial CE and TG accumulation in the heart causing alterations in cardiac insulin sensitiviy

In the present rabbit model, HFD strongly increased the CE content of heart, as previously shown in other translational *in vivo* models [161,170,174,242,290]. In contrast to aorta, where HFD only increased CE content, HFD also increased the TG content in the heart. This reflects the major role of VLDL as a source of TG and CE in the heart [168] compared to the limited role of VLDL as a neutral lipid source in the arterial intima [291].

On the other hand, HFD induced the intracellular accumulation of CE but not of TGs in HL-1 cardiomyocytes treated with serum from control groups. The lack of effect of HFD serum on the intracellular TG content of HL-1 cells could be a result of a short exposure time, since previous studies from our group showed a strong increase in intracellular TG content in HL-1 cells exposed to VLDL for 18 h [292].

In association with myocardial lipid accumulation, HFD induced impairment of cardiac insulin responsiveness due to a reduction of cardiac InsR and GLUT4 membrane levels and LRP1/InsR interactions. In HL-1 cells (in which HFD increased only in intracellular CE), HFD affected the InsR/LRP1 association, InsR membrane translocation, and InsR signaling , suggesting that these alterations are caused by intracellular CE accumulation in cardiomyocytes.

17.1.2.3 HFD upregulates neutral lipid content in the liver of rabbits

HFD also dramatically increased the accumulation of CE, FC, and TG in the liver. These results are in agreement with other studies using this rabbit model, in which the group fed a cholesterol-enriched diet was found to have elevated hepatic cholesterol accumulation already after 2 weeks, which worsened after 7 weeks [293].

17.1.3 Impact of HFD on glucose tolerance testing

Similar to previously reports in rabbits [280], all the groups of rabbits analyzed in this study exhibited a similar increases in body weight throughout the diet period. However, the glucose tolerance test (GTT) showed increased glucose intolerance and higher AUC levels in the HFD-fed groups compared to the chow diet-fed groups. These results indicate that we have developed a rabbit model of diet-induced peripheral insulin resistance. This is consistent with the upregulatory effect of HFD on insulin resistance in animal models [294,295] and in humans [296].

17.2 Impact of lrp1-based immunotherapy on the alterations caused by hypercholesterolemia in the cardiovascular system

17.2.1 Effects of P3-immunization on the production of anti-P3 antibodies against the LRP1 receptor in the rabbit model

Rabbits immunized with the P3 peptide have a strong immune response, resulting in the production of anti-P3 antibodies that specifically block the binding of atherogenic lipoproteins to the LRP1 receptor. Levels of anti-P3 antibodies were maintained in serum from P3-immunized rabbits throughout the whole dietetic period. Immunization approaches have been previously used in this and other animal models to generate antibodies against lipoprotein receptors. For instance, Shen Qu *et al.* immunized NZW rabbits with a polypeptide fragment of the VLDL receptor to generate anti-VLDLR antibodies using a similar immunization pattern (a first injection and 4 reminder doses every 28 days). Anti-VLDLR antibodies efficiently block VLDL binding to VLDL receptor in human and rat samples [297], showing the efficacy of this immunization pattern for producing efficient polyclonal antibodies.

17.2.2 Impact of P3-immunization on lipid accumulation in the vasculature, heart, and liver

17.2.2.1 Anti-P3 Abs reduce cholesteryl ester accumulation in the vasculature

The essential role of LRP1 in signaling [142–146] motivated us to develop antibodies to specifically block aggregated LDL binding by vascular cells. In the vasculature of our rabbit model, anti-P3 antibodies decrease LRP1 levels, resulting in a reduction of vascular CE accumulation and in fatty streak formation, and a decrease in pro-inflammatory signaling.

Interestingly, HFD serum from P3 immunized rabbits failed to induce intracellular CE accumulation in these cell types. Moreover, aggregated LDL also failed to induce intracellular CE accumulation in cells pre-incubated with chow serum from P3 immunized rabbits. These results are in line with previous results from the group showing that Abs generated in P3-immunized rabbits efficiently prevented foam cell formation induced by exposure of human coronary vascular smooth muscle cells to aggregated LDL [93]. Together, these results demonstrate the crucial role of LRP1 in the uptake of rabbit HFD

serum CE-enriched lipoproteins, and highlight that the anti-atherogenic properties of anti-P3 antibodies rest on their efficacy to inhibit foam cell formation from smooth muscle cells and macrophages.

17.2.2.2 Anti-P3 antibodies reduce CE accumulation in the heart

Remarkably, we found that in the heart, anti-P3 antibodies were also extremely efficient at blocking myocardial intramyocardial CE accumulation. In line with the capacity of LRP1 to mediate selective CE uptake from lipoproteins [298], TG accumulation was not blocked in the heart of P3-immunized rabbits. These results are also in agreement with the reduction of intracellular CE accumulation in neonatal rat ventricular myocytes and cardiac-derived HL-1 cells made deficient in LRP1 through RNA silencing approaches [161,170]. Our electron microscopy studies revealed that lipid droplets are undoubedly formed in the cardiomyocytes in tight contact with sarcomeric fibers, mitochondria and endoplasmic reticulum. A remarkably finding has been that cardiomyocytes of HFD P3-injected rabbits, although lower in number, are bigger and more electrodense than those found in the heart of HFD control rabbits, suggesting a different lipid composition. These imaging results combined with molecular studies suggest that lipid droplets in the heart of P3-immunized rabbits contain almost exclusively TG, while those in the heart of IrP rabbits are mixed (e.g., CE and TGs). Previous studies have shown that lipid droplets containing exclusively CE have a reduced size [299,300]. In addition, from the biophysical point of view, the liquid crystalline nature of CE mechanistically determines TG packaging [301,302]. These studies suggest that cholesterol limits lipid droplet growth, and explain the expansion of lipid droplets (mainly composed of TGs) in the heart of HFD-fed P3 rabbits. Together, these results demonstrate that P3-immunization shows specificity for targeting CE accumulation in the heart.

17.2.2.3 Anti-P3 Abs does not modify cholesteryl ester accumulation in the liver

Here, P3 immunization reduced CE accumulation in the vasculature (aorta and carotids) and the heart but not in the liver, where LRP1 plays a secondary role on the uptake of cholesterol-enriched lipoproteins. The differential impact of serum HFD on neutral lipid content in the aorta and heart with respect to the effect on liver could be associated with the lipoproteins that interact mainly with these tissues. In the vasculature and heart, LRP1 putatively interacts with CE-enriched lipoproteins [152,153,161,183,303], while in the liver, LRP1 interacts mainly with ApoE-enriched lipoproteins, such as chylomicrons [304]. ApoB100 and ApoE are known to interact with the LRP1 receptor through different clusters. The new epitope generated on ApoB100 during LDL aggregation interacts with cluster II (CR9 domain) [93], while ApoE interacts with cluster III (CR17 domain) [305,306]. The different lipoproteins that reach the vasculature, heart, and liver may explain the different impact of P3 immunization on the accumulation of CE in these tissues. The CR9 and CR17 domains are so spatially distant that it is structurally impossible for

anti-P3 antibodies to cause any effect on ApoE-enriched lipoprotein binding. This could explain why immunization with P3 exerted no effect on HFD-induced neutral lipid accumulation in the liver. The liver is a key organ that modulates whole-body lipid and lipoprotein metabolism and, consequently, the circulating lipid and lipoprotein profile [307]. Therefore, the lack of impact of Abs anti-P3 on hepatic neutral lipid content could be a determinant of the similar lipoprotein profile between the groups

17.2.3 Consequences of specific inhibition of vascular cholesteryl ester aucmulation on the development of atherosclerosis and inflammation

Imaging studies were complemented with immunohistochemical and molecular studies showing that P3 immunization efficiently prevented the formation of fatty streaks, and particularly, the recruitment of lipids and cells (macrophages and SMCs) in the arterial intima of rabbits. These effects were associated with a significant reduction of pro-inflammatory signal in the vascular wall. The efficacy of P3-immunization as anti-inflammatory strategy was also validated in imaging studies. Note that using ^{18}F-FDG/PET imaging, which was recently validated as read-out of vascular inflammation in rabbits [288,308], showed a significant reduction of SUVmax in the aorta of P3-immunized rabbits. In addition, confocal microscopy studies showed a clear reduction of both intimal SMC and macrophages in the arterial intima of hypercholesterolemic P3-immunized rabbits, Therefore, in our model, both macrophages and SMCs seem to contribute to 18F-FDG uptake and atherosclerotic signal in PET/CT studies Lederman *et al.* showed that ^{3}H-2dG signal from rabbit plaques on autoradiography originates not only from macrophage-rich areas, but also from SMCs [309]. In line with this, it has been also shown that SMCs, but not macrophages, increase theirs glucose uptake when exposed to pro-inflammatory cytokines [310].

While cardiac imaging for the detection of atherosclerotic lesions at different stages has been previously used for rabbit aortas [286,311–313], the impact of HFD on the development of atherosclerosis in the carotids of this animal model, and especially through imaging techniques such as Doppler ultrasonography, has been less investigated. Here, we demonstrated the efficacy of P3 immunization in reducing carotid resistance index (RI), although the effect was different between external and internal carotids (greater for external carotids). In fact, additional carotid lipid analyses showed that P3 immunization reduced CE accumulation in the external carotid but not in the internal carotid. Differential anatomy and hemodynamics could probably explain the differential impact of P3 immunization on these carotids. Based on aortic PET/CT and carotid Doppler ultrasound, our results revealed that P3 immunization effectively reduces HFD-induced atherosclerosis in rabbits, at least in the early stages, and in different vascular territories. Furthermore, these results suggested that PET/CT and ultrasonography are imaging techniques that can track the effect of this new immunotherapy in translational *in vivo* models.

Previous studies have shown the beneficial effects of different immunotherapies for the treatment of atherosclerosis [314,315]. Anti-LDL or anti-apoB Abs reduce atherosclerosis in in ApoE$^{-/-}$ and LDLR$^{-/-}$ mice [103], anti-angiopoietin-2 (cytokine that regulates angiogenesis and inflammation) Abs have efficacy in inhibiting fatty streak formation in brachiocephalic arteries of hypercholesterolemic mice [314], and anti-eotaxin-2 (chemokine linked to inflammatory processes) Abs efficiently decrease early atherosclerotic plaque formation in young *ApoE*$^{-/-}$ mice by decreasing monocyte adhesion and migration [315].

Our results highlight the strategic therapeutic value of anti-P3 antibodies in inhibiting diet-induced cellular CE loading and associated inflammation in the vasculature. Our PET/CT studies show, in line with previous studies [286], that ^{18}F-FDG uptake reaches peak values during early foam cell formation. In addition, our results show the anti-atherosclerotic efficacy of P3 immunization in early lesions traced by PET/CT. Finally, complementary confocal microscopy analysis showed that reduced ^{18}F-FDG uptake in the aorta of P3-immunized rabbits occurred concomitantly with a reduced presence of macrophages and SMCs in the arterial intima.

17.2.4 Implications of specific inhibition of myocardial cholesteryl ester accumulation for cardiac insulin sensitivity

Intramyocardial CE accumulation in the heart is promoted by ischemia [161,242,290], hypercholesterolemia [316], and obesity [174]. However, the clinical impact of intramyocardial CE accumulation (independently of TG accumulation) has not yet been investigated, even though experimental studies have consistently shown that the causes and consequences of intracellular CE and TG accumulation involve differential mechanisms and pathological consequences. TG accumulation is mainly caused by an imbalance between the rates of FA entry and FA oxidation, and it usually occurs in parallel to accumulation of detrimental lipid intermediates, such as long-chain acyl-CoA, ceramides, and diacylglycerol, all of which impair insulin signaling and glucose use in the heart [317]. We and others have proposed that intramyocardial CE accumulation is caused by the uptake of CE-enriched lipoproteins through lipoprotein receptors [161,170,290].

Here, we show for the first time in a high translational *in vivo* model that intramyocardial CE accumulation is linked to a deficiency of InsR and GLUT4 in cardiac membranes as well as to an impaired LRP1/InsR interaction. Both InsR and GLUT4 were recovered in cardiac membranes of hypercholesterolemic rabbits by inhibition of myocardial CE accumulation. In line with this, *ex vivo* experiments showed that rabbit hypercholesterolemic serum strongly induces intracellular CE accumulation in HL-1 cardiomyocytes, decreasing InsR signaling, insulin-induced GLUT4 translocation to plasma membrane, and insulin-induced glucose uptake in these cells. All these outputs were significantly reduced in HL-1 cells exposed to hypercholesterolemic serums containing anti-P3 Abs. These results in the *in*

vivo model are in line with previous studies from our group showing a reduction in the InsR/LRP1 association in CE-loaded HL-1 cells [183]. These novel findings show that cardiomyocyte intracellular CE accumulation plays a crucial role in impaired cardiac insulin response induced by diet, and that these alterations are efficiently reduced by exposure to antibodies against the P3 sequence of the LRP1 CR9 domain. Whether this interaction is direct or is mediated by other intermediate proteins remains to be explored.

A key result from the present study is that anti-P3 Abs, which block LRP1 interactions with CE-enriched lipoproteins and intramyocardial CE accumulation, facilitate the recovery of InsR levels and InsR/LRP1 complex in membranes in the heart of rabbits and HL-1 cells exposed to HFD serum. Unexpectedly, we have also found that HFD increases total InsR levels in rabbit heart, and that anti-P3 Abs also blocks this effect. Interestingly, the presence of excessive InsR levels in muscle tissues has been proposed to contribute to dyslipemia and steatosis [318] and to be a compensatory mechanism in a situation of diet-induced insulin resistance [319]. In our model, both total and membrane LRP1 were higher in HFD-fed groups as compared to standard chow control groups, and anti-P3 Abs reduced the LRP1 levels to near that found in the control group, as expected by the positive transcriptional upregulation of LRP1 by hypercholesterolemia [151]. In the presence of anti-P3 Abs, the cardiac membrane InsR levels and the InsR/LRP1 interactions were even higher than those found in the control group, suggesting that blocking LRP1 interactions with lipoproteins could be a highly efficient process for recovering a correct cardiac insulin response.

Our *ex vivo* studies showed that reducing the levels of the InsR/LRP1 complexes by a HFD was directly responsible for alterations in InsR signaling, in agreement with previous studies showing the pivotal role of LRP1 in insulin-induced InsR phosphorylation [183–185]. Further studies are now required to determine how intramyocardial CE accumulation impairs InsR/LRP1 complex formation, and how anti-P3 Abs overcomes this effect.

Insulin and glucose metabolism are tightly related, and glucose transport across the cell membrane is strongly influenced by membrane fluidity [320] and modulated by cholesterol [321]. Our current results from *ex vivo* studies showed that hypercholesterolemic serum reduces insulin response in terms of glucose uptake, and that anti-P3 Abs restored this response. In rabbit hearts, we showed that GLUT4 trafficking to cardiac membrane was reduced in HFD IrP rabbits but recovered in HFD P3 rabbits.

In line with our results, HFD-mediated membrane cholesterol loading seems to promote the loss of cortical actin filaments required for GLUT4 trafficking to the membrane (a hallmark of skeletal muscle insulin resistance) [322].

We showed that blocking intramyocardial CE accumulation with anti-P3 Abs was sufficient to restore insulin-induced InsR signaling, GLUT4 trafficking to plasma membrane, and

glucose uptake by HL-1 cardiomyocytes. Thus, LRP1-mediated CE accumulation is an early and reversible mechanism linking HFD to altered insulin response. Indeed, the multiple roles for LRP1 in mediating lipoprotein uptake [151,298], InsR signaling [183,184], and GLUT4 trafficking [183,323] also underpin the link between the cardiomyocyte intracellular CE accumulation and cardiac insulin signaling abnormalities. It is tempting to suggest that, by impairing LRP1 binding to CE-enriched lipoproteins, anti-P3 Abs preserve the interaction of LRP1 receptor with other receptors or transporters, such as InsR or GLUT4, respectively, facilitating their movement to plasma membrane. In addition, by reducing CE accumulation, anti-P3 Abs preserve InsR and GLUT4 trafficking. Further studies are required to explore these crucial mechanistic aspects connecting LRP1-mediated intramyocardial CE accumulation and insulin resistance in peripheral tissues. As glucose uptake in the heart is largely controlled by insulin-sensitive mechanisms, insulin resistance is an obstacle for enhanced myocardial glucose utilization. In recent studies, the use of insulin-sensitizing agents, such as metformin or SGLT2 inhibitors, was shown to reduce the risk of cardiovascular death or hospitalizations for heart failure in patients with T2DM [324,325].

MAIN CONCLUSIONS

18 Conclusions of Study I

- Lrp1 deficiency preserves corin activity in cardiomyocytes and favors increased ANP release into the bloodstream.
- Increased circulating ANP levels activate the NPRA/cGMP/pVASP axis in the liver.
- NPRA signaling in the liver is linked to AMPK phosphorylation, increased FA uptake and metabolism, and decreased hepatic TG accumulation.
- Treatment with NPRA antagonist abolish the protection that lrp1 deficiency confers against metabolic alterations and obesity.

19 Conclusions of Study II

- Anti-P3 antibodies prevent the cholesteryl ester accumulation in the vasculature (aorta and carotid arteries)
- P3 immunization efficiently blocks the formation of fatty streaks and pro-inflammatory signaling in the aorta
- Anti-P3 antibodies block foam cell formation from smooth muscle and macrophages
- The beneficial effects of anti-P3 antibodies can be tracked using non-invasive imaging techniques, such as PET/CT and Doppler ultrasonography

20 Conclusions of Study III

- Anti-P3 antibodies decrease cholesteryl ester accumulation in the heart without affecting triglyceride accumulation.
- The reduction in myocardial CE accumulation facilitates the recovery of InsR levels and InsR/LRP1 complex in cardiac membranes of hypercholesterolemic rabbits.
- GLUT4 trafficking is recovered in cardiac membrane of P3-immunized rabbits fed a hypercholesterolemic diet

TRANSLATIONAL POTENTIAL OF THE THESIS

TRANSLATIONAL POTENTIAL OF THE THESIS

Our results show that the favorable metabolic profile and increased energy expenditure in cm-*Lrp1*$^{-/-}$ mice are mainly dependent on ANP signaling involving hepatic AMPK activation. It has been described that patients with a low capacity to degrade active natriuretic peptides have better outcomes [326,327]. In humans, the main protective metabolic effects of ANP are related to the lipolytic effects of ANP in adipose tissue [328–330]. Indeed, high plasma natriuretic peptide levels have been associated with weight loss in humans [331,332]. Here, treatment of cm-*Lrp1*$^{-/-}$ mice with the NPRA antagonist restores energy expenditure to the levels of control mice, suggesting that ANP/NPRA signaling is involved in the increased energy expenditure and weight reduction of cm-*Lrp1*$^{-/-}$ mice. It will be interesting to test in humans whether ANP-induced hepatic FA uptake/oxidation is an additional mechanism contributing to the impact of high circulating natriuretic peptide levels on weight loss. According to the present study, low levels of Lrp1 expression in cardiomyocytes would contribute to the maintenance of high circulating natriuretic peptide levels. This could be very relevant in patients with metabolic disorders. A previous study from our group showed that sLRP1 and sLRP1/ANP ratio are elevated in persons with T2DM, and their temporal progression is closely related to glycemic and lipidic control (unpublished results).

In the rabbit model, we demonstrate that immunization with P3 effectively blocks fatty streak formation in the aorta, and that these beneficial effects can be traced by non-invasive imaging techniques, such as PET/CT and Doppler ultrasonography. Anti-P3 Abs counteracts the cellular proinflammatory signals that enable the recruitment of monocytes and VSMCs into the arterial intima. In addition, anti-P3 Abs are extremely effective in arresting foam cell formation of human macrophages and human coronary vascular smooth muscle cells. Immunization with P3 did not significantly alter the lipid profile but did reduce the intramyocardial accumulation of CE, which facilitated the recovery of the levels of InsR and the InsR/LRP1 complex in cardiac membranes of hypercholesterolemic rabbits. Furthermore, we demonstrated that GLUT4 trafficking is also recovered in the cardiac membrane of P3-immunized rabbits.

The potent anti-inflammatory efficacy of anti-P3 Abs allowed the corroboration of treatment efficacy by non-invasive imaging techniques, such as 18F-FDG/PET and Doppler ultrasound, which gives high translational potential to this innovative immunotherapy that confers cardiac protection against atherosclerosis and heart failure. A major challenge for future research will be to design suitable molecular tools to reduce the vascular impact of most atherogenic lipoproteins. These results highlight the relevance of blocking LRP1 interactions with lipoproteins as a highly efficient process to recover a cardiac insulin response in the context of dyslipidemia. Further studies are required to determine the mechanisms underlying the link between reduced EC accumulation in the heart and

restored insulin response. This aspect deserves further investigation, given the potential role of myocardial EC accumulation on insulin resistance in a wide range of cardiac diseases. The innovative immunization-based approach we took here, which differs from more traditional genetic or pharmacological techniques, showed specificity and selectivity in targeting cardiovascular EC accumulation. These findings have important therapeutic implications in the treatment of CVD and shed new light on the complex role of LRP1 in the regulation of cardiac insulin response associated with hypercholesterolemia, obesity, and T2DM.

REFERENCES

REFERENCES

1. Judge, A., and Dodd, M.S. (2020) Metabolism. *Essays Biochem.*, **64** (4), 607–647.
2. Schetz, M., De Jong, A., Deane, A.M., Druml, W., Hemelaar, P., Pelosi, P., Pickkers, P., Reintam-Blaser, A., Roberts, J., Sakr, Y., and Jaber, S. (2019) Obesity in the critically ill: a narrative review. *Intensive Care Med.*, **45** (6), 757–769.
3. Batsis, J.A., and Villareal, D.T. (2018) Sarcopenic obesity in older adults: aetiology, epidemiology and treatment strategies. *Nat. Rev. Endocrinol.*, **14** (9), 513–537.
4. Neeland, I.J., Poirier, P., and Després, J.-P. (2018) Cardiovascular and Metabolic Heterogeneity of Obesity: Clinical Challenges and Implications for Management. *Circulation*, **137** (13), 1391–1406.
5. Koliaki, C., Liatis, S., and Kokkinos, A. (2019) Obesity and cardiovascular disease: revisiting an old relationship. *Metabolism.*, **92**, 98–107.
6. Gutiérrez-Cuevas, J., Santos, A., and Armendariz-Borunda, J. (2021) Pathophysiological Molecular Mechanisms of Obesity: A Link between MAFLD and NASH with Cardiovascular Diseases. *Int. J. Mol. Sci.*, **22** (21).
7. Heymsfield, S.B., and Wadden, T.A. (2017) Mechanisms, Pathophysiology, and Management of Obesity. *N. Engl. J. Med.*, **376** (3), 254–266.
8. Aguiree, F., Brown, A., Cho, N.H., Dahlquist, G., Dodd, S., Dunning, T., Hirst, M., Hwang, C., Magliano, D., and Patterson, C. (2013) IDF diabetes atlas.
9. Carstensen, B., Rønn, P.F., and Jørgensen, M.E. (2020) Prevalence, incidence and mortality of type 1 and type 2 diabetes in Denmark 1996-2016. *BMJ open diabetes Res. care*, **8** (1).
10. Xu, G., Liu, B., Sun, Y., Du, Y., Snetselaar, L.G., Hu, F.B., and Bao, W. (2018) Prevalence of diagnosed type 1 and type 2 diabetes among US adults in 2016 and 2017: population based study. *BMJ*, **362**, k1497.
11. Unnikrishnan, R., Anjana, R.M., and Mohan, V. (2016) Diabetes mellitus and its complications in India. *Nat. Rev. Endocrinol.*, **12** (6), 357–370.
12. Kim, S.Y., Lee, Y.J., An, S.-M., Kim, M.J., Jeong, J.S., Kim, D.S., Lim, Y., Jung, E.-M., Kim, S.-C., and An, B.-S. (2022) Dynamic regulation of lipid metabolism in the placenta of in vitro and in vivo models of Gestational Diabetes Mellitus. *Biol. Reprod.*
13. Melchior, H., Kurch-Bek, D., and Mund, M. (2017) The Prevalence of Gestational Diabetes. *Dtsch. Arztebl. Int.*, **114** (24), 412–418.
14. Mack, L.R., and Tomich, P.G. (2017) Gestational Diabetes: Diagnosis, Classification, and Clinical Care. *Obstet. Gynecol. Clin. North Am.*, **44** (2), 207–217.
15. Wolosowicz, M., Lukaszuk, B., and Chabowski, A. (2020) The Causes of Insulin Resistance in Type 1 Diabetes Mellitus: Is There a Place for Quaternary Prevention? *Int. J. Environ. Res. Public Health*, **17** (22).
16. Mobasseri, M., Shirmohammadi, M., Amiri, T., Vahed, N., Hosseini Fard, H., and Ghojazadeh, M. (2020) Prevalence and incidence of type 1 diabetes in the world: a systematic review and meta-analysis. *Heal. Promot. Perspect.*, **10** (2), 98–115.
17. Khan, M.A.B., Hashim, M.J., King, J.K., Govender, R.D., Mustafa, H., and Al Kaabi, J. (2020) Epidemiology of Type 2 Diabetes - Global Burden of Disease and Forecasted Trends. *J. Epidemiol. Glob. Health*, **10** (1), 107–111.
18. Gupta, A., Bisht, B., and Dey, C.S. (2011) Peripheral insulin-sensitizer drug metformin ameliorates neuronal insulin resistance and Alzheimer's-like changes. *Neuropharmacology*, **60** (6), 910–920.
19. Dhillon, S. (2021) Aducanumab: First Approval. *Drugs*, **81** (12), 1437–1443.
20. de la Monte, S.M., and Wands, J.R. (2008) Alzheimer's disease is type 3 diabetes-evidence reviewed. *J. Diabetes Sci. Technol.*, **2** (6), 1101–1113.
21. (2012) Diagnosis and classification of diabetes mellitus. *Diabetes Care*, **35 Suppl 1** (Suppl 1),

S64-71.
22. Ganda, O.P. (1996) Prevalence and Incidence of Secondary and Other Types of Diabetes.
23. Nkonge, K.M., Nkonge, D.K., and Nkonge, T.N. (2020) The epidemiology, molecular pathogenesis, diagnosis, and treatment of maturity-onset diabetes of the young (MODY). *Clin. diabetes Endocrinol.*, **6** (1), 20.
24. Dillmann, W.H. (2019) Diabetic Cardiomyopathy. *Circ. Res.*, **124** (8), 1160–1162.
25. Petrie, J.R., Guzik, T.J., and Touyz, R.M. (2018) Diabetes, Hypertension, and Cardiovascular Disease: Clinical Insights and Vascular Mechanisms. *Can. J. Cardiol.*, **34** (5), 575–584.
26. Bugger, H., and Abel, E.D. (2014) Molecular mechanisms of diabetic cardiomyopathy. *Diabetologia*, **57** (4), 660–671.
27. Tan, S.Y., Mei Wong, J.L., Sim, Y.J., Wong, S.S., Mohamed Elhassan, S.A., Tan, S.H., Ling Lim, G.P., Rong Tay, N.W., Annan, N.C., Bhattamisra, S.K., and Candasamy, M. (2019) Type 1 and 2 diabetes mellitus: A review on current treatment approach and gene therapy as potential intervention. *Diabetes Metab. Syndr.*, **13** (1), 364–372.
28. Donnan, K., and Segar, L. (2019) SGLT2 inhibitors and metformin: Dual antihyperglycemic therapy and the risk of metabolic acidosis in type 2 diabetes. *Eur. J. Pharmacol.*, **846**, 23–29.
29. Cotter, T.G., and Rinella, M. (2020) Nonalcoholic Fatty Liver Disease 2020: The State of the Disease. *Gastroenterology*, **158** (7), 1851–1864.
30. Engelmann, C., and Tacke, F. (2022) The Potential Role of Cellular Senescence in Non-Alcoholic Fatty Liver Disease. *Int. J. Mol. Sci.*, **23** (2).
31. Abdelmalek, M.F. (2021) Nonalcoholic fatty liver disease: another leap forward. *Nat. Rev. Gastroenterol. Hepatol.*, **18** (2), 85–86.
32. Yao, Y.S., Li, T. Di, and Zeng, Z.H. (2020) Mechanisms underlying direct actions of hyperlipidemia on myocardium: an updated review. *Lipids Health Dis.*, **19** (1), 23.
33. Ding, W.Y., Protty, M.B., Davies, I.G., and Lip, G.Y.H. (2022) Relationship between lipoproteins, thrombosis, and atrial fibrillation. *Cardiovasc. Res.*, **118** (3), 716–731.
34. Yen, C.-L.E., Nelson, D.W., and Yen, M.-I. (2015) Intestinal triacylglycerol synthesis in fat absorption and systemic energy metabolism. *J. Lipid Res.*, **56** (3), 489–501.
35. Karam, I., Yang, Y.J., and Li, J. (2017) Hyperlipidemia Background and Progress.
36. Stewart, J., McCallin, T., Martinez, J., Chacko, S., and Yusuf, S. (2020) Hyperlipidemia. *Pediatr. Rev.*, **41** (8), 393–402.
37. Han, Y., and Willis, M.S. (2015) The Role of PCSK9 in Lipid Metabolism and its Relationship to New Therapies for Lowering Cholesterol and Reducing Cardiac Disease.
38. Ouimet, M., Barrett, T.J., and Fisher, E.A. (2019) HDL and Reverse Cholesterol Transport. *Circ. Res.*, **124** (10), 1505–1518.
39. Badimon, L., and Chiva-Blanch, G. (2019) Chapter 24 - Lipid Metabolism in Dyslipidemia and Familial Hypercholesterolemia (eds.Patel, V.B.B.T.-T.M.N. of F.), Academic Press, pp. 307–322.
40. Rivera Esteban, J.M., and Augustin Recio, S. (2020) Metabolic comorbidity, the new enemy. Metabolic syndrome and steatohepatitis. *Rev. Esp. Sanid. Penit.*, **22** (2), 55–57.
41. Samson, S.L., and Garber, A.J. (2014) Metabolic syndrome. *Endocrinol. Metab. Clin. North Am.*, **43** (1), 1–23.
42. Eckel, R.H., Grundy, S.M., and Zimmet, P.Z. (2005) The metabolic syndrome. *Lancet (London, England)*, **365** (9468), 1415–1428.
43. Castro-Barquero, S., Ruiz-León, A.M., Sierra-Pérez, M., Estruch, R., and Casas, R. (2020) Dietary Strategies for Metabolic Syndrome: A Comprehensive Review. *Nutrients*, **12** (10).
44. Robinson, N.B., Krieger, K., Khan, F.M., Huffman, W., Chang, M., Naik, A., Yongle, R., Hameed, I., Krieger, K., Girardi, L.N., and Gaudino, M. (2019) The current state of animal models in research: A review. *Int. J. Surg.*, **72**, 9–13.
45. Wong, S.K., Chin, K.-Y., Suhaimi, F.H., Fairus, A., and Ima-Nirwana, S. (2016) Animal models of

metabolic syndrome: a review. *Nutr. Metab. (Lond).*, **13**, 65.
46. Fuchs, T., Loureiro, M. de P., Macedo, L.E., Nocca, D., Nedelcu, M., and Costa-Casagrande, T.A. (2018) Animal models in metabolic syndrome. *Rev. Col. Bras. Cir.*, **45** (5), e1975.
47. Hirata, T., Yoshitomi, T., Inoue, M., Iigo, Y., Matsumoto, K., Kubota, K., and Shinagawa, A. (2017) Pathological and gene expression analysis of a polygenic diabetes model, NONcNZO10/LtJ mice. *Gene*, **629**, 52–58.
48. Kim, J.H., Stewart, T.P., Soltani-Bejnood, M., Wang, L., Fortuna, J.M., Mostafa, O.A., Moustaid-Moussa, N., Shoieb, A.M., McEntee, M.F., Wang, Y., Bechtel, L., and Naggert, J.K. (2006) Phenotypic characterization of polygenic type 2 diabetes in TALLYHO/JngJ mice. *J. Endocrinol.*, **191** (2), 437–446.
49. Hernández-Granados, M.J. (2018) Rodent Models of Obesity and Diabetes (eds.Ramírez-Emiliano, J.), IntechOpen, Rijeka, pp. Ch. 6.
50. O'Brien, P.D., Hur, J., Robell, N.J., Hayes, J.M., Sakowski, S.A., and Feldman, E.L. (2016) Gender-specific differences in diabetic neuropathy in BTBR ob/ob mice. *J. Diabetes Complications*, **30** (1), 30–37.
51. Ranheim, T., Dumke, C., Schueler, K.L., Cartee, G.D., and Attie, A.D. (1997) Interaction between BTBR and C57BL/6J genomes produces an insulin resistance syndrome in (BTBR x C57BL/6J) F1 mice. *Arterioscler. Thromb. Vasc. Biol.*, **17** (11), 3286–3293.
52. Tenopoulou, M., Doulias, P.-T., Nakamoto, K., Berrios, K., Zura, G., Li, C., Faust, M., Yakovishina, V., Evans, P., Tan, L., Bennett, M.J., Snyder, N.W., Quinn, W.J. 3rd, Baur, J.A., Atochin, D.N., Huang, P.L., and Ischiropoulos, H. (2018) Oral nitrite restores age-dependent phenotypes in eNOS-null mice. *JCI insight*, **3** (16).
53. de Bem, A.F., Krolow, R., Farias, H.R., de Rezende, V.L., Gelain, D.P., Moreira, J.C.F., Duarte, J.M. das N., and de Oliveira, J. (2021) Animal Models of Metabolic Disorders in the Study of Neurodegenerative Diseases: An Overview. *Front. Neurosci.*, **14**.
54. Hu, P., McKenzie, J.A., Buettmann, E.G., Migotsky, N., Gardner, M.J., and Silva, M.J. (2021) Type 1 diabetic Akita mice have low bone mass and impaired fracture healing. *Bone*, **147**, 115906.
55. Al-Awar, A., Kupai, K., Veszelka, M., Szűcs, G., Attieh, Z., Murlasits, Z., Török, S., Pósa, A., and Varga, C. (2016) Experimental Diabetes Mellitus in Different Animal Models. *J. Diabetes Res.*, **2016**, 9051426.
56. Weiss, H., Bleich, A., Hedrich, H.-J., Kölsch, B., Elsner, M., Jörns, A., Lenzen, S., Tiedge, M., and Wedekind, D. (2005) Genetic analysis of the LEW.1AR1-iddm rat: an animal model for spontaneous diabetes mellitus. *Mamm. Genome*, **16** (6), 432–441.
57. Gut, P., Reischauer, S., Stainier, D.Y.R., and Arnaout, R. (2017) LITTLE FISH, BIG DATA: ZEBRAFISH AS A MODEL FOR CARDIOVASCULAR AND METABOLIC DISEASE. *Physiol. Rev.*, **97** (3), 889–938.
58. Lau, J.K.C., Zhang, X., and Yu, J. (2017) Animal models of non-alcoholic fatty liver disease: current perspectives and recent advances. *J. Pathol.*, **241** (1), 36–44.
59. Fullenkamp, A.M., Bell, L.N., Robbins, R.D., Lee, L., Saxena, R., Alloosh, M., Klaunig, J.E., Mirmira, R.G., Sturek, M., and Chalasani, N. (2011) Effect of different obesogenic diets on pancreatic histology in Ossabaw miniature swine. *Pancreas*, **40** (3), 438–443.
60. Kennedy, A.J., Ellacott, K.L.J., King, V.L., and Hasty, A.H. (2010) Mouse models of the metabolic syndrome. *Dis. Model. Mech.*, **3** (3–4), 156–166.
61. Andreadou, I., Schulz, R., Badimon, L., Adameová, A., Kleinbongard, P., Lecour, S., Nikolaou, P.-E., Falcão-Pires, I., Vilahur, G., Woudberg, N., Heusch, G., and Ferdinandy, P. (2020) Hyperlipidaemia and cardioprotection: Animal models for translational studies. *Br. J. Pharmacol.*, **177** (23), 5287–5311.
62. Herz, J., Clouthier, D.E., and Hammer, R.E. (1992) LDL receptor-related protein internalizes and degrades uPA-PAI-1 complexes and is essential for embryo implantation. *Cell*, **71** (3), 411–421.

63. Rohlmann, A., Gotthardt, M., Willnow, T.E., Hammer, R.E., and Herz, J. (1996) Sustained somatic gene inactivation by viral transfer of Cre recombinase. *Nat. Biotechnol.*, **14**, 1562.
64. Kim, H., Kim, M., Im, S.-K., and Fang, S. (2018) Mouse Cre-LoxP system: general principles to determine tissue-specific roles of target genes. *lar*, **34** (4), 147–159.
65. Chuang, T.-Y., Guo, Y., Seki, S.M., Rosen, A.M., Johanson, D.M., Mandell, J.W., Lucchinetti, C.F., and Gaultier, A. (2016) LRP1 expression in microglia is protective during CNS autoimmunity. *Acta Neuropathol. Commun.*, **4** (1), 68.
66. Garcia-Arcos, I., Park, S.S., Mai, M., Alvarez-Buve, R., Chow, L., Cai, H., Baumlin-Schmid, N., Agudelo, C.W., Martinez, J., Kim, M.D., Dabo, A.J., Salathe, M., Goldberg, I.J., and Foronjy, R.F. (2022) LRP1 loss in airway epithelium exacerbates smoke-induced oxidative damage and airway remodeling. *J. Lipid Res.*, **63** (4), 100185.
67. Schäfer, I., Kaisler, J., Scheller, A., Kirchhoff, F., Haghikia, A., and Faissner, A. (2019) Conditional Deletion of LRP1 Leads to Progressive Loss of Recombined NG2-Expressing Oligodendrocyte Precursor Cells in a Novel Mouse Model. *Cells*, **8** (12).
68. Au, D.T., Ying, Z., Hernández-Ochoa, E.O., Fondrie, W.E., Hampton, B., Migliorini, M., Galisteo, R., Schneider, M.F., Daugherty, A., Rateri, D.L., Strickland, D.K., and Muratoglu, S.C. (2018) LRP1 (Low-Density Lipoprotein Receptor-Related Protein 1) Regulates Smooth Muscle Contractility by Modulating Ca(2+) Signaling and Expression of Cytoskeleton-Related Proteins. *Arterioscler. Thromb. Vasc. Biol.*, **38** (11), 2651–2664.
69. Ye, R., Gordillo, R., Shao, M., Onodera, T., Chen, Z., Chen, S., Lin, X., SoRelle, J.A., Li, X., Tang, M., Keller, M.P., Kuliawat, R., Attie, A.D., Gupta, R.K., Holland, W.L., Beutler, B., Herz, J., and Scherer, P.E. (2018) Intracellular lipid metabolism impairs β cell compensation during diet-induced obesity. *J. Clin. Invest.*, **128** (3), 1178–1189.
70. Lu, R.-M., Hwang, Y.-C., Liu, I.-J., Lee, C.-C., Tsai, H.-Z., Li, H.-J., and Wu, H.-C. (2020) Development of therapeutic antibodies for the treatment of diseases. *J. Biomed. Sci.*, **27** (1), 1.
71. Singh, A., Mishra, A., and Verma, A. (2020) Chapter 17 - Antibodies: monoclonal and polyclonal (eds.Verma, A.S., and Singh, A.B.T.-A.B. (Second E.), Academic Press, Boston, pp. 327–352.
72. Burns, R. (2009) Immunisation strategies for antibody production. *Methods Mol. Biol.*, **508**, 27–35.
73. Laustsen, A.H., Greiff, V., Karatt-Vellatt, A., Muyldermans, S., and Jenkins, T.P. (2021) Animal Immunization, in Vitro Display Technologies, and Machine Learning for Antibody Discovery. *Trends Biotechnol.*, **39** (12), 1263–1273.
74. Greenfield, E.A. (2020) Standard Immunization of Rabbits. *Cold Spring Harb. Protoc.*, **2020** (9), 100305.
75. Stemme, S., Faber, B., Holm, J., Wiklund, O., Witztum, J.L., and Hansson, G.K. (1995) T lymphocytes from human atherosclerotic plaques recognize oxidized low density lipoprotein. *Proc. Natl. Acad. Sci. U. S. A.*, **92** (9), 3893–7.
76. Palinski, W., and Witztum, J.L. (2000) Immune responses to oxidative neoepitopes on LDL and phospholipids modulate the development of atherosclerosis. *J. Intern. Med.*, **247** (3), 371–380.
77. Gonçalves, I., Nitulescu, M., Ares, M.P.S., Fredrikson, G.N., Jansson, B., Li, Z.C., and Nilsson, J. (2009) Identification of the target for therapeutic recombinant anti-apoB-100 peptide antibodies in human atherosclerotic lesions. *Atherosclerosis*, **205** (1), 96–100.
78. Frederikson, G.N., Andersson, L., Söderberg, I., Dimayuga, P., Chyu, K.Y., Shah, P.K., and Nilsson, J. (2005) Atheroprotective immunization with MDA-modified apo B-100 peptide sequences is associated with activation of Th2 specific antibody expression. *Autoimmunity*, **38** (2), 171–179.
79. Fredrikson, G.N., Björkbacka, H., Söderberg, I., Ljungcrantz, I., and Nilsson, J. (2008) Treatment with apo B peptide vaccines inhibits atherosclerosis in human apo B-100

transgenic mice without inducing an increase in peptide-specific antibodies. *J. Intern. Med.*, **264** (6), 563–570.
80. Fredrikson, G.N., Söderberg, I., Lindholm, M., Dimayuga, P., Chyu, K.Y., Shah, P.K., and Nilsson, J. (2003) Inhibition of atherosclerosis in apoE-null mice by immunization with apoB-100 peptide sequences. *Arterioscler. Thromb. Vasc. Biol.*, **23** (5), 879–884.
81. Frodermann, V., and Nahrendorf, M. (2018) Macrophages and Cardiovascular Health. *Physiol. Rev.*, **98** (4), 2523–2569.
82. Ridker, P.M., Everett, B.M., Thuren, T., MacFadyen, J.G., Chang, W.H., Ballantyne, C., Fonseca, F., Nicolau, J., Koenig, W., Anker, S.D., Kastelein, J.J.P., Cornel, J.H., Pais, P., Pella, D., Genest, J., Cifkova, R., Lorenzatti, A., Forster, T., Kobalava, Z., Vida-Simiti, L., Flather, M., Shimokawa, H., Ogawa, H., Dellborg, M., Rossi, P.R.F., Troquay, R.P.T., Libby, P., and Glynn, R.J. (2017) Antiinflammatory Therapy with Canakinumab for Atherosclerotic Disease. *N. Engl. J. Med.*, **377** (12), 1119–1131.
83. Dhimolea, E. (2010) Canakinumab. *MAbs*, **2** (1), 3–13.
84. Everett, B.M., Cornel, J.H., Lainscak, M., Anker, S.D., Abbate, A., Thuren, T., Libby, P., Glynn, R.J., and Ridker, P.M. (2019) Anti-Inflammatory Therapy With Canakinumab for the Prevention of Hospitalization for Heart Failure. *Circulation*, **139** (10), 1289–1299.
85. Roy, P., Ali, A.J., Kobiyama, K., Ghosheh, Y., and Ley, K. (2020) Opportunities for an atherosclerosis vaccine: From mice to humans. *Vaccine*, **38** (28), 4495–4506.
86. Bourinbaiar, A.S., and Jirathitikal, V. (2010) Effect of oral immunization with pooled antigens derived from adipose tissue on atherosclerosis and obesity indices. *Vaccine*, **28** (15), 2763–2768.
87. Chung, E.S., Packer, M., Lo, K.H., Fasanmade, A.A., and Willerson, J.T. (2003) Randomized, double-blind, placebo-controlled, pilot trial of infliximab, a chimeric monoclonal antibody to tumor necrosis factor-alpha, in patients with moderate-to-severe heart failure: results of the anti-TNF Therapy Against Congestive Heart Failure (A. *Circulation*, **107** (25), 3133–3140.
88. Velasco-Velázquez, M.A., Salinas-Jazmín, N., Hisaki-Itaya, E., Cobos-Puc, L., Xolalpa, W., González, G., Tenorio-Calvo, A., Piña-Lara, N., Juárez-Bayardo, L.C., Flores-Ortiz, L.F., Medina-Rivero, E., Pérez, N.O., and Pérez-Tapia, S.M. (2017) Extensive preclinical evaluation of an infliximab biosimilar candidate. *Eur. J. Pharm. Sci. Off. J. Eur. Fed. Pharm. Sci.*, **102**, 35–45.
89. Sabatine, M.S., Giugliano, R.P., Keech, A.C., Honarpour, N., Wiviott, S.D., Murphy, S.A., Kuder, J.F., Wang, H., Liu, T., Wasserman, S.M., Sever, P.S., and Pedersen, T.R. (2017) Evolocumab and Clinical Outcomes in Patients with Cardiovascular Disease. *N. Engl. J. Med.*, **376** (18), 1713–1722.
90. Khoury, E., Brisson, D., and Gaudet, D. (2020) Preclinical discovery and development of evolocumab for the treatment of hypercholesterolemia. *Expert Opin. Drug Discov.*, **15** (4), 403–414.
91. Schwartz, G.G., Steg, P.G., Szarek, M., Bhatt, D.L., Bittner, V.A., Diaz, R., Edelberg, J.M., Goodman, S.G., Hanotin, C., Harrington, R.A., Jukema, J.W., Lecorps, G., Mahaffey, K.W., Moryusef, A., Pordy, R., Quintero, K., Roe, M.T., Sasiela, W.J., Tamby, J.-F., Tricoci, P., White, H.D., and Zeiher, A.M. (2018) Alirocumab and Cardiovascular Outcomes after Acute Coronary Syndrome. *N. Engl. J. Med.*, **379** (22), 2097–2107.
92. Lutgens, E., Atzler, D., Döring, Y., Duchene, J., Steffens, S., and Weber, C. (2019) Immunotherapy for cardiovascular disease. *Eur. Heart J.*, **40** (48), 3937–3946.
93. Costales, P., Fuentes-Prior, P., Castellano, J., Revuelta-Lopez, E., Corral-Rodríguez, M.Á., Nasarre, L., Badimon, L., and Llorente-Cortes, V. (2015) K domain CR9 of low density lipoprotein (LDL) receptor-related protein 1 (LRP1) is critical for aggregated LDL-induced foam cell formation from human vascular smooth muscle cells. *J. Biol. Chem.*
94. Bres, E.E., and Faissner, A. (2019) Low Density Receptor-Related Protein 1 Interactions With the Extracellular Matrix: More Than Meets the Eye. *Front. cell Dev. Biol.*, **7**, 31.

95. Chen, J., Su, Y., Pi, S., Hu, B., and Mao, L. (2021) The Dual Role of Low-Density Lipoprotein Receptor-Related Protein 1 in Atherosclerosis. *Front. Cardiovasc. Med.*, **8**, 682389.
96. de Gonzalo-Calvo, D., Elosua, R., Vea, A., Subirana, I., Sayols-Baixeras, S., Marrugat, J., and Llorente-Cortés, V. (2019) Soluble low-density lipoprotein receptor-related protein 1 as a biomarker of coronary risk: Predictive capacity and association with clinical events. *Atherosclerosis*, **287**, 93–99.
97. de Gonzalo-Calvo, D., Colom, C., Vilades, D., Rivas-Urbina, A., Moustafa, A.-H., Pérez-Cuellar, M., Sánchez-Quesada, J.L., Pérez, A., and LLorente-Cortes, V. (2018) Soluble LRP1 is an independent biomarker of epicardial fat volume in patients with type 1 diabetes mellitus. *Sci. Rep.*, **8** (1), 1054.
98. Ceschin, D.G., Sánchez, M.C., and Chiabrando, G.A. (2009) Insulin induces the low density lipoprotein receptor-related protein 1 (LRP1) degradation by the proteasomal system in J774 macrophage-derived cells. *J. Cell. Biochem.*, **106** (3), 372–380.
99. Herz, J., and Strickland, D.K. (2001) LRP: a multifunctional scavenger and signaling receptor. *J. Clin. Invest.*, **108** (6), 779–784.
100. Actis Dato, V., and Chiabrando, G.A. (2021) Activated Alpha-2 Macroglobulin Improves Insulin Response via LRP1 in Lipid-Loaded HL-1 Cardiomyocytes. *Int. J. Mol. Sci.*, **22** (13).
101. Murphy, M.P., and LeVine, H. 3rd (2010) Alzheimer's disease and the amyloid-beta peptide. *J. Alzheimers. Dis.*, **19** (1), 311–323.
102. Ma, Q., Zhao, Z., Sagare, A.P., Wu, Y., Wang, M., Owens, N.C., Verghese, P.B., Herz, J., Holtzman, D.M., and Zlokovic, B. V (2018) Blood-brain barrier-associated pericytes internalize and clear aggregated amyloid-β42 by LRP1-dependent apolipoprotein E isoform-specific mechanism. *Mol. Neurodegener.*, **13** (1), 57.
103. Benitez Amaro, A., Solanelles Curco, A., Garcia, E., Julve, J., Rives, J., Benitez, S., and Llorente Cortes, V. (2021) Apolipoprotein and LRP1-Based Peptides as New Therapeutic Tools in Atherosclerosis. *J. Clin. Med.*, **10** (16).
104. Tachibana, M., Holm, M.-L., Liu, C.-C., Shinohara, M., Aikawa, T., Oue, H., Yamazaki, Y., Martens, Y.A., Murray, M.E., Sullivan, P.M., Weyer, K., Glerup, S., Dickson, D.W., Bu, G., and Kanekiyo, T. (2019) APOE4-mediated amyloid-β pathology depends on its neuronal receptor LRP1. *J. Clin. Invest.*, **129** (3), 1272–1277.
105. Wang, L., and Song, Y. (2020) Molecular insights into the effect of an apoptotic raft-like bilayer on the conformation and dynamics of calreticulin. *Biochim. Biophys. acta. Biomembr.*, **1862** (2), 183146.
106. Groenendyk, J., Wang, W.-A., Robinson, A., and Michalak, M. (2022) Calreticulin and the Heart. *Cells*, **11** (11).
107. Fucikova, J., Spisek, R., Kroemer, G., and Galluzzi, L. (2021) Calreticulin and cancer. *Cell Res.*, **31** (1), 5–16.
108. Basu, S., Binder, R.J., Ramalingam, T., and Srivastava, P.K. (2001) CD91 is a common receptor for heat shock proteins gp96, hsp90, hsp70, and calreticulin. *Immunity*, **14** (3), 303–313.
109. Wu, J., Liu, T., Rios, Z., Mei, Q., Lin, X., and Cao, S. (2017) Heat Shock Proteins and Cancer. *Trends Pharmacol. Sci.*, **38** (3), 226–256.
110. Wilsie, L.C., and Orlando, R.A. (2003) The low density lipoprotein receptor-related protein complexes with cell surface heparan sulfate proteoglycans to regulate proteoglycan-mediated lipoprotein catabolism. *J. Biol. Chem.*, **278** (18), 15758–15764.
111. Sarrazin, S., Lamanna, W.C., and Esko, J.D. (2011) Heparan sulfate proteoglycans. *Cold Spring Harb. Perspect. Biol.*, **3** (7).
112. Kounnas, M.Z., Chappell, D.A., Wong, H., Argraves, W.S., and Strickland, D.K. (1995) The cellular internalization and degradation of hepatic lipase is mediated by low density lipoprotein receptor-related protein and requires cell surface proteoglycans. *J. Biol. Chem.*, **270** (16), 9307–9312.

113. Connelly, P.W., and Hegele, R.A. (1998) Hepatic lipase deficiency. *Crit. Rev. Clin. Lab. Sci.*, **35** (6), 547–572.
114. Liu, Q., Zhang, J., Zerbinatti, C., Zhan, Y., Kolber, B.J., Herz, J., Muglia, L.J., and Bu, G. (2011) Lipoprotein Receptor LRP1 Regulates Leptin Signaling and Energy Homeostasis in the Adult Central Nervous System. *PLoS Biol.*, **9** (1), e1000575.
115. Abdel-Hamid, N.M., and Abass, S.A. (2021) Matrix metalloproteinase contribution in management of cancer proliferation, metastasis and drug targeting. *Mol. Biol. Rep.*, **48** (9), 6525–6538.
116. Yang, Z., Strickland, D.K., and Bornstein, P. (2001) Extracellular matrix metalloproteinase 2 levels are regulated by the low density lipoprotein-related scavenger receptor and thrombospondin 2. *J. Biol. Chem.*, **276** (11), 8403–8408.
117. Hahn-Dantona, E., Ruiz, J.F., Bornstein, P., and Strickland, D.K. (2001) The low density lipoprotein receptor-related protein modulates levels of matrix metalloproteinase 9 (MMP-9) by mediating its cellular catabolism. *J. Biol. Chem.*, **276** (18), 15498–15503.
118. Barmina, O.Y., Walling, H.W., Fiacco, G.J., Freije, J.M., López-Otín, C., Jeffrey, J.J., and Partridge, N.C. (1999) Collagenase-3 binds to a specific receptor and requires the low density lipoprotein receptor-related protein for internalization. *J. Biol. Chem.*, **274** (42), 30087–30093.
119. Kozlova, N., Jensen, J.K., Franklin Chi, T., Samoylenko, A., and Kietzmann, T. (2015) PAI-1 modulates cell migration in a LRP1-dependent manner via β-catenin and ERK1/2. *Thromb Haemost*, **113** (05), 988–998.
120. Stefansson, S., Muhammad, S., Cheng, X.F., Battey, F.D., Strickland, D.K., and Lawrence, D.A. (1998) Plasminogen activator inhibitor-1 contains a cryptic high affinity binding site for the low density lipoprotein receptor-related protein. *J. Biol. Chem.*, **273** (11), 6358–6366.
121. Craig, J., Mikhailenko, I., Noyes, N., Migliorini, M., and Strickland, D.K. (2013) The LDL receptor-related protein 1 (LRP1) regulates the PDGF signaling pathway by binding the protein phosphatase SHP-2 and modulating SHP-2- mediated PDGF signaling events. *PLoS One*, **8** (7), e70432.
122. Andrae, J., Gallini, R., and Betsholtz, C. (2008) Role of platelet-derived growth factors in physiology and medicine. *Genes Dev.*, **22** (10), 1276–1312.
123. Huang, S.S., Ling, T.-Y., Tseng, W.-F., Huang, Y.-H., Tang, F.-M., Leal, S.M., and Huang, J.S. (2003) Cellular growth inhibition by IGFBP-3 and TGF-beta1 requires LRP-1. *FASEB J. Off. Publ. Fed. Am. Soc. Exp. Biol.*, **17** (14), 2068–2081.
124. Muratoglu, S.C., Belgrave, S., Lillis, A.P., Migliorini, M., Robinson, S., Smith, E., Zhang, L., and Strickland, D.K. (2011) Macrophage LRP1 suppresses neo-intima formation during vascular remodeling by modulating the TGF-β signaling pathway. *PLoS One*, **6** (12), e28846.
125. Benitez-Amaro, A., Pallara, C., Nasarre, L., Rivas-Urbina, A., Benitez, S., Vea, A., Bornachea, O., de Gonzalo-Calvo, D., Serra-Mir, G., Villegas, S., Prades, R., Sanchez-Quesada, J.L., Chiva, C., Sabido, E., Tarragó, T., and Llorente-Cortés, V. (2019) Molecular basis for the protective effects of low-density lipoprotein receptor-related protein 1 (LRP1)-derived peptides against LDL aggregation. *Biochim. Biophys. Acta - Biomembr.*, **1861** (7), 1302–1316.
126. Kwon, O.Y., Hwang, K., Kim, J.-A., Kim, K., Kwon, I.C., Song, H.K., and Jeon, H. (2010) Dab1 binds to Fe65 and diminishes the effect of Fe65 or LRP1 on APP processing. *J. Cell. Biochem.*, **111** (2), 508–519.
127. Mishra, D., and Dey, C.S. (2021) PKCα: Prospects in Regulating Insulin Resistance and AD. *Trends Endocrinol. Metab.*, **32** (6), 341–350.
128. Barnes, H., Larsen, B., Tyers, M., and van Der Geer, P. (2001) Tyrosine-phosphorylated low density lipoprotein receptor-related protein 1 (Lrp1) associates with the adaptor protein SHC in SRC-transformed cells. *J. Biol. Chem.*, **276** (22), 19119–19125.
129. Whitmarsh, A.J. (2006) The JIP family of MAPK scaffold proteins. *Biochem. Soc. Trans.*, **34** (Pt

5), 828–832.
130. Sullivan, C.S., Scheib, J.L., Ma, Z., Dang, R.P., Schafer, J.M., Hickman, F.E., Brodsky, F.M., Ravichandran, K.S., and Carter, B.D. (2014) The adaptor protein GULP promotes Jedi-1-mediated phagocytosis through a clathrin-dependent mechanism. *Mol. Biol. Cell*, **25** (12), 1925–1936.
131. Park, S.-Y., Kim, S.-Y., Kang, K.-B., and Kim, I.-S. (2010) Adaptor protein GULP is involved in stabilin-1-mediated phagocytosis. *Biochem. Biophys. Res. Commun.*, **398** (3), 467–472.
132. Fani Maleki, A., Cisbani, G., Plante, M.-M., Préfontaine, P., Laflamme, N., Gosselin, J., and Rivest, S. (2020) Muramyl dipeptide-mediated immunomodulation on monocyte subsets exerts therapeutic effects in a mouse model of Alzheimer's disease. *J. Neuroinflammation*, **17** (1), 218.
133. Dumanis, S.B., Chamberlain, K.A., Jin Sohn, Y., Jin Lee, Y., Guénette, S.Y., Suzuki, T., Mathews, P.M., Pak, D.T., Rebeck, G.W., Suh, Y.-H., Park, H.-S., and Hoe, H.-S. (2012) FE65 as a link between VLDLR and APP to regulate their trafficking and processing. *Mol. Neurodegener.*, **7**, 9.
134. Potere, N., Del Buono, M.G., Mauro, A.G., Abbate, A., and Toldo, S. (2019) Low Density Lipoprotein Receptor-Related Protein-1 in Cardiac Inflammation and Infarct Healing. *Front. Cardiovasc. Med.*, **6**.
135. Lu, M., and Gursky, O. (2013) Aggregation and fusion of low-density lipoproteins in vivo and in vitro. *Biomol. Concepts*, **4** (5).
136. Öörni, K., Posio, P., Ala-Korpela, M., Jauhiainen, M., and Kovanen, P.T. (2005) Sphingomyelinase induces aggregation and fusion of small very low-density lipoprotein and intermediate-density lipoprotein particles and increases their retention to human arterial proteoglycans. *Arterioscler. Thromb. Vasc. Biol.*
137. Oorni, K., Pentikainen, M.O., Ala-Korpela, M., and Kovanen, P.T. (2000) Aggregation, fusion, and vesicle formation of modified low density lipoprotein particles: molecular mechanisms and effects on matrix interactions. *J. Lipid Res.*
138. Pahwa, R., and Jialal, I. (2022) Atherosclerosis., Treasure Island (FL).
139. Lillis, A.P., Muratoglu, S.C., Au, D.T., Migliorini, M., Lee, M.-J., Fried, S.K., Mikhailenko, I., and Strickland, D.K. (2016) Correction: LDL Receptor-Related Protein-1 (LRP1) Regulates Cholesterol Accumulation in Macrophages. *PLoS One*, **11** (1), e0147457.
140. Zhou, L., Takayama, Y., Boucher, P., Tallquist, M.D., and Herz, J. (2009) LRP1 regulates architecture of the vascular wall by controlling PDGFRβ-dependent phosphatidylinositol 3-kinase activation. *PLoS One*, **4** (9).
141. Boucher, P., Gotthardt, M., Li, W.P., Anderson, R.G.W., and Herz, J. (2003) LRP: Role in vascular wall integrity and protection from atherosclerosis. *Science (80-.).*, **300** (5617), 329–332.
142. Boucher, P., Liu, P., Gotthardt, M., Hiesberger, T., Anderson, R.G.W., and Herz, J. (2002) Platelet-derived growth factor mediates tyrosine phosphorylation of the cytoplasmic domain of the low density lipoprotein receptor-related protein in caveolae. *J. Biol. Chem.*, **277** (18), 15507–15513.
143. Loukinova, E., Ranganathan, S., Kuznetsov, S., Gorlatova, N., Migliorini, M.M., Loukinov, D., Ulery, P.G., Mikhailenko, I., Lawrence, D.A., and Strickland, D.K. (2002) Platelet-derived Growth Factor (PDGF)-induced Tyrosine Phosphorylation of the Low Density Lipoprotein Receptor-related Protein (LRP): EVIDENCE FOR INTEGRATED CO-RECEPTOR FUNCTION BETWEEN LRP AND THE PDGF . *J. Biol. Chem.* , **277** (18), 15499–15506.
144. Yancey, P.G., Blakemore, J., Ding, L., Fan, D., Overton, C.D., Zhang, Y., Linton, M.F., and Fazio, S. (2010) Macrophage LRP-1 controls plaque cellularity by regulating efferocytosis and Akt activation. *Arterioscler. Thromb. Vasc. Biol.*, **30** (4), 787–795.
145. Yancey, P.G., Ding, Y., Fan, D., Blakemore, J.L., Zhang, Y., Ding, L., Zhang, J., Linton, M.F., and

Fazio, S. (2011) Low-density lipoprotein receptor-related protein 1 prevents early atherosclerosis by limiting lesional apoptosis and inflammatory Ly-6C high monocytosis: Evidence that the effects are not apolipoprotein e dependent. *Circulation*, **124** (4), 454–464.
146. Xian, X., Ding, Y., Dieckmann, M., Zhou, L., Plattner, F., Liu, M., Parks, J.S., Hammer, R.E., Boucher, P., Tsai, S., and Herz, J. (2017) LRP1 integrates murine macrophage cholesterol homeostasis and inflammatory responses in atherosclerosis. *Elife*, **6**.
147. El Asmar, Z., Terrand, J., Jenty, M., Host, L., Mlih, M., Zerr, A., Justiniano, H., Matz, R.L., Boudier, C., Scholler, E., Garnier, J.M., Bertaccini, D., Thiersé, D., Schaeffer, C., Van Dorsselaer, A., Herz, J., Bruban, V., and Boucher, P. (2016) Convergent signaling pathways controlled by LRP1 (Receptor-related Protein 1) cytoplasmic and extracellular domains limit cellular cholesterol accumulation. *J. Biol. Chem.*, **291** (10), 5116–5127.
148. Kawamura, A., Baitsch, D., Telgmann, R., Feuerborn, R., Weissen-Plenz, G., Hagedorn, C., Saku, K., Brand-Herrmann, S.M., Von Eckardstein, A., Assmann, G., and Nofer, J.R. (2007) Apolipoprotein E interrupts interleukin-1β signaling in vascular smooth muscle cells. *Arterioscler. Thromb. Vasc. Biol.*, **27** (7), 1610–1617.
149. Gaultier, A., Arandjelovic, S., Li, X., Janes, J., Dragojlovic, N., Zhou, G.P., Dolkas, J., Myers, R.R., Gonias, S.L., and Campana, W.M. (2008) A shed form of LDL receptor-related protein-1 regulates peripheral nerve injury and neuropathic pain in rodents. *J. Clin. Invest.*, **118** (1), 161–172.
150. Toldo, S., Austin, D., Mauro, A.G., Mezzaroma, E., Van Tassell, B.W., Marchetti, C., Carbone, S., Mogelsvang, S., Gelber, C., and Abbate, A. (2017) Low-Density Lipoprotein Receptor-Related Protein-1 Is a Therapeutic Target in Acute Myocardial Infarction. *JACC. Basic to Transl. Sci.*, **2** (5), 561–574.
151. Llorente-Cortés, V., Otero-Viñas, M., Sánchez, S., Rodríguez, C., and Badimon, L. (2002) Low-density lipoprotein upregulates low-density lipoprotein receptor-related protein expression in vascular smooth muscle cells: possible involvement of sterol regulatory element binding protein-2-dependent mechanism. *Circulation*, **106** (24), 3104–3110.
152. Llorente-Cortés, V., Martínez-González, J., and Badimon, L. (2000) LDL Receptor–Related Protein Mediates Uptake of Aggregated LDL in Human Vascular Smooth Muscle Cells. *Arterioscler. Thromb. Vasc. Biol.*, **20** (6), 1572.
153. Llorente-Cortés, V., Otero-Viñas, M., and Badimon, L. (2002) Differential Role of Heparan Sulfate Proteoglycans on Aggregated LDL Uptake in Human Vascular Smooth Muscle Cells and Mouse Embryonic Fibroblasts. *Arterioscler. Thromb. Vasc. Biol.*, **22** (11), 1905.
154. Sakr, S.W., Eddy, R.J., Barth, H., Wang, F., Greenberg, S., Maxfield, F.R., and Tabas, I. (2001) The Uptake and Degradation of Matrix-bound Lipoproteins by Macrophages Require an Intact Actin Cytoskeleton, Rho Family GTPases, and Myosin ATPase Activity. *J. Biol. Chem.*, **276** (40), 37649–37658.
155. Llorente-Cortés, V., Royo, T., Juan-Babot, O., and Badimon, L. (2007) Adipocyte differentiation-related protein is induced by LRP1-mediated aggregated LDL internalization in human vascular smooth muscle cells and macrophages. *J. Lipid Res.*, **48** (10), 2133–2140.
156. Xu, W., Takahashi, Y., Sakashita, T., Iwasaki, T., Hattori, H., and Yoshimoto, T. (2001) Low density lipoprotein receptor-related protein is required for macrophage-mediated oxidation of low density lipoprotein by 12/15-lipoxygenase. *J. Biol. Chem.*, **276** (39), 36454–36459.
157. Costales, P., Aledo, R., Vérnia, S., Das, A., Shah, V.H., Casado, M., Badimon, L., and Llorente-Cortés, V. (2010) Selective role of sterol regulatory element binding protein isoforms in aggregated LDL-induced vascular low density lipoprotein receptor-related protein-1 expression. *Atherosclerosis*, **213** (2), 458–468.
158. Llorente-Cortes, V., Casani, L., Cal, R., Llenas, A., Juan-Babot, O., Camino-López, S., Sendra, J., and Badimon Maestro, L. (2011) Cholesterol-lowering strategies reduce vascular LRP1 overexpression induced by hypercholesterolaemia. *Eur. J. Clin. Invest.*, **41** (10), 1087–1097.

159. Sendra, J., Llorente-Cortés, V., Costales, P., Huesca-Gómez, C., and Badimon, L. (2008) Angiotensin II upregulates LDL receptor-related protein (LRP1) expression in the vascular wall: a new pro-atherogenic mechanism of hypertension. *Cardiovasc. Res.*, **78** (3), 581–589.
160. Castellano, J., Aledo, R., Sendra, J., Costales, P., Juan-Babot, O., Badimon, L., and Llorente-Cortés, V. (2011) Hypoxia stimulates low-density lipoprotein receptor-related protein-1 expression through hypoxia-inducible factor-1α in human vascular smooth muscle cells. *Arterioscler. Thromb. Vasc. Biol.*, **31** (6), 1411–1420.
161. Cal, R., Castellano, J., Revuelta-López, E., Aledo, R., Barriga, M., Farré, J., Vilahur, G., Nasarre, L., Hove-Madsen, L., Badimon, L., and Llorente-Cortés, V. (2012) Low-density lipoprotein receptor-related protein 1 mediates hypoxia-induced very low density lipoprotein-cholesteryl ester uptake and accumulation in cardiomyocytes. *Cardiovasc. Res.*, **94** (3), 469–479.
162. Llorente-Cortés, V., and Badimon, L. (2005) LDL receptor-related protein and the vascular wall: implications for atherothrombosis. *Arterioscler. Thromb. Vasc. Biol.*, **25** (3), 497–504.
163. Soto, Y., Acosta, E., Delgado, L., Pérez, A., Falcón, V., Bécquer, M.A., Fraga, Á., Brito, V., Álvarez, I., Griñán, T., Fernández-Marrero, Y., López-Requena, A., Noa, M., Fernández, E., and Vázquez, A.M. (2012) Antiatherosclerotic effect of an antibody that binds to extracellular matrix glycosaminoglycans. *Arterioscler. Thromb. Vasc. Biol.*, **32** (3), 595–604.
164. Nguyen, S.D., Javanainen, M., Rissanen, S., Zhao, H., Huusko, J., Kivelä, A.M., Ylä-Herttuala, S., Navab, M., Fogelman, A.M., Vattulainen, I., Kovanen, P.T., and Öörni, K. (2015) Apolipoprotein A-I mimetic peptide 4F blocks sphingomyelinase-induced LDL aggregation. *J. Lipid Res.*
165. Martínez-Bujidos, M., Rull, A., González-Cura, B., Pérez-Cuéllar, M., Montoliu-Gaya, L., Villegas, S., Ordoñez-Llaños, J., and Sánchez-Quesada, J.L. (2015) Clusterin/apolipoprotein J binds to aggregated LDL in human plasma and plays a protective role against LDL aggregation. *FASEB J.*, **29** (5), 1688–1700.
166. Ruuth, M., Nguyen, S.D., Vihervaara, T., Hilvo, M., Laajala, T.D., Kondadi, P.K., Gisterå, A., Lähteenmäki, H., Kittilä, T., Huusko, J., Uusitupa, M., Schwab, U., Savolainen, M.J., Sinisalo, J., Lokki, M.-L., Nieminen, M.S., Jula, A., Perola, M., Ylä-Herttula, S., Rudel, L., Öörni, A., Baumann, M., Baruch, A., Laaksonen, R., Ketelhuth, D.F.J., Aittokallio, T., Jauhiainen, M., Käkelä, R., Borén, J., Williams, K.J., Kovanen, P.T., and Öörni, K. (2018) Susceptibility of low-density lipoprotein particles to aggregate depends on particle lipidome, is modifiable, and associates with future cardiovascular deaths. *Eur. Heart J.*
167. Rijzewijk, L.J., van der Meer, R.W., Smit, J.W.A., Diamant, M., Bax, J.J., Hammer, S., Romijn, J.A., de Roos, A., and Lamb, H.J. (2008) Myocardial Steatosis Is an Independent Predictor of Diastolic Dysfunction in Type 2 Diabetes Mellitus. *J. Am. Coll. Cardiol.*, **52** (22), 1793–1799.
168. Bharadwaj, K.G., Hiyama, Y., Hu, Y., Huggins, L.A., Ramakrishnan, R., Abumrad, N.A., Shulman, G.I., Blaner, W.S., and Goldberg, I.J. (2010) Chylomicron- and VLDL-derived lipids enter the heart through different pathways: In vivo evidence for receptor- and non-receptor-mediated fatty acid uptake. *J. Biol. Chem.*, **285** (49), 37976–37986.
169. Revuelta-López, E., Soler-Botija, C., Nasarre, L., Benitez-Amaro, A., de Gonzalo-Calvo, D., Bayes-Genis, A., and Llorente-Cortés, V. (2017) Relationship among LRP1 expression, Pyk2 phosphorylation and MMP-9 activation in left ventricular remodelling after myocardial infarction. *J. Cell. Mol. Med.*, **21** (9), 1915–1928.
170. Cal, R., Juan-Babot, O., Brossa, V., Roura, S., Gálvez-Montón, C., Portoles, M., Rivera, M., Cinca, J., Badimon, L., and Llorente-Cortés, V. (2012) Low density lipoprotein receptor-related protein 1 expression correlates with cholesteryl ester accumulation in the myocardium of ischemic cardiomyopathy patients. *J. Transl. Med.*, **10** (1).
171. Barriga, M., Cal, R., Cabello, N., Llach, A., Vallmitjana, A., Benítez, R., Badimon, L., Cinca, J., Llorente-Cortés, V., and Hove-Madsen, L. (2013) Low Density Lipoproteins Promote Unstable Calcium Handling Accompanied by Reduced SERCA2 and Connexin-40 Expression in

Cardiomyocytes. *PLoS One*, **8** (3), e58128.
172. Namekata, I., Hamaguchi, S., Wakasugi, Y., Ohhara, M., Hirota, Y., and Tanaka, H. (2013) Ellagic acid and gingerol, activators of the sarco-endoplasmic reticulum Ca2+-ATPase, ameliorate diabetes mellitus-induced diastolic dysfunction in isolated murine ventricular myocardia. *Eur. J. Pharmacol.*, **706** (1), 48–55.
173. Samouillan, V., Dandurand, J., Nasarre, L., Badimon, L., Lacabanne, C., and Llorente-Cortés, V. (2012) Lipid Loading of Human Vascular Smooth Muscle Cells Induces Changes in Tropoelastin Protein Levels and Physical Structure. *Biophys. J.*, **103** (3), 532–540.
174. Samouillan, V., Revuelta-López, E., Dandurand, J., Nasarre, L., Badimon, L., Lacabanne, C., and Llorente-Cortés, V. (2014) Cardiomyocyte intracellular cholesteryl ester accumulation promotes tropoelastin physical alteration and degradation: Role of LRP1 and cathepsin S. *Int. J. Biochem. Cell Biol.*, **55**, 209–219.
175. Reaven, G.M., Knowles, J.W., Leonard, D., Barlow, C.E., Willis, B.L., Haskell, W.L., and Maron, D.J. (2017) Relationship between simple markers of insulin resistance and coronary artery calcification. *J. Clin. Lipidol.*, **11** (4), 1007–1012.
176. Fakhrzadeh, H., Sharifi, F., Alizadeh, M., Arzaghi, S.M., Tajallizade-Khoob, Y., Tootee, A., Alatab, S., Mirarefin, M., Badamchizade, Z., and Kazemi, H. (2015) Relationship between insulin resistance and subclinical atherosclerosis in individuals with and without type 2 diabetes mellitus. *J. Diabetes Metab. Disord.*, **15**, 41.
177. Isomaa, B., Almgren, P., Tuomi, T., Forsén, B., Lahti, K., Nissén, M., Taskinen, M.R., and Groop, L. (2001) Cardiovascular morbidity and mortality associated with the metabolic syndrome. *Diabetes Care*, **24** (4), 683–689.
178. Bonora, E., Formentini, G., Calcaterra, F., Lombardi, S., Marini, F., Zenari, L., Saggiani, F., Poli, M., Perbellini, S., Raffaelli, A., Cacciatori, V., Santi, L., Targher, G., Bonadonna, R., and Muggeo, M. (2002) HOMA-estimated insulin resistance is an independent predictor of cardiovascular disease in type 2 diabetic subjects: prospective data from the Verona Diabetes Complications Study. *Diabetes Care*, **25** (7), 1135–1141.
179. Bonora, E., Kiechl, S., Willeit, J., Oberhollenzer, F., Egger, G., Meigs, J.B., Bonadonna, R.C., and Muggeo, M. (2007) Insulin resistance as estimated by homeostasis model assessment predicts incident symptomatic cardiovascular disease in caucasian subjects from the general population: the Bruneck study. *Diabetes Care*, **30** (2), 318–324.
180. Golden, S.H., Folsom, A.R., Coresh, J., Sharrett, A.R., Szklo, M., and Brancati, F. (2002) Risk factor groupings related to insulin resistance and their synergistic effects on subclinical atherosclerosis: the atherosclerosis risk in communities study. *Diabetes*, **51** (10), 3069–3076.
181. Hanley, A.J.G., Williams, K., Stern, M.P., and Haffner, S.M. (2002) Homeostasis model assessment of insulin resistance in relation to the incidence of cardiovascular disease: the San Antonio Heart Study. *Diabetes Care*, **25** (7), 1177–1184.
182. Lee, J., and Pilch, P.F. (1994) The insulin receptor: structure, function, and signaling. *Am. J. Physiol.*, **266** (2 Pt 1), C319-34.
183. Actis Dato, V., Benitez-Amaro, A., de Gonzalo-Calvo, D., Vazquez, M., Bonacci, G., Llorente-Cortés, V., and Chiabrando, G.A. (2020) LRP1-Mediated AggLDL Endocytosis Promotes Cholesteryl Ester Accumulation and Impairs Insulin Response in HL-1 Cells. *Cells*.
184. Liu, C.-C., Hu, J., Tsai, C.-W., Yue, M., Melrose, H.L., Kanekiyo, T., and Bu, G. (2015) Neuronal LRP1 Regulates Glucose Metabolism and Insulin Signaling in the Brain. *J. Neurosci.*, **35** (14), 5851–5859.
185. Ding, Y., Xian, X., Holland, W.L., Tsai, S., and Herz, J. (2016) Low-Density Lipoprotein Receptor-Related Protein-1 Protects Against Hepatic Insulin Resistance and Hepatic Steatosis. *EBioMedicine*, **7**, 135–145.
186. Kasuga, M. (2019) Structure and function of the insulin receptor-a personal perspective.

Proc. Jpn. Acad. Ser. B. Phys. Biol. Sci., **95** (10), 581–589.
187. Martinez, C.A., and Scafoglio, C. (2020) Heterogeneity of Glucose Transport in Lung Cancer. *Biomolecules*, **10** (6).
188. Lacombe, V.A. (2014) Expression and regulation of facilitative glucose transporters in equine insulin-sensitive tissue: from physiology to pathology. *ISRN Vet. Sci.*, **2014**, 409547.
189. Au, D.T., Strickland, D.K., and Muratoglu, S.C. (2017) The LDL Receptor-Related Protein 1: At the Crossroads of Lipoprotein Metabolism and Insulin Signaling. *J. Diabetes Res.*, **2017**, 8356537.
190. Huang, P.L. (2009) A comprehensive definition for metabolic syndrome. *Dis. Model. Mech.*, **2** (5–6), 231–237.
191. Cartee, G.D., and Funai, K. (2009) Exercise and insulin: Convergence or divergence at AS160 and TBC1D1? *Exerc. Sport Sci. Rev.*, **37** (4), 188–195.
192. Kandror Konstantin, V., and Pilch Paul, F. (2011) The Sugar Is sIRVed: Sorting Glut4 and Its Fellow Travelers. *Traffic*, **12** (6), 665–671.
193. Bogan, J.S., and Kandror, K. V (2010) Biogenesis and regulation of insulin-responsive vesicles containing GLUT4. *Curr. Opin. Cell Biol.*, **22** (4), 506–512.
194. Actis Dato, V., Grosso, R.A., Sánchez, M.C., Fader, C.M., and Chiabrando, G.A. (2018) Insulin-induced exocytosis regulates the cell surface level of low-density lipoprotein-related protein-1 in Müller Glial cells. *Biochem. J.*, **475** (9), 1669–1685.
195. Nakamura, M., and Sadoshima, J. (2014) Heart over mind: metabolic control of white adipose tissue and liver. *EMBO Mol. Med.*, **6** (12), 1521–1524.
196. Shimano, M., Ouchi, N., and Walsh, K. (2012) Cardiokines: Recent progress in elucidating the cardiac secretome. *Circulation*, **126** (21).
197. Members:, A.F., Perk, J., De Backer, G., Gohlke, H., Graham, I., Reiner, Ž., Verschuren, M., Albus, C., Benlian, P., Boysen, G., Cifkova, R., Deaton, C., Ebrahim, S., Fisher, M., Germano, G., Hobbs, R., Hoes, A., Karadeniz, S., Mezzani, A., Prescott, E., Ryden, L., Scherer, M., Syvänne, M., Scholte Op Reimer, W.J.M., Vrints, C., Wood, D., Zamorano, J.L., Zannad, F., guidelines:, O. experts who contributed to parts of the, Cooney, M.T., (CPG):, E.S.C.C. for P.G., Bax, J., Baumgartner, H., Ceconi, C., Dean, V., Deaton, C., Fagard, R., Funck-Brentano, C., Hasdai, D., Hoes, A., Kirchhof, P., Knuuti, J., Kolh, P., McDonagh, T., Moulin, C., Popescu, B.A., Reiner, Ž., Sechtem, U., Sirnes, P.A., Tendera, M., Torbicki, A., Vahanian, A., Windecker, S., Reviewers:, D., Funck-Brentano, C., Sirnes, P.A., Aboyans, V., Ezquerra, E.A., Baigent, C., Brotons, C., Burell, G., Ceriello, A., De Sutter, J., Deckers, J., Del Prato, S., Diener, H.-C., Fitzsimons, D., Fras, Z., Hambrecht, R., Jankowski, P., Keil, U., Kirby, M., Larsen, M.L., Mancia, G., Manolis, A.J., McMurray, J., Pająk, A., Parkhomenko, A., Rallidis, L., Rigo, F., Rocha, E., Ruilope, L.M., van der Velde, E., Vanuzzo, D., Viigimaa, M., Volpe, M., Wiklund, O., and Wolpert, C. (2012) European Guidelines on cardiovascular disease prevention in clinical practice (version 2012)The Fifth Joint Task Force of the European Society of Cardiology and Other Societies on Cardiovascular Disease Prevention in Clinical Practice (constituted by repr. *Eur. Heart J.*, **33** (13), 1635–1701.
198. Yancy, C.W., Jessup, M., Bozkurt, B., Butler, J., Casey, D.E., Drazner, M.H., Fonarow, G.C., Geraci, S.A., Horwich, T., Januzzi, J.L., Johnson, M.R., Kasper, E.K., Levy, W.C., Masoudi, F.A., McBride, P.E., McMurray, J.J. V, Mitchell, J.E., Peterson, P.N., Riegel, B., Sam, F., Stevenson, L.W., Tang, W.H.W., Tsai, E.J., and Wilkoff, B.L. (2013) 2013 ACCF/AHA Guideline for the Management of Heart Failure: Executive Summary. *Circulation*, **128** (16), 1810 LP – 1852.
199. Schlueter, N., de Sterke, A., Willmes, D.M., Spranger, J., Jordan, J., and Birkenfeld, A.L. (2014) Metabolic actions of natriuretic peptides and therapeutic potential in the metabolic syndrome. *Pharmacol. Ther.*, **144** (1), 12–27.
200. Bordicchia, M., Liu, D., Amri, E.-Z., Ailhaud, G., Dessì-Fulgheri, P., Zhang, C., Takahashi, N., Sarzani, R., and Collins, S. (2012) Cardiac natriuretic peptides act via p38 MAPK to induce the brown fat thermogenic program in mouse and human adipocytes. *J. Clin. Invest.*, **122** (3),

1022–1036.
201. Engeli, S., Birkenfeld, A.L., Badin, P.-M., Bourlier, V., Louche, K., Viguerie, N., Thalamas, C., Montastier, E., Larrouy, D., Harant, I., de Glisezinski, I., Lieske, S., Reinke, J., Beckmann, B., Langin, D., Jordan, J., and Moro, C. (2012) Natriuretic peptides enhance the oxidative capacity of human skeletal muscle. *J. Clin. Invest.*, **122** (12), 4675–4679.
202. SENGENES, C. (2000) Natriuretic peptides: a new lipolytic pathway in human adipocytes. *FASEB J.*, **14** (10), 1345–1351.
203. Pandey, K.N. (2021) Molecular Signaling Mechanisms and Function of Natriuretic Peptide Receptor-A in the Pathophysiology of Cardiovascular Homeostasis. *Front. Physiol.*, **12**, 693099.
204. Pemberton, C.J., Siriwardena, M., Kleffmann, T., Ruygrok, P., Palmer, S.C., Yandle, T.G., and Richards, A.M. (2012) First identification of circulating prepro-A-type natriuretic peptide (preproANP) signal peptide fragments in humans: Initial assessment as cardiovascular biomarkers. *Clin. Chem.*, **58** (4), 757–767.
205. Yu, R., Han, X., Zhang, X., Wang, Y., and Wang, T. (2018) Circulating soluble corin as a potential biomarker for cardiovascular diseases: A translational review. *Clin. Chim. Acta.*, **485**, 106–112.
206. Knappe, S., Wu, F., Masikat, M.R., Morser, J., and Wu, Q. (2003) Functional analysis of the transmembrane domain and activation cleavage of human corin: design and characterization of a soluble corin. *J. Biol. Chem.*, **278** (52), 52363–52370.
207. Nakagawa, Y., Nishikimi, T., and Kuwahara, K. (2019) Atrial and brain natriuretic peptides: Hormones secreted from the heart. *Peptides*, **111**, 18–25.
208. Zakeri, R., Sangaralingham, S.J., Sandberg, S.M., Heublein, D.M., Scott, C.G., and Burnett, J.C.J. (2013) Urinary C-type natriuretic peptide: a new heart failure biomarker. *JACC. Heart Fail.*, **1** (2), 170–177.
209. Forte, M., Madonna, M., Schiavon, S., Valenti, V., Versaci, F., Zoccai, G.B., Frati, G., and Sciarretta, S. (2019) Cardiovascular Pleiotropic Effects of Natriuretic Peptides. *Int. J. Mol. Sci.*, **20** (16).
210. Kuwahara, K. (2021) The natriuretic peptide system in heart failure: Diagnostic and therapeutic implications. *Pharmacol. Ther.*, **227**, 107863.
211. Nishikimi, T., Nakagawa, Y., Minamino, N., Ikeda, M., Tabei, K., Fujishima, A., Takayama, K., Akimoto, K., Yamada, C., Nakao, K., Minami, T., Kuwabara, Y., Kinoshita, H., Tsutamoto, T., Ishimitsu, T., Kangawa, K., Kuwahara, K., and Nakao, K. (2015) Pro-B-type natriuretic peptide is cleaved intracellularly: impact of distance between O-glycosylation and cleavage sites. *Am. J. Physiol. Regul. Integr. Comp. Physiol.*, **309** (6), R639-49.
212. Cleasby, M.E. (2015) ANP-ing Up Diabetes: Impaired Natriuretic Peptide Action in Muscle Forms a Mechanistic Link Between Obesity and Diabetes. *Diabetes*, **64** (12), 3978–3980.
213. Moyes, A.J., and Hobbs, A.J. (2019) C-type Natriuretic Peptide: A Multifaceted Paracrine Regulator in the Heart and Vasculature. *Int. J. Mol. Sci.*, **20** (9).
214. Nakao, K., Kuwahara, K., Nishikimi, T., Nakagawa, Y., Kinoshita, H., Minami, T., Kuwabara, Y., Yamada, C., Yamada, Y., Tokudome, T., Nagai-Okatani, C., Minamino, N., Nakao, Y.M., Yasuno, S., Ueshima, K., Sone, M., Kimura, T., Kangawa, K., and Nakao, K. (2017) Endothelium-Derived C-Type Natriuretic Peptide Contributes to Blood Pressure Regulation by Maintaining Endothelial Integrity. *Hypertens. (Dallas, Tex. 1979)*, **69** (2), 286–296.
215. Smolenski, A., Poller, W., Walter, U., and Lohmann, S.M. (2000) Regulation of human endothelial cell focal adhesion sites and migration by cGMP-dependent protein kinase I. *J. Biol. Chem.*, **275** (33), 25723–25732.
216. Ramos, H.R., Birkenfeld, A.L., and de Bold, A.J. (2015) INTERACTING DISCIPLINES: Cardiac natriuretic peptides and obesity: perspectives from an endocrinologist and a cardiologist. *Endocr. Connect.*, **4** (3), R25-36.

217. Tsutsui, H., Isobe, M., Ito, H., Ito, H., Okumura, K., Ono, M., Kitakaze, M., Kinugawa, K., Kihara, Y., Goto, Y., Komuro, I., Saiki, Y., Saito, Y., Sakata, Y., Sato, N., Sawa, Y., Shiose, A., Shimizu, W., Shimokawa, H., Seino, Y., Node, K., Higo, T., Hirayama, A., Makaya, M., Masuyama, T., Murohara, T., Momomura, S.-I., Yano, M., Yamazaki, K., Yamamoto, K., Yoshikawa, T., Yoshimura, M., Akiyama, M., Anzai, T., Ishihara, S., Inomata, T., Imamura, T., Iwasaki, Y.-K., Ohtani, T., Onishi, K., Kasai, T., Kato, M., Kawai, M., Kinugasa, Y., Kinugawa, S., Kuratani, T., Kobayashi, S., Sakata, Y., Tanaka, A., Toda, K., Noda, T., Nochioka, K., Hatano, M., Hidaka, T., Fujino, T., Makita, S., Yamaguchi, O., Ikeda, U., Kimura, T., Kohsaka, S., Kosuge, M., Yamagishi, M., and Yamashina, A. (2019) JCS 2017/JHFS 2017 Guideline on Diagnosis and Treatment of Acute and Chronic Heart Failure - Digest Version. *Circ. J.*, **83** (10), 2084–2184.
218. Zhao, X., Zhang, D.-Q., Song, R., and Zhang, G. (2020) Nesiritide in patients with acute myocardial infarction and heart failure: a meta-analysis. *J. Int. Med. Res.*, **48** (1), 300060519897194.
219. Duggan, S. (2021) Vosoritide: First Approval. *Drugs*, **81** (17), 2057–2062.
220. Högler, W., and Ward, L.M. (2020) New developments in the management of achondroplasia. *Wien. Med. Wochenschr.*, **170** (5–6), 104–111.
221. Tate, M., Grieve, D.J., and Ritchie, R.H. (2017) Are targeted therapies for diabetic cardiomyopathy on the horizon? *Clin. Sci. (Lond).*, **131** (10), 897–915.
222. Frangogiannis, N.G. (2017) The extracellular matrix in myocardial injury, repair, and remodeling. *J. Clin. Invest.*, **127** (5), 1600–1612.
223. Hayden, M.R., Chowdhury, N., Govindarajan, G., Karuparthi, P.R., Habibi, J., and Sowers, J.R. (2006) Myocardial myocyte remodeling and fibrosis in the cardiometabolic syndrome. *J. Cardiometab. Syndr.*, **1** (5), 326–333.
224. Planavila, A., Fernández-Solà, J., and Villarroya, F. (2017) Cardiokines as Modulators of Stress-Induced Cardiac Disorders, in *Advances in Protein Chemistry and Structural Biology*, vol. 108, pp. 227–256.
225. Wu, B., Zhou, B., Wang, Y., Cheng, H.-L., Hang, C.T., Pu, W.T., Chang, C.-P., and Zhou, B. (2010) Inducible cardiomyocyte-specific gene disruption directed by the rat Tnnt2 promoter in the mouse. *Genesis*, **48** (1), 63–72.
226. Claycomb, W.C., Lanson, N.A.J., Stallworth, B.S., Egeland, D.B., Delcarpio, J.B., Bahinski, A., and Izzo, N.J.J. (1998) HL-1 cells: a cardiac muscle cell line that contracts and retains phenotypic characteristics of the adult cardiomyocyte. *Proc. Natl. Acad. Sci. U. S. A.*, **95** (6), 2979–2984.
227. Orellana-Gavaldà, J.M., Herrero, L., Malandrino Maria, I., Pañeda, A., Sol Rodríguez-Peña, M., Petry, H., Asins, G., Van Deventer, S., Hegardt Fausto, G., and Serra, D. (2010) Molecular therapy for obesity and diabetes based on a long-term increase in hepatic fatty-acid oxidation. *Hepatology*, **53** (3), 821–832.
228. Óscar, G., David, O., Marina, G., Montserrat, C., and Joaquin, A. (2014) A collection of open source applications for mass spectrometry data mining. *Proteomics*, **14** (20), 2275–2279.
229. Herrero, L., Rubí, B., Sebastián, D., Serra, D., Asins, G., Maechler, P., Prentki, M., and Hegardt, F.G. (2005) Alteration of the malonyl-CoA/carnitine palmitoyltransferase I interaction in the β-cell impairs glucose-induced insulin secretion. *Diabetes*, **54** (2), 462–471.
230. Escolà-Gil, J.C., Llaverias, G., Julve, J., Jauhiainen, M., Méndez-González, J., and Blanco-Vaca, F. (2011) The Cholesterol Content of Western Diets Plays a Major Role in the Paradoxical Increase in High-Density Lipoprotein Cholesterol and Upregulates the Macrophage Reverse Cholesterol Transport Pathway. *Arterioscler. Thromb. Vasc. Biol.*, **31** (11), 2493 LP – 2499.
231. Julve, J., Escolà-Gil, J.C., Rotllan, N., Fiévet, C., Vallez, E., de la Torre, C., Ribas, V., Sloan, J.H., and Blanco-Vaca, F. (2010) Human Apolipoprotein A-II Determines Plasma Triglycerides by Regulating Lipoprotein Lipase Activity and High-Density Lipoprotein Proteome. *Arterioscler. Thromb. Vasc. Biol.*, **30** (2), 232 LP – 238.
232. Bligh, E.G., and Dyer, W.J. (1959) A Rapid Method of total lipid extraction and purification.

Can. J. Biochem. Physiol., **37** (8), 911–917.
233. Rebollo, A., Roglans, N., Baena, M., Sánchez, R.M., Merlos, M., Alegret, M., and Laguna, J.C. (2014) Liquid fructose downregulates Sirt1 expression and activity and impairs the oxidation of fatty acids in rat and human liver cells. *Biochim. Biophys. Acta - Mol. Cell Biol. Lipids*, **1841** (4), 514–524.
234. Llucià-Valldeperas, A., Soler-Botija, C., Gálvez-Montón, C., Roura, S., Prat-Vidal, C., Perea-Gil, I., Sanchez, B., Bragos, R., Vunjak-Novakovic, G., and Bayes-Genis, A. (2017) Electromechanical Conditioning of Adult Progenitor Cells Improves Recovery of Cardiac Function After Myocardial Infarction. *Stem Cells Transl. Med.*, **6** (3), 970–981.
235. Cedó, L., Metso, J., Santos, D., Sánchez-Quesada, J.L., Julve, J., García-León, A., Mora-Brugués, J., Jauhiainen, M., Blanco-Vaca, F., and Escolà-Gil, J.C. (2015) Consumption of polyunsaturated fat improves the saturated fatty acid-mediated impairment of HDL antioxidant potential. *Mol. Nutr. Food Res.*, **59** (10), 1987–1996.
236. Chen, S., Sen, S., Young, D., Wang, W., Moravec, C.S., and Wu, Q. (2010) Protease corin expression and activity in failing hearts. *Am J Physiol Hear. Circ Physiol*, **299** (5), H1687-92.
237. Virtue, S., and Vidal-Puig, A. (2013) Assessment of brown adipose tissue function. *Front. Physiol.*, **4**, 128.
238. Bruck, B., Brehme, U., Gugel, N., Hanke, S., Finking, G., Lutz, C., Benda, N., Schmahl, F.W., Haasis, R., and Hanke, H. (1997) Gender-specific differences in the effects of testosterone and estrogen on the development of atherosclerosis in rabbits. *Arterioscler. Thromb. Vasc. Biol.*, **17** (10), 2192–2199.
239. Echeverri, D., Delgadillo, A., and Montes, F. (2007) Efecto morfológico y funcional vascular de los andrógenos endógenos en un modelo experimental en conejos ateroscleróticos. *Rev. Colomb. Cardiol.*, **14** (5), 276–283.
240. Avrameas, S. (1969) Coupling of enzymes to proteins with glutaraldehyde. Use of the conjigates for the detection of anyigens and antibodies. *Immunochemistry*, **6** (1), 43–52.
241. Casadei, A., Floreani, M., Catalini, R., Serra, C., Assanti, A.P., and Conci, P. (2012) Sonographic characteristics of carotid artery plaques: Implications for follow-up planning? *J. Ultrasound*, **15** (3), 151–157.
242. Samouillan, V., Martinez de Lejarza Samper, I.M., Amaro, A.B., Vilades, D., Dandurand, J., Casas, J., Jorge, E., Calvo, D. de G., Gallardo, A., Lerma, E., Ramos, J.M.G., Carreras, F., Leta, R., and Llorente Cortes, V. (2020) Biophysical and Lipidomic Biomarkers of Cardiac Remodeling Post-Myocardial Infarction in Humans. *Biomolecules*, **10** (11).
243. Gauthier, M.-S., Favier, R., and Lavoie, J.-M. (2006) Time course of the development of non-alcoholic hepatic steatosis in response to high-fat diet-induced obesity in rats. *Br. J. Nutr.*, **95** (2), 273–281.
244. Kraegen, E.W., Clark, P.W., Jenkins, A.B., Daley, E.A., Chisholm, D.J., and Storlien, L.H. (1991) Development of muscle insulin resistance after liver insulin resistance in high-fat-fed rats. *Diabetes*, **40** (11), 1397–1403.
245. Samuel, V.T., Liu, Z.-X., Qu, X., Elder, B.D., Bilz, S., Befroy, D., Romanelli, A.J., and Shulman, G.I. (2004) Mechanism of hepatic insulin resistance in non-alcoholic fatty liver disease. *J. Biol. Chem.*, **279** (31), 32345–32353.
246. Stefanovic-Racic, M., Perdomo, G., Mantell, B.S., Sipula, I.J., Brown, N.F., and O'Doherty, R.M. (2008) A moderate increase in carnitine palmitoyltransferase 1a activity is sufficient to substantially reduce hepatic triglyceride levels. *Am. J. Physiol. Metab.*, **294** (5), E969–E977.
247. Schlaepfer, I.R., and Joshi, M. (2020) CPT1A-mediated Fat Oxidation, Mechanisms, and Therapeutic Potential. *Endocrinology*, **161** (2).
248. Wang, M., Wang, K., Liao, X., Hu, H., Chen, L., Meng, L., Gao, W., and Li, Q. (2021) Carnitine Palmitoyltransferase System: A New Target for Anti-Inflammatory and Anticancer Therapy? *Front. Pharmacol.*, **12**, 760581.

249. An, J., Muoio, D.M., Shiota, M., Fujimoto, Y., Cline, G.W., Shulman, G.I., Koves, T.R., Stevens, R., Millington, D., and Newgard, C.B. (2004) Hepatic expression of malonyl-CoA decarboxylase reverses muscle, liver and whole-animal insulin resistance. *Nat. Med.*, **10** (3), 268–274.
250. Savage, D.B., Choi, C.S., Samuel, V.T., Liu, Z.-X., Zhang, D., Wang, A., Zhang, X.-M., Cline, G.W., Yu, X.X., Geisler, J.G., Bhanot, S., Monia, B.P., and Shulman, G.I. (2006) Reversal of diet-induced hepatic steatosis and hepatic insulin resistance by antisense oligonucleotide inhibitors of acetyl-CoA carboxylases 1 and 2. *J. Clin. Invest.*, **116** (3), 817–824.
251. Elfers, K., Armbrecht, Y., Brede, M., Mazzuoli-Weber, G., Heldmaier, G., and Breves, G. (2022) How much does it cost? Teaching physiology of energy metabolism in mice using an indirect calorimetry system in a practical course for veterinary students. *Adv. Physiol. Educ.*, **46** (1), 145–157.
252. Chan, J.C.Y., Knudson, O., Wu, F., Morser, J., Dole, W.P., and Wu, Q. (2005) Hypertension in mice lacking the proatrial natriuretic peptide convertase corin. *Proc. Natl. Acad. Sci. U. S. A.*, **102** (3), 785–790.
253. Gladysheva, I.P., Robinson, B.R., Houng, A.K., Kováts, T., and King, S.M. (2008) Corin is co-expressed with pro-ANP and localized on the cardiomyocyte surface in both zymogen and catalytically active forms. *J. Mol. Cell. Cardiol.*, **44** (1), 131–142.
254. Strickland, D.K., Muratoglu, S.C., and Antalis, T.M. (2011) Serpin–Enzyme Receptors: LDL Receptor-Related Protein 1. *Methods Enzymol.*, **499**, 17–31.
255. Gettins, P.G.W., and Dolmer, K. (2016) The High Affinity Binding Site on Plasminogen Activator Inhibitor-1 (PAI-1) for the Low Density Lipoprotein Receptor-related Protein (LRP1) Is Composed of Four Basic Residues. *J. Biol. Chem.*, **291** (2), 800–812.
256. Revuelta-López, E., Cal, R., Herraiz-Martínez, A., de Gonzalo-Calvo, D., Nasarre, L., Roura, S., Gálvez-Montón, C., Bayes-Genis, A., Badimon, L., Hove-Madsen, L., and Llorente-Cortés, V. (2015) Hypoxia-driven sarcoplasmic/endoplasmic reticulum calcium ATPase 2 (SERCA2) downregulation depends on low-density lipoprotein receptor-related protein 1 (LRP1)-signalling in cardiomyocytes. *J. Mol. Cell. Cardiol.*, **85**, 25–36.
257. Schäfer, W., Stroh, A., Berghöfer, S., Seiler, J., Vey, M., Kruse, M.L., Kern, H.F., Klenk, H.D., and Garten, W. (1995) Two independent targeting signals in the cytoplasmic domain determine trans-Golgi network localization and endosomal trafficking of the proprotein convertase furin. *EMBO J.*, **14** (11), 2424–2435.
258. Tonne, J.M., Campbell, J.M., Cataliotti, A., Ohmine, S., Thatava, T., Sakuma, T., Macheret, F., Huntley, B.K., Burnett, J.C.J., and Ikeda, Y. (2011) Secretion of glycosylated pro-B-type natriuretic peptide from normal cardiomyocytes. *Clin. Chem.*, **57** (6), 864–873.
259. Neeland, I.J., Winders, B.R., Ayers, C.R., Das, S.R., Chang, A.Y., Berry, J.D., Khera, A., McGuire, D.K., Vega, G.L., de Lemos, J.A., and Turer, A.T. (2013) Higher Natriuretic Peptide Levels Associate with a Favorable Adipose Tissue Distribution Profile. *J. Am. Coll. Cardiol.*, **62** (8), 10.1016/j.jacc.2013.03.038.
260. Cannone, V., Cefalu, A.B., Noto, D., Scott, C.G., Bailey, K.R., Cavera, G., Pagano, M., Sapienza, M., Averna, M.R., and Burnett, J.C. (2013) The atrial natriuretic peptide genetic ariant rs5068 is associated with a favorable cardiometabolic phenotype in a mediterranean population. *Diabetes Care*, **36** (9), 2850–2856.
261. Pfister, R., Sharp, S., Luben, R., Welsh, P., Barroso, I., Salomaa, V., Meirhaeghe, A., Khaw, K.T., Sattar, N., Langenberg, C., and Wareham, N.J. (2011) Mendelian randomization study of B-type natriuretic peptide and type 2 diabetes: Evidence of causal association from population studies. *PLoS Med.*, **8** (10), e1001112.
262. Norling, L.L., von Geldern, T., and Chevalier, R.L. (1994) Maturation of A71915-dependent inhibition of atrial natriuretic peptide-stimulated cyclic GMP production in isolated rat glomeruli. *Biol. Neonate*, **66** (5), 294–301.
263. Delporte, C., Winand, J., Poloczek, P., Von Geldern, T., and Christophe, J. (1992) Discovery of a

potent atrial natriuretic peptide antagonist for ANPA receptors in the human neuroblastoma NB-OK-1 cell line. *Eur. J. Pharmacol.*, **224** (2–3), 183–188.
264. Moro, C., Galitzky, J., Sengenes, C., Crampes, F., Lafontan, M., and Berlan, M. (2004) Functional and pharmacological characterization of the natriuretic peptide-dependent lipolytic pathway in human fat cells. *J. Pharmacol. Exp. Ther.*, **308** (3), 984–992.
265. Tateya, S., Rizzo-De Leon, N., Handa, P., Cheng, A.M., Morgan-Stevenson, V., Ogimoto, K., Kanter, J.E., Bornfeldt, K.E., Daum, G., Clowes, A.W., Chait, A., and Kim, F. (2013) VASP increases hepatic fatty acid oxidation by activating AMPK in mice. *Diabetes*, **62** (6), 1913–1922.
266. Munday, M.R., Campbell, D.G., Carling, D., and Hardie, D.G. (1988) Identification by amino acid sequencing of three major regulatory phosphorylation sites on rat acetyl-CoA carboxylase. *Eur. J. Biochem.*, **175** (2), 331–338.
267. Schonke, M., Massart, J., and Zierath, J.R. (2018) Effects of high-fat diet and AMPK modulation on the regulation of whole-body lipid metabolism. *J. Lipid Res.* .
268. Herzig, S., and Shaw, R.J. (2018) AMPK: guardian of metabolism and mitochondrial homeostasis. *Nat. Rev. Mol. Cell Biol.*, **19** (2), 121–135.
269. Foster, D.W. (2004) The role of the carnitine system in human metabolism. *Ann. N. Y. Acad. Sci.*, **1033**, 1–16.
270. Foretz, M., Even, P.C., and Viollet, B. (2018) AMPK Activation Reduces Hepatic Lipid Content by Increasing Fat Oxidation In Vivo. *Int. J. Mol. Sci.*, **19** (9).
271. Postic, C., Dentin, R., and Girard, J. (2004) Role of the liver in the control of carbohydrate and lipid homeostasis. *Diabetes & Metab.*, **858** (5), 398 YP – 477.
272. Bartels, E.D., Guo, S., Kousholt, B.S., Larsen, J.R., Hasenkam, J.M., Burnett, J., Nielsen, L.B., Ashina, M., and Goetze, J.P. (2019) High doses of ANP and BNP exacerbate lipolysis in humans and the lipolytic effect of BNP is associated with cardiac triglyceride content in pigs. *Peptides*.
273. Sebastián, D., Hernández-Alvarez, M.I., Segalés, J., Sorianello, E., Muñoz, J.P., Sala, D., Waget, A., Liesa, M., Paz, J.C., Gopalacharyulu, P., Orešič, M., Pich, S., Burcelin, R., Palacín, M., and Zorzano, A. (2012) Mitofusin 2 (Mfn2) links mitochondrial and endoplasmic reticulum function with insulin signaling and is essential for normal glucose homeostasis. *Proc. Natl. Acad. Sci. U. S. A.*, **109** (14), 5523–5528.
274. Bu, S.Y., Mashek, M.T., and Mashek, D.G. (2009) Suppression of long chain acyl-CoA synthetase 3 decreases hepatic de novo fatty acid synthesis through decreased transcriptional activity. *J. Biol. Chem.*, **284** (44), 30474–30483.
275. Miyashita, K., Itoh, H., Tsujimoto, H., Tamura, N., Fukunaga, Y., Sone, M., Yamahara, K., Taura, D., Inuzuka, M., Sonoyama, T., and Nakao, K. (2009) Natriuretic Peptides/cGMP/cGMP-Dependent Protein Kinase Cascades Promote Muscle Mitochondrial Biogenesis and Prevent Obesity. *Diabetes*, **58** (12), 2880–2892.
276. Talha, S., Bouitbir, J., Charles, A.-L., Zoll, J., Goette-Di Marco, P., Meziani, F., Piquard, F., and Geny, B. (2013) Pretreatment with brain natriuretic peptide reduces skeletal muscle mitochondrial dysfunction and oxidative stress after ischemia-reperfusion. *J. Appl. Physiol.*, **114** (2), 172–179.
277. Ratman, D., Mylka, V., Bougarne, N., Pawlak, M., Caron, S., Hennuyer, N., Paumelle, R., De Cauwer, L., Thommis, J., Rider, M.H., Libert, C., Lievens, S., Tavernier, J., Staels, B., and De Bosscher, K. (2016) Chromatin recruitment of activated AMPK drives fasting response genes co-controlled by GR and PPARα. *Nucleic Acids Res.*, **44** (22), 10539–10553.
278. Rudel, L.L., Parks, J.S., Hedrick, C.C., Thomas, M., and Williford, K. (1998) Lipoprotein and cholesterol metabolism in diet-induced coronary artery atherosclerosis in primates. Role of cholesterol and fatty acids. *Prog. Lipid Res.*, **37** (6), 353–370.
279. Checovich, W.J., Fitch, W.L., Krauss, R.M., Smith, M.P., Rapacz, J., Smith, C.L., and Attie, A.D.

(1988) Defective Catabolism and Abnormal Composition of Low-Density Lipoproteins from Mutant Pigs with Hypercholesterolemia. *Biochemistry*, **27** (6), 1934–1941.
280. Kainuma, M., Fujimoto, M., Sekiya, N., Tsuneyama, K., Cheng, C., Takano, Y., Terasawa, K., and Shimada, Y. (2006) Cholesterol-fed rabbit as a unique model of nonalcoholic, nonobese, non-insulin-resistant fatty liver disease with characteristic fibrosis. *J. Gastroenterol.*, **41** (10), 971–980.
281. Phinikaridou, A., Hallock, K.J., Qiao, Y., and Hamilton, J.A. (2009) A robust rabbit model of human atherosclerosis and atherothrombosis. *J. Lipid Res.*, **50** (5), 787–797.
282. Campos, H., López-Miranda, J., Rodríguez, C., Albajar, M., Schaefer, E.J., and Ordovás, J.M. (1997) Urbanization elicits a more atherogenic lipoprotein profile in carriers of the apolipoprotein A-IV-2 allele than in A-IV-1 homozygotes. *Arterioscler. Thromb. Vasc. Biol.*, **17** (6), 1074–1081.
283. Stuart Gray, R., Robbins, D.C., Wang, W., Yeh, J.L., Fabsitz, R.R., Cowan, L.D., Welty, T.K., Lee, E.T., Krauss, R.M., and Howard, B. V. (1997) Relation of LDL size to the insulin resistance syndrome and coronary heart disease in American Indians: The strong heart study. *Arterioscler. Thromb. Vasc. Biol.*, **17** (11), 2713–2720.
284. Bocan, T.M.A., Bak Mueller, S., Mazur, M.J., Uhlendorf, P.D., Quenby Brown, E., and Kieft, K.A. (1993) The relationship between the degree of dietary-induced hypercholesterolemia in the rabbit and atherosclerotic lesion formation. *Atherosclerosis*, **102** (1), 9–22.
285. Llorente-Cortés, V., Costales, P., Bernués, J., Camino-Lopez, S., and Badimon, L. (2006) Sterol Regulatory Element-binding Protein-2 Negatively Regulates Low Density Lipoprotein Receptor-related Protein Transcription. *J. Mol. Biol.*, **359** (4), 950–960.
286. Zhao, Q.M., Feng, T.T., Zhao, X., Xu, Z.M., Liu, Y., Li, D.P., Li, L.Q., Su, G., and Zhang, X.X. (2011) Imaging of atherosclerotic aorta of rabbit model by detection of plaque inflammation with fluorine-18 fluorodeoxyglucose positron emission tomography/computed tomography. *Chin. Med. J. (Engl).*, **124** (6), 911–917.
287. Badimon, J.J., Badimon, L., and Fuster, V. (1990) Regression of atherosclerotic lesions by high density lipoprotein plasma fraction in the cholesterol-fed rabbit. *J. Clin. Invest.*, **85** (4), 1234–1241.
288. Hyafil, F., Cornily, J.-C., Rudd, J.H.F., Machac, J., Feldman, L.J., and Fayad, Z.A. (2009) Quantification of Inflammation Within Rabbit Atherosclerotic Plaques Using the Macrophage-Specific CT Contrast Agent N1177: A Comparison with 18F-FDG PET/CT and Histology. *J. Nucl. Med.*, **50** (6), 959–965.
289. Frauchiger, B., Peter Schmid, H., Roedel, C., Moosmann, P., and Staub, D. (2001) Comparison of carotid arterial resistive indices with intima-media thickness as sonographic markers of atherosclerosis. *Stroke*, **32** (4), 836–841.
290. Drevinge, C., Karlsson, L.O., Ståhlman, M., Larsson, T., Perman Sundelin, J., Grip, L., Andersson, L., Borén, J., and Levin, M.C. (2013) Cholesteryl esters accumulate in the heart in a porcine model of ischemia and reperfusion. *PLoS One*, **8** (4), e61942.
291. Nicoll, A., Duffield, R., and Lewis, B. (1981) Flux of plasma lipoproteins into human arterial intima. Comparison between grossly normal and atheromatous intima. *Atherosclerosis*, **39** (2), 229–242.
292. Castellano, J., Farré, J., Fernandes, J., Bayes-Genis, A., Cinca, J., Badimon, L., Hove-Madsen, L., and Llorente-Cortés, V. (2011) Hypoxia exacerbates Ca(2+)-handling disturbances induced by very low density lipoproteins (VLDL) in neonatal rat cardiomyocytes. *J. Mol. Cell. Cardiol.*, **50** (5), 894–902.
293. Wanless, I.R., Belgiorno, J., and Huet, P.M. (1996) Hepatic sinusoidal fibrosis induced by cholesterol and stilbestrol in the rabbit: 1. Morphology and inhibition of fibrogenesis by dipyridamole. *Hepatology*, **24** (4), 855–864.
294. Aravani, D., Kassi, E., Chatzigeorgiou, A., and Vakrou, S. (2021) Cardiometabolic Syndrome:

An Update on Available Mouse Models. *Thromb. Haemost.*, **121** (6), 703–715.
295. Liu, Z., Patil, I.Y., Jiang, T., Sancheti, H., Walsh, J.P., Stiles, B.L., Yin, F., and Cadenas, E. (2015) High-fat diet induces hepatic insulin resistance and impairment of synaptic plasticity. *PLoS One*, **10** (5), e0128274.
296. Schwingshackl, L., Chaimani, A., Hoffmann, G., Schwedhelm, C., and Boeing, H. (2017) Impact of different dietary approaches on glycemic control and cardiovascular risk factors in patients with type 2 diabetes: a protocol for a systematic review and network meta-analysis. *Syst. Rev.*, **6** (1), 57.
297. Qu, S., Chen, T., Wu, F., Yin, Y., and Bi, H. (2004) Preparation and characterization of polyclonal antibodies against VLDL receptor. *J. Huazhong Univ. Sci. Technol. Med. Sci. = Hua zhong ke ji da xue xue bao. Yi xue Ying wen ban = Huazhong keji daxue xuebao. Yixue Yingdewen ban*, **24** (3), 205–207.
298. Llorente-Cortés, V., Otero-Viñas, M., Camino-López, S., Costales, P., and Badimon, L. (2006) Cholesteryl esters of aggregated LDL are internalized by selective uptake in human vascular smooth muscle cells. *Arterioscler. Thromb. Vasc. Biol.*, **26** (1), 117–123.
299. Shen, W.-J., Azhar, S., and Kraemer, F.B. (2016) Lipid droplets and steroidogenic cells. *Exp. Cell Res.*, **340** (2), 209–214.
300. Zhou, X., Mo, Z., Li, Y., Huang, L., Yu, S., Ge, L., Hu, Y., Shi, S., Zhang, L., Wang, L., Gao, L., Yang, G., and Chu, G. (2022) Oleic acid reduces steroidogenesis by changing the lipid type stored in lipid droplets of ovarian granulosa cells. *J. Anim. Sci. Biotechnol.*, **13** (1), 27.
301. Zoni, V., Khaddaj, R., Campomanes, P., Thiam, A.R., Schneiter, R., and Vanni, S. (2021) Pre-existing bilayer stresses modulate triglyceride accumulation in the ER versus lipid droplets. *Elife*, **10**.
302. Shimobayashi, S.F., and Ohsaki, Y. (2019) Universal phase behaviors of intracellular lipid droplets. *Proc. Natl. Acad. Sci. U. S. A.*, **116** (51), 25440–25445.
303. Llorente-Cortés, V., Otero-Viñas, M., Sánchez, S., Rodríguez, C., and Badimon, L. (2002) Low-Density Lipoprotein Upregulates Low-Density Lipoprotein Receptor-Related Protein Expression in Vascular Smooth Muscle Cells. *Circulation*, **106** (24), 3104.
304. Rohlmann, A., Gotthardt, M., Hammer, R.E., and Herz, J. (1998) Inducible inactivation of hepatic LRP gene by Cre-mediated recombination confirms role of LRP in clearance of chylomicron remnants. *J. Clin. Invest.*, **101** (3), 689–695.
305. Guttman, M., Prieto, J.H., Handel, T.M., Domaille, P.J., and Komives, E.A. (2010) Structure of the minimal interface between ApoE and LRP. *J. Mol. Biol.*, **398** (2), 306–319.
306. Guttman, M., Prieto, J.H., Croy, J.E., and Komives, E.A. (2010) Decoding of lipoprotein-receptor interactions: Properties of ligand binding modules governing interactions with apolipoprotein E. *Biochemistry*, **49** (6), 1207–1216.
307. Dietschy, J.M., Turley, S.D., and Spady, D.K. (1993) Role of liver in the maintenance of cholesterol and low density lipoprotein homeostasis in different animal species, including humans. *J. Lipid Res.*, **34** (10), 1637–1659.
308. Calcagno, C., Cornily, J.C., Hyafil, F., Rudd, J.H.F., Briley-Saebo, K.C., Mani, V., Goldschlager, G., MacHac, J., Fuster, V., and Fayad, Z.A. (2008) Detection of neovessels in atherosclerotic plaques of rabbits using dynamic contrast enhanced MRI and 18F-FDG PET. *Arterioscler. Thromb. Vasc. Biol.*, **28** (7), 1311–1317.
309. Lederman, R.J., Raylman, R.R., Fisher, S.J., Kison, P. V., San, H., Nabel, E.G., and Wahl, R.L. (2001) Detection of atherosclerosis using a novel positron-sensitive probe and 18-fluorodeoxyglucose (FDG). *Nucl. Med. Commun.*, **22** (7), 747–753.
310. Folco, E.J., Sheikine, Y., Rocha, V.Z., Christen, T., Shvartz, E., Sukhova, G.K., Di Carli, M.F., and Libby, P. (2011) Hypoxia but not inflammation augments glucose uptake in human macrophages: Implications for imaging atherosclerosis with 18fluorine-labeled 2-deoxy-D-glucose positron emission tomography. *J. Am. Coll. Cardiol.*, **58** (6), 603–614.

311. Zhang, Y.H., Tian, P., Xu, J.P., Wang, Z.Z., Zhao, X.Z., Nie, M.X., Zhang, M.D., Zhao, Q.M., Zhao, B.T., and Song, S.J. (2019) [The value of (18)F-fluorodeoxyglucose positron emission tomography-computed tomography ((18)F-FDG PET-CT) in evaluating the stability of atherosclerotic plaques]. *Zhonghua nei ke za zhi*, **58** (11), 808–813.
312. Ogawa, M., Magata, Y., Kato, T., Hatano, K., Ishino, S., Mukai, T., Shiomi, M., Ito, K., and Saji, H. (2006) Application of 18F-FDG PET for monitoring the therapeutic effect of antiinflammatory drugs on stabilization of vulnerable atherosclerotic plaques. *J. Nucl. Med.*, **47** (11), 1845–1850.
313. Somford, M.P. (2018) Response to: Comparison of direct anterior, lateral, posterior and posterior-2 approaches in total hip arthroplasty: network meta-analysis. Eur J Orthop Surg Traumatol, 2017 Sep 27, doi: 10.1007/s00590-017-2046-1 [Epub ahead of print]. *Eur. J. Orthop. Surg. Traumatol.*, **28** (4), 753.
314. Theelen, T.L., Lappalainen, J.P., Sluimer, J.C., Gurzeler, E., Cleutjens, J.P., Gijbels, M.J., Biessen, E.A.L., Daemen, M.J.A.P., Alitalo, K., and Ylä-Herttuala, S. (2015) Angiopoietin-2 blocking antibodies reduce early atherosclerotic plaque development in mice. *Atherosclerosis*, **241** (2), 297–304.
315. Mor, A., Afek, A., Entin-Meer, M., Keren, G., and George, J. (2013) Anti eotaxin-2 antibodies attenuate the initiation and progression of experimental atherosclerosis. *World J. Cardiovasc. Dis.*, **03**, 339–346.
316. Huang, Y., Walker, K.E., Hanley, F., Narula, J., Houser, S.R., and Tulenko, T.N. (2004) Cardiac systolic and diastolic dysfunction after a cholesterol-rich diet. *Circulation*, **109** (1), 97–102.
317. Gastaldelli, A., Morales, M.A., Marraccini, P., and Sicari, R. (2012) The role of cardiac fat in insulin resistance. *Curr. Opin. Clin. Nutr. Metab. Care*, **15** (6), 523–528.
318. Semple, R.K., Sleigh, A., Murgatroyd, P.R., Adams, C.A., Bluck, L., Jackson, S., Vottero, A., Kanabar, D., Charlton-Menys, V., Durrington, P., Soos, M.A., Carpenter, T.A., Lomas, D.J., Cochran, E.K., Gorden, P., O'Rahilly, S., and Savage, D.B. (2009) Postreceptor insulin resistance contributes to human dyslipidemia and hepatic steatosis. *J. Clin. Invest.*, **119** (2), 315–322.
319. Wang, G., Yu, Y., Cai, W., Batista, T.M., Suk, S., Noh, H.L., Hirshman, M., Nigro, P., Li, M.E., Softic, S., Goodyear, L., Kim, J.K., and Kahn, C.R. (2020) Muscle-Specific Insulin Receptor Overexpression Protects Mice From Diet-Induced Glucose Intolerance but Leads to Postreceptor Insulin Resistance. *Diabetes*, **69** (11), 2294–2309.
320. Al-Makdissy, N., Younsi, M., Pierre, S., Ziegler, O., and Donner, M. (2003) Sphingomyelin/cholesterol ratio: an important determinant of glucose transport mediated by GLUT-1 in 3T3-L1 preadipocytes. *Cell. Signal.*, **15** (11), 1019–1030.
321. Saxena, N., and Chandra, N.C. (2020) Cholesterol: A Prelate in Cell Nucleus and its Serendipity. *Curr. Mol. Med.*, **20** (9), 692–707.
322. Habegger, K.M., Penque, B.A., Sealls, W., Tackett, L., Bell, L.N., Blue, E.K., Gallagher, P.J., Sturek, M., Alloosh, M.A., Steinberg, H.O., Considine, R. V, and Elmendorf, J.S. (2012) Fat-induced membrane cholesterol accrual provokes cortical filamentous actin destabilisation and glucose transport dysfunction in skeletal muscle. *Diabetologia*, **55** (2), 457–467.
323. Jedrychowski, M.P., Gartner, C.A., Gygi, S.P., Zhou, L., Herz, J., Kandror, K. V, and Pilch, P.F. (2010) Proteomic analysis of GLUT4 storage vesicles reveals LRP1 to be an important vesicle component and target of insulin signaling. *J. Biol. Chem.*, **285** (1), 104–114.
324. Evans, J.M.M., Doney, A.S.F., AlZadjali, M.A., Ogston, S.A., Petrie, J.R., Morris, A.D., Struthers, A.D., Wong, A.K.F., and Lang, C.C. (2010) Effect of Metformin on mortality in patients with heart failure and type 2 diabetes mellitus. *Am. J. Cardiol.*, **106** (7), 1006–1010.
325. Packer, M. (2019) Reconceptualization of the Molecular Mechanism by Which Sodium-Glucose Cotransporter 2 Inhibitors Reduce the Risk of Heart Failure Events. *Circulation*, **140** (6), 443–445.

326. Bayés-Genís, A., Barallat, J., Galán, A., de Antonio, M., Domingo, M., Zamora, E., Urrutia, A., and Lupón, J. (2015) Soluble neprilysin is predictive of cardiovascular death and heart failure hospitalization in heart failure patients. *J. Am. Coll. Cardiol.*, **65** (7), 657–665.
327. Bayés-Genís, A., Barallat, J., Pascual-Figal, D., Nuñez, J., Miñana, G., Sánchez-Mas, J., Galan, A., Sanchis, J., Zamora, E., Pérez-Martínez, M.T., and Lupón, J. (2015) Prognostic Value and Kinetics of Soluble Neprilysin in Acute Heart Failure: A Pilot Study. *JACC. Heart Fail.*, **3** (8), 641–644.
328. Sengenès, C., Bouloumié, A., Hauner, H., Berlan, M., Busse, R., Lafontan, M., and Galitzky, J. (2003) Involvement of a cGMP-dependent pathway in the natriuretic peptide-mediated hormone-sensitive lipase phosphorylation in human adipocytes. *J. Biol. Chem.*, **278** (49), 48617–48626.
329. Birkenfeld, A.L., Budziarek, P., Boschmann, M., Moro, C., Adams, F., Franke, G., Berlan, M., Marques, M.A., Sweep, F.C.G.J., Luft, F.C., Lafontan, M., and Jordan, J. (2008) Atrial Natriuretic Peptide Induces Postprandial Lipid Oxidation in Humans. *Diabetes*, **57** (12), 3199–3204.
330. Moro, C., Crampes, F., Sengenes, C., De glisezinski, I., Galitzky, J., Thalamas, C., Lafontan, M., and Berlan, M. (2004) Atrial natriuretic peptide contributes to physiological control of lipid mobilization in humans. *FASEB J.*, **18** (7), 908–910.
331. Chainani-Wu, N., Weidner, G., Purnell, D.M., Frenda, S., Merritt-Worden, T., Kemp, C., Kersh, E., and Ornish, D. (2010) Relation of B-Type Natriuretic Peptide Levels to Body Mass Index After Comprehensive Lifestyle Changes. *Am. J. Cardiol.*, **105** (11), 1570–1576.
332. Chen-Tournoux, A., Khan, A.M., Baggish, A.L., Castro, V.M., Semigran, M.J., McCabe, E.L., Moukarbel, G., Reingold, J., Durrani, S., Lewis, G.D., Newton-Cheh, C., Scherrer-Crosbie, M., Kaplan, L.M., and Wang, T.J. (2010) Impact of Weight Loss Following Weight Loss Surgery on Levels of Plasma N-Terminal Pro-B-Type Natriuretic Peptide. *Am. J. Cardiol.*, **106** (10), 1450–1455.

ACKNOWLEDGEMENTS

ACKNOWLEDGEMENTS

Los resultados de esta tesis se deben a muchos que de forma incondicional han estado presentes en todo mi proceso de formación, en mi cotidianidad y que hoy forman parte de esta historia y lo mejor, forman parte de mi vida.

Agradezco encarecidamente a Vicenta, la directora de la investigación, por su incansable ayuda, certeras orientaciones, gran dedicación a la investigación científica y expresión diaria de sus admirables valores personales: han sido el sostén de mi trabajo diario en el logro de estos resultados y aseguro que han hecho posible mi crecimiento profesional y personal.

De manera especial quiero agradecer, a Laura Nasarre experimentada técnica de laboratorio del grupo de Lípidos y Patología Cardiovascular que con mucha paciencia y dedicación me enseñó todas las técnicas desde mis estudios de la maestría.

A mi tutor Antonio Zorzano y a su grupo de investigación, en especial a David Sebastián, por toda la ayuda recibida durante toda la investigación.

Al grupo de investigación de Argentina dirigido por Gustavo Chiabrando (en especial a Vicky) y al grupo de la Universidad de Toulese ,en especial a Valerie Samouillan, por facilitar la tecnología, la metodología y la experiencia científica que contribuyeron a los resultados de esta tesis.

A todo el laboratorio 111, mis queridos compañeros, tanto lo que ya no están como los nuevos (David de Gonzalo, Elena Revuelta, Eduardo Garcia, Olga Bornachea, Angela Vea, Lene Claudi, María LaChica, Albert Coloma, Thalía Belmonte y Yazmín Torres) por tantas horas de trabajo colectivo y buena amistad.

Al grupo de Joan Carles y David, ellos fueron verdaderos maestros en el sorteo de obstáculos demostrando con su empeño que podemos lograr resultados valiosos con perseverancia y métodos científicos alternativos.

A Carlos Enrich le agradezco mucho el haber ofrecido su reconocida experiencia en la captación e interpretación de las imágenes de microscopía electrónica.

Diversas instituciones fueron determinantes en el apoyo de esta investigación, a todas agradezco la disponibilidad de sus recursos; quiero destacar: El Ministerio de Ciencia e Innovación de España (que concedió financiación al proyecto), al Instituto de Investigación Biomédica de Barcelona, Instituto de Investigación del Sant Pau y al Instituto de Salud Carlos III (beca PFIS) por financiar el trabajo científico durante estos cinco largos años incluyendo participación en eventos científicos y estancias de investigación internacionales de gran valor para los resultados de esta tesis.

A mi querida familia por apoyar mis interminables horas de trabajo profesional en casa y por su comprensión y amor que sustentaron el logro de mis resultados.

A todos los que me brindaron su apoyo durante estos 5 años, Muchas Gracias!